

**APPLICATION OF ANALYTICAL ELECTRON MICROSCOPY
AND CONVERGENT BEAM ELECTRON DIFFRACTION FOR
THE STUDY OF MICROSTRUCTURAL EVOLUTION IN THE
WELDMENTS OF 9Cr-1Mo STEEL**

Thesis Submitted to the
UNIVERSITY OF MADRAS
for the award of the degree of

DOCTOR OF PHILOSOPHY
in
PHYSICS

By
M. VIJAYALAKSHMI

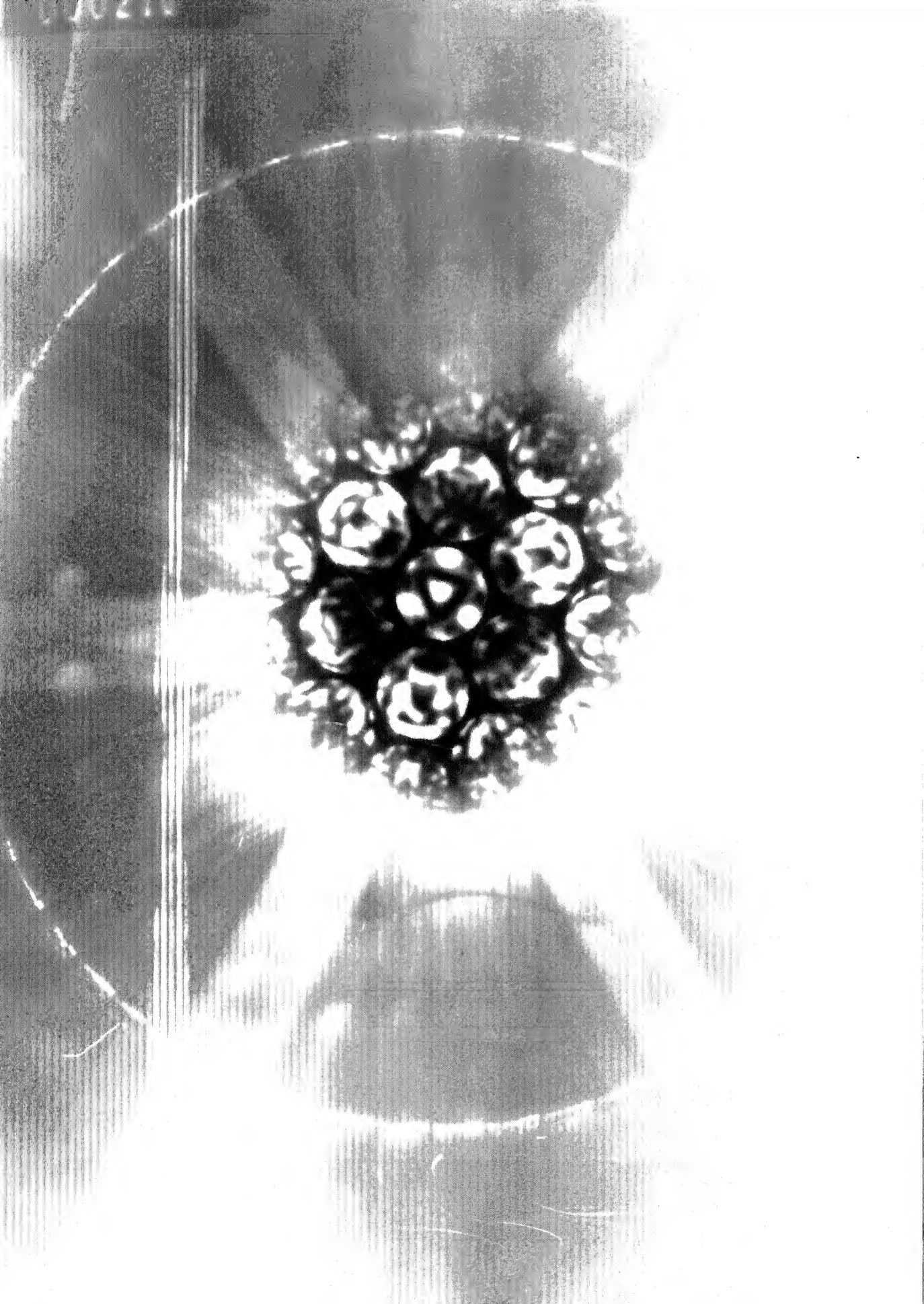
Research Supervisor
Dr. V. S. RAGHUNATHAN
Head, Metallurgy Division
Indira Gandhi Centre for Atomic Research
Kalpakkam 603 102, India

18 JUN 1999
CENTRAL LIBRARY
I. I. T. KANPUR

Acc. No. A 128275

TH
PHY 4297/P
V691a

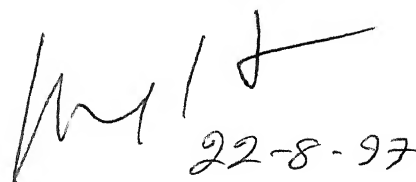




CERTIFICATE

This is to certify that the work reported in this thesis entitled "**APPLICATION OF ANALYTICAL ELECTRON MICROSCOPY AND CONVERGENT BEAM ELECTRON DIFFRACTION FOR THE STUDY OF MICROSTRUCTURAL EVOLUTION IN THE WELDMENTS OF 9Cr-1Mo STEEL**" submitted by **Smt.M.VIJAYALAKSHMI** is a record of bonafide and original research work done by her under my supervision. The work reported in this thesis has not formed the basis for the award of any other degree, diploma or any other similar title.

I further certify that the work reported in this thesis has been independently carried out by the candidate.



(Dr.V.S.RAGHUNATHAN)

Research Supervisor

Dr. V. S. RAGHUNATHAN
Head, Atomic Energy Division
Indira Gandhi Centre for Atomic Research
KALPAKKAM - 603 102

ACKNOWLEDGEMENTS

NOMENCLATURE

SYNOPSIS

CHAPTER 1

INTRODUCTION TO METASTABLE MICROSTRUCTURES

1.1	INTRODUCTION	1
1.2	RECENT ADVANCES IN ELECTRON MICROSCOPY	4
1.2.1	Analytical Electron Microscopy	4
1.2.2	Convergent Beam Electron Diffraction	8
1.3	PROBLEMS IN MICROSTRUCTURAL CHARACTERISATION	11
1.4	SCOPE OF THE THESIS	14
	REFERENCES	16

CHAPTER 2

EXPERIMENTAL DETAILS

2.1	PREPARATION OF THE ALLOYS	26
2.2	HEAT TREATMENTS AND SPECIMEN PREPARATION	27
2.3	IRRADIATION	27
2.4	TECHNIQUES USED IN THE INVESTIGATION	28
2.5	DETAILS OF ANALYTICAL ELECTRON MICROSCOPY	29
2.6	ESTIMATE OF ERRORS IN THE EXPERIMENTAL PARAMETERS	32
2.7	DETAILS OF DIFFERENT SOFTWARES	33
2.7.1	Computation Details of EMS Software	33
2.7.2	Details of TRIM code	34
2.8	Summary	35

CHAPTER 3

FORMATION OF NON-EQUILIBRIUM PHASES DURING SOLIDIFICATION OF WELDMENTS OF 9 Cr-1 Mo STEEL

3.1	INTRODUCTION	36
3.2	CHARACTERISATION OF THE BASE METAL	39
3.3	EXPERIMENTAL CLASSIFICATION SCHEMES	42
3.4	MICROSTRUCTURAL RATIONALISATION OF HARDNESS PROFILES	43
3.5	MICROSTRUTURAL CHARACTERISATION OF THE WELD ZONE	45
3.6	MICROSTRUCTURAL CHARACTERISATION OF THE HEAT AFFECTED ZONE	47
3.6.1	Microstructural Inhomogeneity of HAZ	48
3.6.2	Microchemical Inhomogeneity of HAZ	54
3.7	COMPREHENSIVE MICROSTRUCTURAL PHASE FIELDS OF PRIMARY SOLIDIFICATION STRUCTURE	55
3.7.1	Thermal Cycles of Different Regions of Weldment	56
3.7.2	Microstructural Zones of Primary Solidification Structure	57
3.8	SECONDARY SOLIDIFICATION STRUCTURE: EFFECT OF MULTIPASS	59
3.9	HETEROGENEITY IN MICROSTRUCTURE, MICROCHEMISTRY AND LATTICE STRAIN ALONG WELD CENTRE LINE	61
3.10	COMPREHENSIVE 3-DIMENSIONAL REPRESENTATION OF MICROSTRUCTURE OF 9 Cr-1 Mo WELDMENTS	63
3.11	LATTICE STRAIN ACROSS WELDMENTS	64
3.11.1	Application of CBED for Measurement of Lattice Strain	64
3.11.2	Estimation of Lattice Strain for 9 Cr-1 Mo Weldments Using HOLZ lines in CBED patterns	66

4.5.1	Concept of Phase Evolution Diagrams	91
4.5.2	Applicability of Concept of Phase Evolution Diagrams for 9 Cr- 1 Mo Weldment	92
4.5.3	Phase Evolution Diagrams of 9 Cr-1 Mo Weldment	94
4.5.4	Usefulness of Phase Evolution Diagrams	99
4.6	SUMMARY	100

REFERENCES

CHAPTER 5

STUDY OF LATTICE DISORDER IN ION IRRADIATED CRYSTALS USING CONVERGENT BEAM ELECTRON DIFFRACTION

5.1	INTRODUCTION	105
5.2	SELECTION OF CRYSTALS IN WELDMENTS OF 9 Cr- 1 Mo STEEL FOR THE STUDY OF POINT DEFECTS	108
5.3	CHARACTERISATION OF CBED PATTERNS OF UNIRRADIATED CRYSTALS IN THE WELDMENTS OF 9 Cr-1 Mo STEEL	109
5.4	IDENTIFICATION OF RELEVANT FEATURES OF CBED PATTERNS IN THE STUDY OF POINT DEFECTS	112
5.5	CHARACTERISATION OF CBED PATTERNS OF ION IRRADIATED WELDS OF 9 Cr-1 Mo	113
5.5.1	Changes in the Central Disc of CBED patterns of Ion Irradiated α - Ferrite	114
5.5.2	Changes in High Order Laue Zone (HOLZ) Rings of CBED patterns of Irradiated $M_{23}C_6$	118
5.6	SIGNATURES OF POINT DEFECTS IN CBED PATTERNS OF IRRADIATED WELDS OF 9 Cr-1 Mo	120
5.7	CBED PATTERNS AFTER POST-IRRADIATION ANNEALING	121
5.8	ORIGIN OF CHANGES IN SIGNATURES OF POINT DEFECTS IN CBED PATTERNS: SIMULATION STUDIES IN MODEL Al-14 a/o Mn SYSTEM	124

5.9	CHARACTERISATION OF CBED PATTERNS OF UNIRRADIATED Al-14 a/o Mn ALLOY	125
5.9.1	Characterisation of CBED patterns of Unirradiated α - Al	125
5.9.2	Computation of CBED patterns of unirradiated α - Al	126
5.9.3	Characteristics of CBED patterns of Unirradiated Al ₆ Mn in Al-14 a/o Mn alloy	127
5.10	CHARACTERISATION OF CBED PATTERNS OF ION IRRADIATED Al-14 a/o Mn ALLOY	127
5.10.1	Changes in the Central Disc of CBED patterns of Ion Irradiated α - Al in an Al-14 a/o Mn Alloy	128
5.10.2	Changes in the High Order Laue Zone (HOLZ) Rings of CBED patterns Of Irradiated Al ₆ Mn in Al-14 a/o Mn Alloy	129
5.11	IDENTIFICATION OF ORIGIN OF CHANGES IN CBED PATTERNS OF ION IRRADIATED CRYSTALS	132
5.12	QUANTIFICATION OF POINT DEFECTS	135
5.13	SIMILARITIES IN THE SIGNATURES OF POINT DEFECTS IN CBED PATTERNS OF MODEL SYSTEM AND 9 Cr-1 Mo WELDMENT	136
5.14	SUMMARY	137
REFERENCES		

CHAPTER 6

SUMMARY

6.1	SUMMARY	146
6.2	MICROSTRUCTURAL STUDIES ON WELDMENTS OF 9 Cr-1 Mo STEEL	147
6.2.1	Salient Features of As-welded Structure	147

6.2.2	Modification of the As-Welded Structure of Weldment of 9 Cr-1 Mo Steel At Elevated Temperatures	148
6.3	APPLICATION OF CONVERGENT BEAM ELECTRON DIFFRACTION TO THE ANALYSIS OF STRUCTURES	150
6.4	SCOPE OF FUTURE WORK	152

LIST OF PUBLICATIONS

ACKNOWLEDGEMENTS

Unbelievable but true ! A task which appeared to be impossible even as late as ten days back, has come to a completion. This could not have been accomplished without the willing, generous help of many of my friends and colleagues, to all of whom I owe a lot of thanks.

It would require more than a mere acknowledgement to express the diverse ways in which I am indebted to Smt. Saroja Saibaba and Dr.K.G. Muraleedharan Nair. They have been pillars of strength throughout this venture and have taken a lot of efforts to help me overcome my frequent diffidence to complete this venture.

It is a great pleasure to place on record my sincere thanks to Dr.V.S. Raghunathan, Head, Metallurgy Division and my Ph.D Guide, for having posed a very interesting problem to be solved with a newly emerging technique, like convergent beam electron diffraction. He has been firm in the continuation of the same project, even during very difficult times. Looking back, it has been a tough but a very fruitful decision. Overall, the work was very enjoyable, despite some frustrating moments. I thank Dr.V.S. Raghunathan for his insistence and continued help to complete this project, but for which the project would not have achieved this level of completion. I also thank Dr. V.S. Raghunathan for having read the thesis critically, despite his very busy shedule.

As a physicist, it was difficult for me to get interested in the apparently difficult transformations in steels. It was Dr. Placid Rodriguez, our Director, Indira Gandhi Centre for Atomic Research, who introduced me to this field of transformations in steels, through various assignments. At the end of these assignments, I have found

that my fears were not well founded and physical metallurgy of steels is indeed, a fascinating field. In fact, he had nourished this activity both in size and quality, with an immense vision, skill and energy, that our laboratory is the leading one in this field. I thank Dr. Placid Rodriguez, for giving me this opportunity, which has formed the major focus of the present thesis.

I thank Dr. Baldev Raj, Director, Metallurgy and Materials Group, for his constant support and encouragement, throughout the course of this project. Many positive suggestions have been given by Dr. Baldev Raj, which have helped in improving the quality of the thesis.

I thank Dr.K.G. Muraleedharan Nair, Materials Science Division, who has shaped up my understanding of convergent beam electron diffraction. The understanding of the required basics on solid state physics was lucidly taught to me by Dr.K.G. Muraleedharan Nair, without which it would have been impossible to understand the observed results. In this venture and in the learning of the EMS software, the discussions with Shri M.C. Valsakumar, Dr. B. Panigrahi, Shri E. Mohandas, Shri A.L.E. Terrance and Dr. D. Sundararaman were very useful and are gratefully acknowledged. The frequent discussions with Dr. S. Banerjee, Dr. P. Mukhopadhyay, and Dr. M. Sundararaman of BARC., Bombay were very useful and the deep personal concern shown by them in the completion of my Ph.D. thesis was very encouraging. I was also very much benefitted by discussions with Prof. S. Ranganathan, I.I.Sc., Bangalore, for which I am very thankful to him.

The advise by Prof. John Steeds, University of Bristol, regarding the possible choice of Ph.D.projects based on CBED was very helpful. The methods to overcome the practical problems while doing CBED were taught to me by Prof. Roger Vincent of the same university. The intensive training on EMS software offered by Prof.

Stadelmann, EPFL, Switzerland was very useful in the computations carried out in this thesis.

It is a matter of fact, and not at all an exaggeration, to say that the thesis would not have reached its completion but for the constant, untiring, support given by my friend and colleague, Smt. S. Saroja. The analytical electron microscopy, a voluminous work was carried out within almost an unimaginably short time. I take this opportunity to thank Smt. Saroja Saibaba, profusely for the same. In this venture, many of my colleagues with whom I enjoy working have helped me, like Shri P. Parameswaran, Shri V. Thomas Paul, Smt. R. Mythili and Shri D. Natarajan.

The work presented in the thesis is a result of the perseverant efforts of all the members of this team and it is a great joy to be working with such a friendly, hard-working team. In fact, in addition to sharing my workload, the members of this team shouldered the responsibility of even cheering me up during the few depressed moments which I went through. It is my pleasant duty to thank all the members of this team and I deem it a great privilege to be belonging to such a friendly team.

I thank Shri P. Shankar and Shri Thirumurugesan for their help in carrying out the carbon coating of innumerable number of samples in very short time.

The timely help of Shri P Sundaram of M/s. Philips India Ltd, Madras throughout the period of this report was extremely helpful, which is gratefully acknowledged.

I thank Smt. M. Radhika for not only doing all the SEM work required for the thesis, but for also ably taking care of the requirements of SEM laboratory, without my intervention at times when I could not divert time due to my preoccupation with the Ph.D work

During the time of writing the thesis, it was not possible to attend completely to all my official work. During such times, Smt. T. Ezhilarasi and Shri P. Parameswaran shared all these work, which for their own reasons of urgency, could not be delayed. I thank both of them for their timely help.

I thank Shri Vincent Paulraj for having helped me in the process of printing difficult negatives of CBED, revealing all the important details of the negatives.

It is my pleasure to thank Dr. Indira Murthy, for having very carefully read the thesis, within a very short time.

It is my pleasure to thank Shri Shakthi, for having helped me in the preparation of all the line drawings. I thank Shri T.D. Sundarakshan, for having prepared the whole manuscript in a short time, without which it would have been impossible to meet the time target.

Finally, I come to the most difficult part of thanking my husband and children, for their cooperation. There is no appropriate word to truly express my feelings in this venture. They have put up with my absence during all the holidays and all the evenings till 10 p.m., for a very long time - practically last one year. Very often, I feel guilty for depriving them of their share of my time and question if my judgement of priorities is well-balanced. Having always got a negative answer, I only hope that I would be able to make the loss good, in the coming months.

(M. Vijayalakshmi)

L	Liquid
τ	Austenite
δ	Delta-Ferrite
α	Pro-eutectoid Ferrite
α^{SS}	Supersaturated Ferrite
α'	Martensite
$\sigma,$	Secondary phases
M	Substitutional element in M_xC_y
M_xC_y 's	Different metastable carbides (experimentally identified) like Fe_3C , Cr_2X
X, Y	Two hypothetical metastable carbides
β	Equilibrium hypothetical carbide
n	Number of metastable carbides like M_xC_y
A_f	Area fraction of n^{th} carbide
N_f	Number density of carbides
$N_f(\text{glob.})$	Number density of globular carbides
$N_f(\text{aci})$	Number density of acicular carbides
T	Temperature
M_s	Martensite start temperature
A_{c1}, A_{c3}	Temperature at which τ and α enters $(\tau+\alpha)$ field respectively
T_{max}	Maximum temperature the region is exposed to
T_t	Tempering temperature

α_x, α_y	Interfacial composition of carbon in ferrite which is in local equilibrium with x and y at time $t = t_1$ and t_2 respectively
C_0	Initial composition of any element
α_{eq}	Equilibrium composition of carbon in ferrite
$(C_0 - C_x)$	Composition gradient of the same element
$C_{x,t}$	Composition of the element at x after time t
β_x, β_y	Interfacial composition of carbon in X and Y coexisting with ferrite at time $= t_1$ and t_2 respectively
CS-1 to CS-10	Cross sections 1 to 10, Sections cut parallel to weld centre line
$\frac{C_{Cr}}{C_{Fe}}$	Ratio of concentration of chromium to that of iron
R_1	Reinforcement height
R_2	Reaustenitisation distance
FWHM	Full Width at Half Maximum
s	Strain parameter
HAZ1	HAZ near weld
HAZ2	HAZ near base metal
HOLZ	High Order Laue Zones
FOLZ	First Order Laue Zone
α or α_c	Angle of convergence
θ	Angular position of HOLZ
G	Diameter of FOLZ ring
R	Radius of Ewald sphere
λ	Wavelength of incident beam
H	Reciprocal lattice layer distance

t	Thickness of electron transparent foil
u	Average mean square displacement
F_x	Chemical free energy difference between α of composition C_0 and that of mixture of α and X at t_1
F_y	Same for Y at t_2
F_β	Same for β at equilibrium

SYNOPSIS

APPLICATION OF ANALYTICAL ELECTRON MICROSCOPY AND CONVERGENT BEAM ELECTRON DIFFRACTION FOR THE STUDY OF MICROSTRUCTURAL EVOLUTION IN THE WELDMENTS OF 9Cr-1Mo STEEL.

INTRODUCTION :-

The service life of components in many applications is often limited by the reliability of weld joints. The variations in the properties, as a consequence of microstructural changes across weldments, generally, lower the lifetime of components. The formation of complex microstructure in weldments is attributed to the presence of steep thermal gradients, elastic and plastic strain due to rapid heating and cooling rates and varying microchemistry due to repartitioning of solutes (1). Unique identification of microstructures of welds is difficult, due to presence of low amounts and non-uniform distribution of the phases. The problem is more complicated in steels, since the structurally similar phase, for example, ferrite, can precipitate as different allotriomorphs, resulting in entirely different properties. Hence, it is worthwhile to apply the advances in the methods of microstructural characterisation, for accurate description of such complex structures.

The objective of the present thesis is to understand the microstructural variations in welds of 9Cr-1Mo ferritic steels, using the advanced techniques of transmission electron microscopy, like the analytical electron microscopy (AEM) and convergent beam electron diffraction (CBED). The thesis identifies problems in determining the fine structural variations during evolution of non-equilibrium structures and presents solutions to few selected problems, using AEM and CBED. The systematic studies in the welds of 9Cr-1Mo steel offer insight into the following aspects:- a) evolution of primary and secondary structures and formation of steep strain gradients, during welding, b) growth of series of secondary carbides at elevated temperatures and c) defect production during ion irradiation. The results are analysed based on the principles of phase transformations and thermodynamics. Based on these detailed analyses, 'phase evolution diagrams', have been proposed which can predict the evolution of non-equilibrium phases, in the welds of 9Cr-1Mo steel.

The steel of interest, i.e., 9Cr-1Mo, is used in conventional power industry due to good corrosion resistance and acceptable high temperature mechanical strength. These steels are promising candidate materials for core components of fast breeder nuclear reactors, due to their excellent void swelling resistance (2). Despite these advantages, the use of ferritic steels is limited due to their strong tendency to become brittle. Additionally, the high temperature austenite can decompose (3,4) in many ways, which depends crucially on the rate of cooling and chemistry of the steel. Some of the phases that form in welds of ferritic steels during solidification are deleterious leading to frequent failure of the weldments. Therefore, it becomes essential to prevent the formation of such phases, which needs precise identification of such phases.

SCOPE OF THE THESIS :-

The specific problems which the thesis addresses are as follows:-

Role of thermal cycling in the evolution of metastable phases in the weld condition.

Formation of delta-ferrite in welds using CBED.

Lattice strain measurements across various regions of the welds using CBED and X-ray diffraction.

Generation of 'Phase Evolution Diagrams', using thermodynamic principles. Prediction of the evolution of secondary phases using these diagrams.

Study of lattice disorder introduced during ion irradiation of the parent ferrite phase and the carbide, $M_{23}C_6$. An attempt has been made for the first time, to identify the presence of isolated, point defects, prior to the agglomeration of defects into clusters using CBED.

†

The dependence of 'primary' or 'as deposited' structure on transient conditions which prevail when the liquid solidifies rapidly, during welding, is studied. Effect of multipasses on the evolution of 'secondary' or 're-heated' structure, in manual metal arc welds of 9Cr-1Mo steel is discussed. A brief account of results of the microstructural and analytical electron microscopy studies of the primary and re-heated structures are as follows:-

Concentration of solutes varies as the distance from the weld centreline increases (Figure.1.) and there is an enhancement in the Chromium content in HAZ close to weld.

Primary microstructure is found to show four distinct regions, namely columnar grains cooled rapidly from liquid, re-austenitised zone, inter-critical zone - a narrow region of HAZ exposed to $\gamma + \alpha$ region and the parent metal.

Secondary structure, reveals the repetition of microstructurally distinct regions, like the columnar, coarse-grain and fine grain regions corresponding to various thermal cycles experienced by microscopic regions during multipass welding.

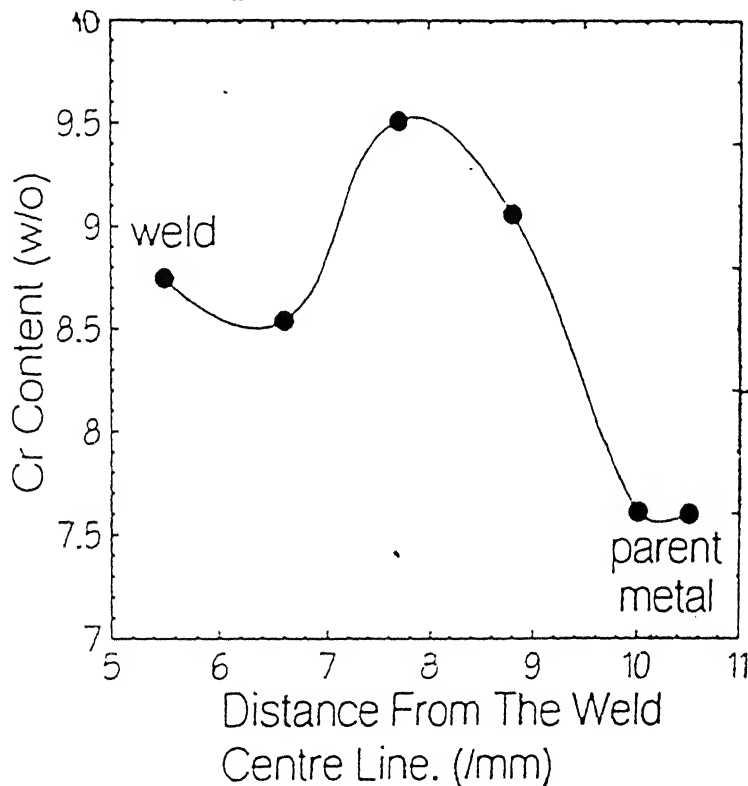


Figure.1. Variation in the composition of chromium of α of various cross-sections, taken from weld to parent metal.

The results of these studies are rationalised (5) based on the thermal cycles, kinetics of various phase transformations which the steel is expected (3) to undergo and the repartitioning of solute elements into various co-existing phases. The microstructural results are presented in comprehensive three-dimensional phase field diagrams (Figure.2.) One

of the uncertainties of microstructural studies in 9Cr-1Mo steel has been the presence of high temperature delta-ferrite phase. CBED technique is ideally suited as it can be used to monitor the lattice strain by means of variation in angular position of high order Laue zone (HOLZ) lines. The lattice strain can be an index to distinguish strain-free delta-ferrite in a highly strained martensitic matrix. The present study shows that delta-ferrite is not likely to be present in the welds of 9Cr-1Mo steel. .

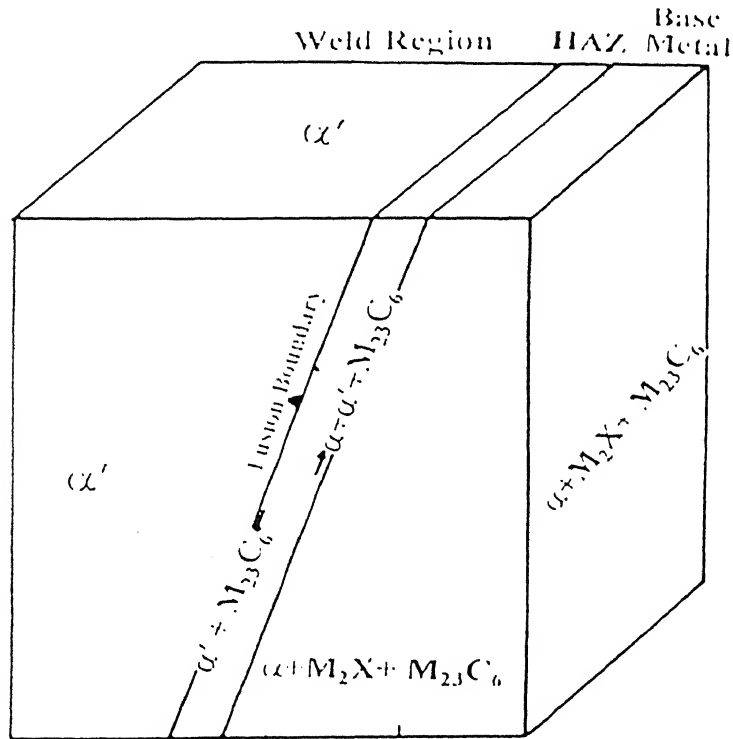


Figure.2. Three dimensional representation of the various phase fields in welds of 9Cr-1Mo.

This is consistent with the chemistry of the steel and the anticipated kinetics (3) of delta-ferrite formation in wrought steel and the time of stay of the welds at the temperatures where delta-ferrite is expected to form. The lattice strain variation of microscopic regions, from weld metal through heat affected zone (HAZ) to the parent metal, arising due to thermal cycles, has been studied using angular position of HOLZ lines in CBED patterns and compared with CBED calculations and X-ray diffraction results (Table.1.).

Microstructural modification of welds of 9Cr-1Mo steel at elevated temperatures has been systematically studied using AEM, the characteristic

compositions of the major phases being shown in Table.2. The symmetry elements of the major microstructural constituents, α ferrite, and $M_{23}C_6$, have been identified (Table.2.), using CBED. The micro-chemistry of the phases is found to vary widely with ageing temperature. A detailed study of the variation of microchemistry of the secondary phases at elevated temperatures has been carried out. The results were analysed in the light

Table.1.

Variation of lattice strain of α from HAZ near weld to parent metal.

Sl. No	HOLZ line*	Region	CBED experimental	% strain		
			Values θ (mrad)	CBED	XRD	
1.	a	Parent	12.069	-	-	*
2.	b	Metal(PM).	13.79	-	-	
3.	a	HAZ				
4.	b	"	18.97	0.38	-	
5.	a	HAZ				
		near weld.	21.429	0.78	0.75	
6.	b	"	23.81	0.73	-	

a and b refer to the two distinct points of intersections of the deficiency lines corresponding to () and () and () and (), respectively. ←

of thermodynamic principles of the driving force for the evolution of secondary phases. Based on these, 'phase evolution diagrams', (PED) are generated, which show the variation of concentration of carbon with ageing time, in which various phase fields are superimposed. A typical example of PED is given in figure 3. The variation in the carbon content of the ferrite matrix was calculated using the mass balance equation. Microstructural parameters like the amount of various co-existing phases, their micro-chemistry and stoichiometry, evaluated based on the exten-

sive studies were useful to arrive at the carbon content of the ferrite matrix. The utility of these diagrams to predict evolution of secondary phases has been discussed.

Table.2. Details of micro-chemistry (a) and symmetry (b) of different phases in 9Cr-1Mo welds, using AEM and CBED respectively.

Table.2.a. AEM results on micro-chemistry (typical at 823K).

Sl. no.	Phase	Micro-chemistry (w/o)		
		Fe	Cr	Mo
1.	α (as welded)	91.35 + 0.3	7.61 + 0.3	1.05 + 0.08
2.	$M_{23}C_6$	20 -21	63 - 64	13 - 14
3.	M_2X	4 - 5	83 - 84	13 - 14

Table.2.b. CBED results on Symmetry.

Sl. no.	Phase	Symmetry Details			
		Zone Axis	Zone Axis symmetry	Diffraction Group	Crystal Point Group
1.	α	$\langle 200 \rangle$	$4mm1_R$	6_Rmm_R	$m3m$
	"	$\langle 220 \rangle$	$2mm1_R$		
	"	$\langle 222 \rangle$	6_Rmm_R		
2.	$M_{23}C_6$	$\langle 200 \rangle$	$4mm1_R$	6_Rmm_R	$m3m$
	"	$\langle 220 \rangle$	$2mm1_R$		
	"	$\langle 222 \rangle$	6_Rmm_R		

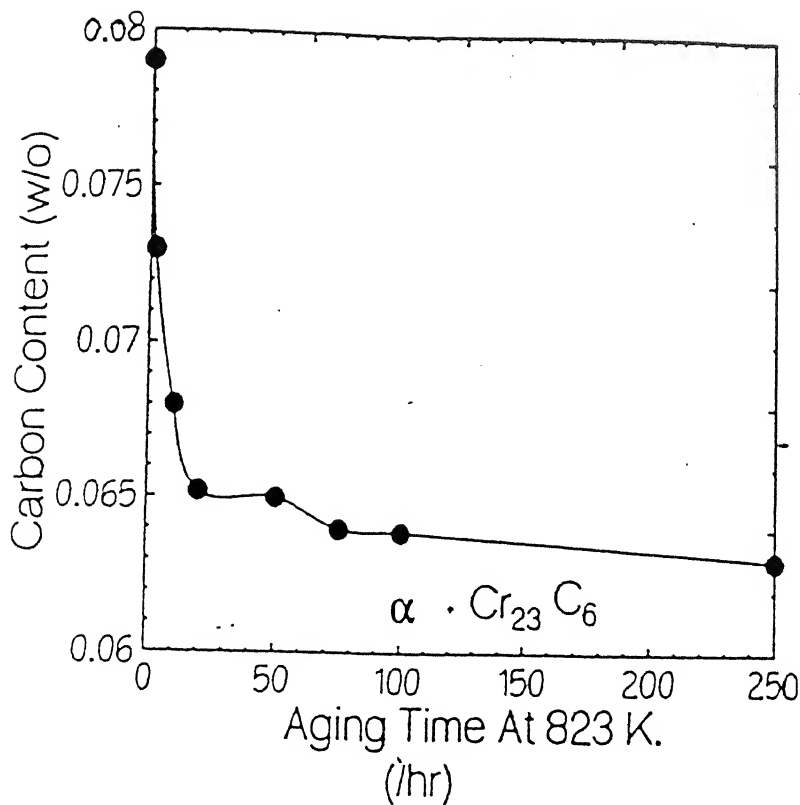


Figure.3. Typical Phase Evolution Diagram of weld region at 823 K.

In view of the excellent void swelling resistance of ferritics, the influence of irradiation on welds of 9Cr-1Mo steel assumes direct relevance in their use as materials for application in nuclear reactors. Though extensive literature is available (6) on the evolution of defect structure in ferritic steels during irradiation, the study of defects prior to their agglomeration into clusters, using electron microscopy has not been attempted so far. In addition, most of the reports pertain to evolution of defect structure in the parent α phase and very few (7) on the secondary phases, though their response to irradiation also is equally important. The present study, on the other hand, reports the early stages of evolution of defect structure and the annihilation during in-situ post-irradiation annealing, in carbides also.

The present study identifies the characteristic signatures of point defects in CBED patterns. The intensity of elastic scattering at large angles, i.e., HOLZ rings has been found to decrease with increase in dose and the mass of the incident ions. Based on simulation studies on a simple, binary alloy like Al-14 at/o Mn, these changes have been explained (8) as resulting

from an increase in static displacement disorder. This interpretation enabled modelling the process using Debye-Waller factor, to obtain relative intensities of HOLZ rings with irradiation dose. The advantage is that CBED pattern can be simulated and compared to experimental pattern. These studies suggest that early stages of defect production during ion implantation of welds of 9Cr-1Mo can be identified using CBED.

ORGANISATION OF THE THESIS :-

There are six chapters in the thesis, entitled APPLICATION OF ANALYTICAL ELECTRON MICROSCOPY AND CONVERGENT BEAM ELECTRON DIFFRACTION FOR THE STUDY OF MICROSTRUCTURAL EVOLUTION IN THE WELDMENTS OF 9Cr-1Mo STEEL.

The first two chapters serve the purpose of introducing the subject of the thesis and the details of the various experimental facets of the thesis. The first chapter provides a detailed review of the present state of the understanding of the behaviour of ferritic steels and the problems which need further attention.

The third chapter titled, **Evolution of Non-Equilibrium Phases During Solidification of Welds of 9Cr-1Mo Steel** deals with the influence of thermal cycling on resultant microstructure and micro-chemistry.

The fourth chapter titled, **Microstructural Modifications During Exposure of 9Cr-1Mo welds to Elevated Temperatures** discusses the evolution of secondary phases in various regions of the weld during exposure of the welds at high temperatures, ranging from 873 to 1273 K.

The fifth chapter deals with **Lattice Disorder in α -iron and $M_{23}C_6$ during ion irradiation.**

The last chapter on **Summary** presents the major conclusions of the studies reported in the thesis and scope for further studies.

REFERENCES

1. V.S.Raghunathan,V.Scetharaman,S.Venkadesan and P.Rodriguez, Met. Trans., 10A, 1683, 1979.
2. P.Rodriguez,S.L.Mannan and Baldev Raj, Proc. of seminar on Fast Reactor Fuel Cycle, Vol.ii, held at IGCAR, Kalpakkam during Feb., 1986.
3. S.Saroja,M.Vijayalakshmi and V.S.Raghunathan, J.Mater.Sci.,27,2389,19
4. S.Saroja,M.Vijayalakshmi and V.S.Raghunathan, J.Nucl.Mater.,232,226,
5. S.Saroja,M.Vijayalakshmi,V.Thomas Paul and V.S.Raghunathan, Presented at the Annual Technical Meeting of Indian Institute of Metals, held at Calcutta, during Nov., 14 - 17, 1995.
6. S.Saroja, M.Vijayalakshmi and V.S.Raghunathan., Materials Science and Engineering, A154, 59, (1992).during Nov., 14 - 17, 1994.
7. D.S.Gelles, J. Nucl. Mater., 108, 512, 1982.
8. B.A.Senior, F.W.Noble and B.L.Eyre, Acta. Metall.,34, 7, 1321, 1986.
9. M.Vijayalakshmi, K.G.M.Nair and V.S.Raghunathan., Proc. of ICEM conference held in Paris, France during June, 1994.

LIST OF FIGURE CAPTIONS

Figure.1. Variation in the composition of chromium of α of various cross-sections, taken from weld to parent metal.

Figure.2. Three dimensional representation of the various phase fields in welds of 9Cr-1Mo.

Figure.3. Typical Phase Evolution Diagram of weld region at 823 K.

LIST OF TABLES

Table.1. Variation of lattice strain of α from HAZ near weld to parent metal.

Table.2. Details of micro-chemistry and symmetry of different phases in 9Cr-1Mo welds, using AEM and CBED respectively.

CHAPTER 1

INTRODUCTION TO METASTABLE MICROSTRUCTURES

1.1 INTRODUCTION

Development of newer materials and novel processing routes has witnessed an unprecedented, revolutionary change in recent decades. Today, the key industries like power industry, electronic industry, aerospace industry etc., demand "tailor-made" materials. The types of newer materials which are developed, depend primarily on the requirements of these industries.

For example, conventionally, the power industry needed (1) steels with only high creep resistance. Subsequently, emergence of nuclear power has imposed a demand (2) for improved steels for reactor vessels, fuel reprocessing etc. The fast breeder reactors exert higher demands (3,4) on materials than thermal reactors, owing to the combination of high neutron flux, high temperatures and specific corrosive environments. Consequently, a number of special steels have been developed like the superalloys (5-8), high alloyed steels (9,10), 316LN steels (11,12), D9 steels (13,14), Mn steels(15), the ferritics (16-20) etc.

Other industries also have witnessed the emergence of a number of novel materials like high temperature superconductors (21,22), intermetallics for turbine engines

(23), ceramics for micro-electronics and high temperature use (24,25) and rapidly solidified materials of amorphous alloys for magnetic applications (26). A rational design of newer alloys needs an understanding of the influence of their microstructure on the properties. This, in turn, enables the selection of appropriate process parameters, in order to obtain the best combination of properties.

Development of continuous casting of steels, components for communication technology, development of procedures of synthesis for exotic compounds are a few success stories of endeavours in this area. Thus, the understanding of the microstructure is essential not only for the design of new materials, but also for developing better processes or synthesis routes. The extensive studies in these fields have led to improvements in the mechanical, electrical and magnetic properties of alloys and the economics of their production.

The sustained effort to extend the vistas of the materials world has had a direct impact in the development of techniques used for microstructural characterisation. Complex, novel microstructures are generated in the newer materials prepared using the new processing routes and, under hostile environments of stress, irradiation and corrosive atmosphere. Consequently, there has been a myriad revolutionary changes in the field of microstructural characterisation.

The historical journey in this field dates back to the days of optical microscopy for biologists and petrographers (27), its extension to the study of structure of metals intercepted by a major breakthrough - the discovery of X-ray diffraction (28,29), followed by electron microscopy. Very often, it is essential to use a number of complimentary techniques (Figure 1.1) to arrive at the complete understanding of the structure of a material. There have been constant efforts in every field to expand the limits of its application range.

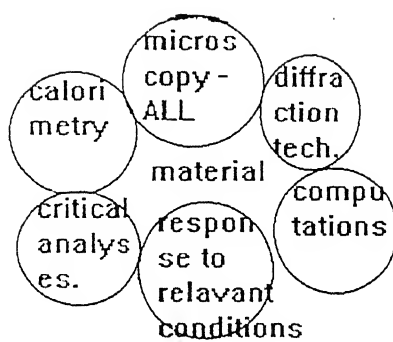


Figure 1.1 Complimentary techniques in the analysis of structure of materials.

One of the most powerful techniques for structure determination is the X-ray diffraction. The advances in this field have reached (30) the level of determination of position of atoms with an accuracy of 0.001%. However, this technique needs large (1 mm) crystals. The emergence of newer processing routes and materials has made it impossible to meet this demand - by providing a wide spectrum of metastable microstructures with submicrometer sizes. The developments in electron diffraction and its application (31-34) to materials science resolved the problem of identification of submicrometer crystals, using electron diffraction. However, it was not possible to obtain accurate structure refinement data as in X-ray diffraction. This is due to strong, dynamic interaction of electrons with crystal ions. Parallel developments of imaging techniques, (34) provided morphological details of the diffracting crystals. Thus, the field which was initially confined to only diffraction, finally evolved into electron microscopy. This single advantage of being able to get morphological details practically widened the range of its application, like the study of tumors, intermetallics and ceramics.

Developments in the field of electron probe micro-analysers (35,36) and solid state X-ray detectors (36) led to the development of a variety of analytical techniques. Some of the common analytical techniques are compared in Table I.1a and b. Today, it is possible to explore the microscopic world and obtain morphological, structural and microchemical data simultaneously from regions as small as 10 nm. All these painstaking, creditable efforts have made it possible today, to view atoms using high resolution electron microscopy.

This introductory chapter discusses the situations wherein unambiguous identification of the microstructural feature is difficult, following the detailed discussion on some of the recent advances in the field of electron microscopy.

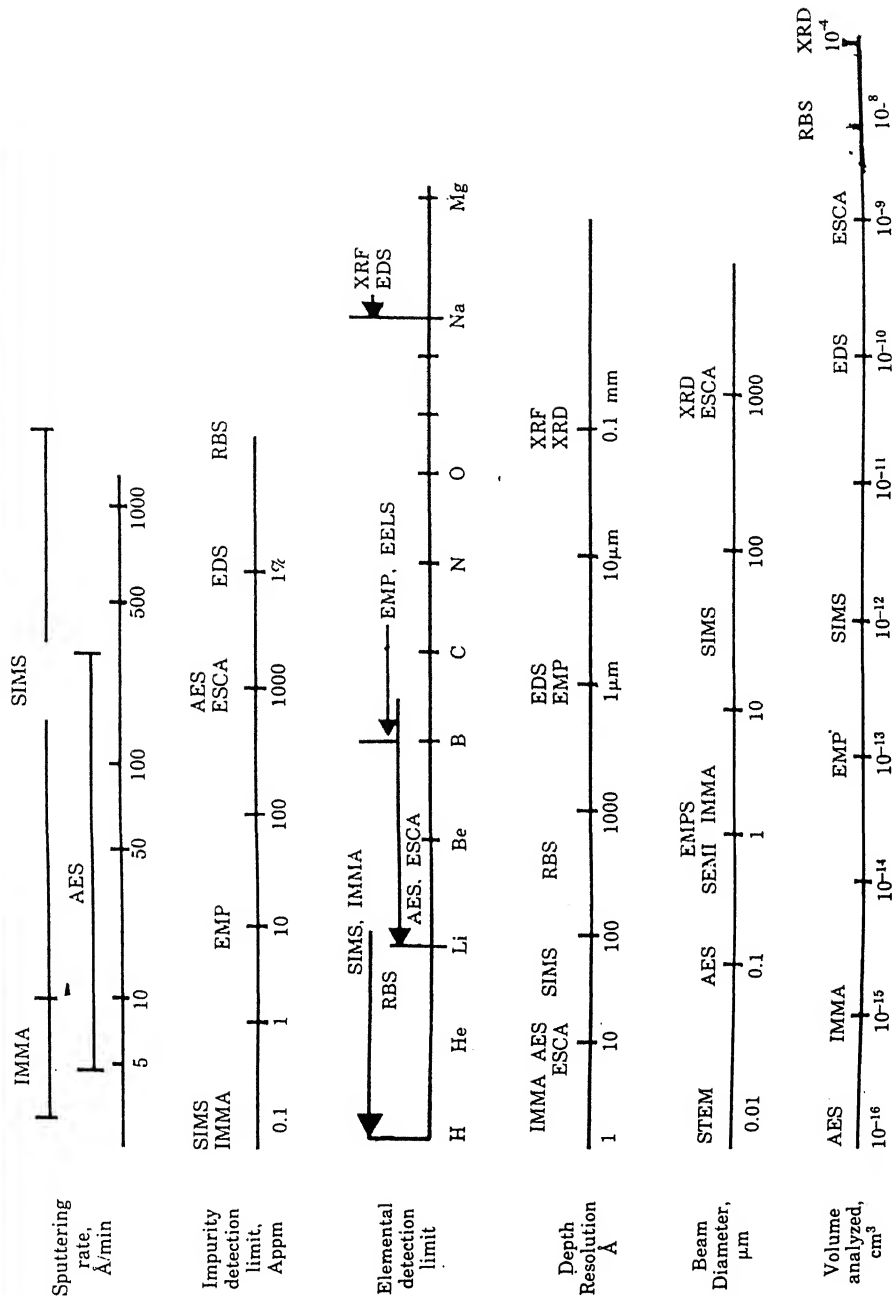
Table I.1a

Most Common Beam Optics Instruments and Analytical Methods

Incident Beam/Resulting Radiation						
	Secondary Electrons	Back- Scattered Electrons	Transmitted Electrons	Photo- electrons	Auger Electrons	X-rays
Electrons	Scanning elec- tron microscopy (SEM) — topography	Scanning elec- tron microscopy — enhanced atomic weight sensi- tivity	(Scanning) trans- mission micro- scopy (S) TEM, energy loss analysis (EELS)	—	(Scanning) Auger electron spectroscopy (AES)	Energy disper- sive analysis — EDS wave- length disper- sive micro- probe
X-rays	—	—	—	X-ray photo- electron spectroscopy (also known as ESCA)	Auger	X-ray diffraction- residual stress
Ions	(SEM)	—	—	—	—	(PIXE)
						Mass spectroscopy (SIMS) or (IMMA) Ruther- ford backscatter (RBS)

Table I.1b

Comparison of Various Analytical Methods



Code: AES: Auger electron spectroscopy
EDS: Energy dispersive x-ray analysis
EMP: Electron microprobe
ESCA: X-ray photoelectron spectroscopy (XPS)
EELS: Electron energy loss spectroscopy
IMMA: Ion microprobe mass analysis
RBS: Rutherford backscatter analysis
SIMS: Secondary ion mass spectroscopy
XRD: X-ray diffraction
XRF: X-ray fluorescence

The most recent advances (37-80) in the field of electron microscopy, like the analytical electron microscopy (AEM) (66-80) and the convergent beam electron diffraction (CBED) (37-65), will be discussed in detail. These two major fields have witnessed a number of successful techniques like ALCHEMI- Atom Location by Chemical information, parallel electron energy loss spectroscopy - PEELS, Z-contrast microscopy, coherent nano-diffraction for STEM lattice imaging, in-line holography and off-line electron holography. These will be briefly discussed in the next section. The additional information using advanced techniques have enabled to resolve some of the controversies in unambiguous characterisation of structures, which will be discussed subsequently. Finally, a brief discussion of the scope of the thesis, is presented.

1.2 RECENT ADVANCES IN ELECTRON MICROSCOPY

Of various attempts in the field of electron microscopy, the Analytical Electron Microscopy (AEM like the ALCHEMI, PEELS, etc.) and the convergent beam electron diffraction (CBED, coherent nano-diffraction, electron holography, in-line and off-line holography) are the recent successes. Table I.2 lists briefly, the principle of each technique and its applications in the recent years, which will be discussed in detail below.

1.2.1 Analytical Electron Microscopy

The field of analytical electron microscopy encompasses a wide range of techniques like the microanalysis using EDAX, atom location using ALCHEMI, light element analysis using parallel electron energy loss spectroscopy PEELS and Z-contrast

Table I.2

Basic Principles and Applications of recent Advances in TEM

Sl.No.	Name	Principle	Additional Information
1.	AEM	Incident electrons generate characteristic X-rays, energy of the X-ray being the signature of the element and intensity of the X-ray signal gives the amount of the element.	Microchemical information from 1 nm regions.
2.	ALCHEMI	Intensity of the X-rays is more if direction of incident electrons is along electron channelling direction and less for other directions.	The difference in X-ray intensity for two different incident angles is used to arrive at the position of atoms.
3.	PEELS	Primary incident electrons lose a part of their energy by primary ionisation events with core electrons.	Microchemical information about light elements, valence states and electron density of states.
4.	CBED	Diffraction of incident electrons, when the angle of convergence of the incident beam is much higher than the Bragg angle.	1) 3-D information about reciprocal lattice. 2) Symmetry. 3) Defects and Atom positions
5.	Z-mapping	Image the ratio of the intensity of elastically scattered and inelastically scattered beam, using PEELS and an annular detector.	Variation in Z can be imaged with high resolution.
6.	Electron Holography or Coherent Nanodiffraction	CBED with FEG electron source and large angle of convergence.	Site symmetries, STEM lattice imaging and atom position.

microscopy. In order to give a complete review of the state-of-art electron microscopy techniques, all these methods are described in this section.

The genesis of ATEM can be traced back to 1968 (66), when Duncumb mounted a wavelength dispersive analyser to TEM, to obtain chemical, structural and diffraction data from the same region of the thin foil. This idea of combining TEM and EPMA has finally evolved into the field of Analytical Electron Microscopy. The development of Scanning Transmission Electron Microscope (STEM) and the field emission guns has offered fine incident probes of the order of 2 nm. This has increased the spatial resolution for analytical electron microscopy. For various design considerations, the energy dispersive analysers have become more useful than the originally used wavelength dispersive analysers. These developments were followed by concerted efforts to quantify the X-ray data obtained. Of various approaches attempted, the most useful method is the Cliff-Lorimer's ratio technique (65). This method is as follows : If the region of interest on the thin foil is assumed to be infinitely thin, the X-rays measured can be assumed to be the same as the X-rays that leave the foil. This is called the 'thin film criterion'. In practice, the thin film criterion is assumed to be satisfied, if the intensity difference between the region of interest and an infinitely thin region of the foil does not vary by more than 10%. Then, the mass concentration ratio of the two elements A and B in a foil is given by

$$C_A/C_B = K_{AB} \times (I_A/I_B) \quad 1.1$$

wherein K_{AB} , the proportionality constant is independent of thickness and composition of the elements, A and B, and I_A/I_B is the ratio of intensities of the characteristic X-rays of A and B. The advantage of the ratio method is that it is independent of the foil thickness and fluctuations in the intensity of the incident beam.

The application of AEM to ALCHEMI was possible due to a large number of parallel developments in other areas. ALCHEMI is a technique to identify Atom Location using CHEMical information using AEM. In early 1940's, Borrmann (66) discovered that the absorption of an X-ray beam by a single crystal was sensitive to its angle of incidence. In 1949, von Laue (67) explained this effect: the incident radiation establishes a standing wave across the crystal (Figure 1.2) with the period of the lattice whose maxima coincide with the atoms for certain incident beam directions, resulting in enhanced absorption; if the maxima fall between the atoms, there is reduced absorption. Subsequently, similar observation of orientation dependence of X-ray emission with various incident beams was observed. For example, increase in the yield of X-rays was as observed with incident beam of X-rays by Batterman (69) and with electrons by Duncumb (70). The application of this effect to obtain structural information, atom location or crystal site location was developed (71-75) in the late periods of 1980's. This effect, i.e., enhanced X-ray emission, generally occurs along 'electron channelling' directions. ALCHEMI uses the variation of characteristic X-ray emission with the direction of an exciting electron beam in an analytical transmission electron microscope. This method may be applied to nanometer-sized crystals and to concentrations as low as 0.1 atomic percent. It is capable of distinguishing neighbours in the periodic table and does not require external standards.

The necessity to analyse light elements, like carbon, nitrogen upto beryllium, had led (76-78) to the development of electron energy loss spectroscopy (EELS). In this technique, the primary event (Figure 1.3a) of the incident electron losing energy to the inner shell excitations is monitored, using a magnetic spectrometer. If the transmitted electrons are collected simultaneously and energy analysed to find out

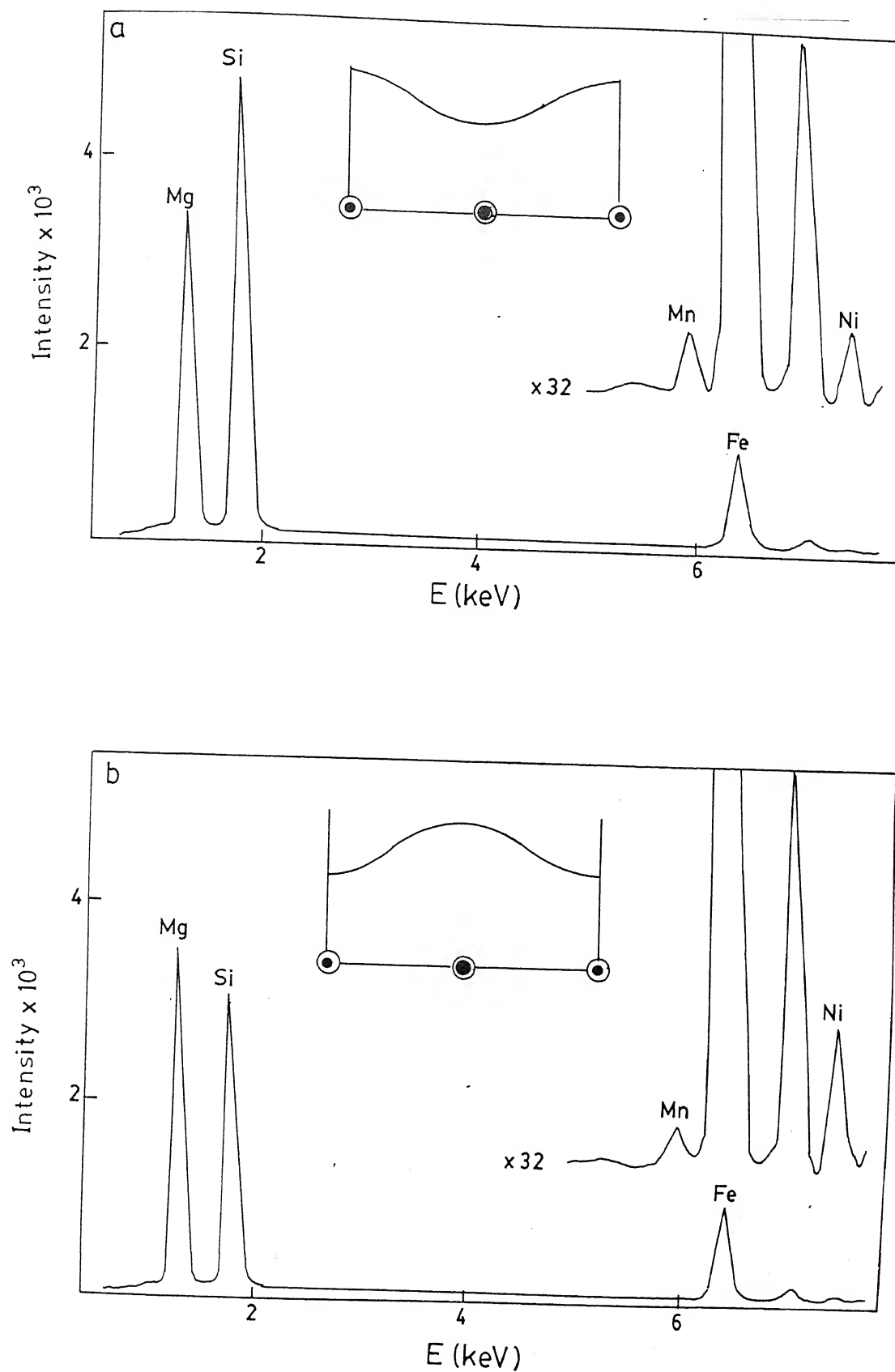


Figure 1.2 Principle of ALCHEMI: EDAX spectra (71) from a crystal of olivine at two different angles of incidence, θ_i . (a) $\theta_i < \theta_{020}$ and (b) $\theta_i > \theta_{020}$. Insets show the atomic arrangement along (010) and the variation of the thickness-averaged electron intensity. O - oxygen; ● silicon and o - cations. Compare the X-ray intensity of Mn and Ni in (a) and (b).

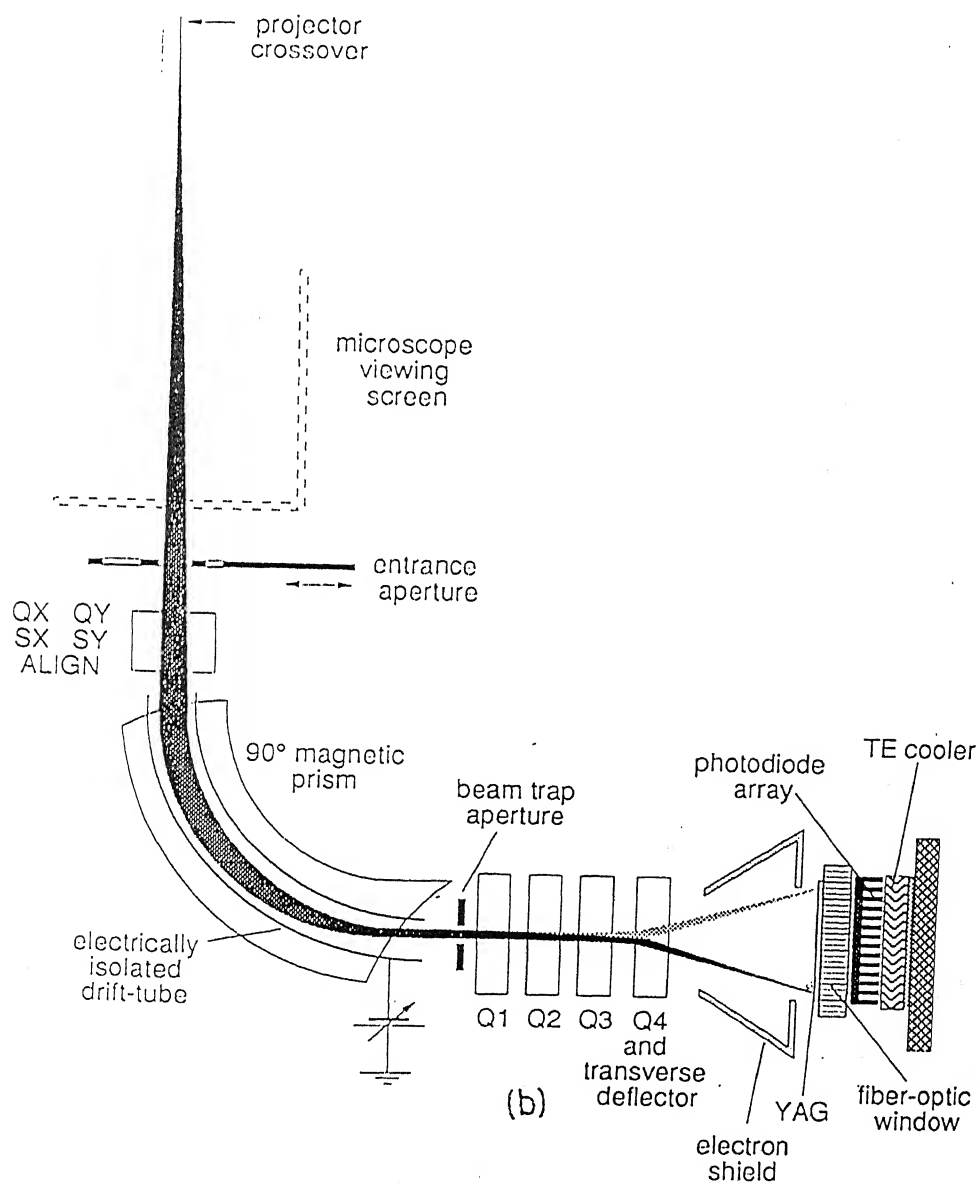
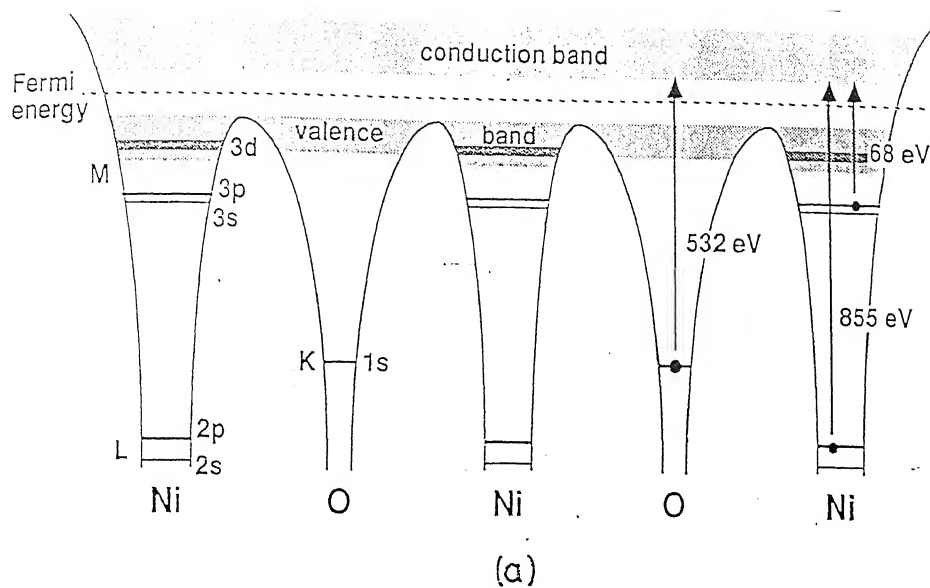
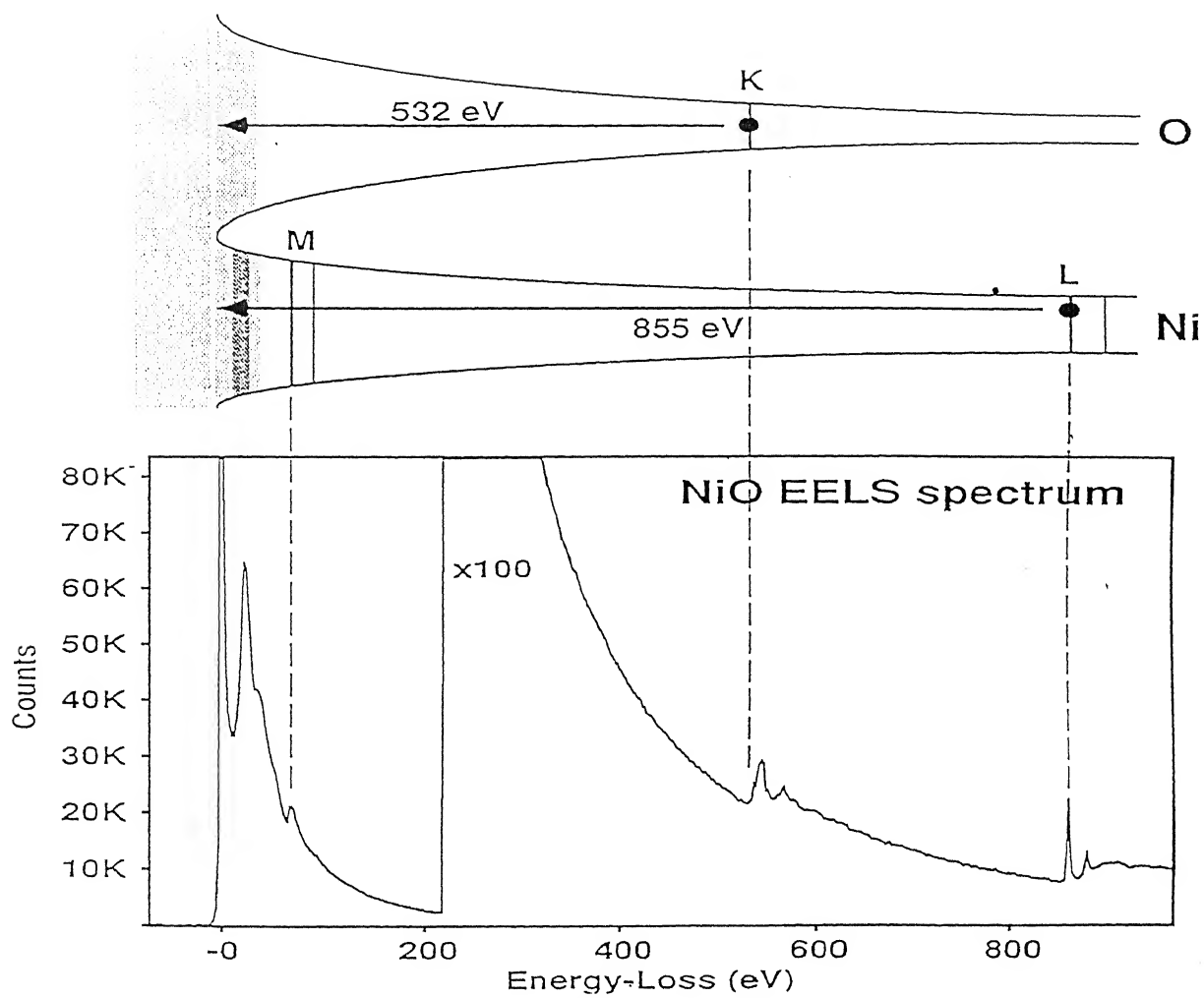


Figure 1.3 Principle of PEELS : (a) Origin of signal and (b) an experimental set up of PEELS spectrometer and (c) a typical PEELS spectrum showing the different regions: (i) zero loss peak, (ii) plasmon losses and (iii) characteristic ionisation edges



(c)

Figure 1.3 (continued)

the loss in energy of incident beam during primary ionisation events, the technique is called the parallel EELS or PEELS. The principle of this technique is illustrated in Figure 1.3b. This technique gives information about the microchemistry of light elements, chemical valence state, atom site location by making use of channelling effect and the electron density of states. The different regions in a typical PEELS spectrum, the origin of these regions and uses are illustrated in Figure 1.3c and Table I. 3. The capabilities of this technique is listed in Table I.4.

The PEELS detector collects the elastically scattered and the inelastically scattered electrons. The angular distribution of these electrons differs substantially and is schematically shown in figure 1.4. Most inelastically scattered electrons are scattered within a narrow cone around (000) and the scattering probability is $Z^{1/2}$. The scattering probability of elastically scattered electrons is $Z^{3/2}$. Ratio of pure elastic to inelastically scattered electrons is proportional to atomic number, Z . It is known (79,80) that elastically scattered electrons are confined to a narrow angular range around the Bragg angles and the inelastically scattered electrons are scattered through larger angles (figure 1.4). Therefore, two detectors, namely, the bright field BF and an annular dark field DF detectors are mounted. The signals from the BF and the annular DF detectors are collected and their ratio is imaged. The main principle of Z-contrast microscopy is to image the ratio of the signals from the two detectors, i.e., the two types of elastically scattered and inelastically scattered electrons. Hence, in the experiments involving Z-contrast microscopy mostly in biological applications, the PEELS is fitted with two annular detectors. The bright field detector collects the elastically scattered electrons and the dark field annular detector collects the inelastically scattered electrons. The signals from these two detectors are processed electronically to get the Z-contrast.

Table I.3

Useful Signals in PEELS spectrum, their origin and uses.

Sl. No.	Signal	Origin	Use
1.	Zero Loss Peak	Incident electrons, which have not interacted with specimen; elastically scattered electrons ; electrons scattered by phonons, with $E < .1\text{eV}$.	Total scattering ring power
2.	Low-Loss Region	Energy loss due to interactions which excite valence or conduction electrons $E \approx 50\text{ eV}$.	Thickness measurement
3.	High-Loss Region	Energy loss due to inner shell ionisations. $E > 50\text{ eV}$.	Microchemistry of light elements using ionisation edges; Chemical valence state by shift in peak position. Density of unoccupied boundstates by pre-ionisation fine structure.

Table I.4

Capabilities of PEELS

Range of energy detected	0 to 2 keV
Dispersion E/X (X is the distance of the focus from center of the spectrometer)	$4 \mu\text{m}/\text{eV}$.
Energy Resolution (Width of the slit/ Dispersion)	2 to 3 eV for a collection angle of 10 mrad.
Collection Efficiency	50%, better than any other detector.
Average Analysis Time	Few minutes.
Light Element Detection	Ideal for light elements.
Minimum Detectable Mass	$10^{(-18)}$ g.
Minimum Mass Fraction	0.1 %
Typical P/B ratio	Good for Zero Loss Peak and Plasmon peaks.

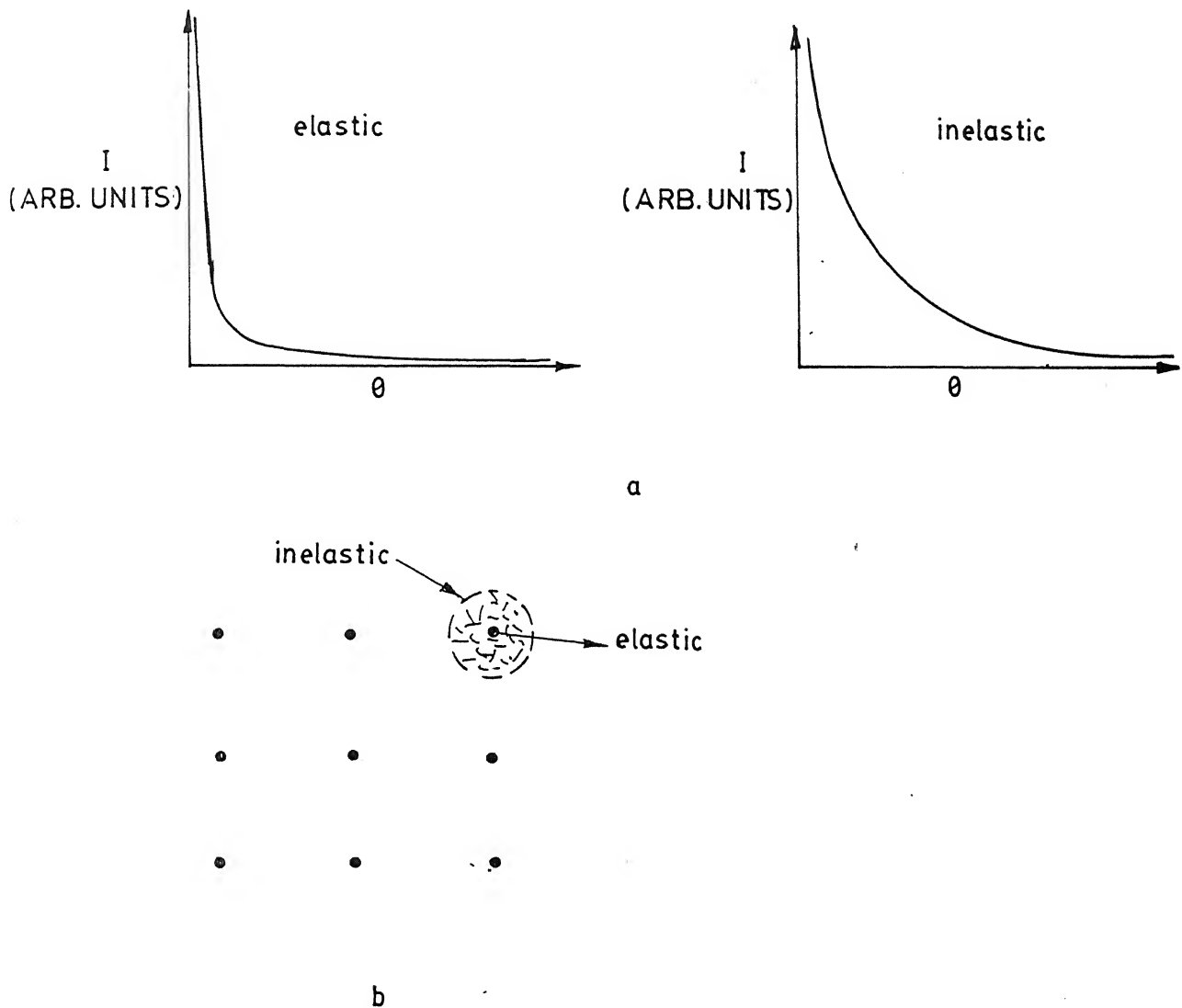
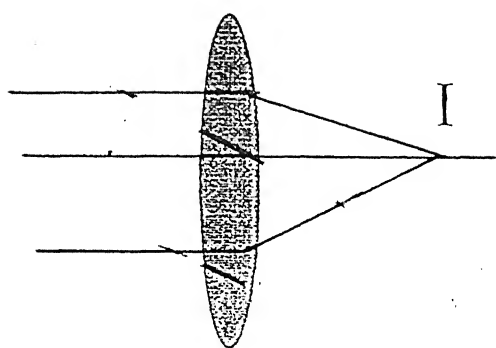


Figure 1.4 Angular distribution of the elastically scattered and the inelastically scattered electrons. (a) Variation in the intensity of the two types of scattered electrons vs scattering angle and (b) The representation of the variation in 'a' in a typical SAD pattern.

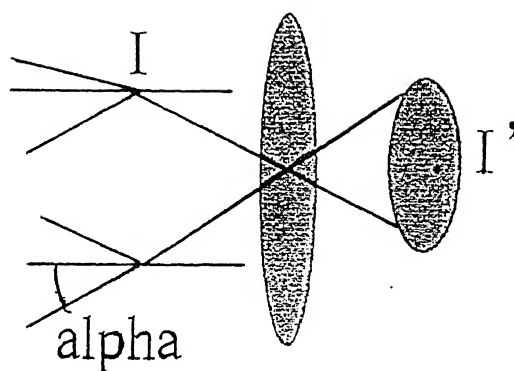
1.2.2 Convergent Beam Electron Diffraction

The discovery of CBED dates back to 1939 by Kossel and Mollenstedt (37). However, the widespread use of the same started only after the development of STEM, due to the availability of focussed probes. Focussed probes are essential to obtain the fine variations of the intensity of the diffracted discs. The fine details would be lost if the probe is too large. The averaging effects due to variations in thickness and orientation, cannot be avoided, in the case of large size of the probe.

Figure 1.5 shows the geometry of the selected area diffraction and CBED. It is seen that if a parallel beam of incident ions is replaced by a convergent beam, diffraction spots of the SAD's get enlarged into CBED discs. The same effect can be introduced by rocking the specimen, in the case of a parallel beam. The incident convergent beam can be imagined to consist of a large number of parallel beams, as shown in figure 1.5. In such a case, for each parallel beam, a diffraction spot is formed at the back focal plane of the objective lens, but away from the optic axis. The distance of the diffracted spot from the optic axis depends on the inclination of the parallel beam, in consideration. For every parallel beam, which is contributing to the convergent beam, a diffraction spot is formed, depending on the angle of incidence. Thus, the intensity distribution within CBED disc provides information about the angular dependence of diffracted intensity on the angle of incidence. For every point in the (000) disc of CBED pattern, there is a corresponding point in every other diffracted disc, satisfying the Bragg's law. As the angle of convergence, α reduces, a parallel beam case is approached and the disc pattern is replaced by a spot pattern, corresponding to the center of each disc. A brief comparison of the three methods of diffraction, the SAD, micro-diffraction and CBED is given in Table I.5.



(a)



(b)

Figure 1.5 Two different geometries of electron diffraction. (a) Selected area diffraction and (b) convergent beam electron diffraction.

Table I.5

Comparison between different geometries of diffraction

CBED	Microdiffraction	SAD
Small probe and large convergence	Small probe and very little convergence	Large probe size. No convergence
Large angular view of back focal plane of objective. So ZOLZ, FOLZ & HOLZ can be seen	Not much Only ZOLZ Rarely FOLZ	only ZOLZ
Finer details if I vs. Θ is not averaged due to crystal thickness & orientation difference within diffracting volume	I vs Θ information lost due to averaging effects	Information lost

ZOLZ - Zero Order Lane Zone
FOLZ - First Order Lane Zone
HOLZ - High Order Lane Zone

The additional information offered by CBED are as follows: three-dimensional information about the reciprocal lattice (38), strain from regions of diameter as small as 10 nm (39,40), symmetry details (41 - 45) of the crystal, determination of low order and high order structure factors (46,47), atom positions (48-50) and charge density redistribution due to bonding (51). Table I.6. provides the salient features of CBED which is made use of for each of these additional information.

Methods for doing quantitative CBED are presently being developed (51). This makes use of the quantitative comparison of intensity distribution of (000) disc obtained in CBED experiments and computations. The experimental determination of the intensity of elastically scattered electrons (the available signal contains a mixture of elastic and inelastically scattered electrons) uses the image filtering procedures using the PEELS image filters. This method is useful to estimate the low order structure factors.

The development of small probes using field emission gun (52) for better spatial resolution in analytical electron microscopy and atomic resolution in STEM imaging, has led to 'coherent nano-diffraction'. It is found (53) that the smaller probes increase the coherency of the incident electron beam. If the discs of CBED patterns obtained using such probes with large convergence angle are allowed to overlap (Figure.1.6.), lattice fringes can be imaged (54) in the overlapping region. This leads to STEM lattice imaging. It is possible by this method to locate the probe accurately at various regions within a unit cell and the CBED patterns obtained from these regions show different site symmetries (55,56).

Instead of obtaining the conventional CBED patterns, if the probe-forming lens is defocussed, each disc of the CBED pattern becomes a small, shadow image of the

Table I.6

Various Additional Features of CBED, their origin and uses.

Sl.No.	Feature	Major Cause Responsible for the Observed Feature	Use
1.	Intensity distribution within each disc.	Large convergence angle, equivalent to a number of parallel beams.	Symmetry under specific condition
2.	Large number of high order Laue zones (HOLZ)	Intersection of Ewald sphere on discs of various orders of Laue zones and their excitation due to large convergence angle.	3-D information about reciprocal lattice
3.	HOLZ deficiency lines in (000) disc.	Intersection of dispersion curve of (hkl) of HOLZ reflection with those corresponding to the transmitted beam (k_0).	Lattice strain if acceleration voltage is constant
4.	HOLZ excess lines in CBED discs of HOLZ.	Same as above. The complimentary lines.	Position of atoms

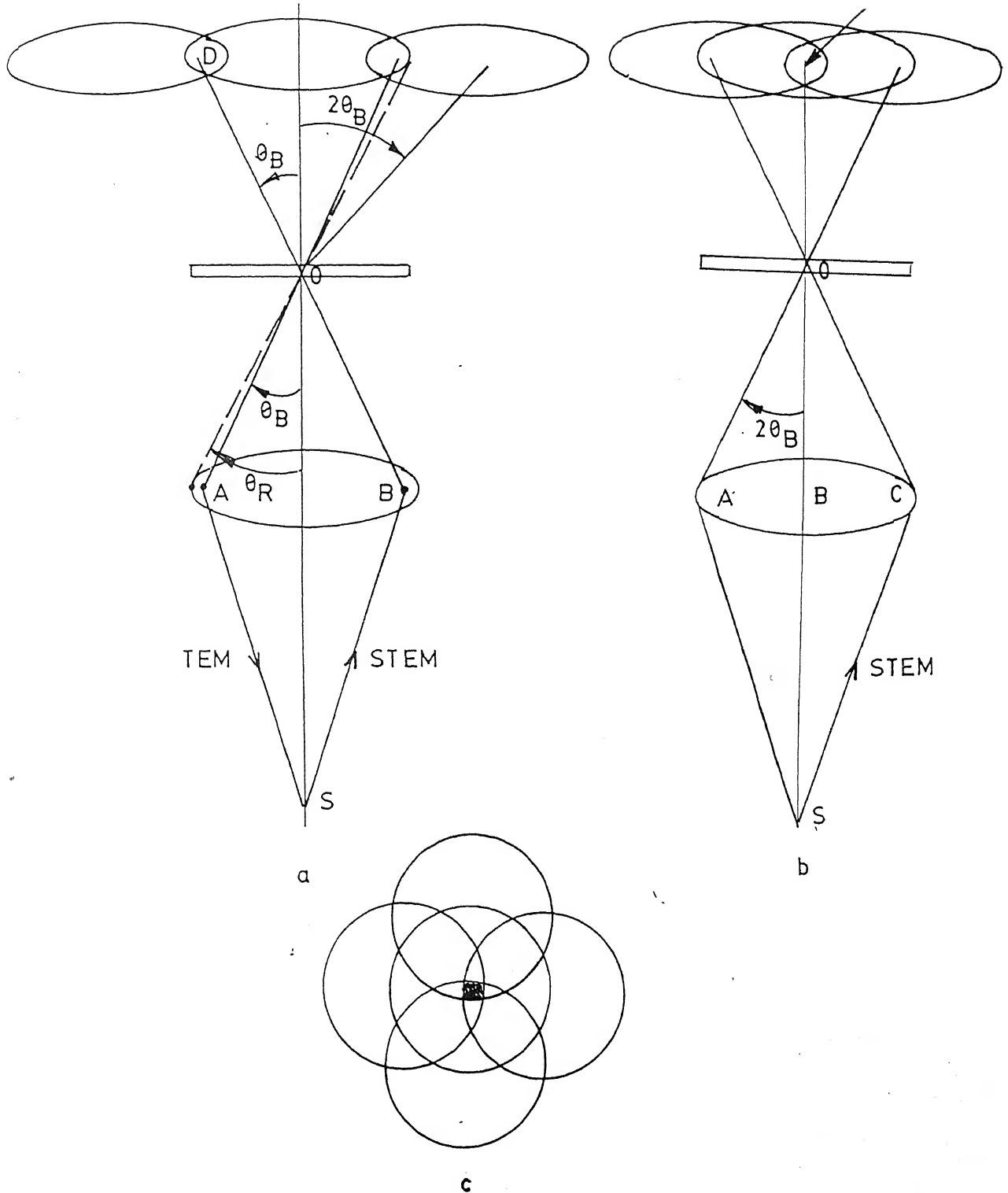


Figure 1.6 Lattice imaging in STEM : (a) Two illumination angles θ_R and θ_B are shown. Use of θ_R allows small overlap of CBED discs. Detector at D records a two beam lattice image as the probe is scanned. Interchanging S and D shows that this is equivalent to inclined illuminations in the lattice imaging using TEM. (b) Axial three beam lattice imaging in STEM of $\theta_R \approx 2\theta_B$, the Bragg angle. Three orders overlap at D. (c) The appearance of a two-dimensional coherent CBED pattern used for axial

sample. For such an optical shadow image, if no post-specimen lens is used, magnification would be (Figure 1.7) equal to the probe-to-screen distance divided by the defocus - probe to sample distance. New imaging possibilities arise presently, if the probe is coherent. If CBED discs are allowed to overlap upto the center of the disc, i.e., very large size of condenser aperture or even removal of the aperture, the shadow image becomes an atomic resolution image. Thus, for crystalline foils, a point - projection lattice image is formed (57) without scanning. The image may be distorted by spherical aberration, at distances away from the optic axis. These patterns are called Ronchigrams - coherent CBED pattern with either very large aperture or with the aperture removed entirely. For very thin samples, the Ronchigram is called an in-line Gabor electron hologram (58-62).

In fact, as an extreme case, if an ideal point source was available, the arrangement in Figure 1.7 would produce an unaberrated lattice image of the crystal, without using either lens or scanning. This point projection method for electron lattice imaging was proposed by Cowley (57) in 1957. The resulting images are called Fourier images. The availability of coherent, fine FEG guns has revitalised this field, which has attracted a lot of attention in recent years.

Another field which is developing based on coherent nanodiffraction is the electron holography (52) and super-resolution schemes (63-65) for imaging. In the original papers on holography, Gabor (58,59) dealt with the case of in-line holograms obtained by forming the shadow image of a thin object using a small electron source. He envisaged the possibility of forming a reconstructed image of the original object. The initial concept of holography was thus developed as a proposal for improving the resolution of electron microscopes. The term "hologram" was suggested in recognition of the fact that in a shadow image, the whole of diffraction information including relative phases is present as a result of interference of coherent electron

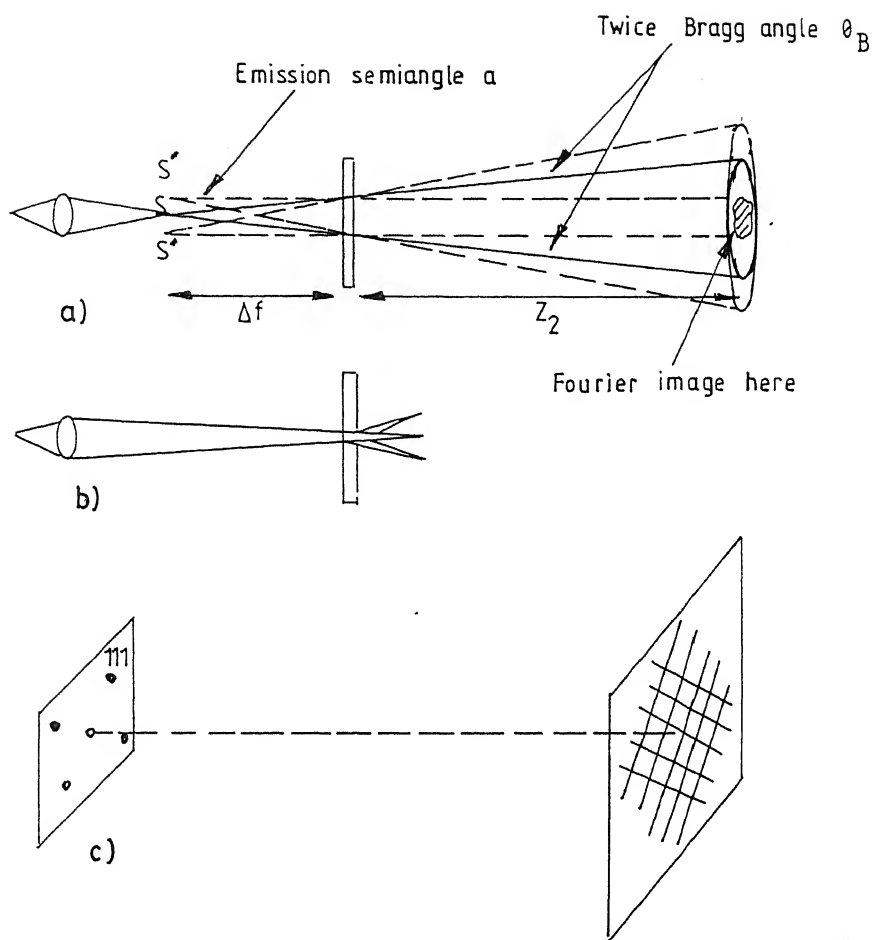


Figure 1.7 (a) Overlapping of CBED discs when a coherent point electron source is used, with the angle of convergence $\alpha > 2\theta_B$. S' 's are the virtual sources, resulting from Bragg diffraction. (b) Corresponding underfocus case, for large angle CBED patterns and (c) Position of the virtual sources in reciprocal lattice, producing an ideal lattice image without lens or scan coil (for a coherent point source).

waves scattered from each point of the specimen. The directly transmitted wave for a thin sample is considered to act as a reference wave and information on the phases of diffracted waves is given by the interference between the diffracted and reference waves. The coherent nano-diffraction from thin crystals, called the Gabor in-line holography, needs a point source and a weakly, scattering transmission object. This condition is not normally met with, in CBED patterns. Under kinematic (weak scattering approximation) conditions, holographic reconstruction techniques help to reconstruct the complex wavefunction at the exit surface of the thin foil. The question of object reconstruction, i.e., reconstruction of the crystal potential from the image wave function, depends on the scattering approximations. Extensive literature (58-62) exists on the subject of electron holography. A number of reconstruction schemes using coherent microdiffraction patterns are attempted.

Another method of achieving the same result as in-line holography, was adopted by Cowley. The use of biprism in STEM, by Cowley (61,65) in 1991, has led to the development of off-line holography. Using a biprism, it is possible to pass one probe through the sample and another outside the sample. A reference wave is made to interfere with the coherent CBED pattern, allowing reconstruction of the object wavefunction, i.e., the crystal potential. This method has been found to be successful in determining the position of atoms upto 0.2 Å.

1.3 PROBLEMS IN MICROSTRUCTURAL CHARACTERISATION

The advanced techniques in electron microscopy explained earlier have been used to identify many complex structures and extensively employed in the design of alloys by appropriate structure-property correlations. However, there have been many instances,

CENTRAL LIBRARY
I. I. T., KANPUR

wherein unambiguous characterisation of structures has been very difficult. Classic examples in literature are the difficulty in uniquely distinguishing the spinodal decomposition (81) products from G.P.zones (82), spinodal ordering and continuous ordering (83-89), nucleation of martensite (90-92), mechanism of formation of bainite (93-97), distinction between voids and bubbles, aligned loops and platelets (98-100) formed during irradiation, inability to identify low volume fraction of fine, metastable, δ -ferrite in martensitic matrix of Cr-Mo steels (101) and the difference (46) between phases with close lattice parameters and composition, like $M_{23}C_6$ and M_6C . Additionally, there are some parameters like mobile dislocation density which has strong influence on mechanical properties and quite difficult to estimate.

Origin of some of these problems could be traced to the evolution of complex, metastable microstructures. For example, consider the identification of secondary phases, like σ , $M_{23}C_6$ and M_6C etc. The two crystals of $M_{23}C_6$ and M_6C have the same crystal structure of f.c.c. with lattice parameter of 1.08 and 1.12 nm respectively, at equilibrium. They always form as a minor constituent in steels, $<0.1\%$. Microchemistry of these phases, even at equilibrium - which is not the case most of the times - can be quite varied. The crystal structure of either of the two carbides does not depend on the degree of metastability. However, the lattice parameters are sensitive to strain and composition. Though the equilibrium composition and lattice parameters for most of the crystals are well documented, they are not valid for metastable phases. In such cases, any additional information, like symmetry, if it is different for the two phases, could be a very useful asset and can help in the unique identification of the two phases. For example, $M_{23}C_6$ has $m\bar{3}m$ symmetry and M_6C has a symmetry of $d\bar{3}m$. This is the confirmatory method for distinguishing the two phases.

Another example is the case of distinguishing low volume fractions of metastable δ -ferrite in a martensitic ferrite (α') matrix in Cr-Mo steels - an unsolved problem till today. The metastable δ -ferrite forms as stringers with few Å width, not permitting the use of conventional hardness measurements. The volume fraction is too low in metastable situations and the two forms of ferrite have the same crystal structure. Hence, the X-ray diffraction methods are not very useful. Since the δ -ferrite is metastable, sufficient repartitioning of alloying elements between δ -ferrite and austenite - τ (which transforms to martensite - α' , inheriting the composition of τ) is not expected to take place, making microchemical information insufficient to distinguish the two forms of ferrite. In such instances, the only parameter that can be used for the distinction of the two forms of ferrite is the lattice strain. The δ -ferrite forms as fine, strain free nuclei at high temperatures, while the martensite - α' forms as a highly strained lath at low temperatures. The difference in such strain within fine crystals can be an additional information which can be obtained using CBED. Measurement of such a parameter could help in finding out the difference between martensite α' and δ -ferrite.

Despite the above limitations posed by novel microstructures, new metastable phases are discovered using transmission electron microscopy, like the G-phase (101) which forms in steels only during irradiation, the quasicrystals (102) and so on. In fact, it is interesting to observe that after the G-phase was cited using electron microscopy, it was synthesised and identified in conventional type 308 steels (103) and studied in detail.

Some of the problems mentioned above, if not all, can be resolved if useful additional information can be obtained simultaneously, apart from lattice parameter, morphology and orientation relations. Some of these are the micro-chemistry, symmetry of the

crystal, strain, three dimensional information of the reciprocal lattice and so on. These additional information can be provided by the techniques, AEM and CBED.

1.4 SCOPE OF THE THESIS

The state-of-art of electron microscopic techniques and the problems in the field of microstructural characterisation have been explained so far. Inspired by the availability of these methodologies, the present study has examined the possibility of resolving some of the controversies relating to the evolution of secondary phases in alloys of technological interest. In order to give a comprehensive summary of the state-of-art of electron microscopy, all the available techniques have been reviewed in the previous sections. However, for the study of the steel of interest in the thesis, namely, 9Cr-1Mo, only those techniques which are relevant to the particular problems addressed in the thesis have been employed. The present state of literature concerning the subject of interest to the thesis, i.e., the weldment of 9Cr-1Mo steel, is reviewed in the chapters 3, 4 and 5.

The main theme of the present thesis is to examine if the newer developments in the field of electron microscopy, like AEM and CBED can be utilised for the detailed study of the microstructures that evolve in the weldments of a technologically important alloy, i.e., 9Cr-1Mo steel. The second chapter explains the details of the materials used, welding procedures, various heat treatment and preparation stages of the experiments, the techniques employed and their operating conditions. The third chapter, titled **Formation of Non-Equilibrium Phases During Solidification of Weldments of 9Cr-1Mo Steel** discusses the effect of thermal cycle on the 'primary' and 'secondary' microstructures generated, the three dimensional phase field maps based on these results, lattice strain variation across the

weldment and the attempts to resolve the controversy on the formation of δ -ferrite using CBED. The fourth chapter, titled **Microstructural Modifications in Weldments of 9Cr-1Mo Steel at Elevated Temperatures** presents the results on the study of evolution of secondary carbides at high temperatures, the concept of phase evolution diagram, its validity to weldments with concentration gradient and the evaluation of phase evolution diagrams at the high temperatures for the three different regions of the weldment. The fifth chapter deals with the **Study of Lattice Disorder in Ion Irradiated Crystals using Convergent Beam Electron Diffraction**. Two characteristic features of CBED patterns which show systematic changes with increase in defect density are identified, in this study. The results agree well with similar changes in a model Al-Mn alloy. The experimental results in the model Al-Mn alloy were compared with computations of CBED patterns of the same and found to agree satisfactorily. These studies have been useful to confirm that CBED technique is effective in the identification of presence of point defects. The last chapter summarises the major findings and briefly discusses the scope of future work in this area.

REFERENCES

1. L. Egnell and N.G. Persson, Proc. Int. Conf. on "*Ferritic Steels for Fast Reactor Steam Generators*", BNES, London (1978) p.212
2. P.J. Maziasz, *J. Nucl. Mater.* 169 (1989) 95
3. R.T. King and L. Egnell, Proc. Int. Conf. on "*Ferritic Steels for Fast Reactor Steam Generators*", BNES, London (1978) p.74
4. M.K. Booker, V.K. Sikka and B.L.P. Booker, Proc. Int. Conf. on "*Production, Fabrication Properties and Applications of Ferritic Steels for High Temperature Applications*", Warren, Pennsylvania (ASM, Metals Park, 1982) p.257
5. *A Status Review of Alloy 800*, Proc. Conf. on "A Status Review on Alloy 800", organised by British Nuclear Energy Society at University of Reading, September 1974, Eds. S.F. Pugh, AERE Harwell BNES (1975)
6. J. Orr, in *Alloy 800*, Proc. Patten Int. Conf. on "*Alloy 800*", Eds. W. Betteridge, et. al., North Holland Publishing Co., New York (1978), Paper 2-1, p.25
7. M. Valsan, P. Parameswaran, K.B.S. Rao, M. Vijayalakshmi and S.L. Mannan, *Metall. Trans.* 23A (1992) 175
8. V. Seetharaman, Ph.D. Thesis, submitted to the Indian Institute of Technology, Bombay (1984)
9. J.J. Kai and G.L. Kulcinski, *Scripta Metall.* 23 (1989) 1151

10. T.M. Williams, J.M. Titchmarsh and D.R. Arkell, *J. Nucl. Mater.* 107 (1982) 222
11. E. Hornbogen, *Acta Met. Metall.* 33 (1985) 595
12. D. Kumar, A.D. King and T. Bell, *Met. Sci.* 17 (1983) 32
13. S. Venkadesan, Ph.D. Thesis, submitted to Indian Institute of Technology, Madras (1991)
14. F.A. Garner, *Mater. Sci. and Technol. - A Comprehensive Treatment*, Eds. R.W. Cahn, P. Haasen and E.J. Kramer, Vol.10A on Nuclear Materials Part I, Volume edited by Brian R.T. Frost, (VCH, Weinheim, 1994) p.419
15. U.R. Lenel and B.R. Knott, *Met. Trans.* 18A (1987) 847
16. C.V. Sundaram, P. Rodriguez and S.L. Mannan, *J. Min. Met.* (Institution of Engineers, India) 67 (1986) 1
17. P. Patriarca, in Proc. Conf. on "*Ferritic Alloys for use in Nuclear Energy Technologies*", Eds. J.W. Davis and D.J. Michel, TMS-AIME (1984) 425
18. P. Rodriguez, S.L. Mannan and Baldev Raj, Proc. Seminar on "*Fast Reactor Fuel Cycle*", Vol.2, February 10-12, 1986, IGCAR, Kalpakkam, Tamil Nadu, India, p.53

19. P. Rodriguez, R. Krishnan and C.V. Sundaram, *Bull. Mater. Sci.* 6(2) (1984) 339
20. Baldev Raj, S.L. Mannan, P.R. Vasudeva Rao and M.D. Mathew, Communicated to *Current Science*
21. M.K. Wu, J.R. Ashburn, C.J. Torng, P.H. Hor, R.L. Meng, L. Gao, Z.J. Hunang, Q. Wang and C.W. Chu, *Phys. Rev. Lett.* 58 (1987) 908
22. R.J. Cava, B. Batlogg, J.J. Krayewski, R. Farrow, L.W. Rupp. Jr., A.E. White, K. Short, W.F. Peck and T. Kometani, *Nature* 332 (1988) 814
23. J.W. Patten, in *High Temperature Aluminides and Intermetallics*, Eds. S.H. Whang, C.T. Liu, D.P. Pope and J.O. Steglar, Proc. Symp. on *High Temperature Aluminides and Intermetallics*, TMS, ASM at Indianapolis, October 1989, TMS Publication (1990) p.493
24. F. Aldinger, in *High-Tech Ceramics*, Invited papers at the ETHZ Latsis Symposium, Zurich, November 10-11, 1988, Ed. Gernot Kostorz, Academic Press Ltd., London (1989) p. 161
25. F. Esper, *ibid.*, p.119
26. R. Boll, H.R. Hilzinger and H. Warlimont, in *Glassy Metals : Magnetic, Chemical and Structural Properties*, Ed. Ryusuke Hasegawa, CRC Press Inc., Florida (1983) Chapter 6, p. 183

27. H.E. Knechtel, W.F. Kindle, J.L. McCall and R.D. Buchheit, in *"Tools and Techniques in Physical Metallurgy*, Vol.1, Ed. F. Weinberg, Pub. Marcel Dekker Inc., New York (1970) p.329
28. Sir Lawrence Bragg, *The Development of X-ray Analysis*, Hafner Press, New York (1975), Chapter 5, p.53
29. *ibid.*, Chapter 2, p.14
30. G.H. Stout and L.H. Jensen, *X-ray Structure Determination*, McMillan, London (1968)
31. L. de Broglie, *Fifty Years of Electron Diffraction*, Ed. P. Goodman, D. Reidel Publication Co., Dordrecht, Boston (1981) p.5
32. C.J. Davisson and L.H. Germer, *Nature* 117 (1927) 558
33. G.P. Thompson and A. Reid, *Nature* 119 (1927) 890
34. *Electron Microscopy*, Proc. First Regional Conf. on "Electron Microscopy in Asia and Oceania", Tokyo, October 1956
35. *The Electron Microprobe*, Eds. T.D. McKinley, K.F.J. Heinrich and D.B. Withy, John Wiley and Sons, New York (1966)
36. K.F.J. Heinrich, *Electron Beam X-ray Microanalysis*, van Nostrand Reinhold Co., New York (1981)

37. W. Kossel and G. Mollenstedt, *Ann. Phys.* 36 (1939) 113
38. M. Raghavan, J.Y. Koo and R. Petkovic-Luton, *J. of Metals*, June (1983) 44
39. R.W. Carpenter and J.C.H. Spence, *Acta Cryst.* A38 (1982) 55
40. P.M. Jone, G.M. Rackham and J.W. Steeds, *Proc. R. Soc. London* A354 (1977) 197
41. F.W. Schapink, S.K.E. Forghany and B.F. Buxton, *Acta Cryst.* A39 (1983) 805
42. B.F. Buxton, J.A. Eades, J.W. Steeds and G.M. Rackham, *Phil. Trans. R. Soc. London* A1301, 281 (1976) 15
43. P. Goodman, *Acta Cryst.* A31 (1975) 804
44. M. Tanaka, H. Sekii and T. Nagasawa, *Acta Cryst.* A39 (1983) 825
45. J.P. Morniroli, H. Ayatti and M. Gantois, *J. Micros. Spectros. Elect.* 14 (1989) 23
46. J.W. Steeds, in *Introduction to Analytical Electron Microscopy*, Eds. J.I. Goldstein and D.C. Joy, Plenum Press, New York (1979), Chapter 15, p.387
47. R. Vincent, D.M. Bird and J.W. Steeds, *Phil. Mag.* A50(6) (1984) 765
48. R. Vincent and D.R. Exelby, *Phil. Mag. Letters* 63(1) (1991) 31

49. P.A. Midgley and R. Vincent, Int. Phys. Conf. Ser. No.119, Section 9, p.371, paper presented at EMAG 91, Bristol, September 10-13, 1991
50. D.M. Bird and M. Saunders, *Ultramicroscopy* 45 (1992) 241
51. D.M. Bird, on "*Quantitative CBED*", Lecture notes for Second International School on "Electron Diffraction", July 1994 at Bristol, U.K.
52. A.V. Crewe and D.N. Eggenberger, *J. Wall Rev. Sci. Ins.* 36 (1968) 576
53. J. Zhu, L.M. Peng and J.M. Cowley, *J. Micros. Techn.* 7 (1987) 177
54. W.C.T. Dowell and P. Goodman, *Phil. Mag.* 28 (1973) 471
55. J.C.H. Spence and J. Lynch, *Ultramicroscopy* 9 (1982) 267
56. J.M. Cowley, *Ultramicroscopy* 4 (1979) 435
57. J.M. Cowley and A.F. Moodie, *Proc. R. Phys. Soc.* B70 (1957) 486
58. D. Gabor, *Proc. Roy. Soc. (London)* A197 (1949) 454
59. D. Gabor, *Proc. Roy. Soc. (London)* A64 (1951) 449
60. H. Lichte, *A Short Glimpse at Electron Holography*, in "Microphysical Reality and Quantum Formalism", Ed. A. van der Merwe, Kluwer, New York (1988) p. 137

61. M. Tanaka and M. Terauchi, *Convergent Beam Electron Diffraction*, JEOL Ltd. (1985)
62. M. Tanaka, R. Saito and H. Sekii, *Acta. Cryst.* A39 (1982) 357
63. J.A. Lin and J.M. Cowley, *Ultramicroscopy* 19 (1986) 179
64. J.M. Cowley and D.J. Walker, *Ultramicroscopy* 6 (1981) 71
65. J.C.H. Spence, *Coherent Nondiffraction - in Line Holography, Shadow Images and STEM*, Lecture for Second International School on "Electron Crystallography", Bristol, July 1994
66. P. Duncumb, Fifth International Conf. on "Electron Microscopy", Paper KK4, Academic Press, New York (1962)
67. G. Cliff and G.W. Lorimer, *J. Microscopy* 103 (1975) 203
68. B.W. Batterman, *Phys. Rev.* A133 (1964) 759
69. P. Duncumb, *Phil. Mag.* 7 (1962) 2101
70. J. Taftø and J.C.H. Spence, *Ultramicroscopy* 9 (1982) 243
71. J. Taftø and J.C.H. Spence, *Science*, October 218 (1982) 49
72. J. Taftø, J.C.H. Spence and P. Fejes, *J. Appl. Phys.* 54(9) (1983) 5014

73. J. Tafto, *J. Appl. Cryst.* 15 (1982) 378
74. J. Tafto, *Phys. Rev. Letters* 51(8) (1983) 654
75. J. Tafto and Z. Liliental, *J. Appl. Crystallogr.* 15 (1982) 260
76. D.C. Joy and D.M. Maher, *Ultramicroscopy* 3 (1978) 69
77. R.F. Egerton, *Ultramicroscopy* 4 (1979) 169
78. D.C. Joy, R.F. Egerton and D.M. Maher, *Scanning Electron Microscopy 1979* published by SEM Inc., Chicago (1979) p. 817
79. D.B. Williams and J.W. Edington, *J. Microsc.* 108 (1976) 113
80. J.W. Edington, *Practical Electron Microscopy in Materials Science*, published by van Nostrand, Reinhold, New York (1976)
81. Rodolfo Acuna and Alberto Bonfiglioli, *Acta Metall.* 22 (1974) 399
82. W.A. Soffa and D.E. Laughlin, Proc. Int. Conf. on "Solid State Phase Transformations", Pittsburgh, AIME, Warrendale, PA (1981) 159
83. B. Ditchek and L.H. Schwartz, *Ann. Rev. Mater. Sci.* 9 (1979) 219
84. J.M. Cowley, *Acta Cryst.* 29A (1973) 537

85. J.P. Chevalier and W.M. Stobbs, *Acta Metall.* 27 (1979) 285
86. J. Higgins, R.B. Nicholson and P. Wilkes, *Acta Metall.* 22 (1974) 201
87. S.M. Allen and J.W. Cahn, *Acta Metall.* 24 (1976) 425
88. J.P. Chevalier, Ph.D. Thesis, University of Cambridge (1976)
89. R. de Ridder, G. van Tandeloo and S. Amelinckx, *Acta Crystall.* A32 (1976) 216
90. M. Suezawa and H.E. Cook, *Acta Metall.* 28 (1980) 423
91. T.A. Schroeder and C.M. Wayman, *Scripta Metall.* 10 (1976) 241
92. D.S. Lieberman, M.A. Schmerling and R.W. Karz, *Shape Memory Effects in Alloys*, Ed. J. Perkins, Plenum Press, New York (1975) 203
93. H.K.D.H. Bhadeshia and J.W. Christian, *Metall. Trans.* 21A (1990) 767
94. J.W. Christian, *Phase Transformations*, Vol.1, No.11, Series 3, Institute of Metallurgists, London (1979) 1
95. H.K.D.H. Bhadeshia and D.V. Edmonds, *Metall. Trans.* 10A (1979) 895
96. R.F. Hehemann, K.R. Kinsman and H.I. Aaronson, *Metall. Trans.* 3 (1970) 1077
97. H.I. Aaronson, M.G. Hall, D.M. Barnett and K.R. Kinsman, *Scripta Metall.* 9 (1975) 705

98. A. van Veen, L.M. Caspers and J.H. Evans, *J. Nucl. Mater.* 103&104 (1981) 1181
99. L.M. Brown and P. Mazey, *Phil. Mag.* 10 (1964) 1081
100. K. Kamada, A. Sagara, H. Kinoshita and H. Takahashi, *Rad. Eff.* 106 (1988) 219
101. D.P. Edmonds and B. Chew, CGGB Report TPRD/M/1258/N82, July (1982)
102. C. Cawthorne and C. Brown, *J. Nucl. Mater.* 66 (1977) 201
103. D. Schectman, I. Blech, D. Gratias and J.W. Cahn, *Phys. Rev. Letters* 53 (1984) 1951
104. J.M. Vitek and S.A. David, *Met. Trans.* 18A (1987) 1195

CHAPTER 2

EXPERIMENTAL DETAILS

The present chapter on experimental details is organised as follows : the first section discusses the preparation of the two alloys and their chemical composition. This is followed by the details of the heat treatment, irradiation conditions and the specimen preparation methods. Next, the various experimental techniques employed in the present study and the precautions taken during the use of these techniques are explained. The experimental procedures of collection of EDAX spectra and their quantitative analyses are discussed in the next section. Following this, the origin and estimation of errors in various parameters are discussed. This is followed by the details of the two softwares, the TRIM Code and the EMS software which are used for computations.

2.1 PREPARATION OF THE ALLOYS

The two systems studied were the weldments of 9Cr-1Mo steel and an Al-14 a/o Mn alloy. The weldments of 9Cr-1Mo steel were prepared from the normalised and tempered steel supplied by M/s. Creusot Loire Co., France. The nominal composition of the steels supplied is given in Table II.1. The welding parameters and the method of welding are given in Table II.2.

Table II.1

Nominal Chemical Composition of the Alloys used

Sl. No.	Alloys used	Chemical Composition							
		Cr	Mo	Si	Ni	(w/o) C	Fe	Al	Mn
1.	Weldments of 9Cr-1Mo	8.24	0.94	.19	-	11.	Bal.	-	-
2.	Al-Mn alloy	-	-	-	-	-	-	59.5	40.5
3.	316LN steel*	16.9	2.3	-	11.9	0.05	67.6	-	-
4.	361LN steel@	17.34	2.67	-	12.92	-	66.87	-	-

* Wet chemical analysis

@ By quantitative analysis of EDAX using experimentally determined K_{AB} values.

Table II.2

Welding Method and Parameters

Welding Process	Manual Metal Arc
Welding Parameters	
Pre-heat	• 200°C
Electrode	Basic Coated 9Cr-1Mo Electrodes
Electrode Diameter Arc	3.15 mm
Voltage Arc	22 V
Current	100-130 Amps.
No. of Passes	Four

The Al-Mn alloy was melted using accurately weighed 99.99% pure Al and Mn in an induction furnace. Alumina crucibles were used for melting the alloy. The liquid alloy was chill cast, into a brass mould and was homogenised at 873 K for ten days. The homogenised alloy was cut and rolled into 100 μm sheets in steps, with intermittent annealing at 873 K. Finally, the samples were solutionised at 873 K for one hour. The alloy obtained by slow cooling was found to be homogeneous with respect to chemical composition and microstructure, which were confirmed using electron probe microanalyser and optical microscope respectively. The results of chemical analysis of Al-Mn alloy are also included in Table II.1.

2.2 HEAT TREATMENTS AND SPECIMEN PREPARATION

All the post-weld heat treatments were carried out in well calibrated tubular furnaces, ensuring that the specimen is maintained in the uniform temperature zone. The temperature during the long term ageing treatments was constant within ± 2 C and proper measurement of temperature was ensured using well calibrated thermocouples.

The specimens were cut from the required regions using diamond cutting machine. The samples for optical microscopy, hardness measurements and scanning electron microscopy were prepared by mounting the cut samples in suitable mounts and standard polishing and etching techniques were used. Table II.3 gives the details of the etchants for the two alloys studied. Irradiation was carried out in pre-thinned electron transparent samples. The samples for transmission electron microscopy were prepared by jet thinning or window thinning and preparation of carbon extraction replicas. The etchants and solutions used for electro thinning are also given in Table II.3.

Table II.3

Specimen Preparation Methods for Various Techniques

Sl. No.	Investigation Technique	Specimen Preparation Method	Details	
			9Cr-1Mo	Al-Mn
1.	Optical Microscopy Hardness, XRD and SEM	Conventional Metallography Methods	2% Nital	Perchloric Acid + Methanol
2.	Transmission Electron Microscopy	Jet Thinning + Window Polishing	Same as above; T = -20°C; 20 V	
3.	Transmission Electron Microscopy	Carbon Extraction Replica	Coat carbon on polished and lightly etched surface. Extract carbides in films, removed from sample surface by additional etching.	

2.3 IRRADIATION

The irradiations were carried out at room temperature using the beam from a 150 keV accelerator. Clean, hydrocarbon free vacuum of 10^{-7} mbar was maintained inside the irradiation chamber using a turbomolecular pump. The samples were mounted on a thick copper block, insulated from the rest of the chamber to facilitate beam current measurements. The beam from the accelerator was collimated and positioning of the beam was carried out through a viewing window.

The irradiation dose and beam current (dose rate) were measured by a beam current integrator - calibrated using a constant current source. A secondary electron trap was used to eliminate error in the measurements of beam current due to secondary electron emission.

2.4 TECHNIQUES USED IN THE INVESTIGATION

Initial characterisation of the alloys was carried out using optical microscope, Vickers macro and micro hardness tester, electron probe microanalyser, scanning electron microscope and X-ray diffraction. The model number of each of these and the operating conditions are given in Table II.4. The convergent beam electron diffraction (CBED) experiments were carried out using EM400 T transmission electron microscope and analytical electron microscopy was carried out using a CM200 transmission electron microscope fitted with an EDAX analyser with super ultra thin window. The operating voltage was 100 kV for CBED experiments. C2 apertures used for CBED experiments were either 200 or 100 or 50 μm .

Table II.4

Details of Different Techniques Employed in the Present Study

Sl. No.	Technique	Instrument Used	Operating Conditions
1.	Optical Microscopy	Reichert MeF2	---
2.	Microhardness	Leitz Vickers Microhardness tester	Applied Load = 100 g
3.	SEM	Philips SEM 501 with EDAX	Accelerating Voltage - 30 kV
4.	XRD		Cu Target. = .1547 nm
5.	TEM	Philips EM400T and CM 200 with SUTW EDAX	Accelerating Voltage - 100/120 kV; EDS quantification by Cliff-Lorimer Method. (K_{AB} experimentally evaluated). Details in Section 2.4

2.5 DETAILS OF ANALYTICAL ELECTRON MICROSCOPY

The microchemistry of carbides using the procedure described is given below:

The characteristic X-rays from the various elements present in the region illuminated with a parallel beam of 120 kV electrons are collected using a super ultra thin window energy dispersive analyser, fitted to a CM200 microscope. The X-rays collected by the EDAX detector are analysed using a DX-4 analyser. Conditions of microscope during collection of X-rays are given in Table II.5. All the apertures in the column, other than condenser aperture were removed. A low background single tilt holder was used to reduce the collection of spurious X-rays. However, the characteristic X-ray peak from the copper grid, in which extraction replica is mounted, could not be avoided. However, for quantification purposes, only iron K_{α} , chromium K_{α} and molybdenum L_{α} were chosen as region of interest. Prior to the collection of X-rays, the analyser was given sufficient time to stabilise. In-hole spectra were collected periodically to ensure that the goniometer and the microscope column were not noisy.

Prior to the actual experiments, the calibration of the EDAX analyser, with respect to gain and resolution, was checked and found to be alright. The quantification of the spectra using mDX-4 program, required evaluation of Cliff-Lorimer constants, i.e., the K_{AB} 's. The direct experimental evaluation of K_{AB} using an alloy of known chemical composition was followed in the present work. A sample of 316LN steel of known chemical composition (Table II.1) was used for the purpose of evaluating K_{AB} values, under identical experimental conditions like the accelerating voltage of 120 kV, tilt angle of 20° and beam diameter of 200 nm. These K_{AB} values were used for the determination of composition. The values thus determined, are also listed in Table II.1. These values agree well with those of wet chemical analysis

Table II.5

Input Parameters for Quantification of EDAX Spectra

Accelerating Voltage	120 kV
Angle of Tilt	20°
Beam Diameter	200 nm
Thickness of the Sample	100 nm
Density in g/cc	8

(Table II.1). Thus, having evaluated reliable k_{AB} values, these were used for the quantification purposes of all the EDAX spectra using the following Cliff-Lorimer equation

$$\frac{C_A}{C_B} = k_{AB} \frac{I_A}{I_B} \quad (2.1)$$

wherein C_A and C_B refer to the concentration of A and B in an alloy AB, I_A and I_B refer to the intensity of characteristic X-rays from A and B, respectively. The other input parameters used for quantification of EDAX spectra are listed in Table II.5.

The quantification of spectra obtained from α -ferrite ignored the presence of .06% carbon. This is reasonable since carbon is in very low amounts and a light element. Thus C is not expected to alter the values of ZAF corrections. The various options available for quantification are as follows: normalising the elements, oxide method and oxide by difference. Of these, the first method of normalising all the elements in the regions of interest, i.e., FeK_{α} , CrK_{α} and MoL_{α} was chosen in the present work. In alloys of known composition, the quantification procedure chosen, and the k_{AB} values determined were found to provide satisfactory results.

In the case of carbides, the following sequence of steps was adopted to arrive at the microchemistry of carbides:

- * Assuming that C is not present, the X-ray spectra from the carbides are analysed using the above procedure of normalising the contents of three elements, i.e., Fe, Cr and Mo. Thin foil approximation was used and absorption correction was applied.

- * The result of this first step does not give the composition of the carbide. But, the distribution of Fe, Cr and Mo in M of $M_{23}C_6$ is obtained as the result of this quantification step.
- * Based on the analysis of SAD or microdiffraction pattern, the type of carbide is identified to be either M_2X or $M_{23}C_6$.
- * Since the formula of the carbide and the specific ratio in which the three elements have to be distributed are known, the stoichiometry of the carbide is calculated as follows:

$$X_{Fe} = \frac{\%Fe \text{ in } M}{100} \times 23 \quad (2.2)$$

- * Based on the exact evaluation of the stoichiometry of the carbide, the w/o of each element in the carbide is evaluated using the equation

$$w/o \text{ of } Fe = \frac{X_{Fe} \times \text{At. Wt. of } Fe(A_{Fe})}{X_{Fe}A_{Fe} + X_{Cr}A_{Cr} + X_{Mo}A_{Mo} + X_C A_C} \quad (2.3)$$

Thus, the composition of various elements Fe, Cr, Mo and C in the carbides is calculated. The statistical error for 99% confidence limit ($\pm 2\sigma$) in the calculation of around ten spectra is about $\pm 5\%$ for Fe, $\pm 4\%$ for Cr and $\pm 6\%$ for Mo. The values of composition of all the elements in the carbides, thus evaluated were found to agree well with those obtained by the spectroscopic elemental analysis of carbides that are extracted by dissolving the matrix.

2.6 ESTIMATION OF ERRORS IN THE EXPERIMENTAL PARAMETERS

This section describes the sources of error in each of the experimental parameter used in the study and an estimation of corresponding error limits.

The parameters used in the present study in the subsequent sections are as follows: macrohardness and microhardness, size of carbides, laths and τ grains, number density and area fraction of carbides and microchemistry of carbides and α -ferrite in weldments of 9Cr-1Mo steel.

The values of hardness were obtained after standardising the equipment to ensure that the hardness of the standards was obtained within a deviation of ± 2 VHN. This standardising was checked every time prior to the measurement of hardness profiles. The 2σ value for 99% confidence limits, therefore was found to be only ± 4 VHN. The reported changes were considered to be genuine, only if the difference was much higher than the error bars.

The size of microstructural features like the size of lath and grain size of τ were measured frequently. Though the accuracy of measurements in this parameter is extremely good ($\pm 1\%$), due to well calibrated values of magnifications of the microscopes, the statistical scatter from as many as 50 measurements turns out to be high, of the order of $\pm 5\%$. The next microstructural parameter measured was the area fraction of carbides. This parameter could not be measured accurately at all. The area fraction of carbides was measured as follows:

The number of carbides in a rectangular grid of chosen area at a known magnification was counted. These values, i.e., number of carbides in a chosen area at a known magnification provide the value of number density N_f of carbides. Since the average dimensions of the globular (radius - r) and acicular particles (length - l and breadth -

b) are already calculated, area fraction is calculated as the product of number density and the average area of a carbide, as follows:

$$A_f = N_f(\text{glob.}) \times \pi r^2(\text{glob.}) + N_f(\text{aci.}) \times l \times b \quad (2.4)$$

The values thus calculated from many grids were found to be accurate to only within $\pm 10\%$. There are a number of sources of error like: (i) It is assumed that the distribution of carbides in the carbon extraction replica is a true representation of the same in the sample. (ii) Carbides were not found to be uniformly distributed. Very often, N_f was found to be extremely high along the lath boundaries, with very low values of N_f within the laths. Hence, a correction to take this factor into account had to be applied. The correction factor represents the area fraction of the lath boundaries to the total area. (iii) The scatter in the values of r , l and b , the dimensions of the carbides, contributed directly to the scatter in the values of A_f .

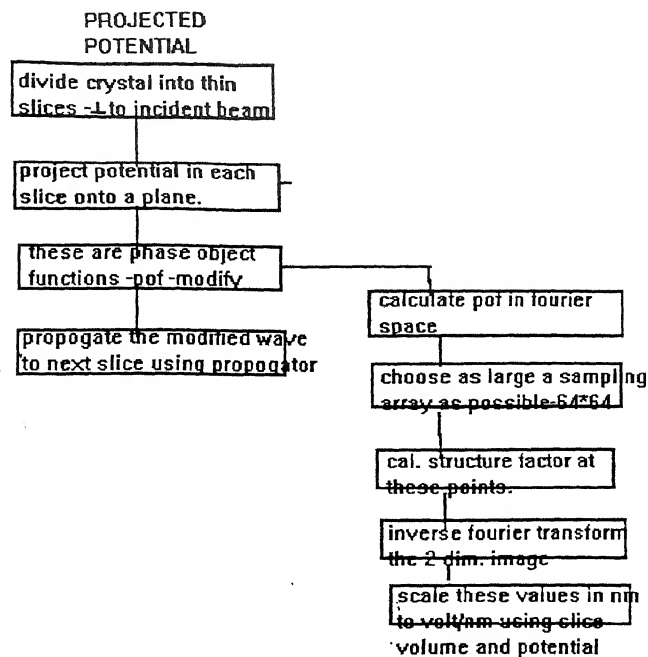
In the presentation of the above parameters in the subsequent chapters, the error bar is shown as a vertical line at the top (right side) of each figure.

2.7 DETAILS OF DIFFERENT SOFTWARES

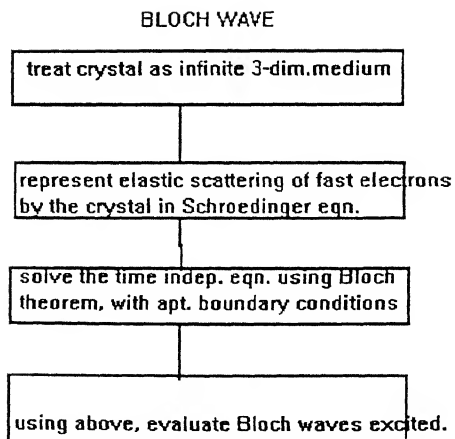
Two programs have been used in chapter 5 of this thesis. One of them is the TRIM Code and the other, the EMS Code. The details of these two programs are given below.

2.7.1 Computation Details of EMS Software

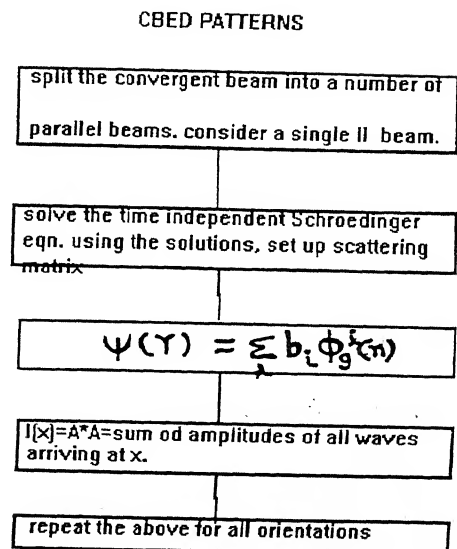
The calculation of CBED patterns, projected potential and the Bloch states are carried out using the EMS software. The different steps involved in the calculations are shown in the flow charts, figure 2.1 a to c. The definition of the unit cell, which is common to



(a)



(b)



(c)

Figure 2.1 Flow chart of EMS calculations: (a) Projected potential (b) Bloch waves and (c) CBED patterns.

all the calculations is carried out using the Bravais lattice, the point group and position of the atoms. The Bravais lattice is defined by the cell dimensions.

The point group is defined by the Herman-Mauguin space-group number (1 to 230). Each atom is also associated with a Debye-Waller factor and an occupancy factor if several atoms share the atom sites. Once the crystal is defined, the calculations proceed as shown in the flow charts, figure 2.1 a to c.

2.7.2 Details of TRIM Code

TRIM Code is used to evaluate the depth dependent profiles of a number of incident ions and the defects generated. When a crystal is implanted with energetic ions, a number of processes take place within the host lattice, which are as follows: A fraction of the incident ions collide with the atoms of the host lattice, transferring energy to the atom of the host lattice R which is given as follows:

$$E = \frac{4 m_1 m_0}{(m_1 + m_0)}$$

where E is the energy transferred, m_1 and m_0 are the masses of the host lattice atom and the incident ion. Consequently, the incident ion loses a part of its energy, with a corresponding gain in the energy of the host atom. If the energy transferred is more than the energy required for displacement of target atoms from their equilibrium position, the target atom is "knocked off" from its position. Additionally if the excess energy, i.e., $(E - E_d)$ is high, then the target atoms also produce subsequent cascades. This process repeats till the incident ion is thermalised in the host lattice. Hence, the maximum distance upto which the projectile ions penetrate into the host lattice, called the range of the incident ions depends on the incident energy, mass of the target ions and the host lattice atoms. These factors also influence the number of defects generated

in the crystal. The TRIM code calculates these two parameters, namely, the number of incident ions deposited and defect density as a function of distance from the surface of the crystal. The procedure adopted is as follows:

In TRIM code, the displacement cascades are obtained in the following way. Suppose a projectile atom having energy E collides with a target atom resulting in energies E_1 and E_2 for the projectile and target atoms respectively. Let E_d be the displacement energy and E_b , the binding energy of a lattice atom to its site. In this collision, a vacancy is created if E_1 and E_2 are both greater than E_d . Both atoms then become moving atoms of the cascade. If $E_1 > E_d$ and $E_2 < E_d$, then the struck atom does not have enough energy and it relaxes back to its original site releasing E_2 to the lattice phonons. If $E_1 < E_d$ and $E_2 > E_d$, then projectile atom remains at the collision site and such a collision is called a replacement collision. The charges Z_1 and Z_2 of the projectile and target atoms also have a role to play. If Z_1 differs from Z_2 , then the projectile atom having atomic number Z_1 becomes antisite lattice atom if $Z_1 = Z_2$, then Z_2 merely replaces Z_1 in the cascade and energy E_1 is released to the lattice as phonons. If $E_1 < E_d$ and $E_2 < E_d$, then Z_1 becomes an interstitial and $E_1 + E_2$ is released to the lattice as phonons.

TRIM code repeats these calculations for every collision till there is no more cascade and calculates the implantation and damage profiles for any incident ion of a chosen energy in any matrix, containing host lattice atoms.

2.7 SUMMARY

This chapter has explained the preparation of the alloys, their chemical composition, heat treatments, specimen preparation for various techniques, the techniques employed and the details of the software used for CBED computations.

CHAPTER 3

FORMATION OF NON-EQUILIBRIUM PHASES DURING SOLIDIFICATION OF WELDMENTS OF 9Cr-1Mo STEEL

3.1 INTRODUCTION

A reliable, long service performance of components of 'ferritic steels' has been one of the major considerations in power industry, in view of their extensive use in steam generator applications. Quite often, the failure of many components is initiated in a localised, microscopic region of the weldment, either during welding or in service (1,2). Such situations arise, even if the properties of the weld joints satisfy all the quality control tests for the components. The frequent failures of components are due to significant differences in the behaviour of various regions of the weldments of ferritic steels (3-6). These steep variations are caused by the formation of heterogeneous structures in different regions of the weldments, due to differences in the thermal cycles introduced during welding.

The major causes of failure of weldments of ferritics have been identified as follows: formation of δ -ferrite (3,7), over-coarsening of austenite (τ) grains near the weld (8-10), hydrogen cracking (11) and cooling along the duplex phase field between Ac3 and Ac1 (1,2). Ac3 refers to the temperature at which the high temperature τ phase

enters the duplex phase field. A_{c1} is the temperature at which the proeutectoid ferrite - α enters the duplex ($\tau + \alpha$) phase field. It has been found that most of the ferritics, in the range of 9 to 12 wt. % Cr have small amounts of δ -ferrite, which is found to cause brittle failures (1,7). The problem is more severe in thick sections of the components of 'high Cr' steels, with 9Cr steel being the lower limit of Cr content (12). Frequent failures were found to occur in the coarse grained region of the welds of ferritics (12-14). These regions correspond to the microscopic locations wherein extensive softening had occurred, due to the growth of prior austenite grains. The formation of such regions had introduced steep strain gradients, an undesirable microstructural effect. This problem has been overcome by appropriate control of chemistry and welding parameters (3-6). Another unavoidable microstructural feature is the formation of intercritical zone in the heat affected zone, HAZ of welds of ferritics (3). Extensive softening takes place in this region due to formation of pro-eutectoid ferrite (α). This is another region which is prone to high incidence of nucleation of cracks.

Apart from these microstructural heterogeneities, the welding process sometimes introduces significant differences in the microchemistry of different regions (1). This is due to the differences in the repartitioning coefficients of various solute elements in the liquid and other phases that form in the solid state. The stability and formation of the phases during cooling, depend crucially on the microchemistry, i.e., the degree of repartitioning of solutes. These deleterious microstructural and microchemical modifications of the base metal during welding, take place in regions which are as small as a few nanometers. Hence, the application of analytical electron microscopy becomes essential for the complete understanding and control of microstructure.

The present chapter offers a complete description of the as-welded state of 9Cr-1Mo weldment, in terms of microstructure, microchemistry and lattice strain. The

rationalisation of the observed changes in these factors has been attempted, based on the possible maximum temperature achieved and the rate of cooling. The first section describes the influence of the thermal cycle on the evolution of 'primary' or 'as deposited' structure. The thermal cycle each region undergoes depends on its distance from the source of heat. Accordingly, various 'microstructural zones' are identified, representing the typical 'primary' microstructure. Based on the microstructural studies, temperature isotherms are generated for the various zones, representing the primary microstructure.

The second section discusses the influence of multiple passes on the evolution of microstructure in the weld. The changes in the microstructure due to thermal cycles and recovery of strain during multipass have been studied in detail. Based on the results of these studies, a three dimensional phase field map has been proposed. This diagram represents the various phases that form in the weldments of 9Cr-1Mo steel, during the manual metal arc welding process.

The present studies reveal that the microstructural evolution depends on the degree of relief of strain, during multipass welding. Therefore, the strain of various regions of the weld has been measured using a fine electron probe, of diameter few hundreds of nanometers. This has been possible due to the newly emerging technique, convergent beam electron diffraction, CBED. These results are compared with that of conventional X-ray diffraction techniques. Since CBED was found to provide a reasonable measure of the locked-in strain over microscopic regions, it has been applied to identify the presence of δ -ferrite in the martensitic matrix of 9Cr-1Mo weldments. Detection of stringers of non-equilibrium δ -ferrite in a matrix containing laths of martensitic ferrite (α') using conventional transmission electron microscopy is quite difficult. The method of overcoming these difficulties using CBED is discussed in the last section of this chapter.

Thus, the present chapter provides the following important features:

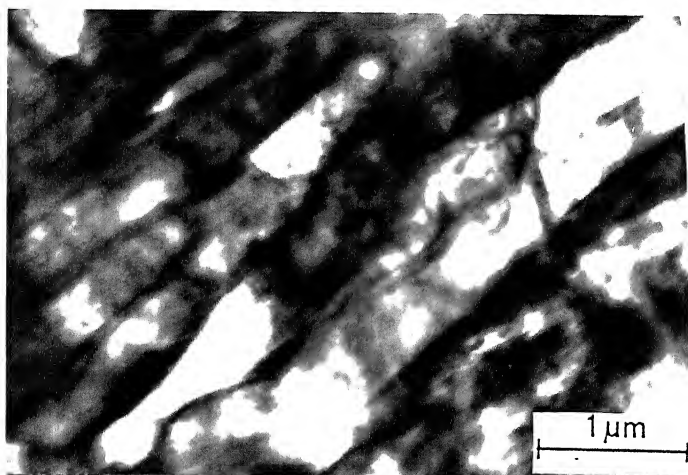
- * complete microstructural description of all sections of weldments;
- * identification of microstructural constituents in terms of morphological features, crystallography and microchemistry;
- * role of multiple passes in modifying the primary solidification structure;
- * identification of lattice strain using CBED technique; and
- * elucidating the ambiguity with respect to an important microstructural constituent, namely, the δ -ferrite.

3.2 CHARACTERISATION OF THE BASE METAL

It is essential to characterise the microstructure of the base metal, prior to the discussion on the microstructural modification of the base metal during welding. Therefore, the structure of the base metal is discussed below.

The 9Cr-1Mo steel plates were supplied by M/s. Creusot Loire Industries, France, in the normalised and tempered condition. The chemical composition of the steel supplied is given in chapter 2. It is expected to have a distribution of globular carbides of $M_{23}C_6$ along the lath boundaries of tempered martensite α' , uniform distribution of M_2X inside the ferrite laths and a matrix containing laths of α' :

The micrograph of the base metal is given in figure 3.1a, showing the typical martensitic ferrite laths, having an average size of about $0.5\ \mu\text{m}$. The distribution of carbides which are expected to be present, is not clearly visible, due to their low volume fraction and fine size. Therefore, carbon extraction replica of the base metal was prepared to observe the presence of fine carbides. The corresponding micrograph is shown in figure 3.1b. The micrograph clearly shows the presence of two different types of carbides : the coarse, globular carbides of average size $10\ \text{nm}$, along the boundaries of ferrite laths and uniform dispersion of acicular carbides of average length $100\ \text{nm}$ and width $8\ \text{nm}$, within the ferrite laths. Image analysis of these carbides was carried out to estimate the total number density of the carbides (N_f), area fraction (A_f) of acicular and globular carbides, which are listed in Table III.1a. The analysis of several microdiffraction patterns from these carbides revealed that the coarse, globular carbides along the lath boundary are M_{23}C_6 and the acicular carbides are M_2X . A typical microdiffraction pattern of M_2X is shown in the inset of figure 3.1b. Energy dispersive analysis of X-rays (EDAX) of a large number of carbides was carried out. Typical spectra of the two carbides are given in figure 3.2a and b. It is seen that the spectra consist of characteristic X-ray peaks from iron, chromium and molybdenum - the three elements which constitute the component M in M_{23}C_6 and M_2X . Carbon, being a light element, has not been detected. The percentage of different elements in M was calculated based on the quantitative analysis of the EDAX spectra, from a large number of carbides, as per the procedures explained in chapter 2. Table III.1b gives the constituents of M in M_{23}C_6 and M_2X , i.e., the relative amount of iron, chromium and molybdenum in percentage. The microchemistry, especially the concentration of chromium in M of the carbides was a fingerprint of the type of carbide. For example, the chromium content of M in M_2X was always around 90%, in contrast to around 60% in M_{23}C_6 . The constituents of M are fairly easy to



(a)



(b)

Figure 3.1 Microstructure of the normalised and tempered wrought 9Cr-1Mo steel.

(a) Micrograph showing the lath structure and (b) carbon extraction replica of the same showing the distribution of inter and intralath carbides of type $M_{23}C_6$ and M_2X . Inset shows microdiffraction pattern of M_2X along $\langle 200 \rangle$.

Table III.1

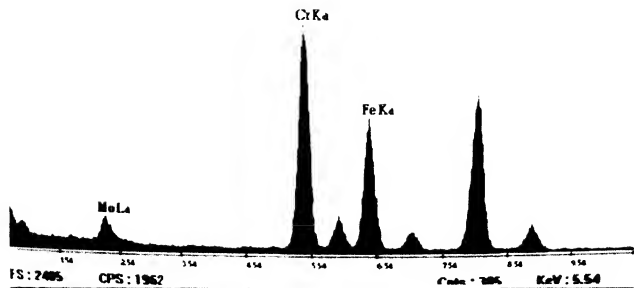
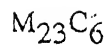
Microstructural and microchemical details of base metal.

a) Microstructural parameters of carbides in the base metal.

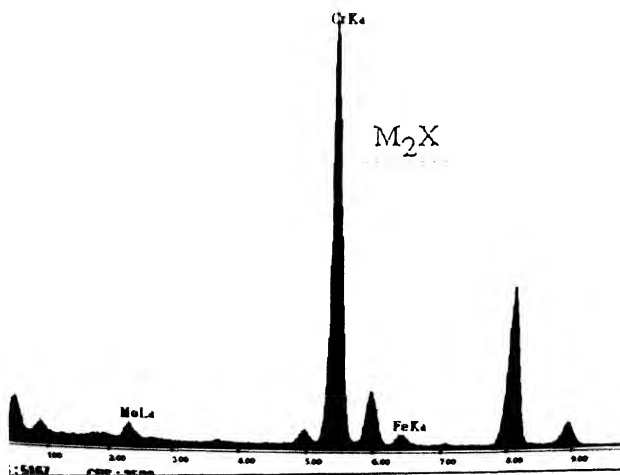
Sl.No.	Type	Shape	Site	$N_f / (\mu m)^2$	A_f
1	M_2X	Acicular	within laths	--	0.0019
2	$M_{23}C_6$	Globular	lath boundaries	--	0.0018
3	Total		--	2.66	0.0037

b) Quantitative microanalysis of different phases.

Sl.No. Description		% Element in Metal Sublattice		
		Fe	Cr	Mo
(i)	<u>Carbides</u>			
1	M_2X	3.4	92.3	4.3
2	$M_{23}C_6$	31.0	61.0	8.2
(ii)	<u>Parent α matrix</u>	<u>Composition (a/o)</u>		
3	α -ferrite (mass balance)	91.0	8.08	0.91
4	α -ferrite (thin foil)	91.3	7.6	1.1



(a)



(b)

Figure 3.2 Typical EDAX spectra of (a) $M_{23}C_6$ and (b) M_2X in normalised and tempered wrought 9Cr-1Mo steel. The higher ratio of concentration of chromium to iron is a fingerprint of M_2X .

determine. Sometimes, it is possible that the component C in $M_{23}C_6$ could have been replaced by small amount of nitrogen, retaining the stoichiometry as $M_{23}(CN)_6$. The extent of replacement by nitrogen depends upon the nitrogen content of the original steel ($<0.005\%$ in the present study). In the case of M_2X , the ambiguity regarding the composition of X has not been completely resolved. It is believed that X is mainly nitrogen or occasionally, a mixture of carbon and nitrogen (15).

The composition of the ferrite matrix was calculated, based on the microstructural parameters and using the mass balance equation,

$$A_f(\text{carbide}) \times \%M(\text{carbide}) + (1-A_f) \times \%M(\text{ferrite}) = \%M \text{ in the original steel.} \quad (3.1)$$

wherein A_f is the area fraction of carbide and $\%M$ is the concentration of element M in $M_{23}C_6$. The values of $A_f(\text{carbide})$ and $\%M(\text{carbide})$ are given in Table III.1.

The amount ($\%M$) of solute elements in ferrite is calculated (Table III.1b) and these were compared with the experimental values. These values agree well with those evaluated using quantitative analysis of EDAX spectra from a number of regions of ferrite, in thin foils of the base metal.

The above results may be summarised as follows: the parent metal prior to welding is found to consist of α -ferrite, M_2X and $M_{23}C_6$. Based on the available data (16) on the solubility of carbon (0.001%) in α -ferrite, the supersaturation of carbon (0.051%) in ferrite is found to be the parameter that governs the evolution of carbides.

3.3 EXPERIMENTAL CLASSIFICATION SCHEMES

The microstructure developed in the weldment as the liquid pool cools to ambient temperature is referred to as the 'primary' or the 'as deposited' structure (17). The primary structure depends on the welding conditions and the physico-chemical properties of the steel. These include the weld geometry and the welding conditions, the phases that can form during cooling, their kinetics, the repartitioning coefficients of various solutes and the repartitioning kinetics. The geometry of the weld zone of the steel during manual metal arc welding in the present study is given in figure 3.3. The welding conditions are given in Table III.2.

The three major themes of the present chapter are as follows: (i) the primary solidification structure, (ii) the effect of multipass and (iii) the variation of lattice strain using convergent beam electron diffraction (CBED) technique. Therefore, three different experimental classifications are used to understand the microstructural evolution. Since, multipass manual metal arc welding is used in the present study, most of the structures away from the top surface of the weld do not necessarily represent the 'primary' or 'as welded' structure. The top surface alone could best be approximated to represent the primary solidification structure. Hence, discussion of the primary structure is restricted to the changes observed at the top surface of the welds. The as welded samples have been sectioned as shown in figure.3.4a. The microstructural studies are carried out along a number of cross-sections (hereafter, referred to as CS-1 to CS-10) in the top surface. The distances of each of these cross-sections from the weld centreline, quoted in this chapter, do not take into account the loss in thickness during sectioning. Hence, these values are only approximate. The primary microstructure is derived based on studies on the top surface of various cross-sections, cut parallel to the weld center line.

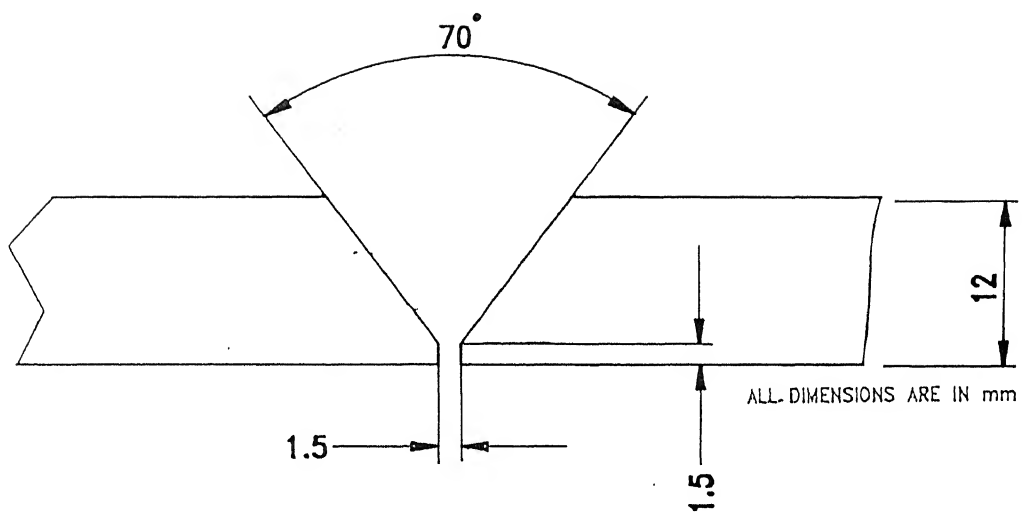


Figure 3.3 Geometry of the manual metal arc weld used in the present study.

Table III.2

Welding Parameters.

Welding Process	:	Manual Metal Arc.
Electrode	:	Basic Coated 9Cr-1Mo electrodes.
Composition of Electrode in wt. %	:	Cr=8.9%; Mo=0.98%; C=0.12%; Si=0.52%; Mn=0.52%; P=0.003% and S=0.03%;
Diameter	:	3.15 mm
Arc Voltage	:	22 V
Arc Current	:	100 - 130 Amps.
Number of Passes	:	Four.

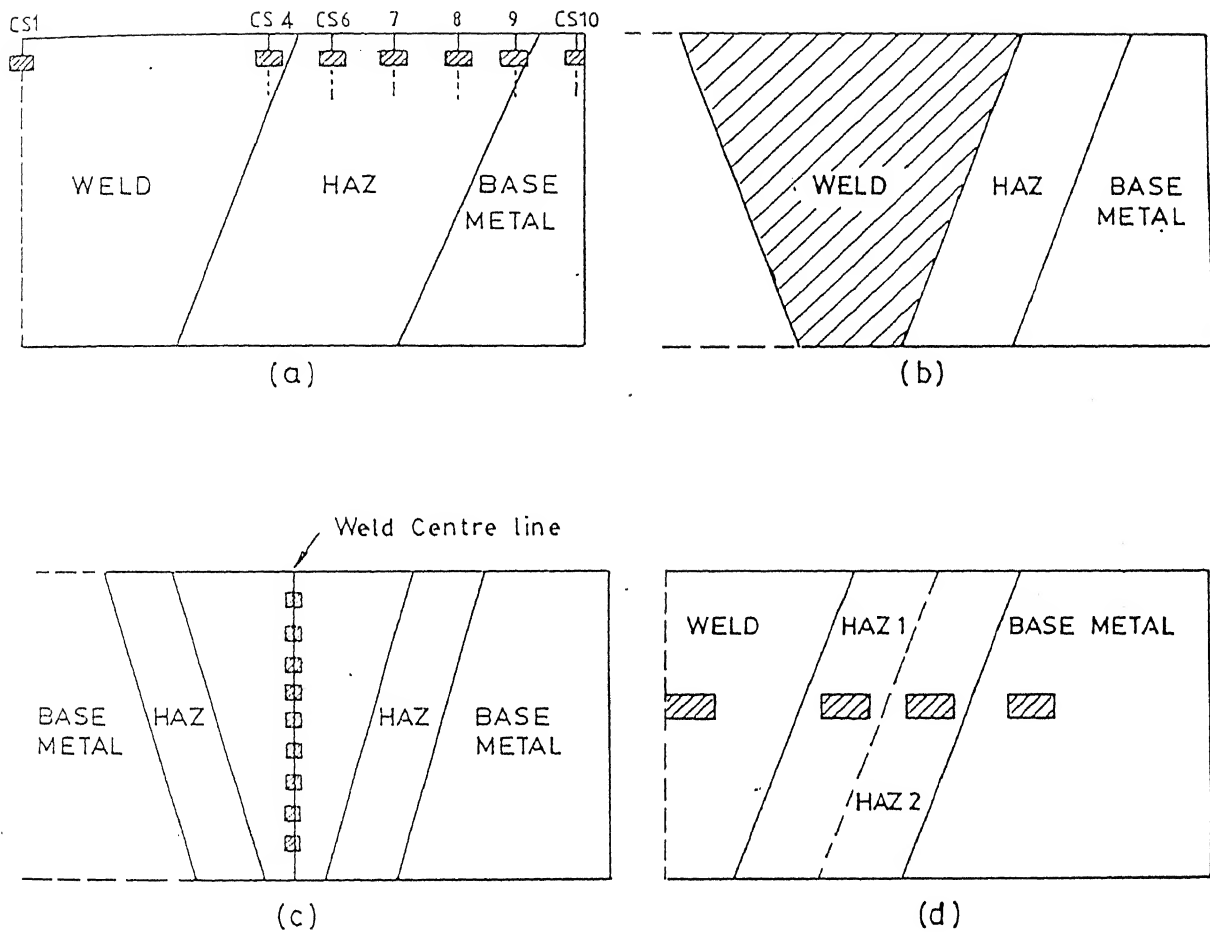


Figure 3.4 Locations of the chosen cross-sections for the four different experimental schemes. The shaded regions indicate the position of the samples.

- (a) Cross-section 1 (CS-1) to cross-section 10 (CS-10) for the determination of primary solidification structure.
- (b) Weld region for the effect of multipass.
- (c) Strain variation from top to root of the weld along the weld centre line and
- (d) The four sections chosen for CBED experiments to determine lattice strains.

The effect of multipass has been studied in the weld region of the weldment, as shown in figure 3.4b. In order to understand the effect of distance from the top surface, carbon extraction replica from nine regions (figure 3.4c) along the weld centreline were prepared and studied using analytical electron microscope. For the study of lattice strain from the weld region upto the base metal using convergent beam electron diffraction, thin foils were prepared in regions, as shown in figure 3.4d. The regions chosen are the weld, the portion of HAZ near the weld - HAZ1, region of HAZ near the base metal - HAZ2 and the base metal.

The microstructural parameters and microchemistry of the carbides are evaluated as described in chapter 2. The variation of these parameters with distance from the weld centre line is discussed frequently in this chapter. In all these evaluations, the statistical error is indicated by a vertical line at the (right side) top of each figure.

3.4 MICROSTRUCTURAL RATIONALISATION OF HARDNESS PROFILES

Conventionally, hardness profiles have been used as a preliminary guide to indicate the extent of changes during welding. Hence, microhardness profiles were taken along the top surface of the weldment with a load of 100 gm and is shown in figure 3.5. A gradual reduction in the hardness from weld region to base metal is seen in figure 3.5. In addition, there are three specific regions of interest, shown in figure 3.5. Region A, very near the weld zone, shows a steep reduction in the hardness level upto about 310 VHN, from the original value of 420 VHN. This is followed by (region B) an increase to the original value, in the adjacent area of the heat affected zone. Another steep reduction (region C) in the hardness level near the end of HAZ close to the base metal represents the third region. Similar changes have been reported in the weldments of a

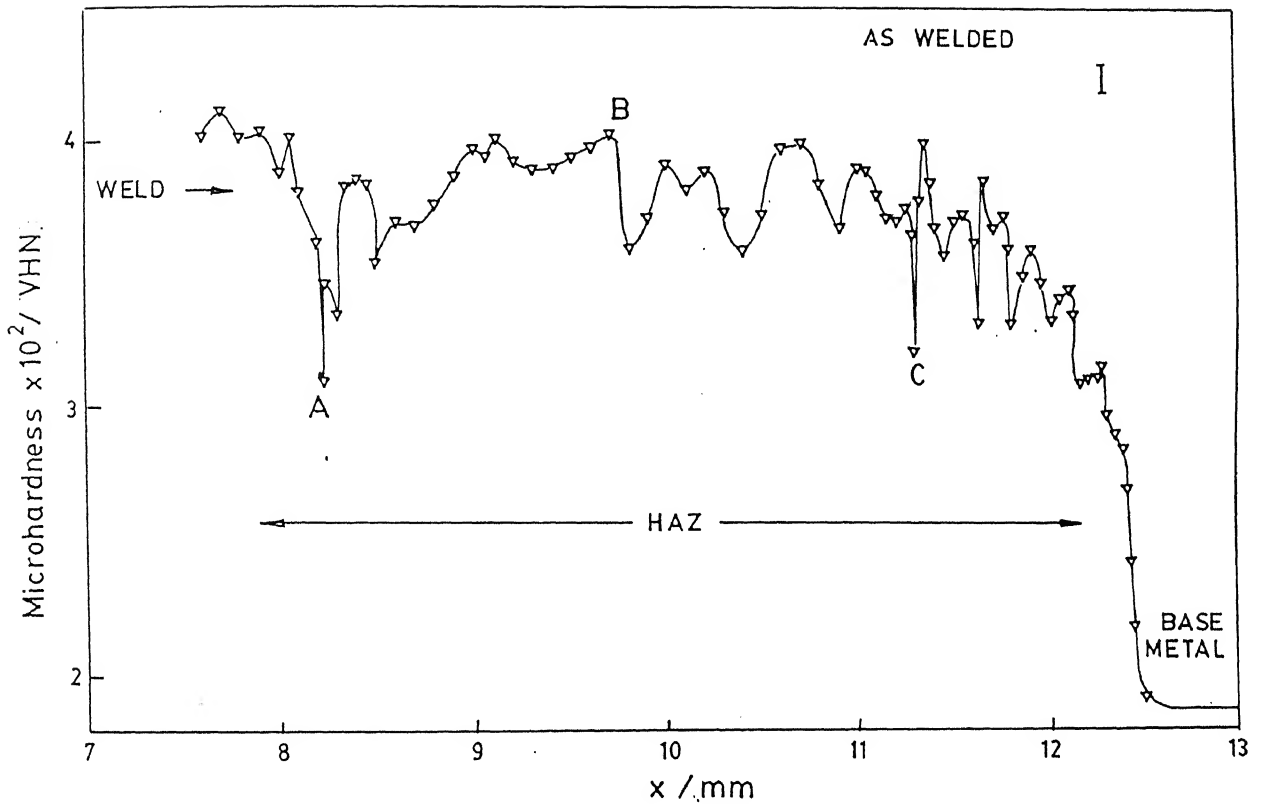


Figure 3.5 Microhardness profile along the top surface of the weldment of 9Cr-1Mo. 'x' is the distance of the region from the weld centre line. Steep softening is seen at locations A and C, corresponding to CS-5 and CS-9 respectively. Otherwise, generally high hardness is seen in the weld and HAZ. As the distance increases, the hardness reduces gradually to that of the base metal.

number of ferritic steels (18). These special features, and the general, gradual reduction in hardness with increase in the distance from the centre line of the weld are indicative of the significant changes in the microstructural features.

The hardness value of the weld zone is about 420 VHN. This value remains constant upto the end of weld zone. The high hardness value is due to the formation of martensite (α') as shown in figure 3.6a. This region extends from cross-sections CS-1 to CS-4. The steep reduction of hardness in regions near the boundary between the weld and the heat affected zone, HAZ, namely, CS-5, is found to be due to 'reaustenitisation' of the unliquified parent metal (figure 3.6b). The narrow region of base metal close to the weld liquid pool, is expected to have reached high temperatures within the τ phase field, for short durations. At these temperatures, the pre-existing carbides of the base metal dissolve completely. This favours unhindered movement of the austenite (τ) grain boundaries, resulting in coarse austenite grains. The 'reaustenitisation' of these regions is responsible for the observed softening, at A. With further increase in the distance, x, from the weld centre line, i.e., CS-6 to CS-8, hardness approaches a high value of ≈ 400 VHN, similar to that of the weld zone. This increase in hardness is due to the formation of martensite, α' (figure 3.6c). As the base metal is approached, a sharp reduction in hardness is seen near the interface between HAZ and base metal, corresponding to region CS-9. The microstructure, corresponding to this region (figure 3.6d) shows the evidence for the formation of soft 'proeutectoid ferrite' (α). This suggests that the region has been exposed to the duplex ($\tau + \alpha$) phase field. The rapid softening is thus attributed to the formation of proeutectoid ferrite, α .

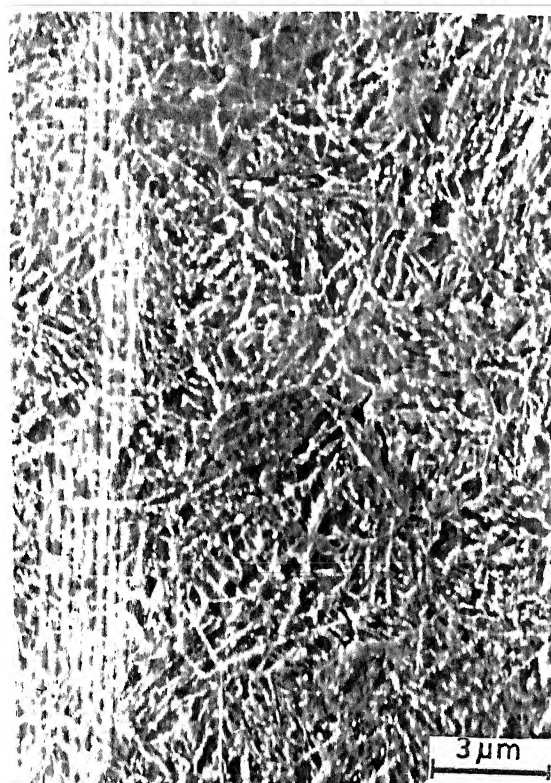
Thus, the steep variations in microhardness profile have been correlated to the observed microstructural features, as follows: high hardness of the weld zone consisting of only martensite α' , followed by a gradual softening as the base metal is approached, due to



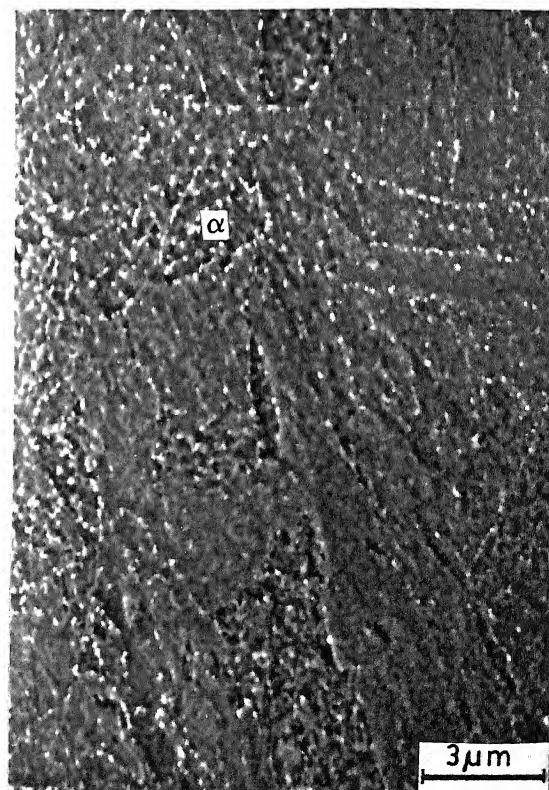
(a)



(b)



(c)



(d)

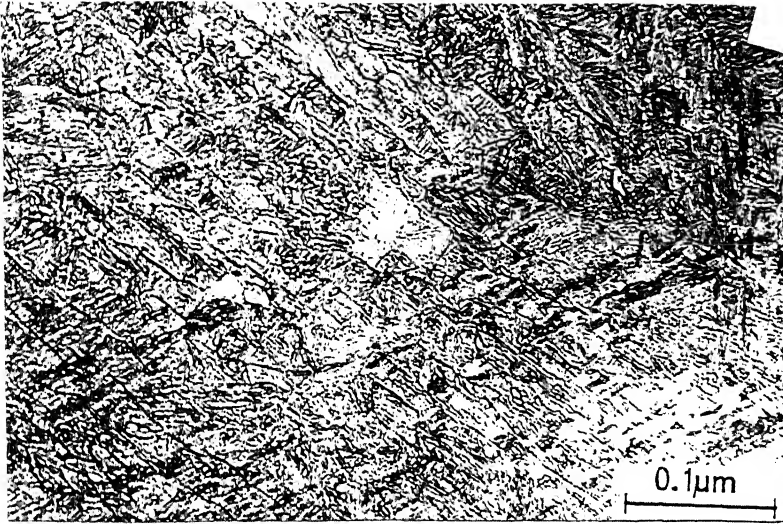
Figure 3.6 Micrographs of regions at various distances from the weld centre line to the base metal. (a) Representative structure of weld zone (CS-1 to CS-4). (b) Reaustenitised region, CS-5 corresponding to softening at A in Fig. 3.5. (c) Representative general structure of region B, CS-6 to CS-8 and (d) Microstructure of

reduction in the amount of α' . In addition to the gradual decrease in the hardness, significant softening is observed at two regions - one near the interface between weld and HAZ and another near the interface between HAZ and base metal. These softening effects have been identified as due to "reaustenitisation" of the base metal at very high temperatures near the weld pool and exposure within the duplex ($\tau + \alpha$) phase field, respectively.

In order to understand the microstructural variations at much finer levels, detailed microstructural characterisation of the different regions of the weldment has been carried out. Conventionally, the weldments are classified into the weld, the heat affected zone (HAZ) and the base metal. Since detailed study of the base metal has already been provided, the microstructural characterisation of the weld and the HAZ will be presented in the next section.

3.5 MICROSTRUCTURAL CHARACTERISATION OF THE WELD ZONE

The microstructure of the weld zone upto a distance of about 4 mm (upto cross-section, CS-4) from the weld centreline was found to be uniform. A typical representative structure of the same is shown in figure 3.7a. The structure is characteristic of a martensitic ferrite phase, consistent with a high value of hardness around 420 VHN. The prior austenite grains are elongated, with a typical size of about 1 mm x 150 μm . The lath size was about 4 to 5 μm . The scatter in these values was not high. This suggests that the cooling rate within the weld region was uniformly high. At high cooling rates, the 'stay time' at different temperature intervals in the τ phase field is very low. Hence, the nucleation and growth of prior austenite grains over a wide range of temperature intervals could not proceed. Consequently, a wide range of values of prior austenite grain size (PAGS) has not been observed.



(a)



(b)

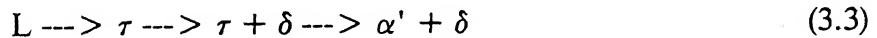
Figure 3.7 Typical microstructure of the weld zone. (a) The martensitic structure and (b) the laths within the same.

In addition, the prior austenite grain boundaries in the weld region were found to be elongated along a specific direction, indicating rapid solidification of the liquid, along the direction of maximum rate of cooling. The steep temperature gradient across the interface between liquid and solid during cooling, is responsible for the directionality of prior austenite grains with their major axes along the direction of maximum heat flow.

The weld zone represents the region which had liquified during welding and undergone solidification. The chemistry of the weld region is expected to be the same as that of the filler material, the composition of which is given in Table III.2. The solidification of the liquid metal could proceed by two different routes, depending upon the chemistry and rate of cooling: liquid transforms directly to 100% τ , which could subsequently undergo a solid state transformation into α' . Alternately, a mixture of τ and δ -ferrite could form, where τ is the dominant phase. In the present study, δ -ferrite was not observed in the weld region of 9Cr-1Mo weldments. This suggests that neither the chemistry of the weld nor the cooling rate favoured the transformation,



or



It is therefore reasonable to assume that



represents the transformation in the weld zone. The solidified τ should have inherited the composition of the liquid metal.

Solidification of the liquid metal into the duplex phase field, δ and τ has been reported in a series of steels with Cr content in the range of 9 - 12 wt.%, with 9% being the border line case (7). The solidification of 9 Cr steel into the duplex phase field depends crucially on the amount of ferrite stabilisers, especially Si, the cooling rates and the degree of repartitioning of Cr into the liquid. In the present study, the liquid has been found to solidify into the τ phase, without any detectable δ -ferrite. This could be attributed to the low amount of silicon and high cooling rate. The influence of these two factors in the formation of δ -ferrite is understood as follows: δ -ferrite is found in weldments with silicon content higher than 0.5% since silicon is a ferrite stabiliser; slow cooling rate enhances the "time of stay" in the high temperature duplex $\tau + \delta$ phase field. In the present study, δ -ferrite is not seen since the two factors mentioned above are not favourable.

3.6 MICROSTRUCTURAL CHARACTERISATION OF HEAT AFFECTED ZONE

Generally, the microstructure of the heat affected zone, HAZ, is martensitic, as shown in figure 3.6. However, variations exist in the structure, at finer levels. Though the basic microstructure consists of martensitic ferrite, there are distinct microstructural and microchemical variations at much finer levels, within the HAZ. It is seen that the microstructure of any region of the weldment is sensitive to the thermal cycle it has experienced during welding. Therefore, the distance of the region from the weld centreline is a crucial parameter in determining the microstructure of the region. In order to identify these changes, detailed studies were carried out following the experimental scheme, shown in figure 3.4a. The results of these experiments are discussed in detail below.

3.6.1 Microstructural Inhomogeneity of HAZ

The regions within the heat affected zone, correspond to cross-sections, CS-5 to CS-9, the region CS-5 being very close to the liquified metal and CS-9 being adjacent to the unaffected base metal. Figure 3.8 shows the micrograph of the region corresponding to CS-5. It is clearly seen that there are coarse (around $300\text{ }\mu\text{m}$) grains of τ , which transform subsequently to α' . This value needs to be compared with that of the base metal, wherein the PAGS is only around $50\text{ }\mu\text{m}$. The hardness of this cross-section is lower (300 VHN), than in cross-sections 4 and 6 (420VHN).

This region CS-5 corresponds to the portion of the base metal, which has not liquified, but is in contact with the liquid. Hence, CS-5 represents the region which has been exposed to the maximum temperature, retaining the solid state. The time of stay at such high temperatures below the 'solidus' temperature, is controlled by the welding speed and cooling rate. The initial modification of the normalised and tempered microstructure of the base metal is expected to have occurred during the heating cycle. Since the maximum temperature achieved is above the normalising temperature range of the steel, the dissolution of the pre-existing carbides and growth of austenite grains are expected to take place, during heating. The extent of completion of these two events is governed by the degree of superheating and the time of stay at the 'reaustenitising' temperature. The observations in the present study suggest that the superheating is sufficient to completely dissolve all the pre-existing carbides. This, in turn, favours the unhindered movement of the grain boundaries of τ , resulting in a high value of the 'reaustenitised' grain size.

Another relevant factor is the possible formation of δ -ferrite in this cross-section, which is close to the liquified zone. Most of the failures of weldments of 9Cr-1Mo steel are

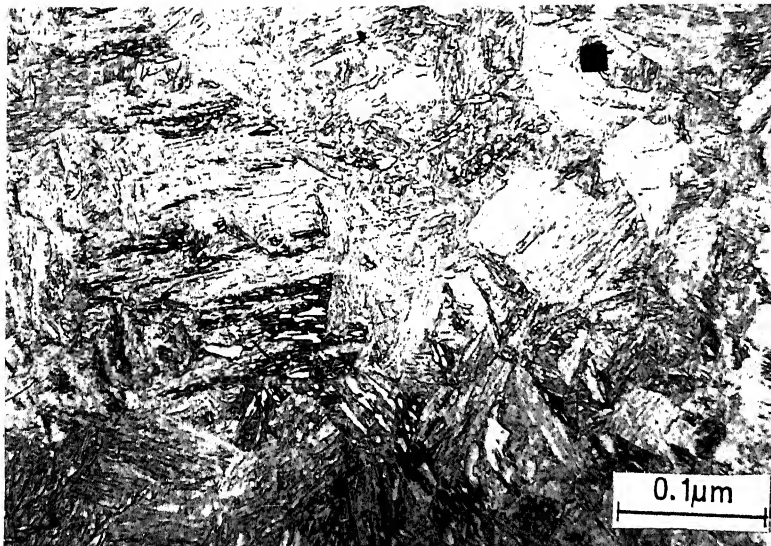
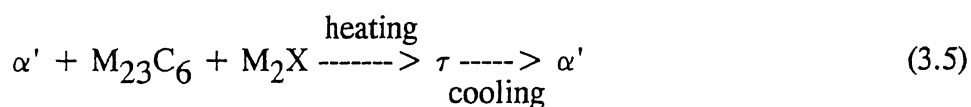


Figure 3.8 Evidence for 'reaustenitisation' in CS-5. Prior austenite grain size is about 300 μm , much higher than that of base metal (50 μm).

expected to be due to the formation of small amounts of δ -ferrite at regions of HAZ close to weld region. The formation of δ -ferrite in 'microscopic' regions at the interface between HAZ and weld zone is favoured by the following factors: (i) repartitioning of ferrite stabilising elements like Cr and Mo, (ii) Si content much higher than 0.5% and (iii) slow cooling rates. However, present studies do not show the presence of δ -ferrite. In fact, the evaluation of concentration of chromium at various cross-sections, to be discussed later, suggests that the concentration of chromium is not high in this particular cross-section. Based on the studies of wrought 9Cr-1Mo steel, it was found that the δ -ferrite requires atleast 30 minutes to grow to a size of 10 μm at 1573 K (19). Hence, at such high temperatures, wherein δ -ferrite could have formed in this region (CS-5), the available time is probably not adequate. The absence of δ -ferrite could also be due to low Si content of the steel and the small dimensions i.e., higher cooling rate of the welds.

The results discussed above suggest that the possible transformations in CS-5 can be deduced as follows:



The next region corresponds to CS-6, wherein excessive reaustenitising has not occurred, as can be seen in figure 3.9. The value of PAGS is around 100 μm and the hardness is quite high, 420 VHN. The PAGS and the lath size of α' in CS-6 have been carefully compared with those evaluated in wrought steels austenitised at various temperatures (19). The values of PAGS in CS-6 and that of wrought steel solutionised at 1450 K have nearly same values, 100 μm and 96 μm respectively. This suggests that the structure in the region CS-6 is typical of the same developed at around 1450K.

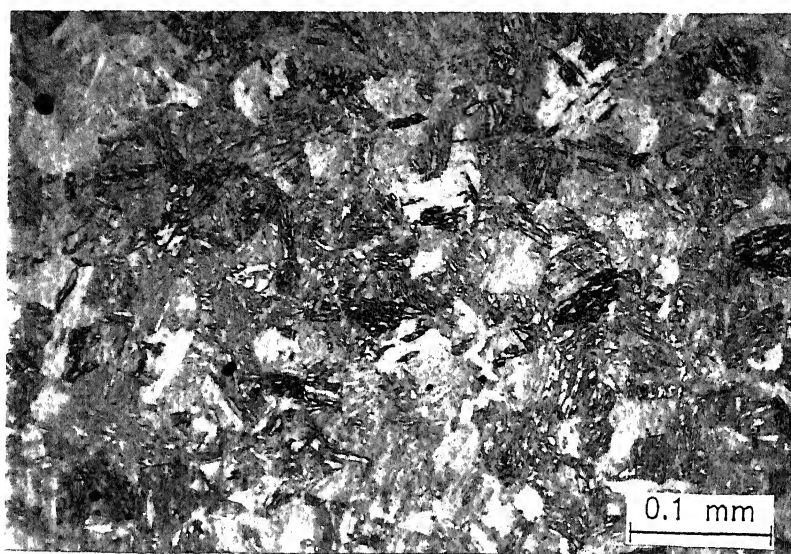
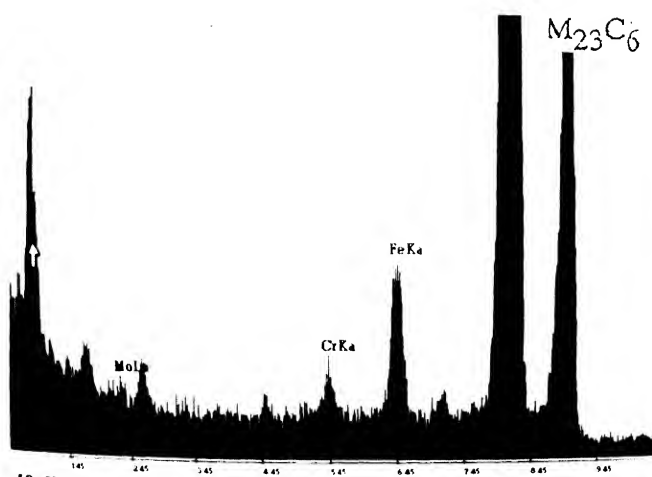


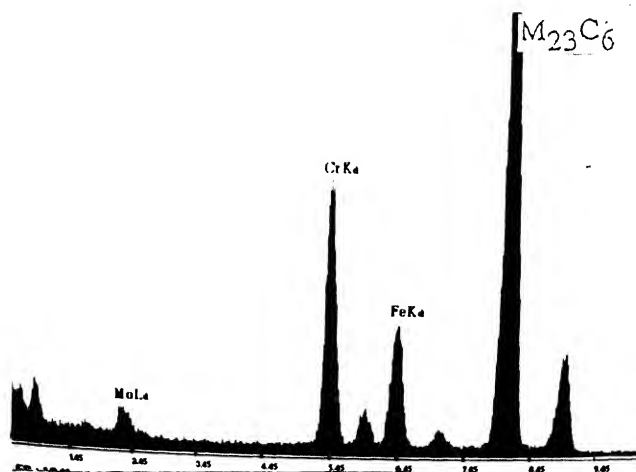
Figure 3.9 Martensitic structure in CS-6.

Figure 3.10 shows the micrographs of carbon extraction replica of region CS-6. Coarse laths of size $\approx 5 \mu\text{m}$ are seen, in addition to uniform distribution of fine carbides. The EDAX analysis of a number of these carbides, confirmed that only M_{23}C_6 carbides have formed, with two different types of distribution in M. The iron rich carbides, shown in figure 3.10a were predominant along with a few, chromium rich ones, arrow-marked, in figure 3.10b. The typical spectra from these two types of carbides are shown in figure 3.11. The relative amounts of different elements in M of M_{23}C_6 are as follows: 5% Mo, 17% Cr and 78% Fe in iron rich carbides and 8% Mo, 58% Cr and 34% Fe in chromium rich carbides. Despite these differences in the microchemistry of the two types of carbides, crystallographically both correspond to only M_{23}C_6 , a typical microdiffraction of which is given as an inset in figure 3.10a. Neither iron rich Fe_3C nor chromium rich M_2X was observed. Careful observation of many regions and EDAX analyses of a number of carbides confirm the absence of pre-existing carbides, i.e., the coarse, globular M_{23}C_6 along the lath boundaries and the chromium rich M_2X carbides, within the laths. This observation suggests that CS-6 of the HAZ has been exposed to temperatures which are high enough to dissolve all the pre-existing carbides. The size, area fraction (A_f) and number density (N_f) of carbides are measured and listed in Table III.3. It is seen that area fraction of carbides in CS-6 is much more than that of base metal. Based on these observations, it is expected that the carbides in CS-6 have freshly nucleated.

A critical analysis of the above observations can offer insight regarding the possible thermal cycle this region could have experienced during welding. The value of PAGS is nearly close to an austenitising treatment of 1400 K. No significant coarsening of the τ grains has occurred. However, the maximum temperature this region has achieved is sufficient to dissolve (figure 3.10) all the pre-existing carbides. The size of the laths in the region CS-6 is quite large and has a wide spectrum from 1 to 3 μm .



(a)



(b)

Figure 3.11 Typical EDAX spectra from the two types of carbides in Figure 3.10.

(a) Fe rich carbide and (b) Cr rich carbide.

Table III.3

Microstructural parameters of carbides in different cross-sections.

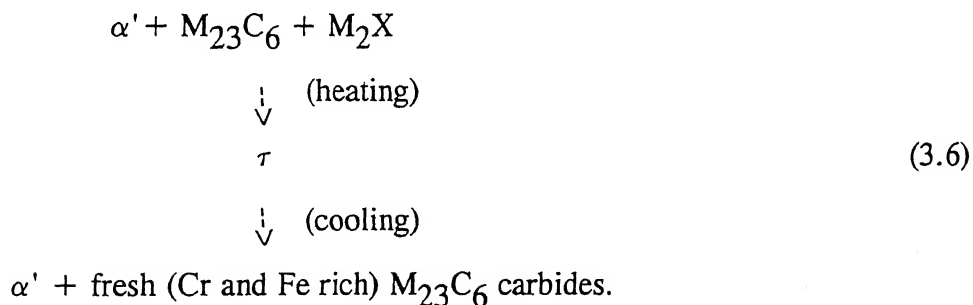
Sl.No.	C.S.*	Type	Size μm	A_f	N_f $/\mu\text{m}^2$
1	6	Glob. $M_{23}C_6$.	0.025	0.0018	--
2	6	Acicular	.	0.0061	--
3	6	Total	---	0.0079	14.6
4	7	Glob.	0.13	0.0013	---
5	7	Total	--	0.0013	1
6	8	Glob.	0.05	0.0004	
7	8	Acicular			
8	8	Total	---	0.0014	2.4
9	9	Glob.	0.13	0.0005	
10	9	Acicular		0.003	
11	9	Total	---	0.0036	3.8
12	B.M. ⁺	Total	--	0.0037	2.66

* CS-1 to CS-5 - carbides are seen only rarely.

+ B.M. corresponds to base metal for which details are given in Table III.1 also.

This is much larger than that of the normalised and tempered condition ($0.5 \mu\text{m}$). This suggests that the region CS-6 has experienced slower cooling rates than that of normalised steel. Consequently, the temperature range of formation of the observed laths is closer to the martensite start temperature - M_s , than that of normalised and tempered steel. Such a high temperature range of formation of α' leads to the observed coarse size of laths.

The presence of very few, chromium rich $M_{23}C_6$ suggests low stay time around 1030K, the nose temperature of the TTT curve for this transformation. It has been shown that the microchemistry of carbides is extremely sensitive to the temperature (20). The ratio, concentration of Cr to Fe, C_{Cr}/C_{Fe} in $M_{23}C_6$ increases as the temperature increases. Based on this observation, it is possible to deduce that the Fe-rich $M_{23}C_6$ carbides in CS-6 could have formed at lower temperatures. The sequence of transformations, for the region CS-6 can therefore, be summarised as follows :



The microstructure in figure 3.12 corresponds to cross-section 7 (CS-7). This shows a typical martensitic structure of the steel. The size of either the prior austenite grains or the laths is not too large. This region represents the portion of the base metal which is heated upto high temperatures which are less than regions CS-5 or CS-6. The dissolution of pre-existing carbides in this region is shown clearly in figure 3.12a. However, there has been fresh precipitation of $M_{23}C_6$ carbides. The identification of the carbides was carried out using the microdiffraction pattern. With respect to

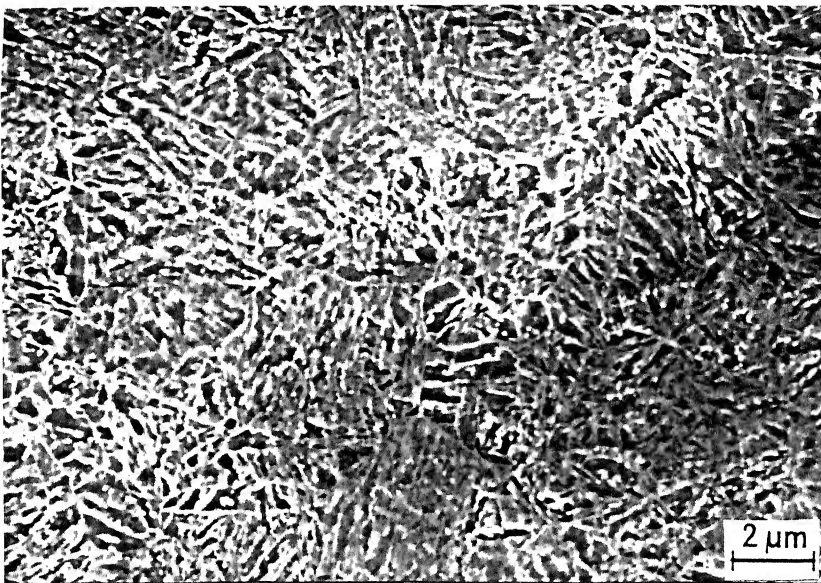
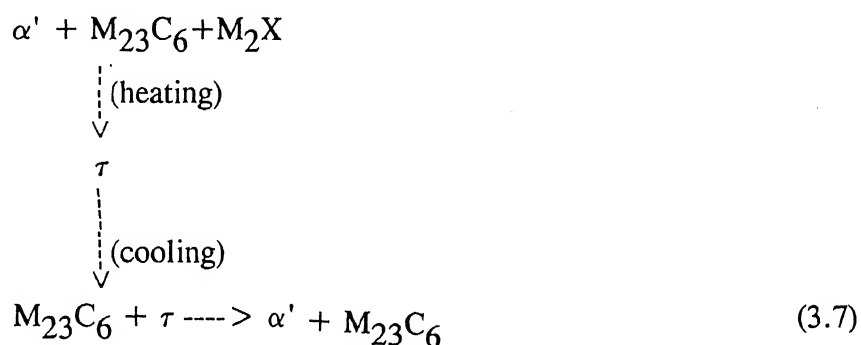
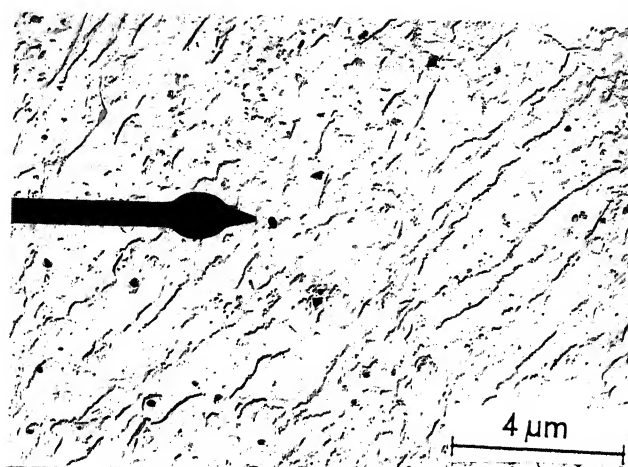


Figure 3.12 Scanning electron micrograph of the martensitic structure in CS-7, representing HAZ.

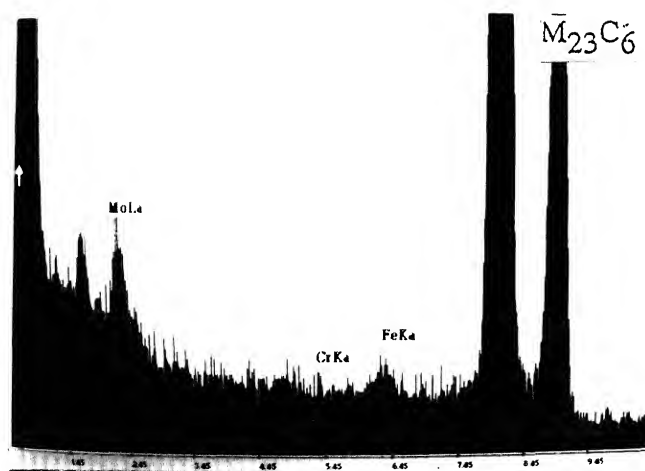
microchemistry of the newly formed $M_{23}C_6$, most of them were rich in chromium. However, there were a few carbides (arrow-marked in figure 3.13a) rich in Mo, and not chromium, as can be seen in the EDAX spectrum in figure 3.13b. It is expected, that this could have formed at around 1073 K, near the high temperature plateau of the TTT curve. The precipitation of fresh carbides in this cross-section during cooling has proceeded to a larger extent than in CS-6. However, it is far less than the base metal. This is due to availability of shorter time in the corresponding temperature range. Based on these studies, the evolution of the microstructure in region CS-7 of the HAZ can be written as follows:



The next region, i.e., CS-8 is characterised by retention of the laths of same size and PAGS, as that of base metal. Figure 3.14a shows the microstructure of carbon extraction replica of region CS-8, revealing the presence of coarse carbides along the lath boundaries. The carbides were found to be $M_{23}C_6$, with the percentage of M as 8% Mo, 60% Cr and 32% Fe. These values are similar to those observed in the base metal. M_2X carbides with 91% chromium in M (figure 3.14b) were also found to be present, without dissolving. The size and number density of carbides in CS-8 were compared (Table III.3) with that of the normalised and tempered base metal. This suggests clearly that the dissolution of the carbides has taken place, but has not proceeded to completion. The observed structure is typical of the lower temperature regimes of τ phase field. The superheating is not enough to dissolve the carbides completely. The pinning effect of the carbides on the τ boundaries, could be



(a)



(b)

Figure 3.13 Fresh nucleation of isolated Mo rich $\bar{M}_{23}\bar{C}_6$ in CS-7. (a) Micrograph from carbon extraction replica and (b) the corresponding EDAX spectrum from the carbide which is arrow marked in (a).

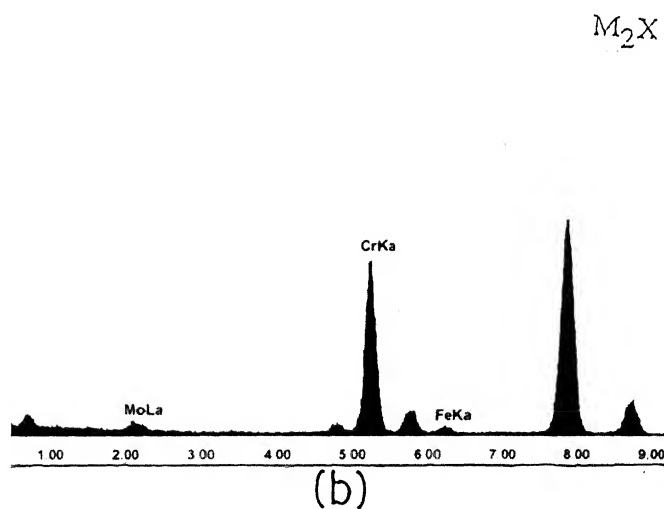
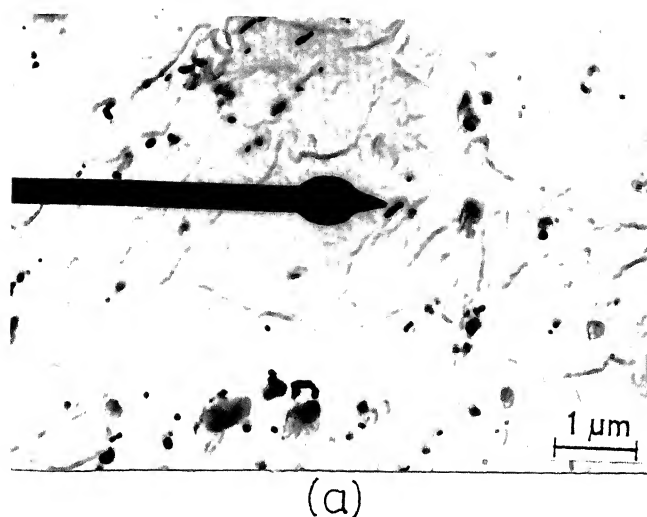
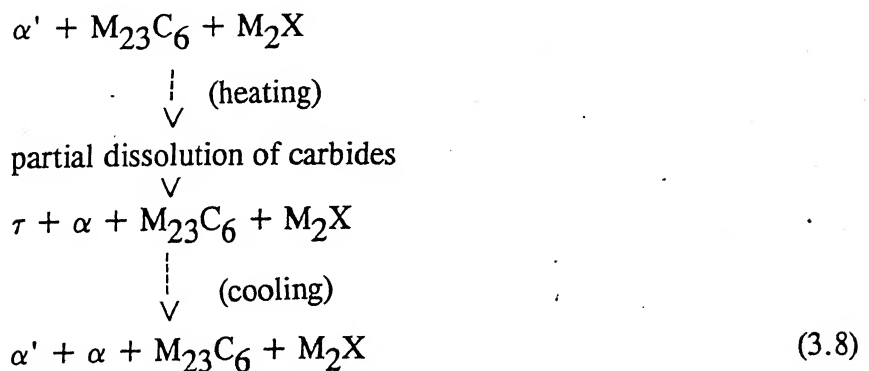


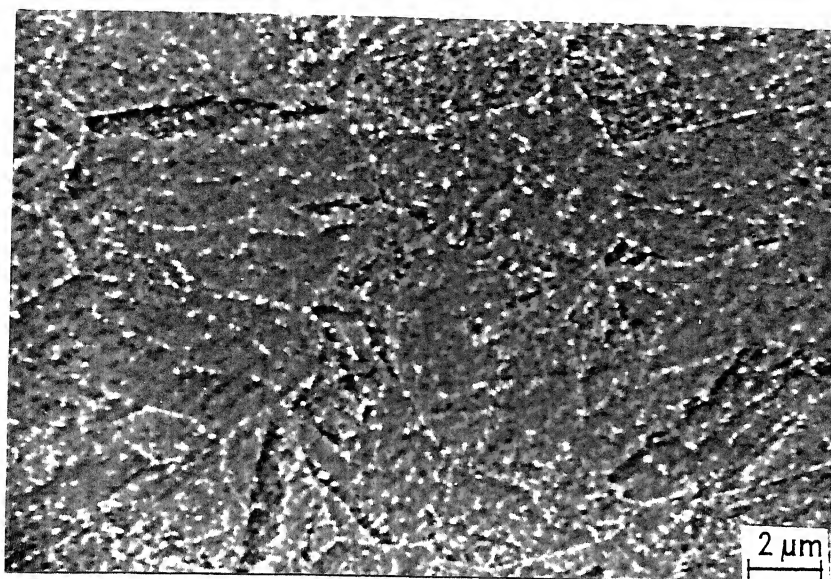
Figure 3.14 (a) Micrograph from a carbon extraction replica of CS-8, a region within HAZ. This shows the retention of pre-existing carbides of the base metal. The arrow mark shows M_2X . (b) EDAX spectrum of the carbide (arrow marked) confirming chromium rich M_2X .

responsible for the observed low values of PAGS and lath size and hence the high value of hardness (350 VHN).

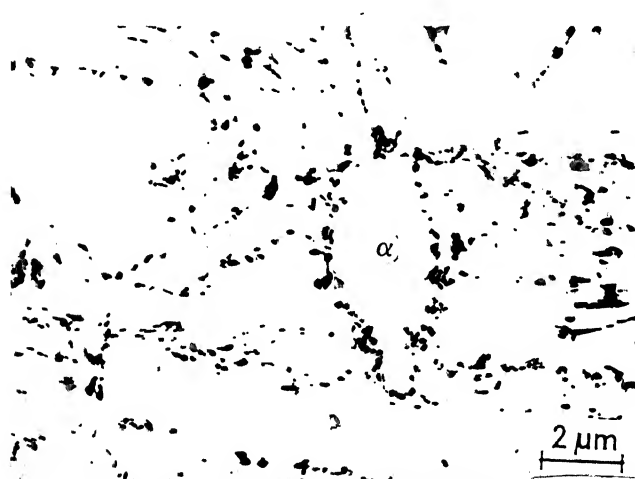
The microstructure of region CS-9 is shown in figure 3.15. This consists of tempered α' (figure 3.15a), along with low volume fraction of pro-eutectoid ferrite α (figure 3.15b). Generally, the distribution of carbides is typical of the base metal. In addition, there appears to be fresh nucleation of additional precipitates and coarsening of the pre-existing carbides (Figure 3.16 and Table III.3). Figure 3.16 shows the variation of number density of carbides with distance from the weld center line, i.e., for different cross-sections, CS-7 to CS-10. It is seen that the maximum in the number density is achieved at 9.5 mm i.e., cross-section 9. (The vertical line in the figure shows the error bar.) This suggests that the maximum temperature experienced by this region is neither too high for dissolution of pre-existing carbides nor too low to prevent nucleation of fresh carbides and coarsening of pre-existing carbides. This also suggests a very low rate of cooling in this region, providing sufficient time for growth and hence coarsening of carbides. The hardness in this region had reduced significantly to a value of around 200 VHN, consistent with the microstructural observation.

These observations suggest that the region CS-9 has been cooled through the duplex $\tau + \alpha$ temperature regime, i.e., between A_{c1} and A_{c3} . The region corresponding to CS-9 can be represented by the following transformation sequence:





(a)



(b)

Figure 3.15 Microstructure of CS-9, a region within HAZ of 9Cr-1Mo weldment. (a) Scanning electron micrograph showing the progress of considerable tempering. (b) Micrograph from carbon extraction replica of the same showing the presence of lath free, proeutectoid ferrite (α) in a martensitic matrix. This region corresponds to the intercritical region which has been exposed to the duplex ($\tau + \alpha$) phase field during the thermal cycling.

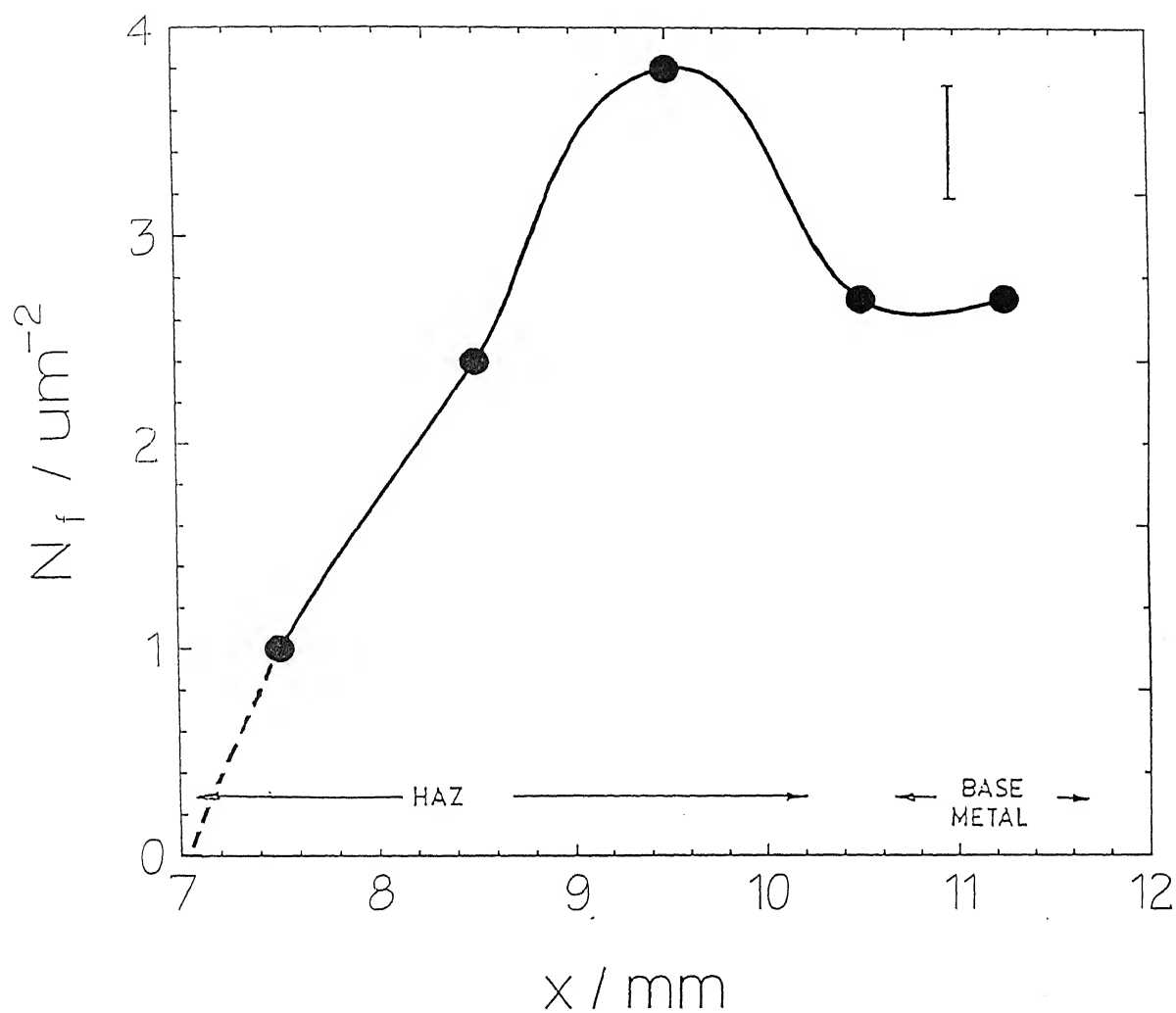


Figure 3.16 Variation in the number density of the carbides in different cross-sections. HAZ corresponds to CS-6 to CS-9 and base metal corresponds to CS-10.

3.6.2 Microchemical Inhomogeneity of HAZ

Another feature of interest, which was referred in section 3.1, is the repartitioning of the solute elements, between the coexisting phases, the liquid and the parent metal, across the interface. In addition, the different degree of dissolution of carbides, shown earlier is expected to alter the solute concentration of α -ferrite. The third factor, which could change the composition of the solutes across the weldment is the diffusion of solute elements due to differences in the activity of each solute in different regions. Hence, detailed analytical electron microscopy studies on the thin foils of various cross-sections described above were carried out.

Figure 3.17 shows the change in the concentration of chromium (figure 3.17a) and molybdenum (figure 3.17b), of α -ferrite across various cross-sections discussed earlier. These values were estimated using thin foils of the corresponding regions. The following precautions were taken during the analysis. The thicknesses were more or less uniform; no fine carbide was enclosed in the ferrite region from which microanalysis was carried out and the ZAF correction was applied during quantification of the data. The values of concentration of chromium showed limited scatter and the values obtained from the base metal and the weld metal were close to the wet chemical analysis data (marked in figure 3.17a). The minor difference (roughly 0.1% more than AEM data) observed is due to the fact that the wet chemical analysis provides the bulk composition, in contrast to microanalysis, which offers composition of the α -ferrite alone. It can be seen in Table III.1 that the total amount of chromium locked up in all the carbides in the normalised and tempered steel is about 0.15%. This accounts for the observed difference in the concentration of chromium determined using analytical electron microscopy (AEM) and wet chemical analysis.

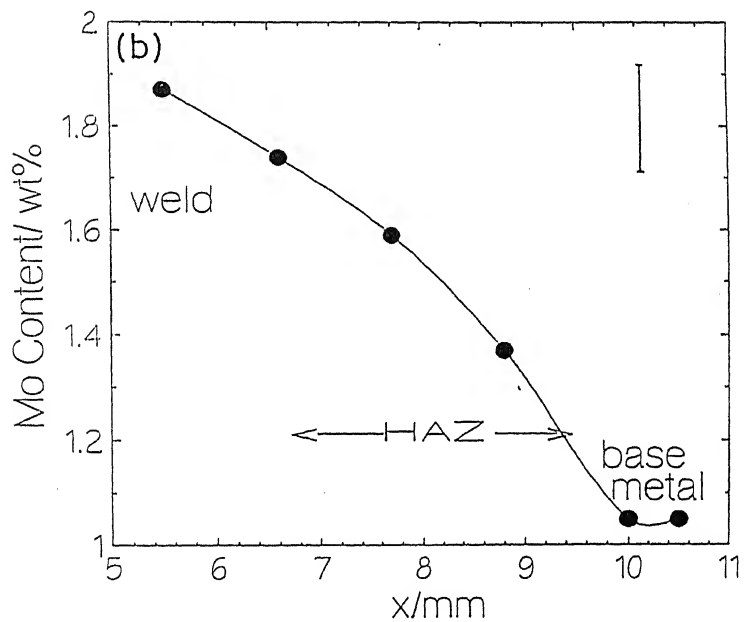
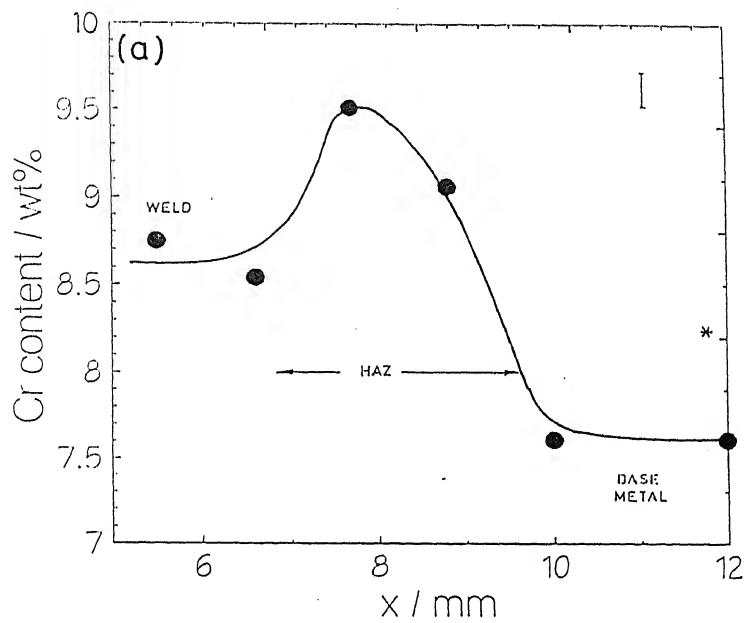


Figure 3.17 Variation in the concentration of (a) chromium and (b) molybdenum, as a function of distance from the weld centre line. * corresponds to the composition of the base metal determined by wet chemical analysis.

The chromium enrichment observed in CS-8, is more likely to be due to the dissolution of carbides. The possibility of repartitioning of chromium between the co-existing phases, liquid and τ is not likely to be the cause, since solubility of chromium in liquid is more than that of either δ -ferrite or τ . The third reason stated earlier, i.e., the solid state diffusion of chromium due to difference in activity, is not likely to contribute to the observed enrichment of chromium in α of CS-9. It has been shown in chapter 4 that the difference in activity in the three regions, weld, HAZ and base metal is very small (in the present study) that even carbon does not diffuse significantly.

The estimation of molybdenum in α -ferrite was found to be less accurate. The statistical scatter in the values was high. The average values of molybdenum in the base metal and the weld metal were found to be consistently higher than the corresponding values based on wet chemical analysis. This could be associated probably with the problems in detection of low amounts (0.955%) of heavy element like molybdenum in the steel. Moreover, concentration of Mo was determined using MoL_{α} which required a high value of absorption correction. The final values are thus expected to be very sensitive even to minor variations in the thickness of the thin foil from which microanalysis is carried out. Despite these problems, there appears to be a gradual increase in the molybdenum content of the HAZ, as shown in figure 3.17 b. This could be due to the differences in the degree of dissolution of carbides, within the short duration of time of residence of that region.

3.7 COMPREHENSIVE MICROSTRUCTURAL PHASE FIELDS OF PRIMARY SOLIDIFICATION STRUCTURE

The extensive studies described above, have helped to deduce the scenario of microstructural evolution, during primary solidification process. It has been shown that

the finer details of the microstructure of different cross-sections are heterogeneous and extremely sensitive to the distance of the region from the weld centre line. The cause of these variations is related to the differences in the thermal cycle each region is subjected to. The relevant parameters of the thermal cycle are the maximum temperature attained by each region, the 'residence time' at this temperature and the rate of cooling. It is possible to deduce some of these factors based on the microstructural studies presented earlier. The first part of this section provides the details of these "thermal cycles" and the second part proposes a comprehensive microstructural phase field map of primary solidification structure.

3.7.1 Thermal Cycles of Different Regions of Weldment

Based on the detailed studies presented above, a schematic representation of the temperature-distance profiles (figure 3.18) is attempted. The possible maximum temperature (T_{\max}) each cross-section could have been exposed to, is shown in figure 3.18a. An attempt has been made to identify the time-temperature profiles at various distances, based on the microstructural studies, without resorting to heat transfer calculations. Schematic time-temperature plot depicting the various events, during the heating and cooling cycles, for various cross-sections are shown in figure 3.18b. It is quite clear that those regions which do not experience temperatures beyond the tempering temperature of 1023 K, remain unaffected. Curve '1' in figure 3.18b shows that T_{\max} is close to temperatures above the liquidus of the steel in regions, very near to the heat source during welding. 2 represents the region which has not liquified, but has reaustenitised, resulting in coarse τ grains with dissolution of pre-existing carbides. 3 depicts the regions which have reached temperatures sufficiently high for the dissolution of carbides but not enough for reaustenitisation. The curve 4 corresponds to the region lying between Ac_3 and Ac_1 temperatures, wherein sufficient coarsening of

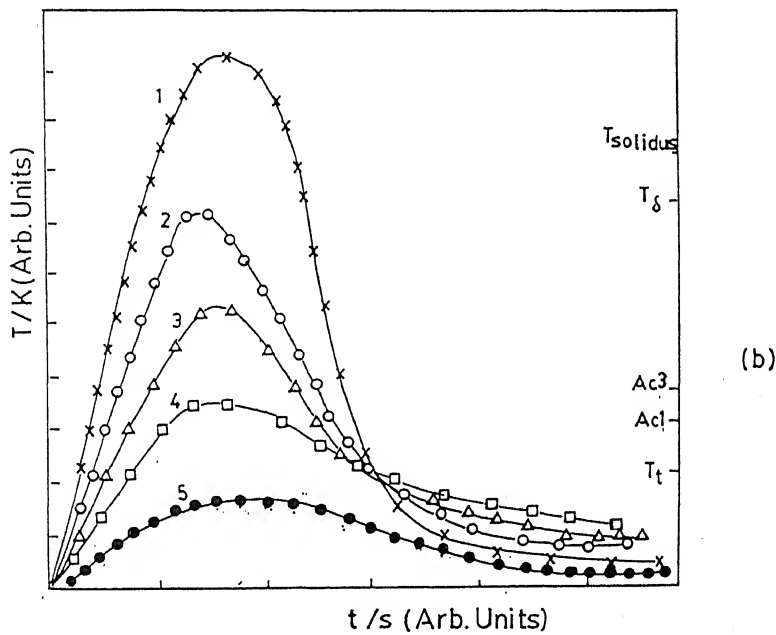
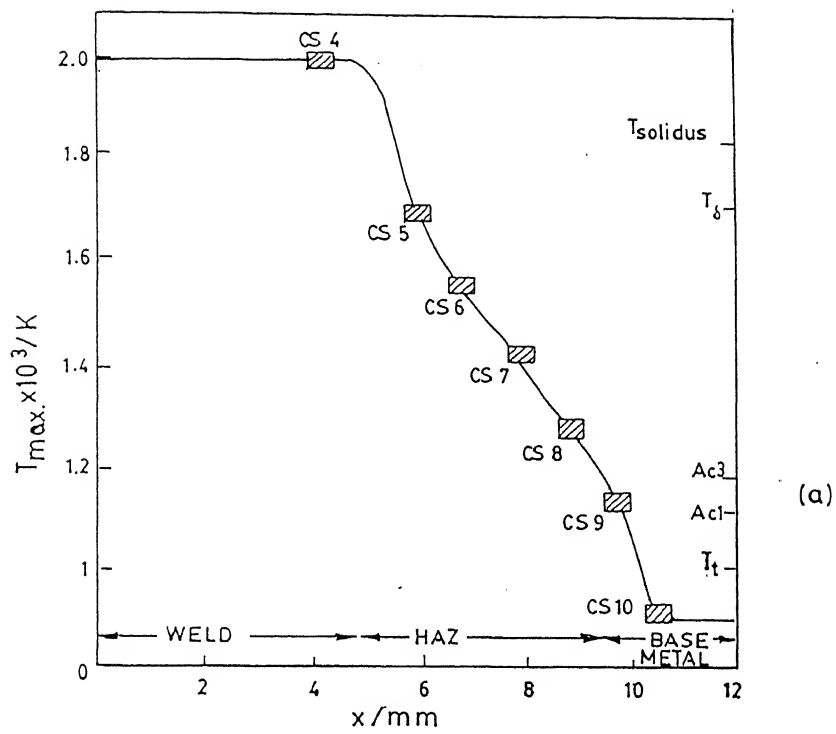


Figure 3.18 Deductions based on microstructural variations of different cross-sections, CS-1 to CS-10, constituting primary solidification structure.

(a) Variation of maximum temperature, T_{\max} , achieved as a function of distance, 'x', from the weld centre line. (b) Possible thermal cycles of different cross-sections. The numbers 1 to 5 are explained in the text.

the pre-existing carbides have taken place in addition to the formation of α . The regions beyond 5, do not get exposed to temperatures higher than tempering temperature T_t due to larger distance from the heat source. Hence, these regions do not undergo microstructural modification.

3.7.2 Microstructural Zones of Primary Solidification Structure

A schematic microstructural map has been proposed to depict all the experimental observations explained so far, in a comprehensive diagram. Figure 3.19 shows the schematic map, illustrating the various distinct microstructural zones of the primary solidification structure. The heat source, during welding is located at the centre of the weld pool. The liquid metal used to fill the V groove, solidifies into τ , corresponding to the weld zone at high temperature. During cooling to room temperature subsequently, the τ undergoes a solid state transformation forming the hard and brittle α' . This "weld zone" is surrounded by microstructurally distinct regions of HAZ. These regions represent part of the base metal, whose initial structure is modified due to unavoidable, transient thermal treatments they are subjected to, during welding.

The maximum temperature upto which any region gets heated reduces, as the distance from the source of heat increases. Beyond a distance, where the maximum temperature does not exceed the tempering temperature, the structure of the base metal remains more or less unaltered. The various reactions in these regions can be summarised as follows:

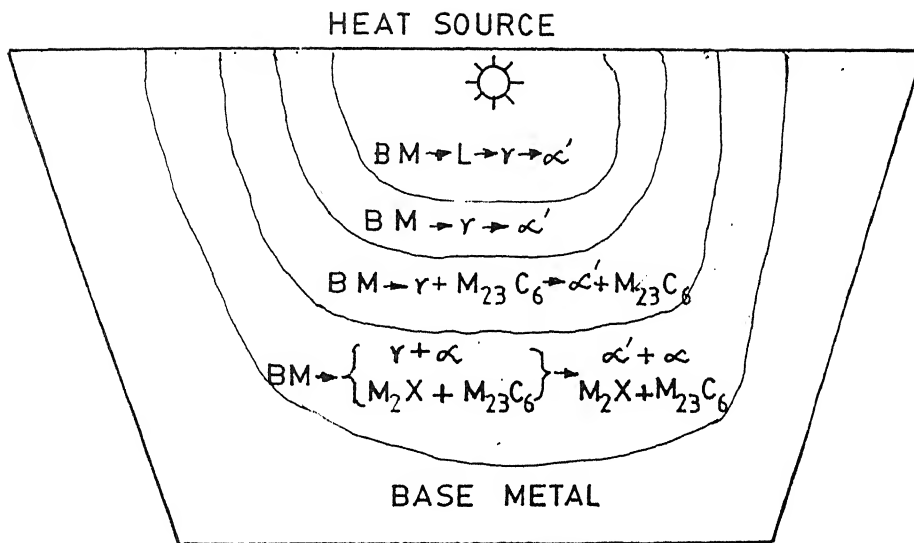
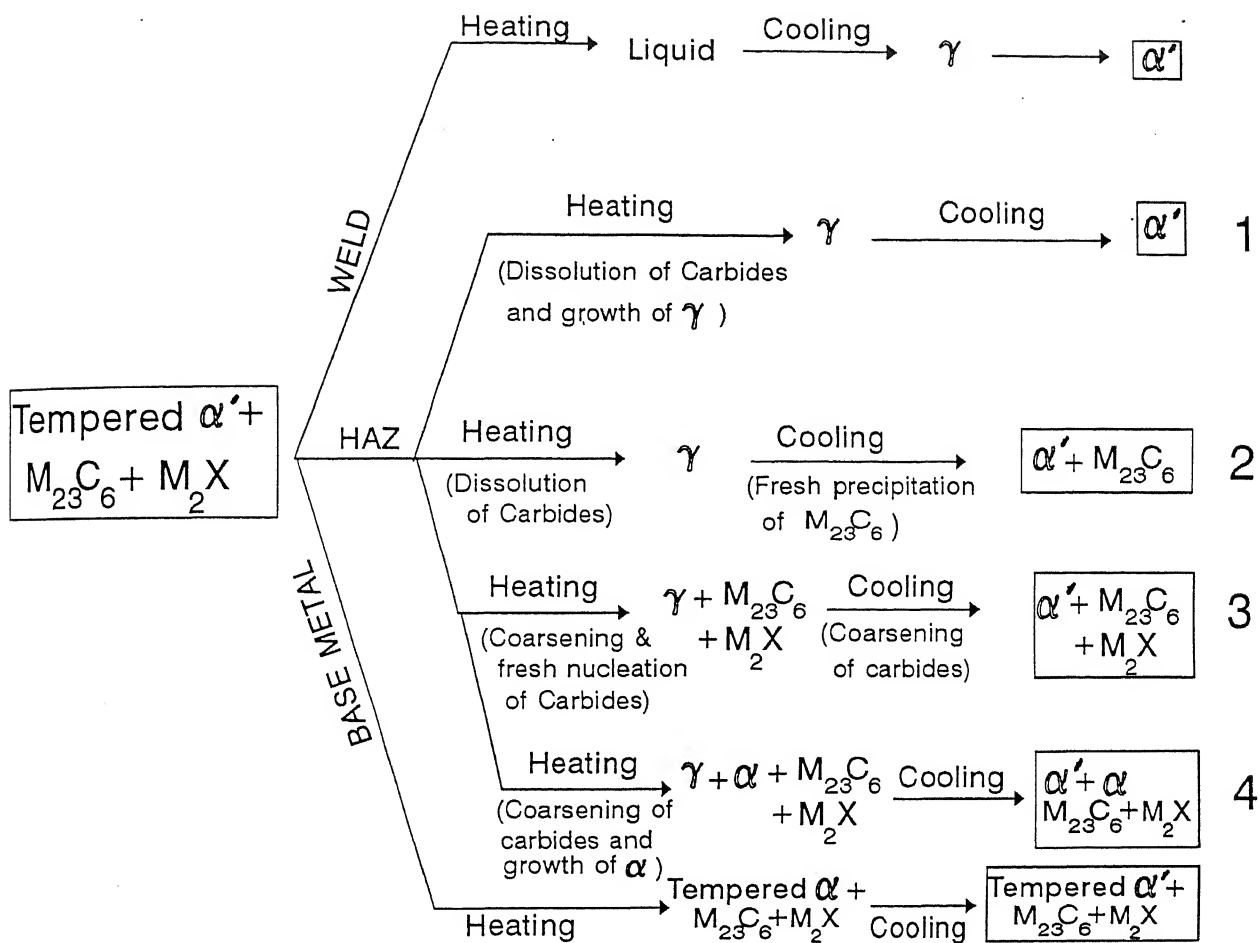


Figure 3. 19 Microstructural zones of primary solification structure.



The above sequence of events provides a complete and comprehensive understanding of the various microstructural results discussed so far.

3.8 SECONDARY SOLIDIFICATION STRUCTURE :

EFFECT OF MULTIPASS

A detailed understanding of the structure of a commercial multipass manual metal arc (MMA) weld will not be complete with the description of the 'primary' microstructure, alone. The 'primary' structure is, in fact, far from the true structure, for multipass welds. In practice, the original, 'primary' structure is reheated to high temperatures, during multipass runs. These temperatures, may, sometimes be large enough to initiate reversion of α' into τ , either partially or completely. This would retransform to entirely new structure, very much different from the primary structure, when cooled again. Therefore, the structure of the weld subjected to multiple passes called 'reheated' or 'secondary' structure is quite different from the original 'primary' or 'as-deposited' weld structure.

The structure developed is very sensitive to the variation in the welding process parameters and the physical metallurgical behaviour of the steel. Though the microstructural evaluation for a given weld is possible, its generalisation is valid only under the assumption that the welding parameters like weld bead spacing and overlap between weld beads are maintained reasonably constant. Some of the details of the welding conditions like the weld bead spacing, overlaps between beads, etc. cannot be generally predicted or controlled, in an industrial practice. However, the physical metallurgy behaviour can be fairly accurately evaluated. The differences in the microstructure and properties of the weldments depend critically on the factors like bead spacing and overlap between beads.

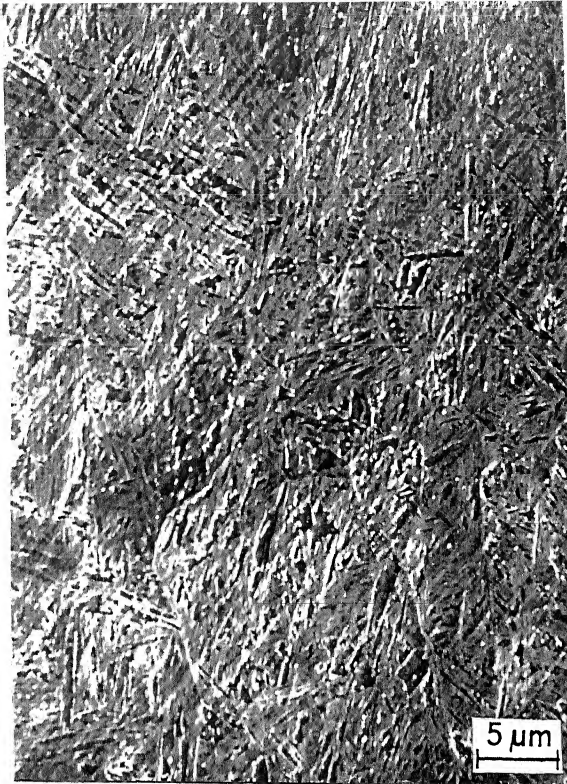
The weld beads during multipass MMA welding are deposited both side-by-side and one above the other. The microstructural evolution would depend on the thermal cycles experienced by the sections of the weld due to both the types of deposits. Therefore,

detailed microscopy needs to be carried out at various regions from the root to the top, along the weld centre line, and also at various parallel planes at varying distances from the weld centre line. However, all the observations were confined to the weld zone alone, in this part of the study. The schematic diagram showing the section chosen is given in figure 3.4 (b and c).

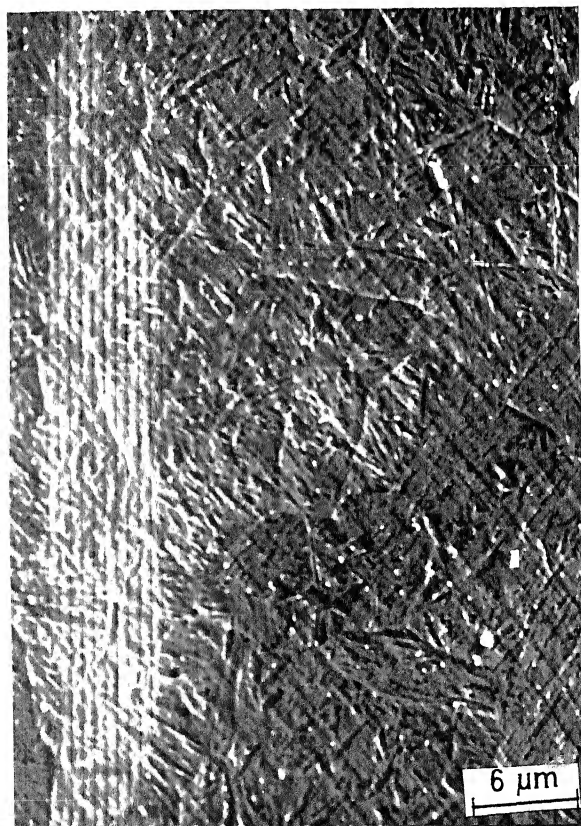
A careful observation of microstructures at various regions within the weld suggests that a distinct pattern of structure repeats periodically at various locations in the weld. Figure 3.20 (a to d) shows the typical sequence of such microstructures. These three regions clearly reveal structures which have columnar grains, coarse grains, fine grains and the unaffected structure. Figure 3.21 shows the locations (intersection of the cross-wire) within the weld, where these sequence of structures is repeated. A repetition of a characteristic pattern (figure 3.20) is observed, at periodic distances. Such repetitive structures are seen at locations which are one above the other and also at periodic distances from one side to the other side of the weld. The above observations of repetitive microstructures at periodic distances within the weld regions suggest that these could be due to modification of the primary structure during subsequent passes. The extent of microstructural modification depends on the temperature of the liquid, welding speed and the distance of the region from the heat source. The columnar grains in figure 3.20a represent the regions which have been heated above the solidus and cooled rapidly. Coarse grains represent regions which have been reaustenitised at high temperature of the τ phase field of the steel and cooled rapidly. In this region, complete dissolution of carbides is expected. The fine grain region, probably has not attained very high temperatures. Hence, the undissolved carbides impart a strong pinning force on the mobile grain boundaries of τ , preventing coarsening of the grains. The region adjacent to this zone, has not undergone any microstructural modification during subsequent passes. This is due to the larger distance from the heat source.



(a)



(b)



(c)



(d)

Figure 3.20 Effect of subsequent passes on the primary solidification structure.

Repetition of microstructure within the weld region. (a) Columnar, (b) coarse grains of γ , (c) fine grains of γ and (d) the unaffected region.

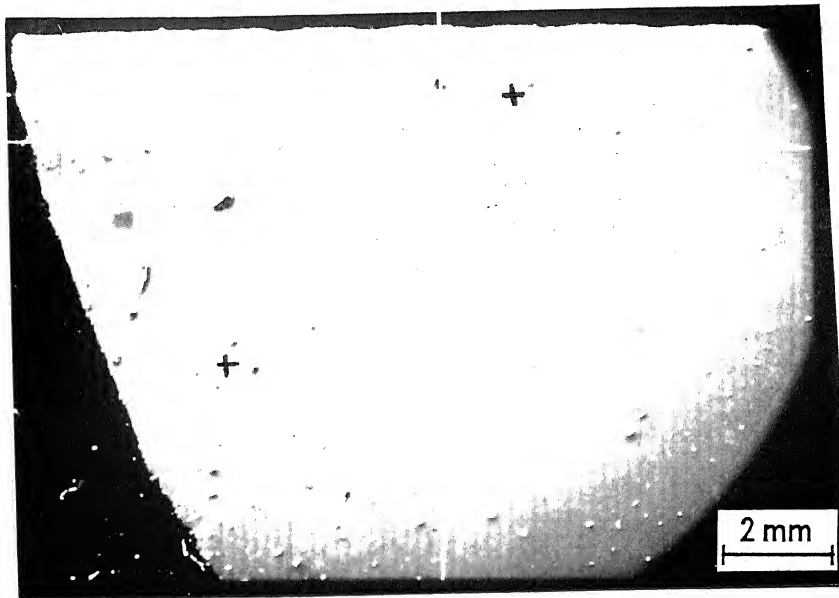


Figure 3.21 Locations (+) wherein the structures in Figure 3.20 repeats (intersection of the different cross-wires).

The above observations in multipass welds, can be understood in the light of a model proposed by H.K.D.H. Bhadeshia for multipass manual metal arc welds (21). It has been shown that the microstructure of multipass welds depends upon the degree of overlap between the adjacent weld beads. The condition for complete reaustenitisation of the underlying bead has been understood in terms of the relative differences between reinforcement height R_1 and reaustenitisation distance, R_2 . Figure 3.22a shows the definition of these two terms in single bead weld. The reinforcement height is the average distance to which the height of the work piece is increased and the reaustenitisation distance is the width of the base metal which is exposed to temperatures between A_{c3} and the solidus temperatures. In a multipass weld (figure 3.22 b and c), wherein weld beads are placed either one above the other or side by side, complete reaustenitisation occurs when $R_2 > R_1$ (21). Depending upon the degree of overlap of the subsequent passes, any region of the weld undergoes a number of thermal cycles and the final structure is influenced by all these temperature cycles. A schematic representation of the above features is shown in figure 3.23a. This explains the effect of subsequent passes on the microstructure of the underlying region, during multipass welding. Each pass influences only a small region (shown in figure 3.23a) of the previous pass, below which remains the unaffected structure. Within this "disturbed" layer, three types of structures are repeatedly observed, as schematically illustrated in figure 3.23b. Experimental evidence for the same has been provided earlier.

3.9 HETEROGENEITY IN MICROSTRUCTURE, MICROCHEMISTRY AND LATTICE STRAIN ALONG WELD CENTRELINE

In addition to the changes in the macroscopic features, the precipitation of carbides also is expected to be influenced by multiple passes. Therefore, carbon extraction replica of

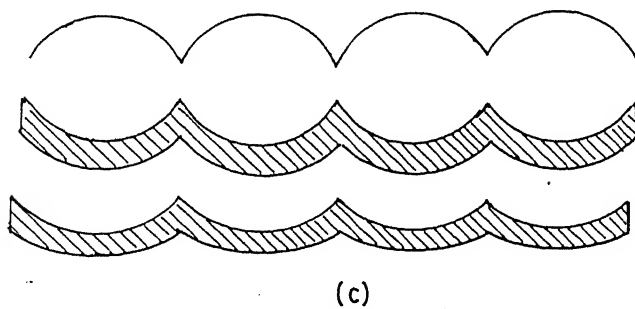
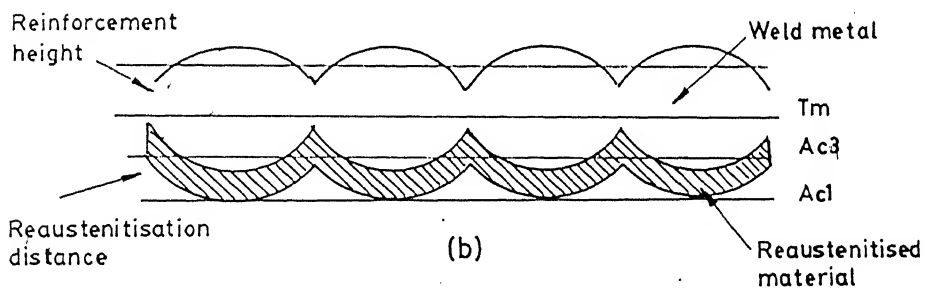
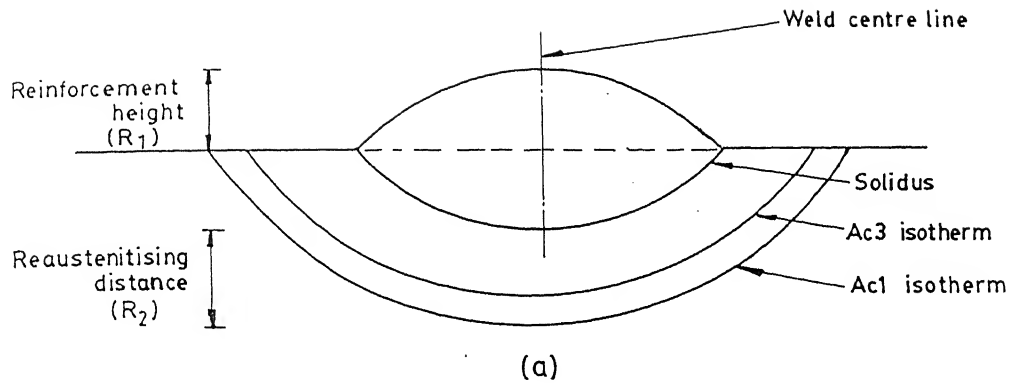


Figure 3.22 Schematic representation of reinforcement height (R_1) and reaustenitising distance (R_2).

(a) Definition of R_1 and R_2 in a single bead weld. Explanation of same terms in a multipass weld, when there are layers, (b) side by side and (c) one above another.

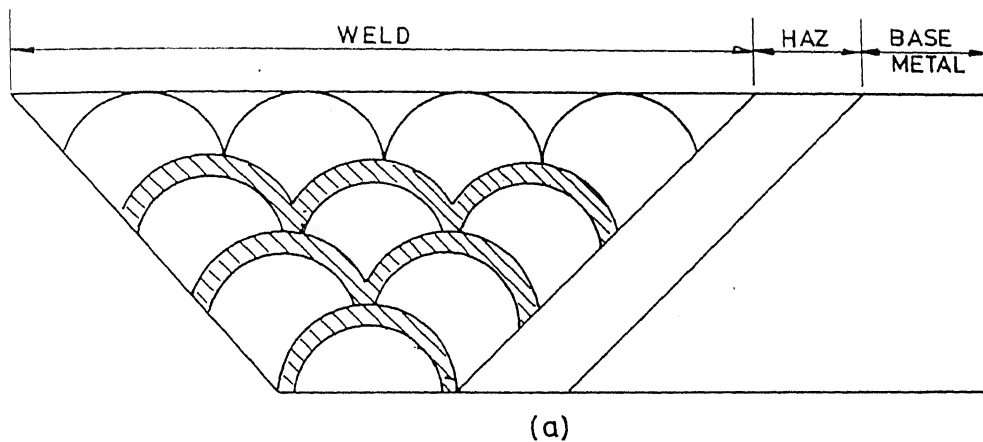


Figure 3.23 Schematic representation of the (a) multipass profiles and (b) repetitive structures. The shaded portion in each of the multipass profile in (a) represents the region over which the structure is modified due to subsequent passes.

the regions along the weld centre line, at intervals of 1mm distance from the top surface till the root, were observed. Figure 3.24 (a, c and e) shows the typical microstructures of the top (about 2 mm from the top), middle (about 5 mm from the top) and the root (about 8 mm from the top) of the weld region, along the weld center line. While the top surface shows the presence of few carbides as shown in figure 3.24a, there is a gradual increase in the number density of carbides, as the root portion is approached (figure 3.24 c and e). The analytical electron microscopy analysis of these carbides, shows that the carbides at the top surface are rich in iron (figure 3.24b), while those near the root are chromium rich $M_{23}C_6$ carbides (figure 3.24(d and f)), whose composition is given in Table III.4.

The extensive precipitation of carbides at the root, with a gradual reduction towards the top, suggests that the degree of strain would be different in these regions. Therefore, an attempt has been made to measure the lattice strain using full width at half maximum (FWHM) of X-ray diffraction peaks. A strain parameter, s , is calculated using the following equation:

$$\frac{FWHM - (FWHM)_{BM}}{(FWHM)_{BM}} \times 100 \quad (3.10)$$

wherein FWHM refer to the value of FWHM of the region of interest, say, top, middle and root and $(FWHM)_{BM}$ refers to that of base metal. Table III.5 shows the values of 's' calculated using FWHM of X-ray diffraction peaks, in addition to the hardness and microstructural parameters like lath size. There is a decrease in the value of FWHM, as the distance of the region from the top is increased, consistent with the decrease in hardness. The changes in these parameters correlate well with the increase in lath size (figure 3.25) and the number density of carbides, observed in the corresponding

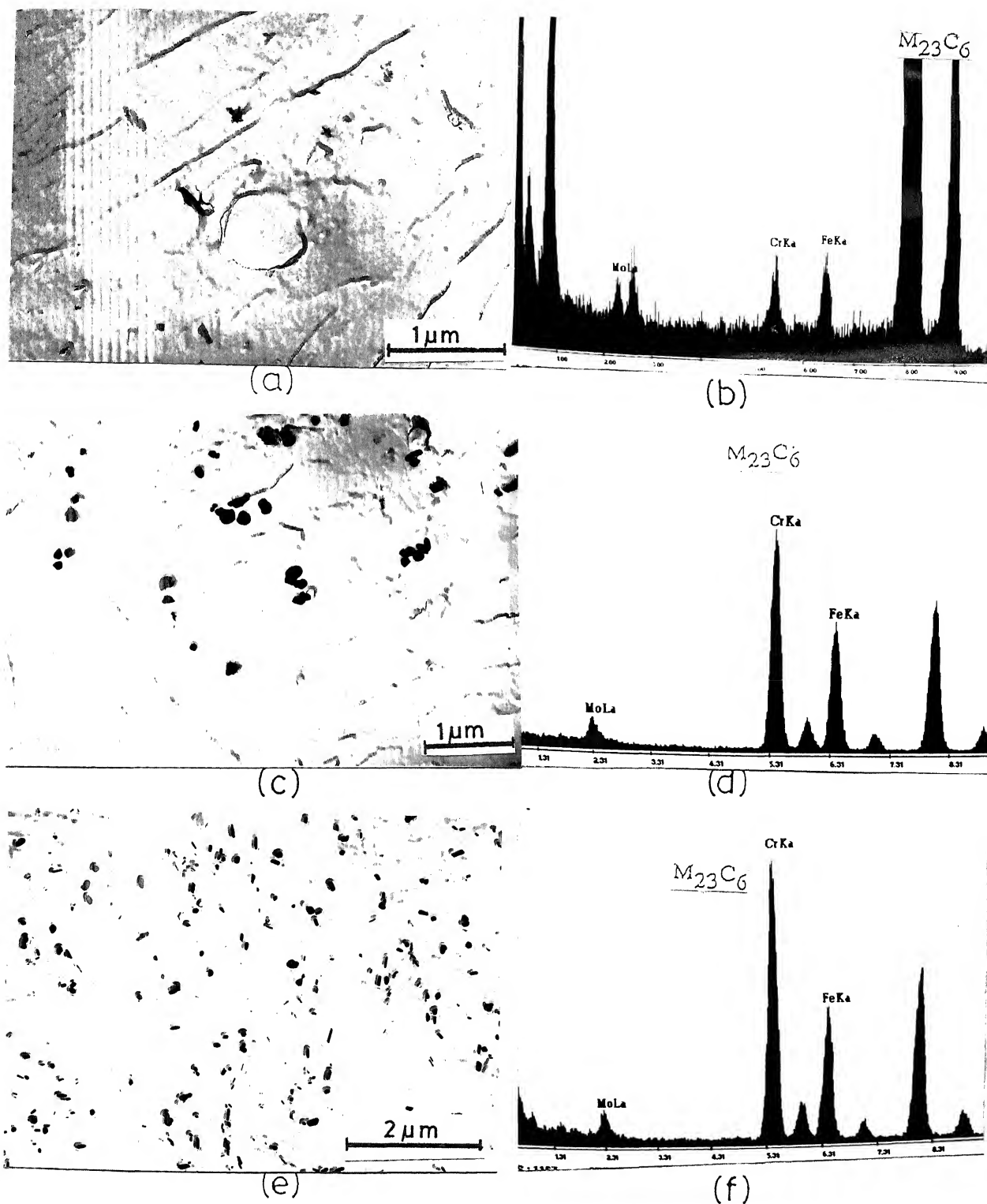


Figure 3.24 Microstructural inhomogeneity from the top to the root portion of the weld region, along the weld centre line. (a) Micrograph of carbon extraction replica, from top region. (b) EDAX spectrum from one of the carbides. Similar information for (c) and (d) the middle portion and (e) and (f) the root of the weld. Absence of precipitation in the top portion (a) is in contrast to extensive precipitation in the root (e) - an effect of tempering during multiple passes. Enrichment of chromium in the carbides at the root is seen.

Table III.4

Microchemistry of carbides along the weld center line from the top to the root.

Sl.no.	Region	% element in metal sublattice		
		Fe	Cr	Mo
1	Top (2mm from top)	53	20	27
2	Middle (5mm from top)	21	47	32
3	Root (8mm from top)	36	57	7

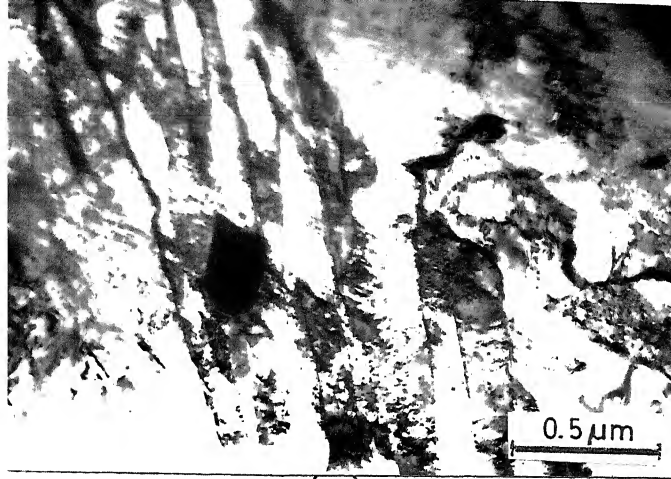
Table III.5

Lattice strain measurements and the relevant microstructural parameters
of carbides along weld centre line

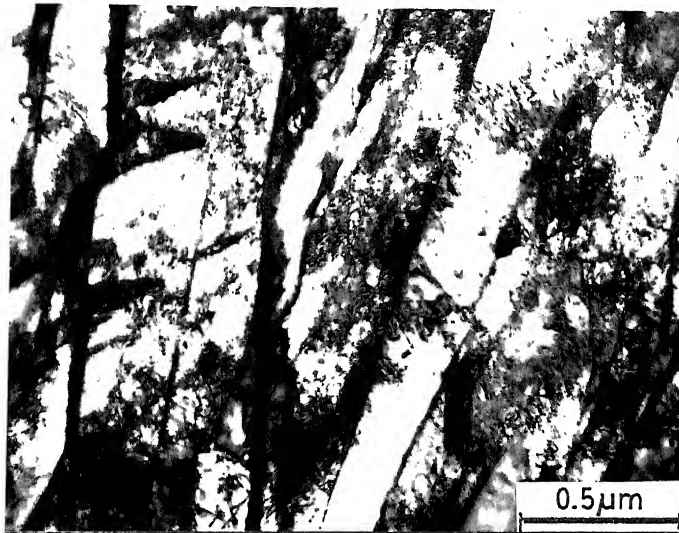
Sl.No.	Region	s^* (%)	Micro- Hardness VHN (Load = 100g)	Lath Size μm $\pm 10\%$
1	Top	33	438	0.11
2	Middle	33	444	0.24
3	Root	25	384	0.36

* The strain parameter, $s = \frac{(\text{FWHM}) - (\text{FWHM})_{\text{BM}}}{(\text{FWHM})_{\text{BM}}} \times 100$

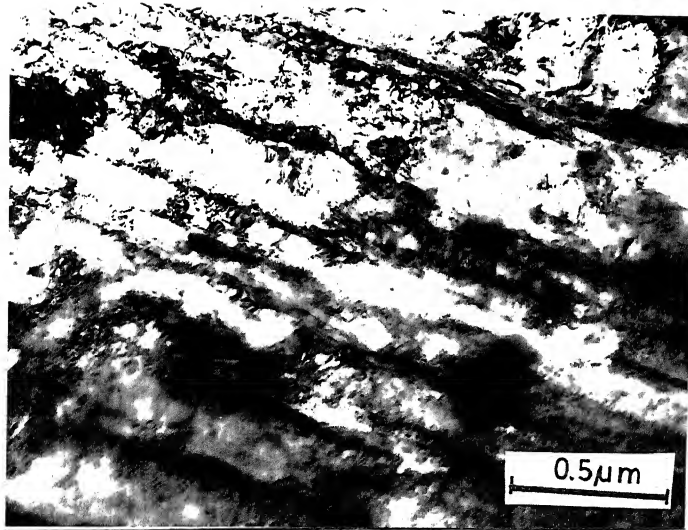
wherein FWHM is the full width at half maximum of the X-ray diffraction peaks taken from the region of interest, say, top, middle and root and $(\text{FWHM})_{\text{BM}}$ is the same parameter of the base metal.



(a)



(b)



(c)

Figure 3.25 Coarsening of laths from top to root of the weld. (a) top, (b) middle and (c) root.

regions. It is seen that the root portion has experienced the maximum degree of tempering.

3.10 COMPREHENSIVE 3-DIMENSIONAL REPRESENTATION OF MICROSTRUCTURE OF 9Cr-1Mo WELDMENTS

The observations discussed above have been summarised in a comprehensive three-dimensional representation of the hardness fields, microstructural fields and finally, the phase field diagram. Figure 3.26 (a to c), shows the three diagrams, comprising of the various hardness, microstructural and phase fields. The salient features of the hardness variations, microstructural map and the phase field diagram are as follows:

- * Maximum hardness zone of the weldment correlates well with the regions characterised by the formation of α' .
- * The second lower range of hardness at the root of the weld corresponds to tempering by precipitation of carbides and coarsening of laths.
- * The hardness profiles of HAZ compare well with general tempered α' structure.
- * Microstructurally distinct zones of HAZ do not significantly alter the microhardness profiles, except for softening in two distinct regions.
- * Softening in two regions, i.e., near the interfaces of HAZ with weld and base metal, correlates well with re-austenitisation and exposure to the inter-critical ($\tau + \alpha$) region.

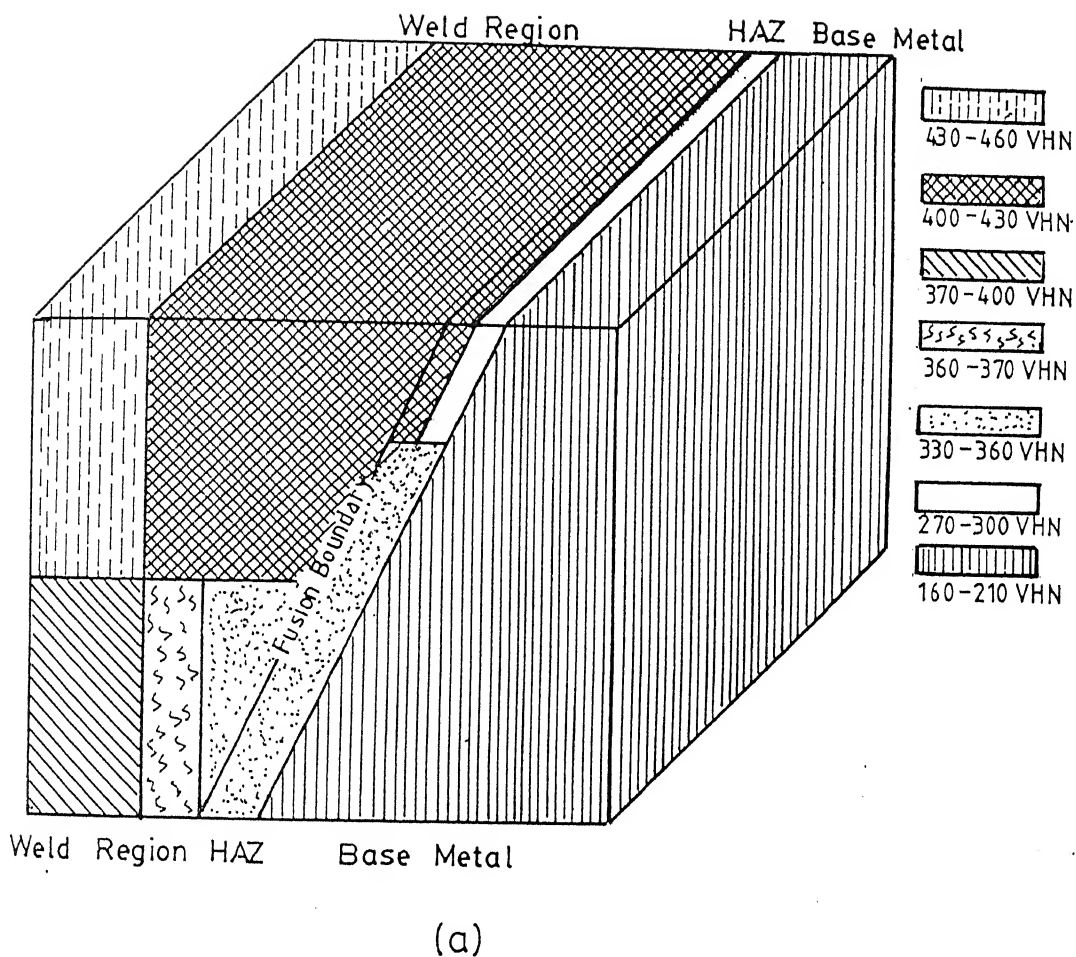


Figure 3.26 A comprehensive three-dimensional representation of (a) hardness variations, (b) microstructural changes and (c) phase fields of the weldments of 9Cr-1Mo steel. The regions marked 1 to 4 in HAZ correspond to HAZ 1, HAZ 2, HAZ 3 and HAZ 4, explained in equation 3.9.

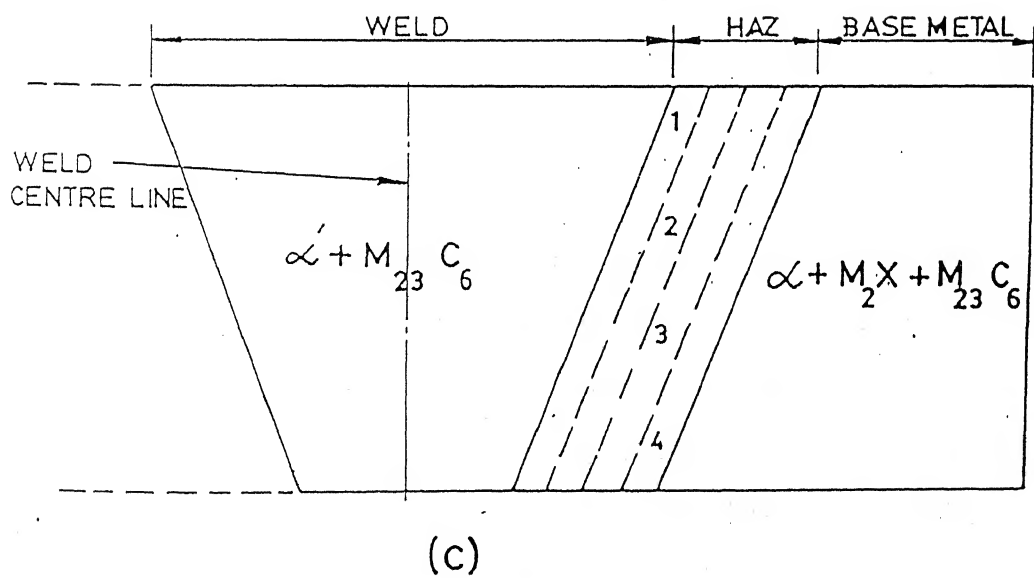
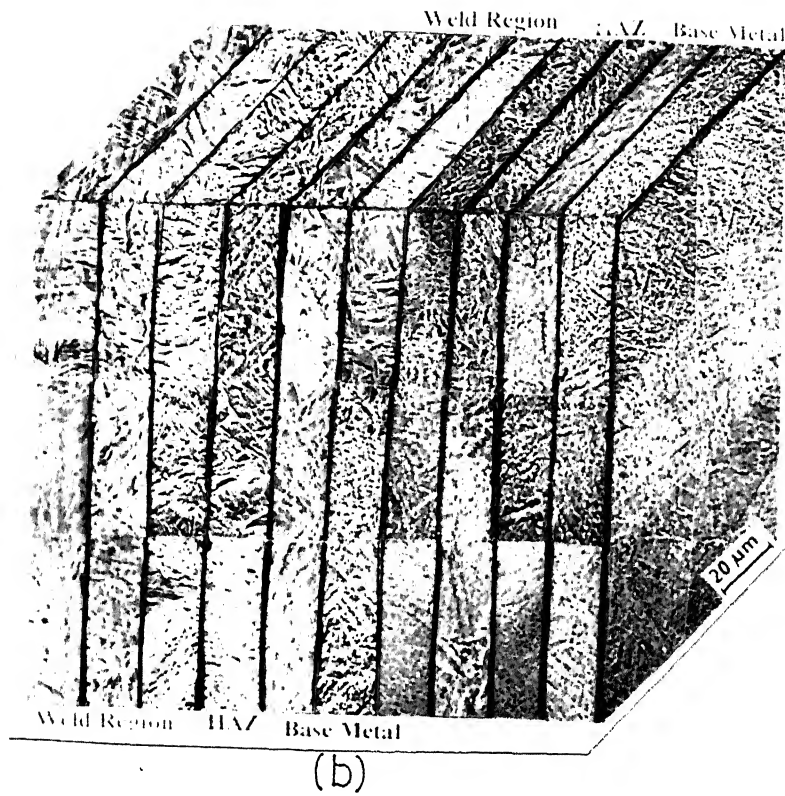


Figure 3.26 Continued....

3.11 LATTICE STRAIN ACROSS WELDMENTS

In addition to the microstructural and microchemical heterogeneities in various zones of the weldment, the amount of uniform lattice strain locked up in small regions of the weldment varies with distance from the weld centre. The amount of strain resulting in a measurable change in lattice parameter is very sensitive to the thermal cycle. The present section discusses the results on the variation of such lattice strain in four regions: the weld, the HAZ near weld (HAZ1), HAZ near base metal (HAZ2) and the base metal. These regions were chosen as per the experimental scheme explained in figure 3.4d.

3.11.1 Application of CBED for Measurement of Lattice Strain

The present section attempts to find out the suitability of CBED to determine lattice strain in small regions of diameter far less than $0.1\ \mu\text{m}$. The lattice strain measurements using CBED are carried out by making use of features called the high order Laue zone (HOLZ) lines present in the CBED patterns (Figure 3.27) of α -ferrite. These lines always appear in pairs and are called the 'deficiency lines' (figure 3.27b) and the 'excess lines' (figure 3.27c). The 'deficiency lines' are seen in the (000) disc of CBED patterns and the corresponding 'excess' lines are seen in the discs of first order Laue zone (FOLZ). The origin of HOLZ lines, procedure for imaging the HOLZ lines and the precautions taken while imaging, the indexing of these lines and the factors which govern the position of HOLZ lines are discussed in many books and review papers (22-24). The most important feature of relevance to the present discussion is that the angular position of these lines is sensitive to the

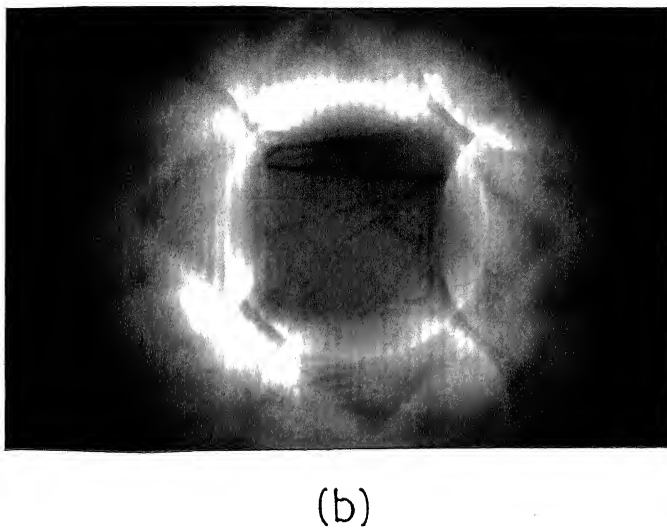
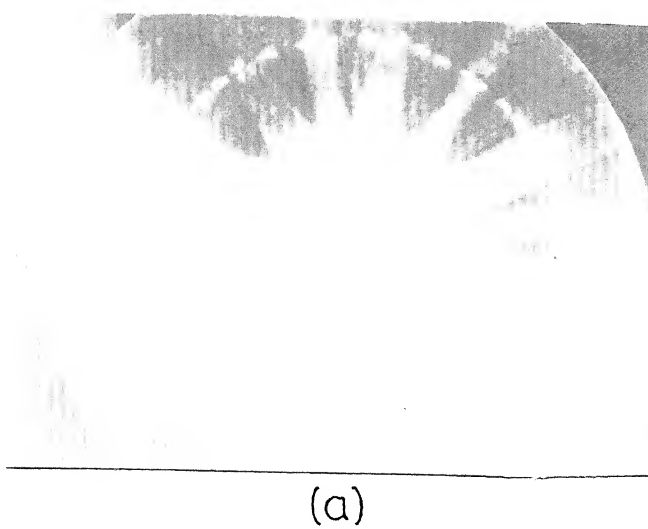


Figure 3.27 A typical convergent beam electron diffraction (CBED) pattern of α -ferrite of base metal of 9Cr-1Mo weldment. (a) Whole pattern symmetry along $\langle 200 \rangle$, (b) high order Laue zone (HOLZ) deficiency lines within (000) disc of (a) and (c) HOLZ excess lines in the discs of FOLZ ring of (a).

accelerating voltage and the lattice parameter. Hence, if the accelerating voltage of the incident electrons is maintained constant, the changes in the angular position of these HOLZ lines can be directly correlated to the variations in the lattice parameter.

The estimation of changes in the lattice parameter is as follows: a unique, distinctly identifiable point is chosen within the (000) disc, which contains a number of HOLZ lines. The angle Θ corresponding to this chosen point of interest A is given by

$$\Theta_A = r_A/CL \quad (3.11)$$

where r_A is the distance of the point A from the centre of (000) and CL is the camera length in mm. The same parameter is measured in CBED patterns of same zone axis corresponding to the three different regions, HAZ1, HAZ2 and base metal. The CBED patterns from the weld region were found to be distorted and clear, resolvable HOLZ lines could not be obtained. Hence, CBED studies were confined to only three regions. It is known that

$$\frac{\Delta a}{a} = \frac{\Delta \Theta}{\Theta} \quad (3.12)$$

Since 'a' of the base metal is known, Δa can be calculated directly. This method is ideally suitable for the determination of lattice strain around coherent precipitates or other defects. However, in the present study, regions which are much coarser than the size of the incident probe are chosen, i.e., HAZ1 and HAZ2. This is mainly due to the possibility of confirming the results of CBED with conventional X-ray diffraction results.

The present section deals with the experimental determination of lattice strain across different zones of the weldments of 9Cr-1Mo steel. These results are compared with the results of X-ray diffraction obtained from the same regions of the weldment.

3.11.2 Estimation of Lattice Strain for 9Cr-1Mo Weldments Using HOLZ

Lines in CBED Patterns

The weldment of 9Cr-1Mo steel was divided into the following four regions : the weld region, the heat affected zone (HAZ1) near the weld region, the heat affected zone near the base metal (HAZ2) and the base metal - schematically shown in figure 3.28. The parent phase i.e., the bcc α -ferrite has been chosen for the measurement of lattice strain.

Figure 3.29 (a to f) shows the general CBED patterns taken along three major zone axes of α -ferrite, of the base metal of the weldment. The patterns show the whole pattern symmetry, the interference pattern within zero order Laue zone (ZOLZ) and the HOLZ rings. The whole pattern symmetry of the zone axis is very clear in these figures. For example, a four fold axis along $\langle 200 \rangle$, a six fold axis along $\langle 111 \rangle$ and a two-fold axis along $\langle 113 \rangle$ are seen quite clearly. The concentric, geometric figures in the (000) disc also reflect the same symmetry. These are the interference patterns within the (000) discs, suggesting the presence of strong string potentials, along these directions. Their use in the identification of point defects is discussed in detail in chapter 5. The number of HOLZ rings in figure 3.29 (a,c and e) is restricted to one or two due to the small unit cell dimension of the crystal. However, if the individual discs constituting the FOLZ ring could be imaged, it is possible to see HOLZ excess lines (figure 3.27), corresponding to deficiency lines in the (000) disc of the same CBED pattern. Figure 3.30 (a and b) shows the HOLZ lines in the (000) disc

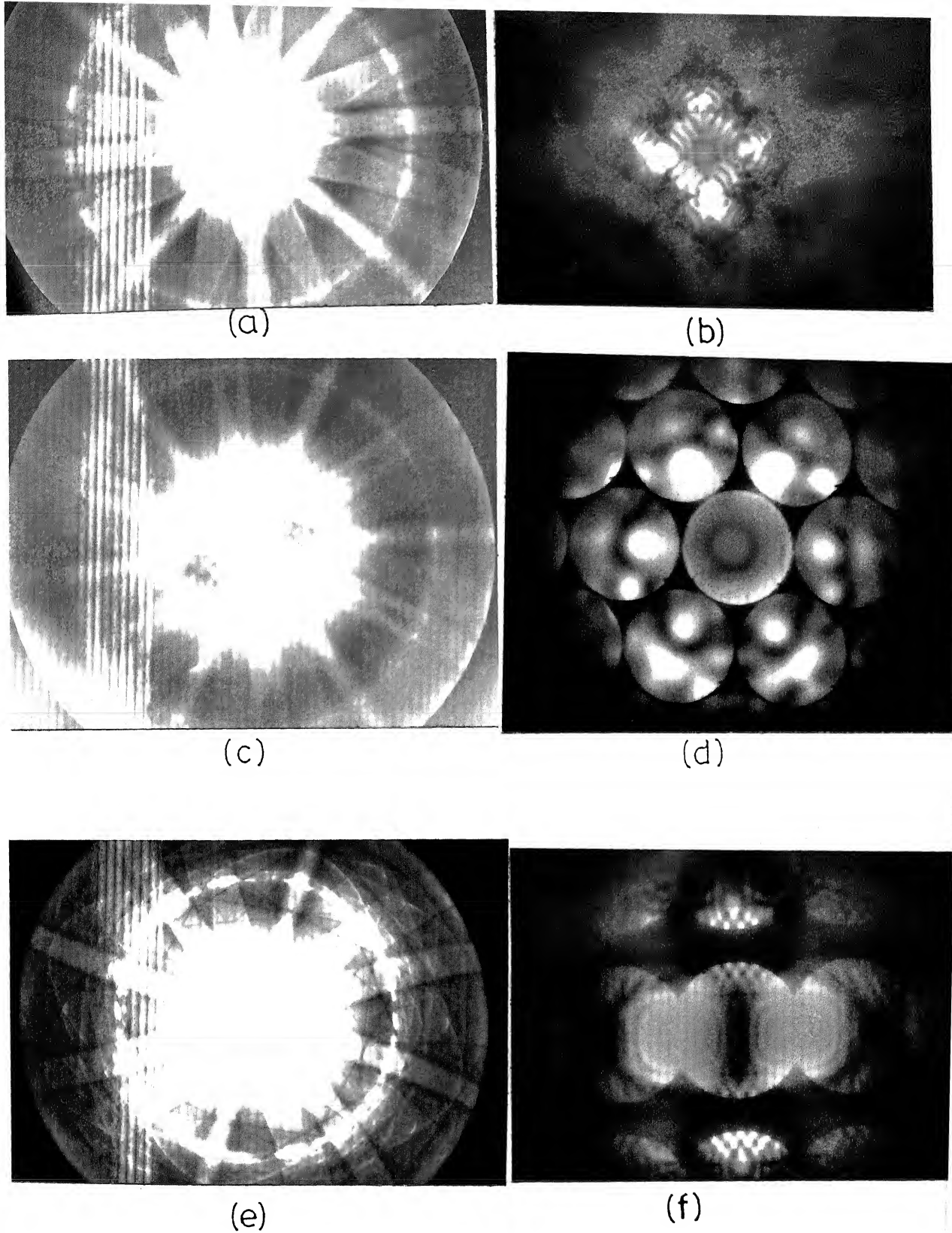
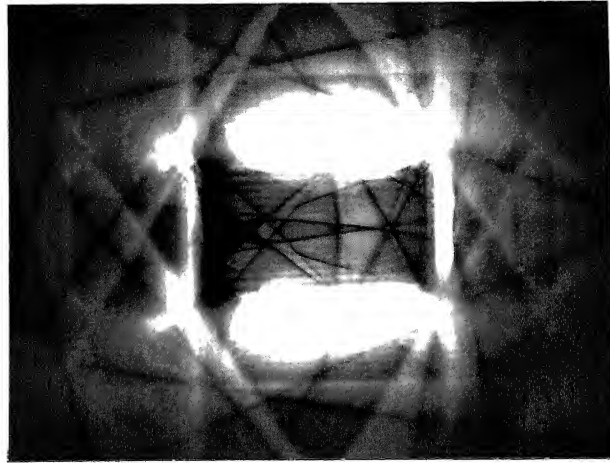
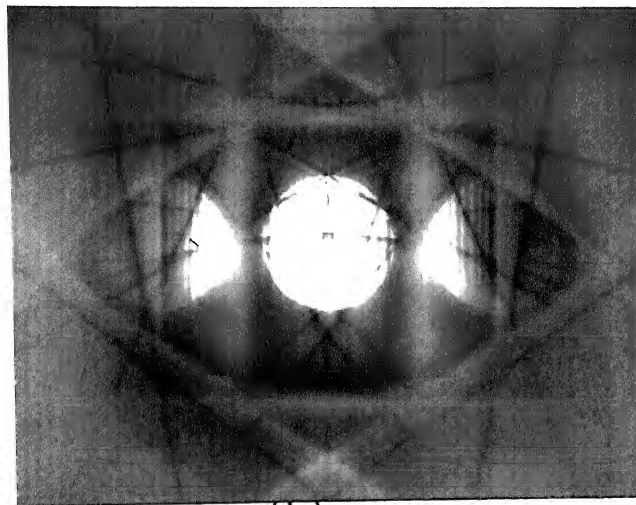


Figure 3.29 Typical CBED patterns of α -ferrite of base metal along three different zone axes. (a) and (b) $\langle 200 \rangle$, (c) and (d) $\langle 111 \rangle$ and (e) and (f) $\langle 113 \rangle$. Whole pattern symmetry is shown in (a), (c) and (e) along different zone axes. (b), (d) and (f) show the zone axis pattern (ZAP) symmetry.



(a)



(b)

Figure 3.30 HOLZ deficiency lines in the (000) - central disc of CBED patterns of α -ferrite along (a) $\langle 200 \rangle$ and (b) $\langle 113 \rangle$.

of two typical zone axes of bcc α -ferrite in the base metal of 9Cr-1Mo weldment. Of these, since the HOLZ lines in the CBED patterns of $\langle 113 \rangle$ are excited strongly and are quite sharp, the HOLZ lines of $\langle 113 \rangle$ are chosen for the evaluation of lattice strain. The indexing of these lines is carried out with the aid of computed patterns. The input parameters for the computation of the pattern is shown in Table III.6. The computed HOLZ lines for bcc α -ferrite with lattice parameter of 0.29 nm, along $\langle 113 \rangle$ with the convergence angle of 6.3 mrad are seen in figure 3.31. The convergence angle - α_c value is deliberately maintained low in order to make the pattern recognition easier, without crowding the disc with HOLZ lines which are not excited experimentally.

This particular value of α_c was arrived at by trial and error and comparison of the pattern with experimental patterns. The indexing is shown in figure 3.32. The HOLZ lines in the experimental pattern are indexed based on the comparison with the computed pattern. The variation in the lattice parameter is determined based on the shift in the angular position of the HOLZ lines. The measurement of lattice strain using shift in the HOLZ lines does not depend on the indices of the HOLZ lines, if the chosen point remains the same.

Figure 3.33 (a to c) shows the same HOLZ lines in the CBED patterns of α -ferrite along $\langle 113 \rangle$ for the three regions of the weldment, taken at the same accelerating voltage of 100 kV. The angle of convergence is maintained the same as far as possible. The cameralelength is the same in all the three patterns, to facilitate the visual judgement of position of HOLZ lines. There are important observations as one attempts to compare the (000) disc of the three regions, base metal, HAZ1 and HAZ2. The angular spread (width) of each of the HOLZ lines is less, making them sharper as one

Table III.6

Input parameters for the computation of HOLZ lines.

Crystal	:	Fe.
Acceleration Voltage	:	100 kV.
Number of Laue Zones	:	2.
Convergence Angle	:	Step 2; 6.4 mrad
Zone Axis	:	<113>.

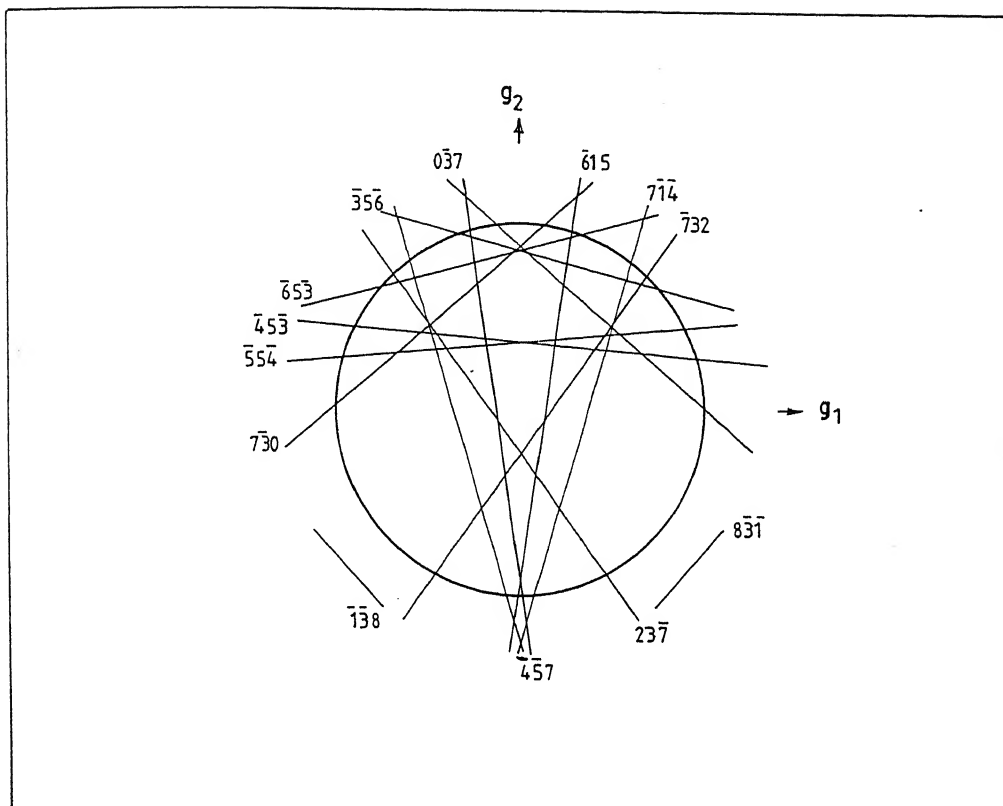
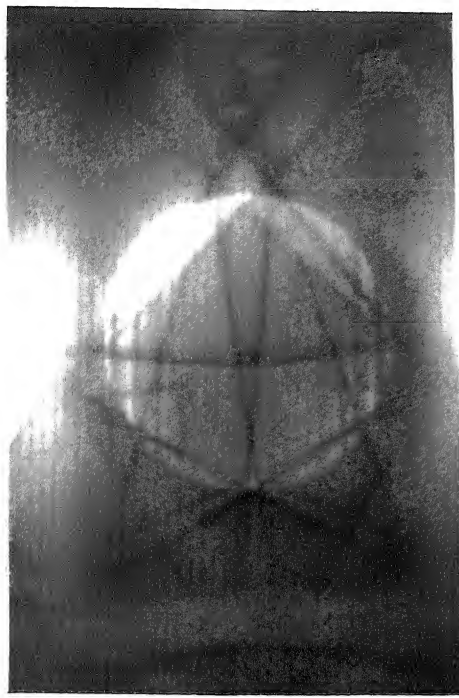
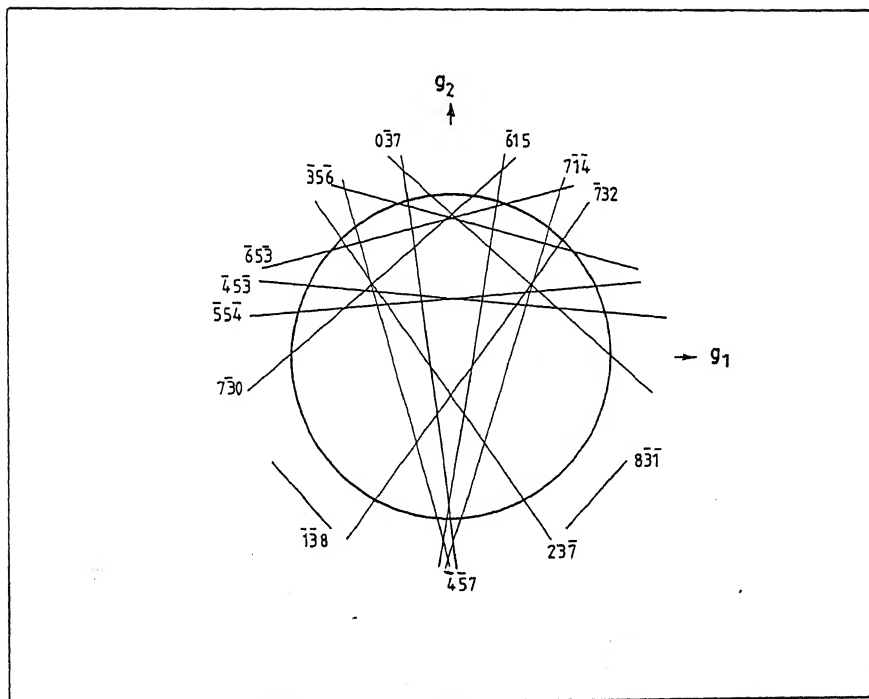


Figure 3.31 HOLZ deficiency lines along $\langle 113 \rangle$, computed using EMS software (input details in Table III.6).

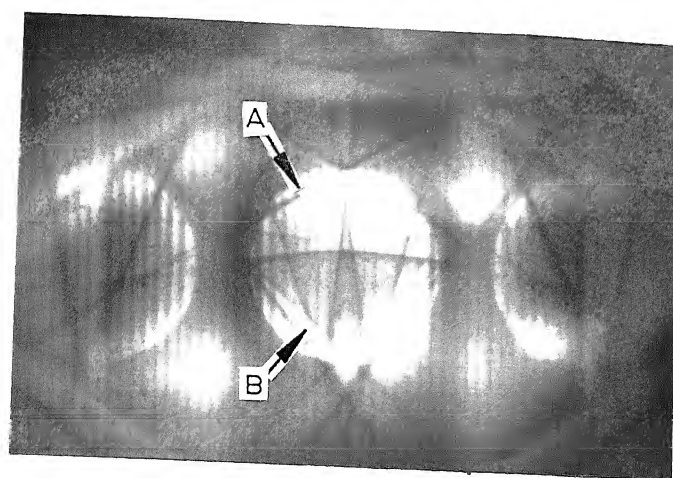


(a)

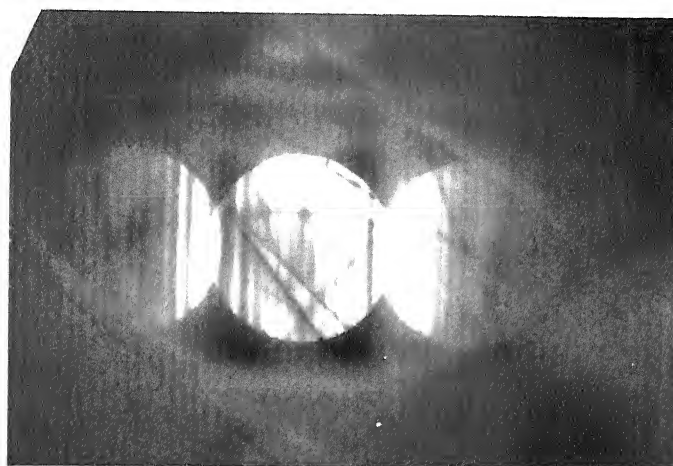


(b)

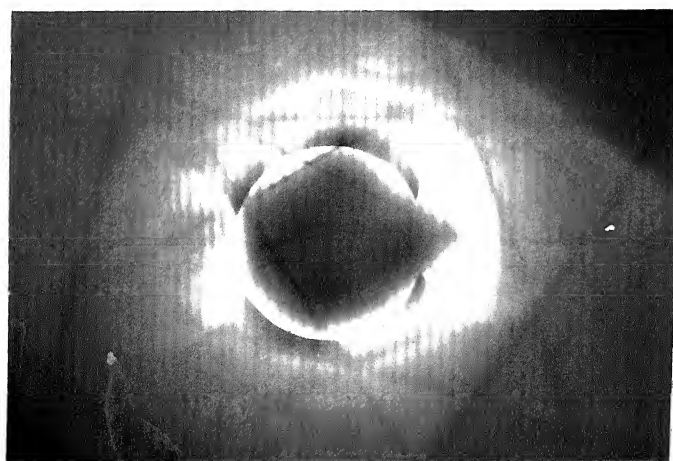
Figure 3.32 Indexing of HOLZ deficiency lines. (a) Experimental pattern along $\langle 113 \rangle$ - α -ferrite and (b) computed pattern along the same.



(a)



(b)



(c)

Figure 3.33 HOLZ deficiency lines in the (000) disc of CBED pattern of α -ferrite along $\langle 113 \rangle$ in the (a) base metal, (b) HAZ2 and (c) HAZ1. A and B are the points chosen for strain measurement.

proceeds towards base metal. Finally, the diffuse scattering background increases gradually as the weld region is approached making it difficult to image HOLZ lines. In view of the above difficulties, only those lines which can be uniquely identified in patterns of all the regions, HAZ1, HAZ2 and the base metal are chosen for measurement purposes. Such patterns correspond to those from CBED patterns of α -ferrite along $\langle 113 \rangle$ in the different regions of weldment. The chosen points are marked as A and B, in figure 3.33 (a to c). Table III.7 shows the values of Θ , $\Delta \Theta$ and strain $\left(\frac{\Delta a}{a} \times 100 \right)$ calculated using equation 3.12. The percentage of change in 'a', i.e., the uniform lattice strain, as a function of distance from fusion line is shown in figure 3.34. The observed increase in percentage change, as the weld region is approached is consistent with the expected larger increase in lattice strain closer to the weld. However, the absolute values of strain are quite high. Therefore, X-ray diffraction experiments from the same regions were performed.

The results obtained using CBED were compared with those of conventional X-ray diffraction method. Figure 3.35 (a to d) shows the X-ray diffraction peaks, from the four chosen regions, the weld, HAZ1, HAZ2 and the base metal. The values of 'a' were measured using the position of the three diffracted peaks. Table III.8 includes these values for comparison. It is seen that the change in 'a' is very low. However, there is a high degree of non-uniform strain leading to high value of FWHM. It is possible that the use of fine probe in CBED has provided the strain only from a very small region and hence, not an averaged value over larger area, like in X-ray diffraction. The high value of strain can be understood only in terms of high value of FWHM in X-ray diffraction peaks and the fine probe used in CBED experiments.

The results illustrated above, show that the CBED technique can provide relative changes in the lattice strain, though not absolute values.

Table III.7

Computed values of angular positions of HOLZ lines.

Sl. No	Region Chosen*	Chosen Points	Dist. 'r' from the centre mm	Camera length mm	θ (mrad)	$\Delta\theta$ (mrad)	Strain %
1	B.M.	A	3.5	290	12.07	0	0
2	HAZ2	A	5.0	290	17.24	0.429	0.4
3	HAZ1	A	4.5	210	21.43	0.776	0.75
4	B.M.	B	4.0	290	13.79	0	0
5	HAZ2	B	5.5	290	18.97	0.376	0.38
6	HAZ1	B	5.0	210	23.81	0.727	0.73

* Weld region has not been included, since it was not possible to get resolvable, clear HOLZ lines.

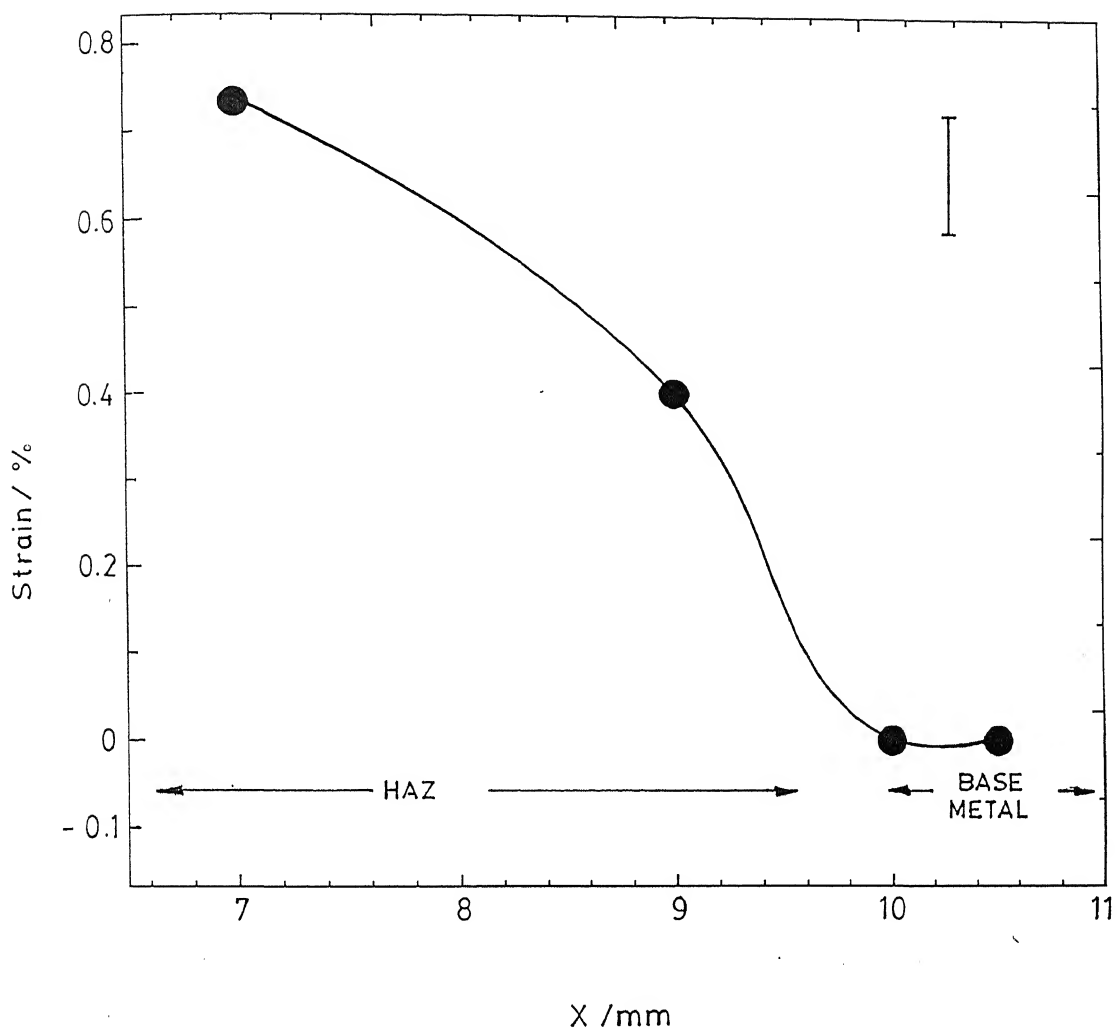


Figure 3.34 Variation of lattice strain as a function of distance from the weld centre line.

WELD

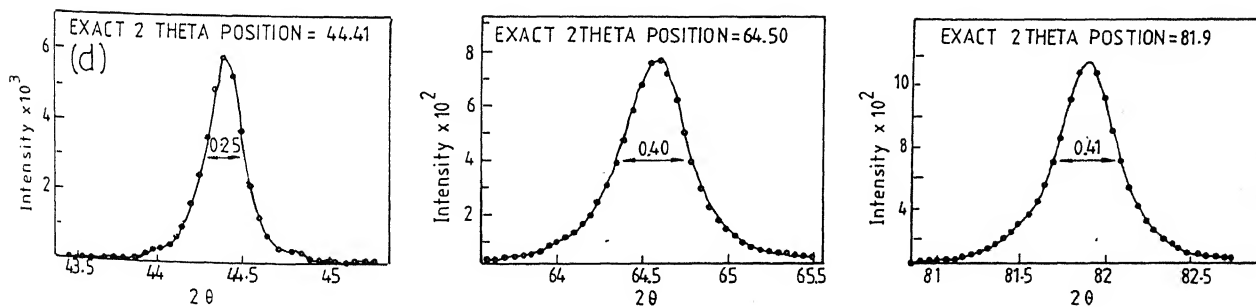
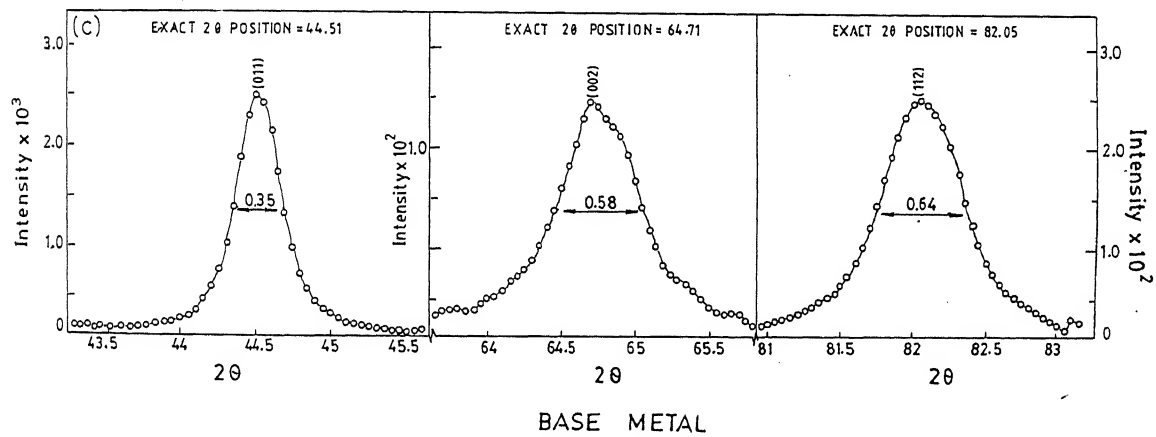
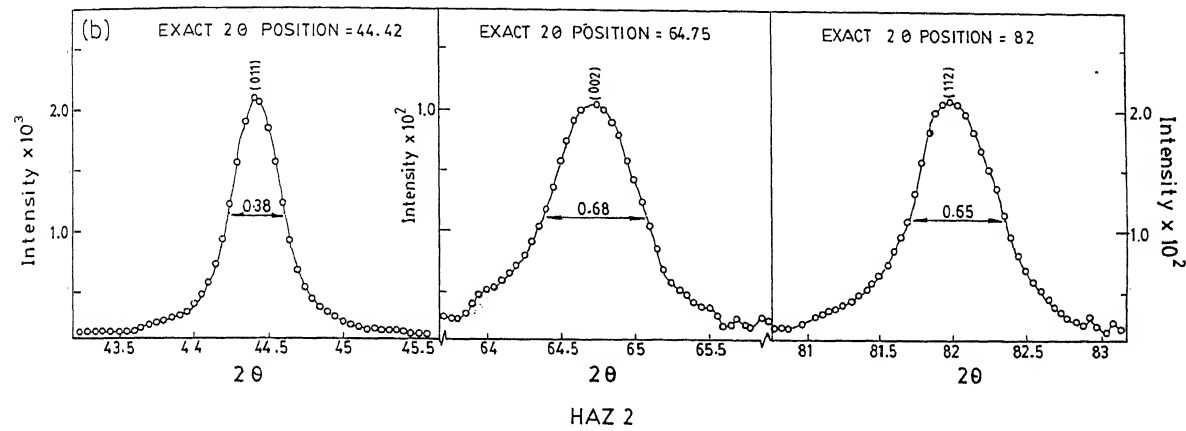
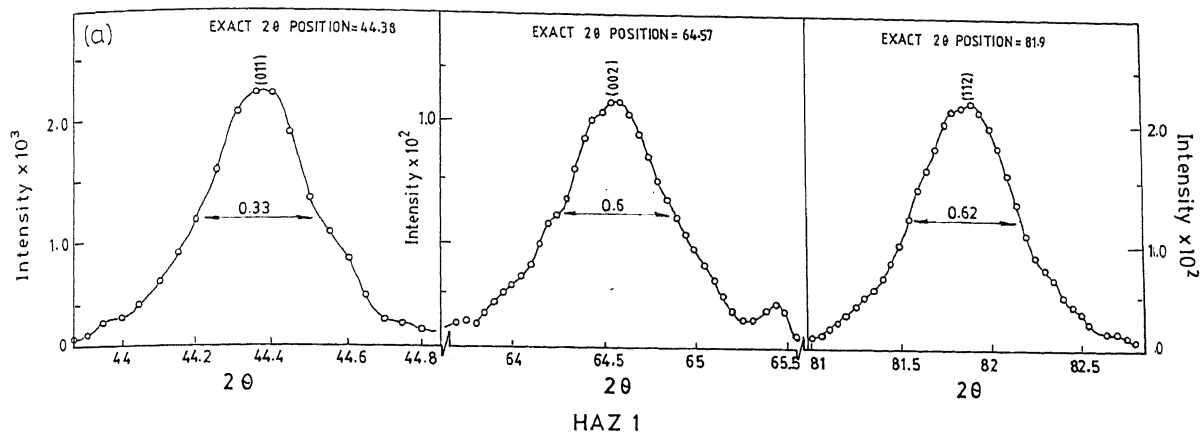


Figure 3.35 X-ray diffraction peaks of α -ferrite from the same three regions, as in Figure 3.33. 'a' is measured using three peaks for each region. The diffraction peaks of the three (hkl)'s for (a) weld, (b) HAZ1, (c) HAZ2 and (d) the base metal, are shown.

Table III.8

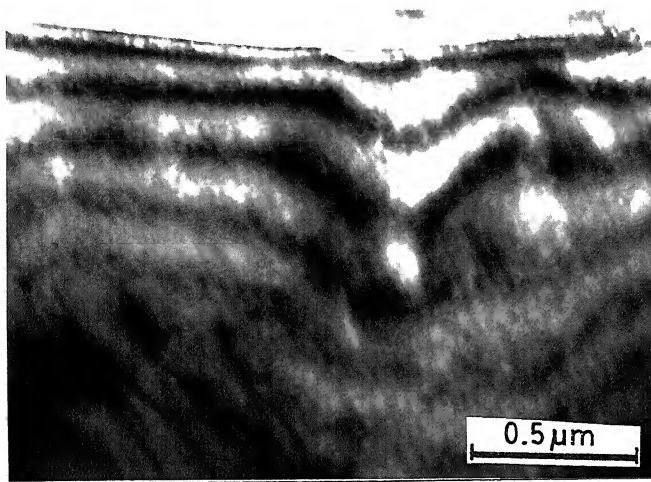
Measurement of lattice strain using X-ray
diffraction peaks

Sl.No.	Region	(hkl)	a Å	FWHM $\Delta\theta(^{\circ})$
1	B.M	(112)	2.888	.41
2	HAZ2	(112)	2.885	.64
3	HAZ1	(112)	2.888	.65
4	Weld	(112)	2.890	.7
5	B.M	(200)	2.892	.44
6	HAZ2	(200)	2.89	.58
7	HAZ1	(200)	2.88	.68
8	Weld	(200)	2.896	.6

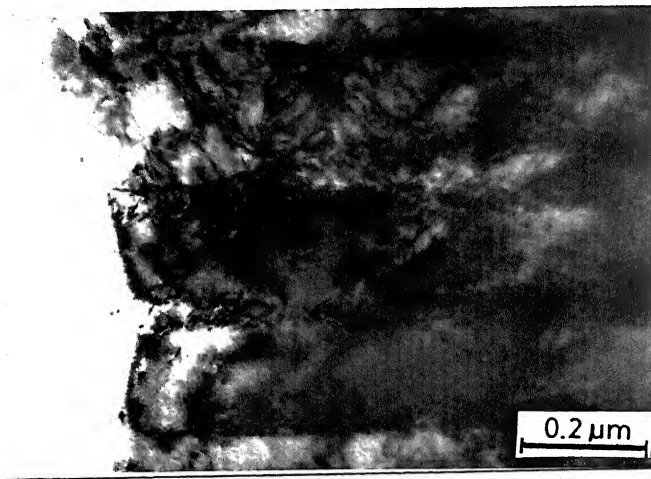
3.12 IDENTIFICATION OF δ -FERRITE IN A MARTENSITIC MATRIX USING CBED

The last problem studied in this chapter is to distinguish δ -ferrite in a martensitic matrix, of 9Cr-1Mo steel which has been quite difficult so far (19). This problem was resolved using the sensitivity of angular position of HOLZ lines to lattice strain. Identification of δ -ferrite in a martensitic matrix is difficult mainly because of the following problems: similarity in the crystal structure of the high temperature and the low temperature ferrite, low volume fractions of δ in most situations and metastable nature of δ -ferrite. The last of these, namely the metastability of δ -ferrite, prevents the application of conventional signatures like microhardness, morphology and microchemistry, to identify δ -ferrite in a martensitic matrix. Under these circumstances, the only feature that distinguishes the metastable, high temperature δ -ferrite in a martensitic matrix, is their transformation temperature and the mode of decomposition. The δ -ferrite forms as a strain free nucleus at high temperature and grows to the extent dictated by the 'stay time' i.e., cooling rate. On the contrary, α' is a product of an athermal decomposition of τ during cooling, locking up a lot of strain, leading to a possible small change in lattice parameter. Therefore, it is expected that a localised probe like CBED which is sensitive to lattice strain would help to distinguish the two forms of ferrite.

In the present study, it was required to compare the results in the welds with a reference sample in which δ -ferrite is confirmed to be present. Hence, the high temperature δ -ferrite was deliberately introduced in the wrought steel by solutionising the steel in the duplex phase field of τ and δ . Figure 3.36a shows the presence of δ -ferrite in a wrought 9Cr-1Mo steel aged at 1573 K for 30 minutes, followed by water quenching. A well annealed crystal of δ -ferrite, with only thickness contours and a few



(a)



(b)

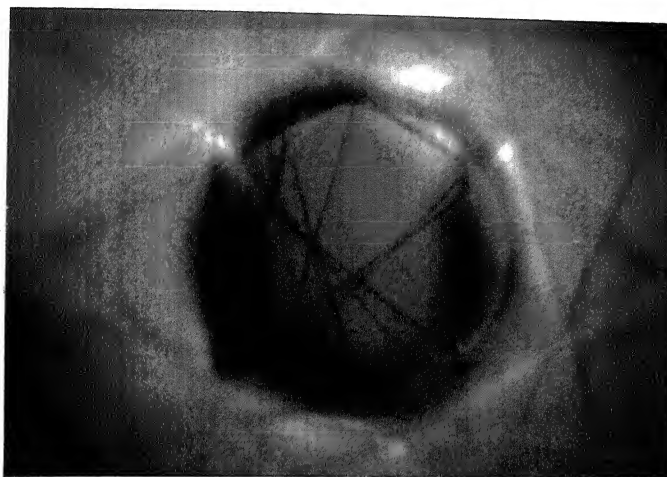
Figure 3.36 Microstructure of (a) δ -ferrite and (b) α' ferrite in the wrought 9Cr-1Mo steel solutionised at 1573 K for 30 minutes and water quenched.

dislocations is seen. In contrast, the typical lath martensite in the same wrought 9Cr-1Mo steel is shown in figure 3.36b. This martensitic crystal contains a high density of dislocations, typical of lath martensite. The angular positions of HOLZ lines (figure 3.37) within the δ -ferrite and the martensitic ferrite are studied. Based on this base line data, the angular positions of HOLZ lines in the various laths of welds of 9Cr-1Mo weldment are monitored to check if any of them correspond to that of δ -ferrite. No evidence for the presence of δ -ferrite could be observed. These studies suggest that δ -ferrite is not likely to be present in the welds of 9Cr-1Mo steel. The absence of δ -ferrite is expected to be due to low amount of silicon in the filler material used and possibly high cooling rates.

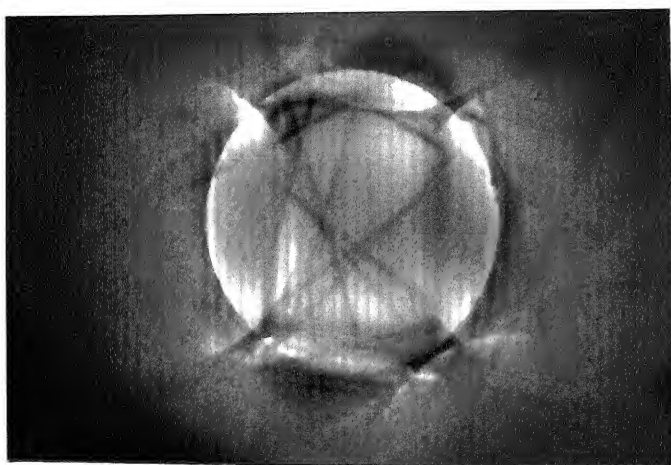
The above method of detecting the presence of microscopic phases in fine regions, is very useful especially in the absence of suitable techniques to carry out the same. It is possible to apply this method with ease and satisfactory accuracy only if the phase of interest is available within the transparent regions of the thin foil. The possibility of not being able to retain the phase of interest within the transparent regions cannot be completely ruled out. This problem can be overcome only by high, reliable statistics.

3.13 CONCLUSIONS

Microstructural variation in the as welded multi-pass weldment of 9Cr-1Mo steels is studied in detail. Based on analytical electron microscopy studies of ten different cross-sections near the top surface of the weldment, microstructurally distinct zones of "primary solidification" structures have been identified. The presence of "repetitive microstructures" within the weld zone of the weldment, confirms that there is significant modification of microstructures due to multiple passes in a multipass manual metal arc welding process.



(a)



(b)

Figure 3.37 HOLZ 'deficiency' lines in (a) δ -ferrite and (b) α' ferrite seen in Figure 3.36 (a) and (b) respectively.

A three-dimensional microstructural phase field map has been generated for 9Cr-1Mo weldment. This map depicts the steep variations in the phase fields of the different regions of the weldment.

CBED has been applied to measure lattice strain of different regions of the weldment. The same principle has been found to be useful in finding out if δ -ferrite is present in a martensitic matrix. In the present study, δ -ferrite has not been found to be present which has been understood in terms of low silicon content and high cooling rate.

Thus, a complete description of the 9Cr-1Mo weldments, in their as-welded state, with respect to microstructure, microchemistry and strain has been provided, based on detailed studies using analytical electron microscopy and convergent beam electron diffraction.

REFERENCES

1. P.T. Oldland, C.W. Ramasay, D.K. Matlock and D.L. Olson, *Welding Research Supplement*, April (1989) 158-S
2. M. Dewitte and C. Coussement, *Materials at High Temperatures*, 9,4 Nov. (1991) 178
3. R.S. Fidler and D.J. Gooch, Proc. International Conf. on *Ferritic Steels for Fast Reactor Steam Generators*, (Eds. S.F. Pugh and E.A. Little), British Nuclear Energy Society (BNES), London (1978), p.128
4. P. Roy and T. Lauritzen, *Welding Research Supplement*, Feb. (1986) 45-S
5. J.G. Zhang, F.W. Noble and B.L. Eyre, *Materials Science and Technology* 7 (1991) 315
6. K. Laha, K.B.S. Rao and S.L. Mannan, *Materials Sci. and Engg.*, A129 (1990) 183
7. J.N. Soo, *C.E.G.B. Report RD/L/R 1918*, 1950 (cross Ref. in 3)
8. G.R. Odette and G.E. Lucas, *J. Nucl. Materials* 117 (1983) 276
9. G.R. Odette and G.E. Lucas, *J. Nucl. Materials* 117 (1983) 264
10. G.R. Odette, G.E. Lucas, R. Maiti and J.W. Sheckerd, *J. Nucl. Materials* 122/123 (1984) 442

11. T.G. Gooch, *Welding Institute Research Bulletin* 18, 12 (1977) 343
12. R.A. Tait and J.F. Knott, *Grain Boundary*, Proc. Spring Residential Conference, The Institute of Metallurgists, Series 3, No.5 (1976) p.C1 (cross Ref. in 3)
13. D.A. Wolstenholme, *ibid.*, p. C7
14. J.M. Brear and B.L. King, *ibid.*, p. C13
15. R.D. Leapman, S.J. Sanderson and M.J. Whelan, *Metals Sci.* (1978) 215
16. W.D. Forgeng and W.D. Forgeng Jr., *Metal Handbook* 8, ASM, Metals Park, Ohio (1973), p. 402
17. H.K.D.H. Bhadeshia, *Materials Science and Technology* 8, Feb. (1992) 123
18. S. Saroja, M. Vijayalakshmi, V. Thomas Paul and V.S. Raghunathan, Presented at the Annual Technical Meeting of the Indian Institute of Metals, Calcutta, Nov. 14-17 (1995)
19. S. Saroja, M. Vijayalakshmi and V.S. Raghunathan, *Mater. Sci. and Engg.* 59 (1992) 154
20. S. Saroja, M. Vijayalakshmi and V.S. Raghunathan, *Mater. Trans. JIM* 34 (1993) 901

21. R.C. Reed and H.K.D.H. Bhadeshia, *Acta Metall. Mater.* 42,11 (1994) 3663
22. J.W. Steeds, *Introduction to AEM*, Eds. J.J. Hren, et al., Chapter 15, p.387
23. *Convergent Beam Electron Diffraction*, M. Tanaka and M. Terauchi, JEOL Ltd. (1985)
24. M. Tanaka, R. Saito and H. Sekii, *Acta Cryst.* A39 (1982) 357

CHAPTER 4

MICROSTRUCTURAL MODIFICATIONS IN WELDMENTS OF 9Cr-1Mo STEEL AT ELEVATED TEMPERATURES

4.1 INTRODUCTION

The ferritics, in their wrought and welded conditions are used as boilers and superheaters in the steam generator circuits of power industry. These applications require stringent control of properties, which in turn are dictated by their microstructures. The microstructures that develop in the weldments of ferritic steel during welding, are quite complex and heterogeneous. These heterogeneities are detrimental for the commercial utilisation of these steels. However, the commercial suitability of the weldments of the ferritics, depends not only on the heterogeneities of the weldments in the "as-welded" state, but also on their stability at the operating temperature over long durations. Thus, one of the important requirements of power industry is the stability of the microstructures and properties of the components, at the temperature of operation, throughout the lifetime of the components. Therefore, it becomes essential to ensure that there is no degradation of long term, high temperature properties. The lifetime of these components in typical power generating units is around thirty years during which they are exposed to service temperatures of the order of 573 to 773 K. Hence, the microstructural stability, which influences the properties in this temperature range, assumes an important role in the selection of materials, for these applications (1,2).

A large number of ferritics have been evaluated for their long term properties. Cr-Mo steels ranging from 1/2 w/o Cr-1/2 w/o Mo to 12 w/o Cr-2 w/o Mo steels, have been extensively studied (3-10). Substitution of Mo with tungsten, resulting in the development of low activation steels has also been attempted, for their suitability in commercial applications (11,12). Most of these studies are related to structure-property correlations. A brief summary of these studies is given in Table IV.1.(13). It has been shown that the type and distribution of carbides have a direct bearing on the mechanical properties and their in-service performance. The general trend in 'evolution of carbides' is as follows: predominance of iron-rich carbide in low chromium steel, molybdenum rich carbides in steels with medium concentration of chromium and chromium rich carbides in high chromium steels. However, precipitation of carbides typical of medium Cr steels is observed in high Cr steel, after exposure of these steels to elevated temperatures, for prolonged times of the order of 45,000 hours (7,13). Thus, there is a wide variation in the nature and chemistry of carbides from one steel to another, at comparable ageing conditions.

It is found that the low Cr ferritics are not stable with respect to long term creep properties. This has been identified as due to the continuous evolution of different kinds of carbides, M_2X , M_7C_3 , M_6C and $M_{23}C_6$. Increase in chromium content shifts the stability towards the equilibrium carbide $M_{23}C_6$, in most steels. This makes the steels with high or medium concentration of chromium preferable with respect to the stability of long term properties.

Additional problems arise in the case of weldments of ferritics. The structure of weldments of ferritics is heterogeneous and the extent of heterogeneity depends very much on the initial composition and the welding parameters. There are a number of mechanisms by which the high temperature austenite can decompose during cooling of the weld. The exact mode of decomposition depends crucially on the chemistry of

Table IV.1

Comparison of precipitation behaviour in some Cr-Mo steels (13)

Steel	Treatment	Microstructure	Type of carbides
1Cr-0.5Mo-0.1C	Normalised(n) and tempered (t)	Pearlite/Bainite Bainite + ferrite	M_3C $M_2C + M_6C$
2.25Cr-1Mo-0.1C	n n and t n, t and aged at 1023 K	Bainite Bainite + ferrite Ferrite	M_3C $M_{23}C_6 + M_6C$ M_6C
3Cr-1Mo-0.1C	n and t	Bainite + ferrite	$M_7C_3 + M_{23}C_6$ + M_6C
9Cr-1Mo-0.1C	n and t n, t and aged at 1023 K	Tempered martensite Ferrite	$M_2X + M_{23}C_6$ $M_{23}C_6$
9Cr-2Mo-Nb- V-0.1C	n and t	δ -ferrite + martensite + ferrite	$MX + M_{23}C_6$ + M_6C
12Cr-1Mo-V- W-0.1C	n and t n, t and aged at 1023 K	Martensite + ferrite Ferrite	$MX + M_2X +$ $M_{23}C_6$ $M_{23}C_6$

the weld and the rate of cooling, resulting in widely varying structures (14). The modification of such heterogeneous structures at elevated temperatures depends on many parameters. These parameters, which are specific to only weldments are as follows: type of initial phase, its microchemistry and the differences in the activity of the solutes in the different regions of the weldment like the weld, HAZ and the base metal.

The wide variations in the different types of steels discussed above suggest that the comparison of these steels would be easier, if it is possible to identify a basic parameter in terms of which the precipitation sequence in each steel/weldment can be rationalised. The present chapter of the thesis attempts to identify such a parameter, using the extensive data base generated on the evolution of carbides in different locations of the weldment at high temperatures.

This chapter on 'MICROSTRUCTURAL MODIFICATIONS IN WELDMENTS OF 9Cr-1Mo STEEL AT ELEVATED TEMPERATURES' is organised in the following sequence: initially, the tempering kinetics of the weld region of the 9Cr-1Mo weldment is discussed, in which the apparent activation energy of the tempering process is evaluated and the corresponding rate-controlling process is identified. Next, the sequence of evolution of secondary carbides at the three distinct regions, weld, HAZ and the base metal of the weldment is derived, based on microstructural studies. The evaluation of detailed microstructural parameters is used to arrive at the sequence of evolution of carbides at various temperatures. Following this, the concept of 'phase evolution diagram' is proposed. This section confirms the validity of the above concept for application to a heterogeneous structure like that of 'weldment', formulate an experimental procedure for its evaluation and demonstrate its predictive capability.

4.2 EXPERIMENTAL PARAMETERS FOR CHARACTERISATION

Figure 4.1. provides the microstructural phase field map of the weldment in the as-welded condition, which is explained in detail in chapter 3 (repeated here for the purpose of continuity). The most relevant feature in this figure is the presence of steep variations in the microstructure and microchemistry. The evolution of these phases towards their equilibrium structures is followed at different temperatures, in the range 823 to 1223 K, for ageing times ranging from 2 to 250 h. A number of techniques have been used to obtain information on various parameters, like the microhardness, microchemistry of carbides, type of carbides, size, total number density N_f , area fraction of acicular ($A_f(\text{aci})$), and globular ($A_f(\text{glo})$) carbides. The scheme of quantification of these parameters, the sources of error and their estimation of all these parameters are described in chapter 2. These error bars are shown in the appropriate figures. A comprehensive understanding of the microstructural modifications in the three different zones of the weldments during exposure to high temperatures is arrived at, based on detailed study of variation of all these parameters. The present section discusses these results following three major classifications, namely, (i) the tempering kinetics, (ii) microstructural evolution at high temperatures and (iii) prediction of microstructural state using Phase Evolution Diagrams (PED).

4.3 TEMPERING KINETICS OF WELDMENTS

4.3.1 Hardness

Hardness is the most suitable index for evaluating the tempering process. In the case of weldments, the initial microhardness depends upon the distance from the weld centre line, as has been shown in chapter 3. Figure 4.2 (a to c) shows the

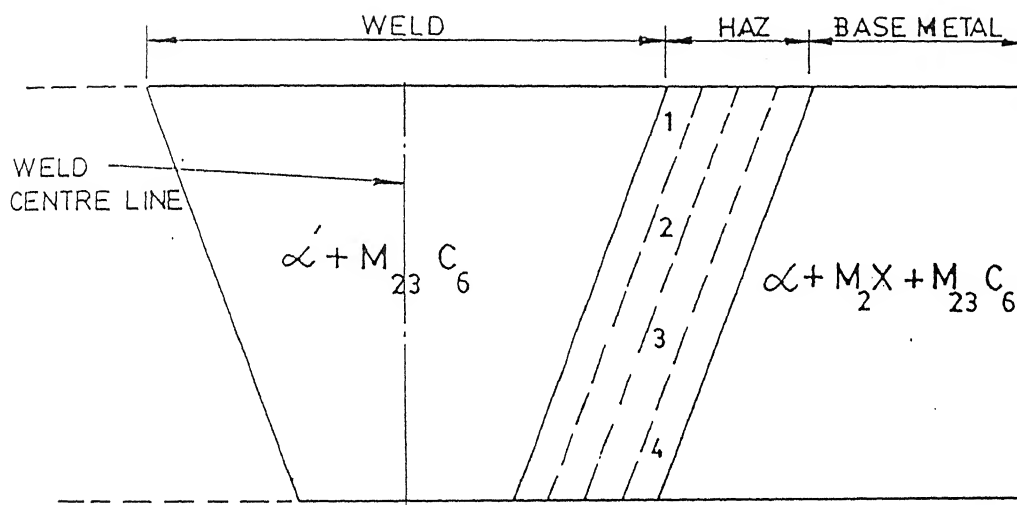


Figure 4.1 Microstructural phase field map of the weldment of 9Cr-1Mo steel, in the 'as-welded' condition. The numbers 1 to 4 represent different regions of HAZ, explained in figure 3.26.

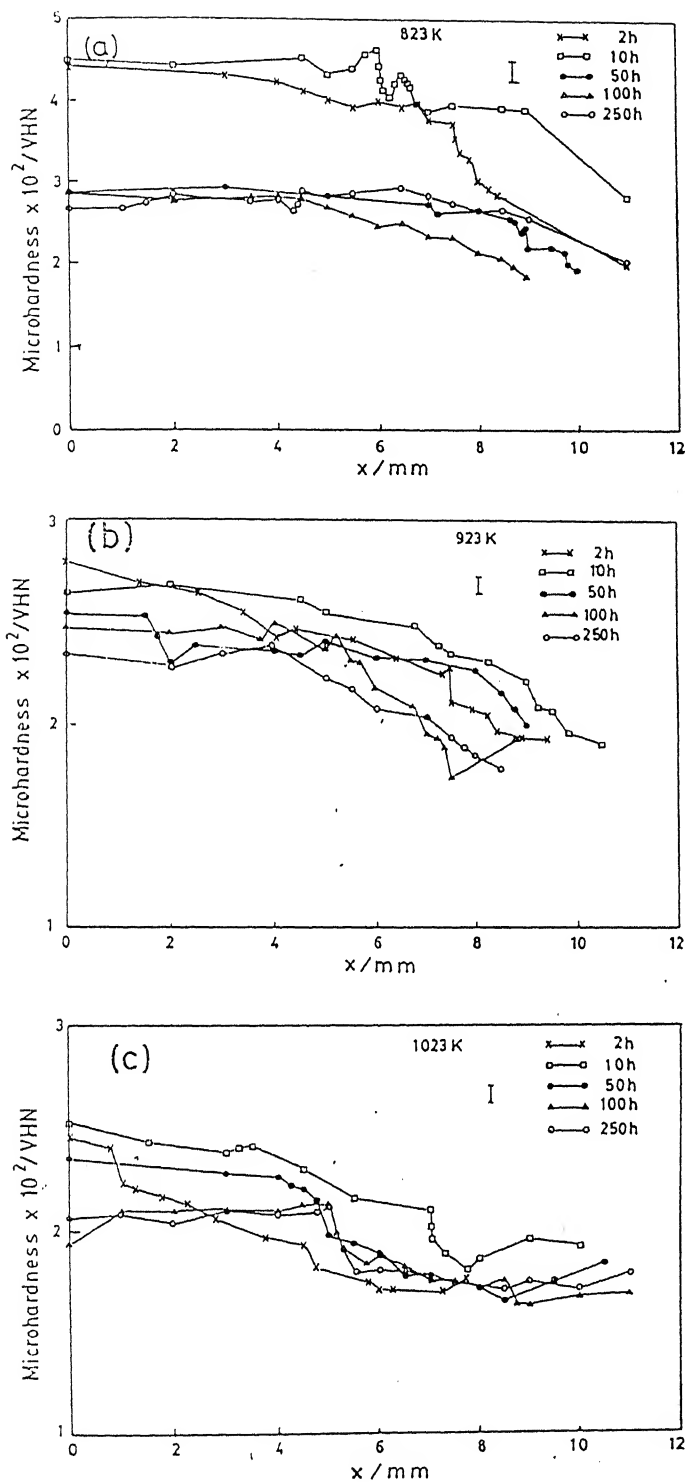


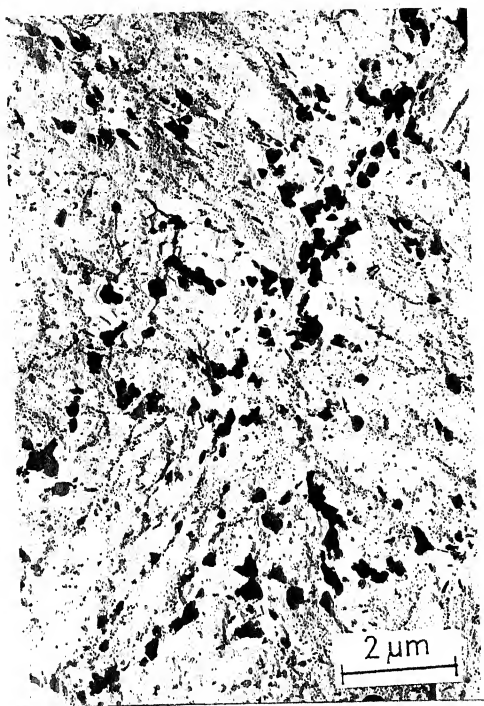
Figure 4.2 Variation of microhardness (load = 100 g) with distance, x , from the weld centre line. The weldments of 9Cr-1Mo steel have been tempered at (a) 823 K, (b) 923 K and (c) 1023 K for different durations.

variation of microhardness as a function of distance from the weld centre line of the weldments tempered at different temperatures for various durations. There is a gradual reduction in the microhardness, as the distance from the weld centre line is increased. The variation in the microhardness of the weldment across the three different regions, like weld, HAZ and the base metal is very steep at 823 K, unlike the other two temperatures. There is a significant reduction in the hardness of the weld close to weld centre line after tempering at 823 K for 10 h. Such steep reductions are observed within a short time of two hours, at the higher temperatures (figure 4.2). There is no remarkable change in the microhardness values of the base metal for the different tempering times at the higher temperatures.

4.3.2 Microstructural Changes During Tempering

The microstructural observations of the individual regions at various temperatures, suggest that there are distinct processes that contribute to the gradual reduction in hardness with increase in the distance from the weld centre line.

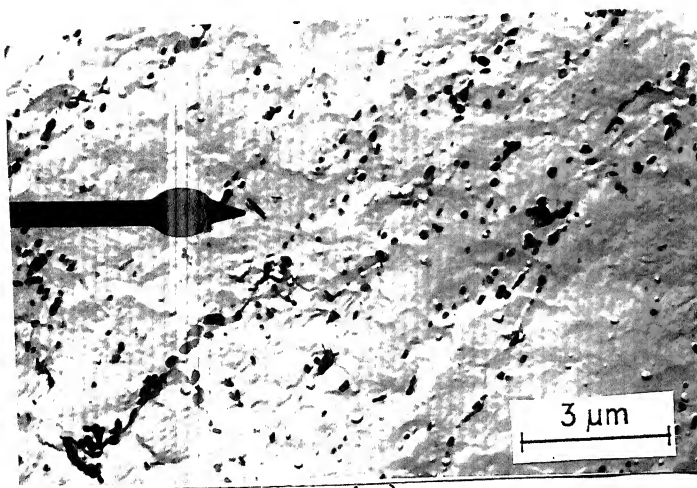
Figure 4.3 (a to c) shows the micrographs of typical carbon extraction replica of the three regions, weld, HAZ and the base metal, aged at 823 K for 250 h. The retention of lath structure, despite prolonged ageing and the extensive precipitation of carbides are clearly seen, in all the three regions. Most of these carbides are only $M_{23}C_6$, though M_2X is seen rarely in base metal (arrow marked in figure 4.3c). M_2X is identified by the characteristic high ratio of concentration of chromium and iron, shown in the EDAX spectrum (figure 4.3d). Figure 4.4 (a to c) shows the micrographs of the carbon extraction replica of the three regions, the weld, the HAZ and the base metal in a weldment tempered at 1023 K for 2 h. The carbides are found to be along the subgrain boundaries, suggesting a significant degree of recovery and precipitation. There is extensive precipitation of carbides, since 1023 K happens to be



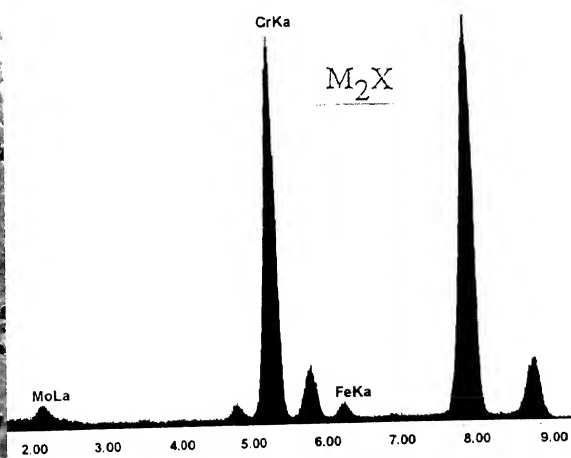
(a)



(b)



(c)



(d)

Figure 4.3 Microstructural evidence for the tempering process at 823 K after 250 h. (a) weld, (b) HAZ, (c) base metal and (d) EDAX spectrum of carbide arrow marked in c. Retention of lath structure is seen in addition to precipitation of fine carbides along the lath boundaries. Cr rich M_2X (d) in the base metal is characteristic of the initial microstructure of normalised and tempered 9Cr-1Mo steel.

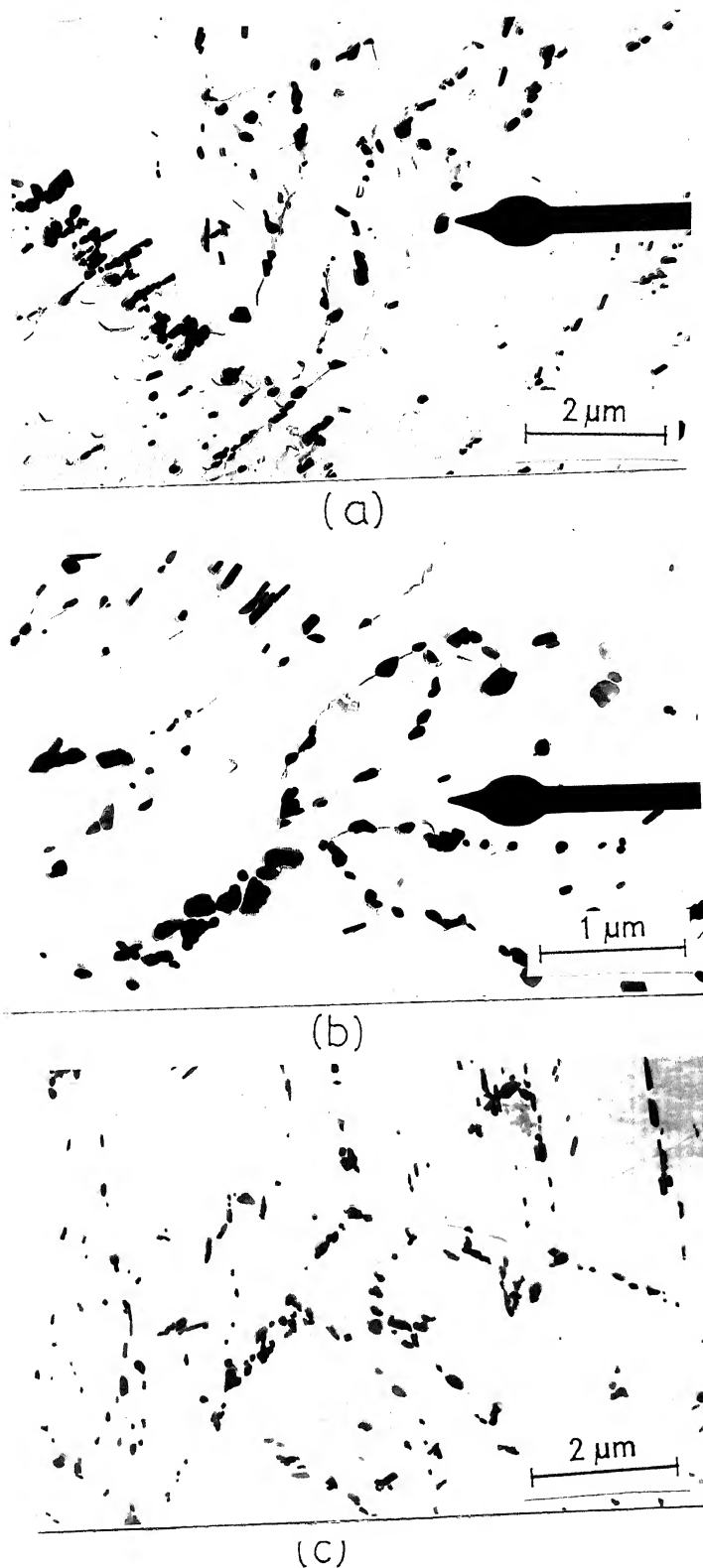


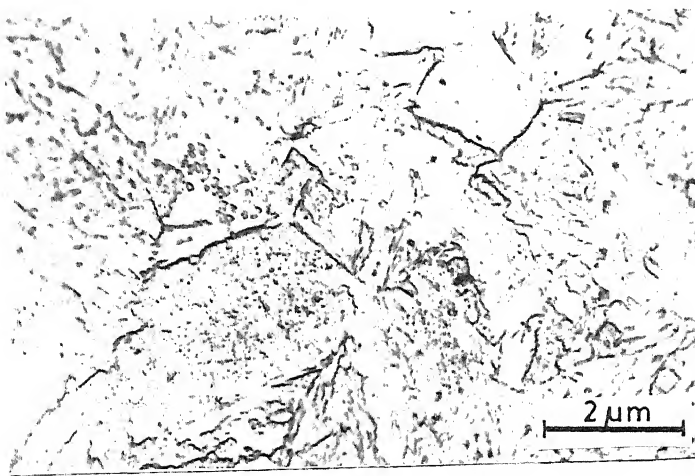
Figure 4.4 Microstructural evidence for the tempering process at 1023 K for 2 h. (a) weld, (b) HAZ and (c) base metal. A significant degree of recovery, with carbides along the subgrain boundaries is seen. The arrow marks in (a) and (b) show the carbides from which Cr rich EDAX spectra were obtained. Formation of M_2X is characteristic of the high tempering temperature, 1023 K.

the nose temperature of the TTT diagram for precipitation of carbides. Tempering at 1223 K has led to an additional mode of softening, i.e., the precipitation of pro-eutectoid ferrite (α), as can be seen in figure 4.5. In fact, observations on carbon extraction replica of these samples suggested that there were no carbides in any of the regions of the weldment tempered at 1223 K, due to the complete dissolution of the pre-existing carbides.

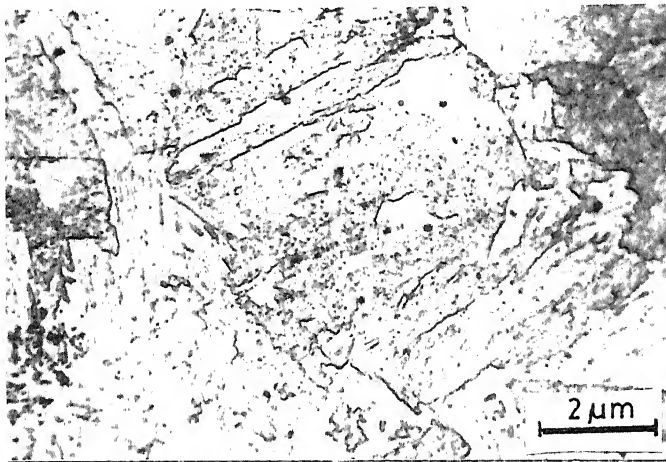
4.3.3 Mechanisms of Softening Process During Tempering

Based on the microstructural studies of the various regions of the weldment tempered at different temperatures, three distinct mechanisms could be identified for the gradual softening observed in the weldments. The softening at low temperatures is due to the precipitation of carbides, retaining the lath structure of the parent martensite (α'). Whereas, at medium temperatures, the recovery and recrystallisation of the lath structure, proceed to a considerable extent, along with precipitation. At temperatures between A_{c3} and A_{c1} , the third factor, namely the growth of soft α -ferrite is the operative mechanism. In the present study, choice of high temperatures is useful for identification of tempering mechanisms. However, the commercial practice of tempering is confined to temperatures less than 1023 K. The classifications of tempering processes, similar to those described above have been reported in earlier studies also (15-17).

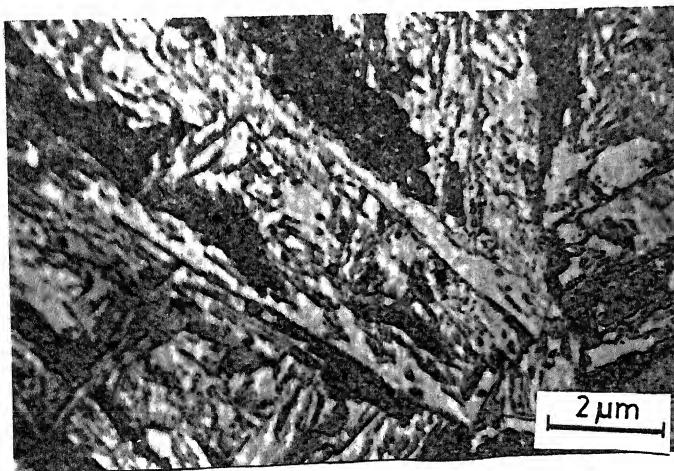
The rationalisation of the different temperature regimes over which tempering proceeds via different mechanisms, discussed above, is in agreement with the classification scheme for steels proposed by Nutting (17), shown in figure.4.6. It is reasonable to propose a similar classification with respect to ageing time at those temperatures where the different processes overlap. The results of the present study, discussed above, support the following classification of the processes:



(a)



(b)



(c)

Figure 4.5 Formation of pro-eutectoid ferrite (α) in the martensitic (α') matrix is seen in the weldment aged at 1223 K for 500 h. (a) weld, (b) HAZ and (c) base metal.

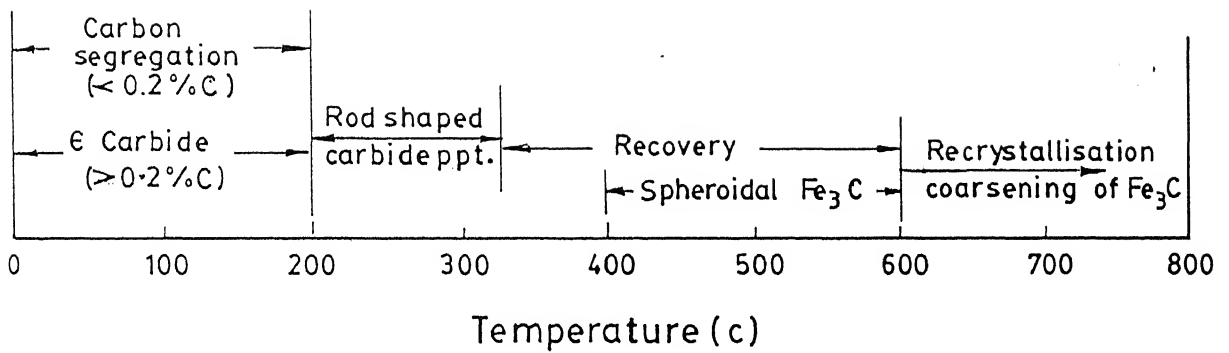
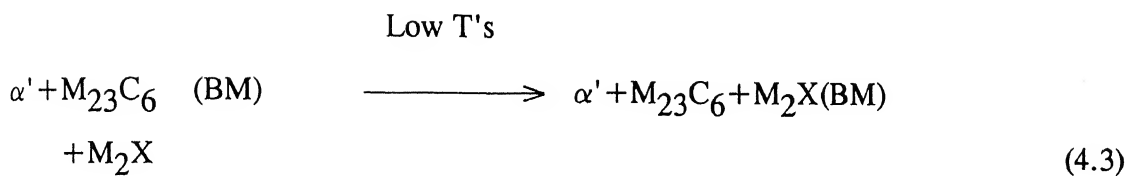
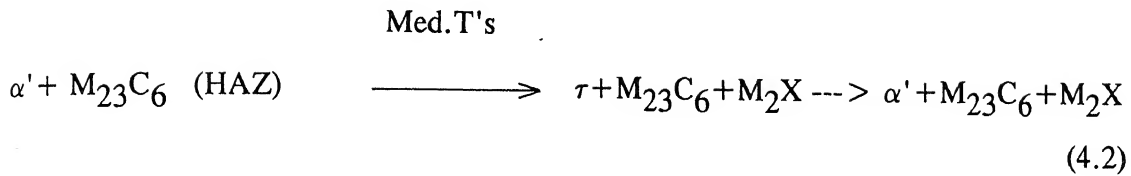
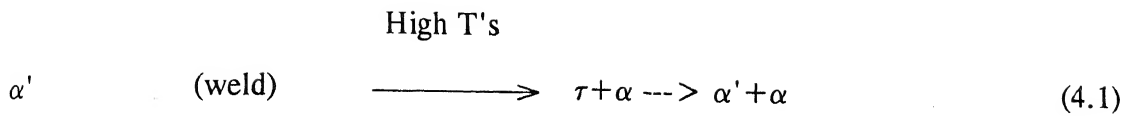


Figure 4.6 Classification of temperature regimes in terms of important tempering processes (Ref.17).



4.3.4 Operative Mechanism of Tempering : Diffusion of Carbon

The operative mechanism that contributes to the softening process is found to be characteristic of the tempering temperature (18). Therefore, the kinetics of tempering has been studied using any one of the regions. Of the three regions, the middle of the weld region is chosen for this purpose, due to the following reasons: high initial hardness and uniform structure within the weld zone. The heat affected zone has been avoided due to the presence of microstructurally different zones, explained in chapter 3.

Figure 4.7 shows the variation of hardness of the weld region as a function of tempering time at different tempering temperatures. The rate of tempering increases with the tempering temperature in the range 823 to 1023 K, while at 1223 K, there is

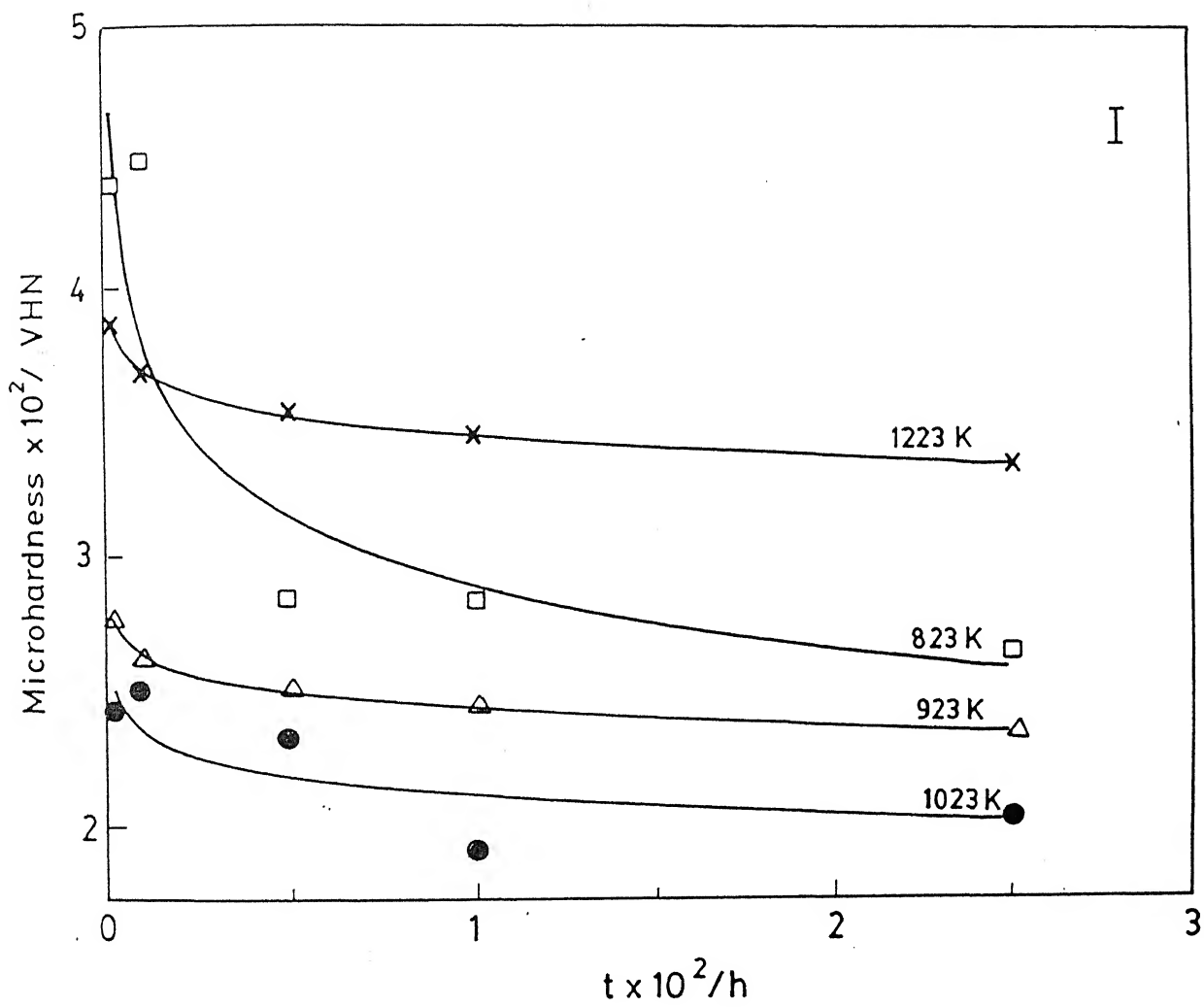


Figure 4.7 Variation of microhardness (load = 100 g) of the weld region with time at various temperatures.

a significant deviation. At 1223 K, there is a small, rapid reduction in hardness initially, followed by a high saturation value of hardness. The formation of proeutectoid α -ferrite and the decomposition of remaining τ to α' are responsible for the above observations. The tempering kinetics at the other three temperatures, follow a similar behaviour : lower saturation hardness at higher temperatures and timings, and less time to reach the saturation hardness at higher tempering temperature. Therefore, the tempering kinetics was studied using the data at these three temperatures. In order to verify if the kinetics of tempering follows an Arrhenius behaviour and to identify the underlying operative mechanism of the tempering processes, the temperature dependence of an appropriate kinetic parameter has been studied. In the present case, the recovery rate i.e., the variation of hardness in a given time interval, has been chosen as the appropriate kinetic parameter. Figure 4.7 shows that the hardness at any temperature reduces rapidly initially, followed by a saturation. This suggests that most of the tempering is complete within few hours of tempering and thereafter, recovery is negligible. Hence, the initial portion of each of the curves in figure 4.7 is fitted to a straight line and its slope calculated. The values of the slope of these lines, the kinetic parameter at the three temperatures of interest are listed in Table IV.2. The temperature dependence of this parameter, i.e., the recovery rate, is studied. An Arrhenius plot, variation of $\log(\text{recovery rate})$ vs $(1/T)$ is shown in figure.4.8. The linear behaviour with a negative slope suggests that the process follows an Arrhenius behaviour. The steep nature of the line, suggesting a high value of the slope, implies that the controlling step has a very low activation energy. The apparent activation energy, calculated based on figure 4.8 is around 0.63 eV. This value compares very well with the value of interstitial diffusion of carbon in α -ferrite (80kJ/mole), which is 0.83 eV (17). Therefore, it is reasonable to conclude that the rate limiting step in the tempering kinetics of the weld is the interstitial diffusion of carbon.

Table IV.2

Recovery rate of weld region of 9Cr-1Mo weldment at high temperatures

Sl.No.	Temperature K	Recovery rate $\Delta\text{VHN}/\Delta t$
1	823	1.44
2	923	2.24
3	1023	2.84

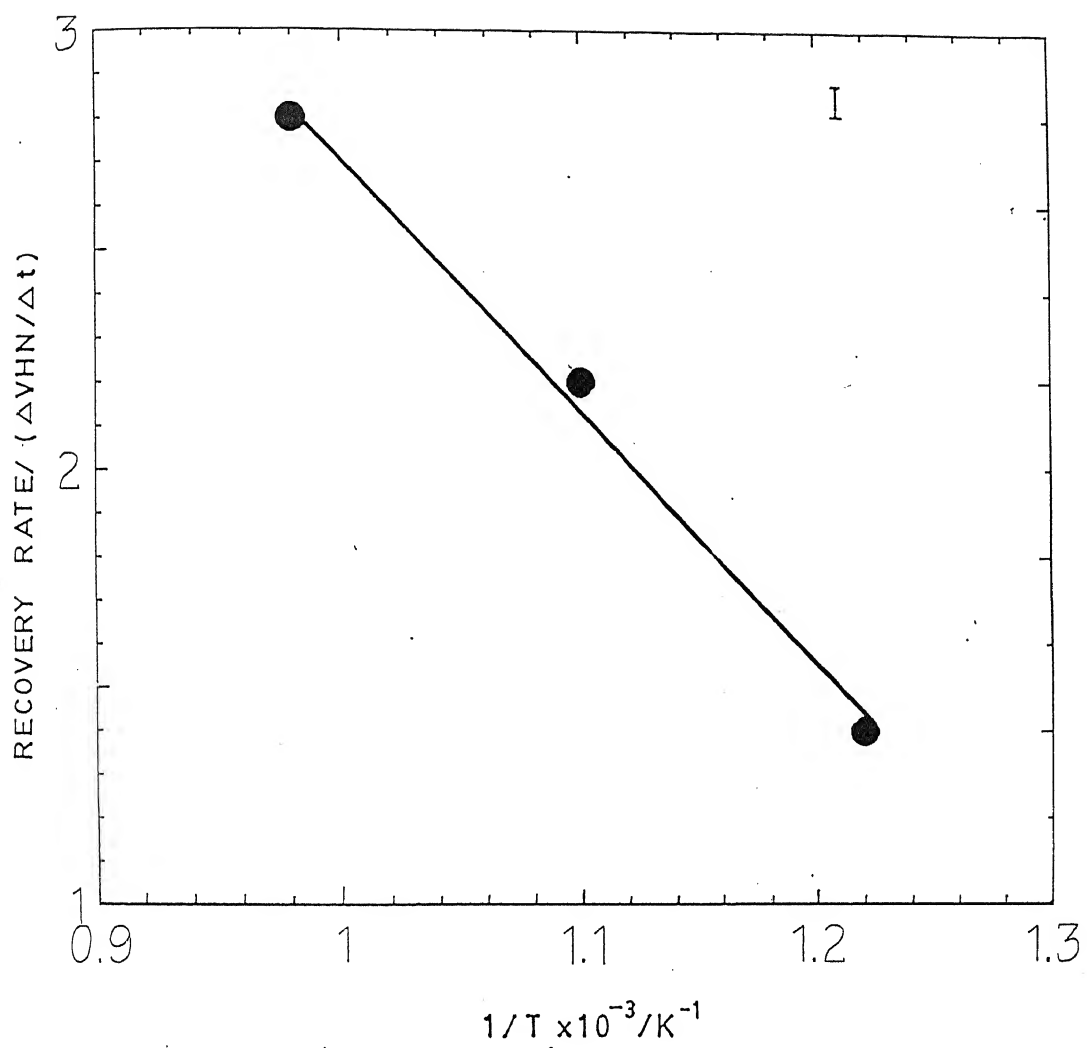


Figure 4.8 Arrhenius plot of the rate of recovery of weld region of 9Cr-1Mo weldment.

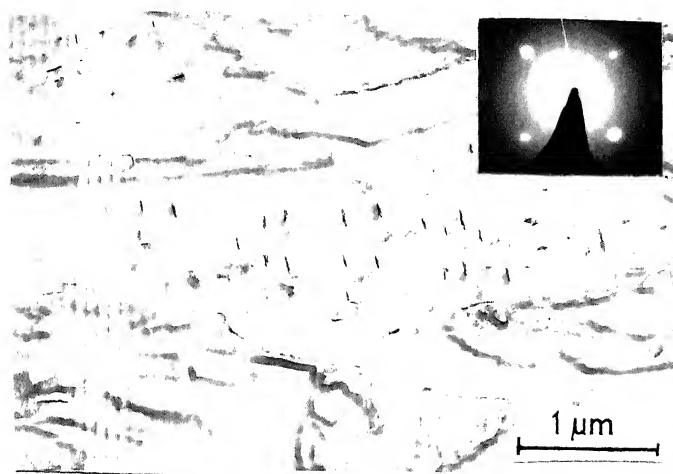
4.4 EVOLUTION OF SECONDARY PHASES

The different regions of the heat treated weldment were studied individually for understanding the microstructural evolution in each region. It is shown in chapter 3 that HAZ consists of several microstructurally distinct regions. Therefore, initial studies were carried out on two distinct regions of HAZ of the weldment aged at 823 K for 50 h: HAZ-1 the region near to the weld and HAZ-2 the region near the base metal. These studies suggested that there is no remarkable change between the two regions. Therefore, further studies were confined to only the following regions: the weld, the HAZ and the base metal. The carbon extraction replica from each one of these regions were studied, for the detailed understanding of the evolution of carbides.

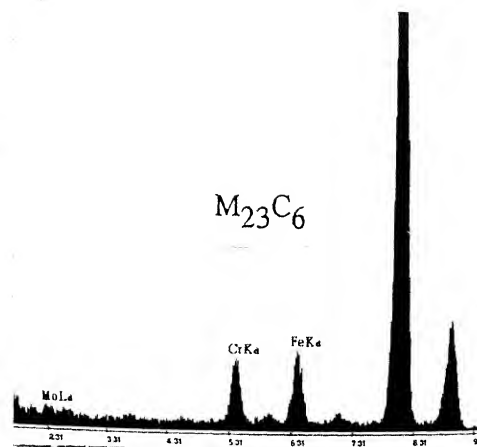
4.4.1 Microstructural Evolution of Weld Region at High Temperatures

It has been shown in chapter 3 that the middle region of weld consists of predominantly a martensitic structure, with few isolated carbides, formed during multipass. Figures 4.9.to 4.11 show a series of micrographs of carbon extraction replica of the weld region of the weldment aged at the three different temperatures, namely, 823 K, 923 K and 1023 K. The salient features are as follows:

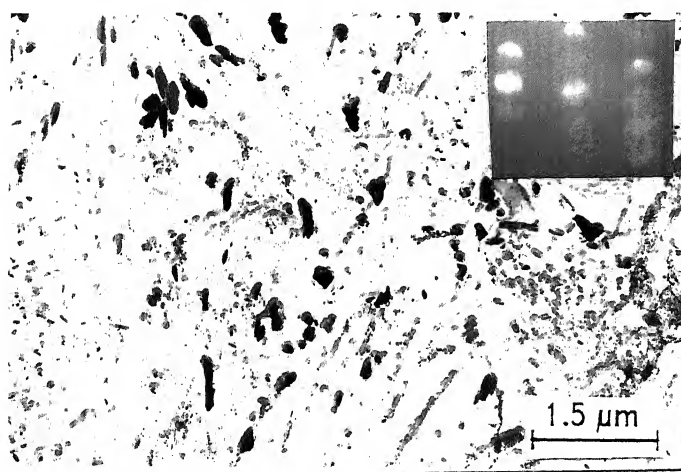
- **** Ageing at 823 K for 2 and 10 h has resulted in a uniform distribution of fine, needle-like carbides (figure 4.9a). The degree of undercooling is high at 823 K. Consequently, the driving force for the relief of supersaturation of α is also high, which favours the nucleation of a high density of fine carbides along the matrix dislocations. The lower diffusivity at 823 K is the factor which restricts



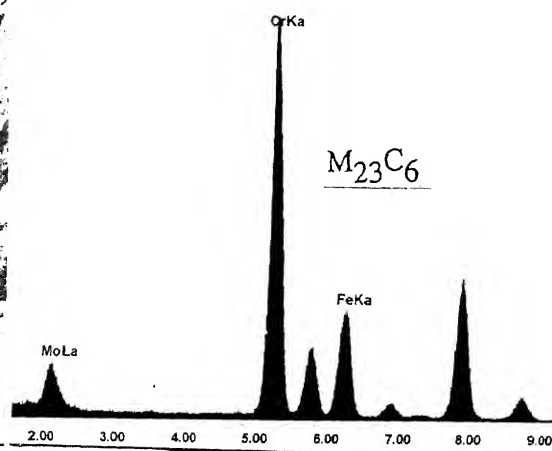
(a)



(b)

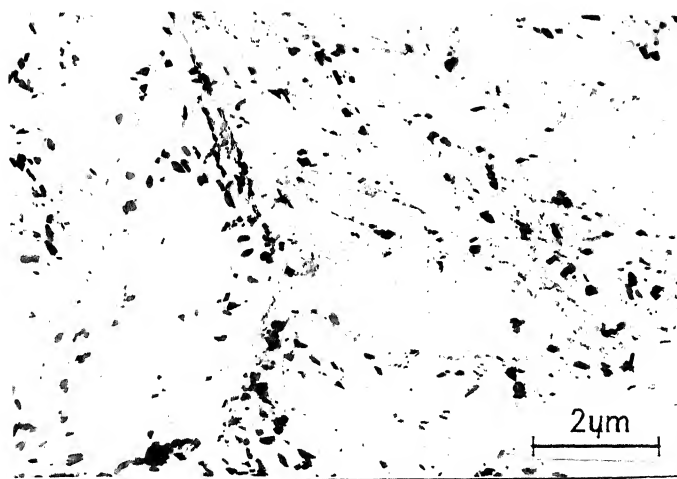


(c)

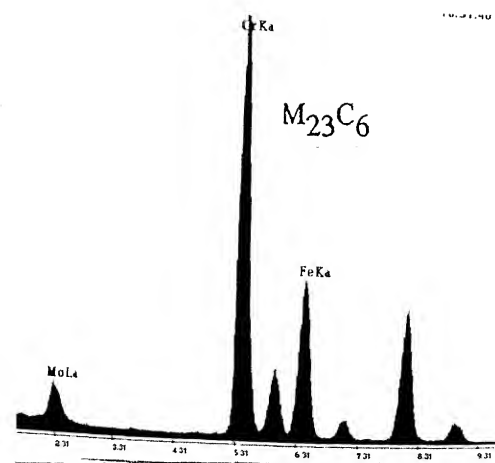


(d)

Figure 4.9 Evolution of secondary carbides in the weld region at 823 K. (a) Iron rich $M_{23}C_6$ after 2 h. Inset shows microdiffraction pattern of $M_{23}C_6$ along $\langle 220 \rangle$. (b) Typical EDAX spectrum from the iron rich carbide. (c) Growth of coarse carbides after 250 h. Inset shows microdiffraction pattern of $M_{23}C_6$ along $\langle 7112 \rangle$. (d) EDAX spectrum from a representative carbide in (c), showing the enrichment of chromium in $M_{23}C_6$.



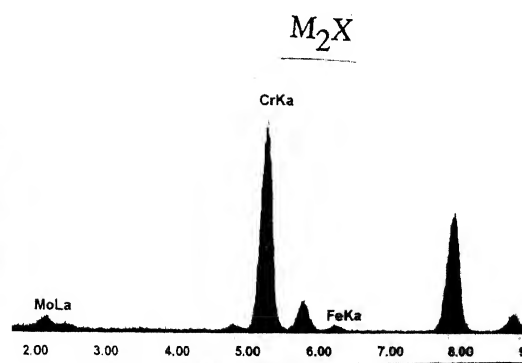
(a)



(b)

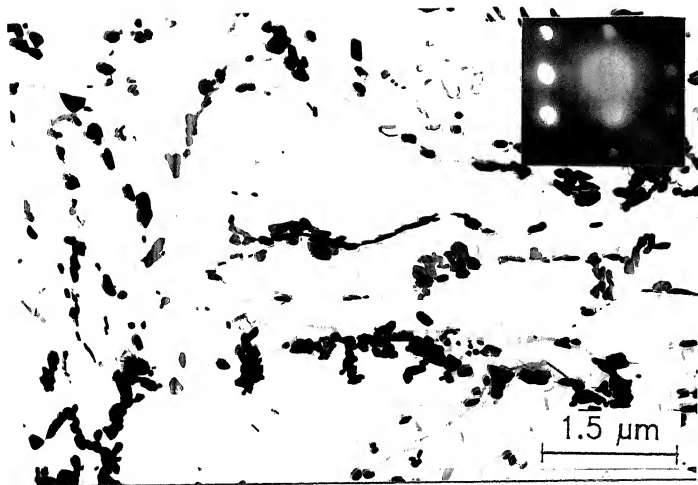


(c)

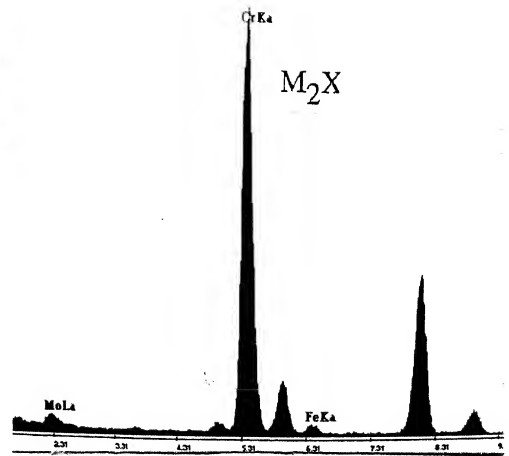


(d)

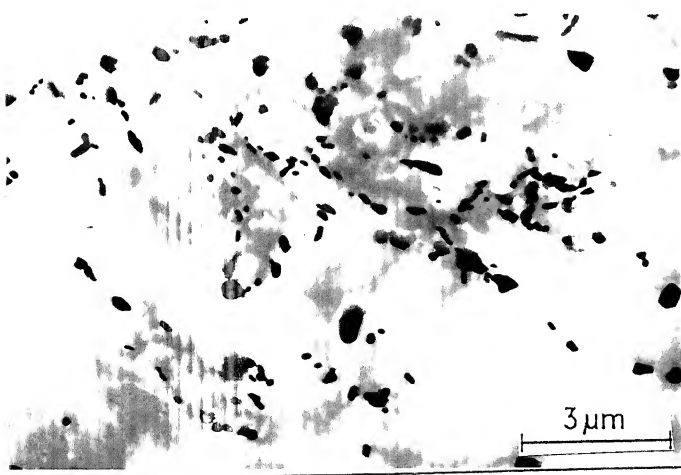
Figure 4.10 Evolution of secondary carbides in the weld region at 923 K. (a) 2 h., (b) EDAX spectrum from a representative $M_{23}C_6$ carbide and (c) growth of carbides after 75 h. Arrow mark shows the formation of Cr rich M_2X , as confirmed by EDAX spectrum, shown in (d).



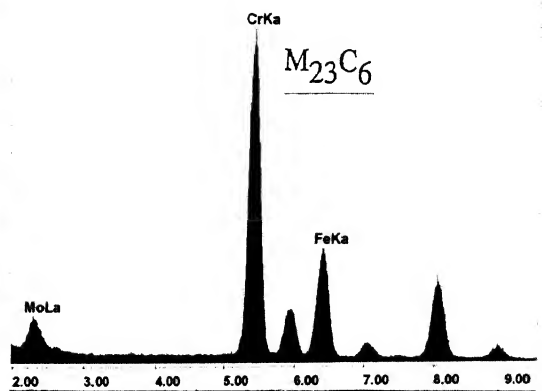
(a)



(b)



(c)



(d)

Figure 4.11 Evolution of secondary carbides in the weld region at 1023 K. (a) 2 h. Inset shows microdiffraction pattern of M_2X along $\langle 111 \rangle$. (b) EDAX spectrum of the same. (c) Carbide morphology after 250 h. (d) EDAX spectrum from a typical $M_{23}C_6$ carbide.

the coarsening of fine precipitates within the laths. Though these carbides are $M_{23}C_6$ (inset of figure 4.9a), the composition (rich in iron - figure 4.9b) is far from that of an equilibrium carbide at this temperature. Beyond 10 h, globular carbides with higher concentration of chromium are found (figure 4.9 (c and d)) to nucleate and grow along the lath boundaries. The concentration of chromium in these carbides was close to that of the equilibrium carbide. This particular sequence of events is directly related to the low diffusion distances for the solute elements and the high initial supersaturation, at low temperatures. The microstructural parameters like the number density of different types of carbides and their size are given in Table IV.3. The microchemistry of the various carbides are given in Table IV.4.

* At 923 K, the faster precipitation of $M_{23}C_6$ carbides along the lath boundaries, precedes the sluggish growth of M_2X . Upto about 20 h, there is a rapid precipitation of boundary carbides of $M_{23}C_6$ (figure 4.10(a and b)). The nucleation of acicular, fine M_2X sets in at about 75 h (figure 4.10(c and d)) and continues to be very rare till about 250 h. Tables IV.5 and IV.6 summarise the microstructural and microchemical data of the carbides at 923 K.

** Ageing at 1023 K resulted in a precipitation behaviour similar to that at 923 K. However, considerable differences in the rate of precipitation of carbides and their microchemistry (Tables IV.7 and IV.8) were observed. The precipitation of M_2X was quite rapid (Figure 4.11 (a and b)). Simultaneously faster growth of the more stable $M_{23}C_6$ is also seen (Figure 4.11 (c and d)). The microstructural parameters at 1023 K show a rapid increase in the dimensions of the carbides, without any change in A_f , when compared with those at 823 K. This suggests that the growth of precipitates is faster at 1023 K (Table IV.7). A significant difference in the microchemistry of $M_{23}C_6$ is observed. The ratio of

Table IV.3
Microstructural parameters of carbides that evolve in the weld
region at 823 K

Sl. No.	Ageing time	Number density			Dimensions		Area fraction
		Total(N_f)	Globular	Acicular	Globular(d)	Acicular(lxb)	
	t	$/\mu\text{m}^2$	$/\mu\text{m}^2$	$/\mu\text{m}^2$	μm	μm	A_f
	h						
1	2	9	0	9	0	0.07	0.0012
2	10	4	0	4	0	0.13	0.0025
3	20	22	5	17	0.016	0.06	0.0027
4	50	11	7	4	0.022	0.12	0.0029
5	75	6	3	3	0.032	0.14	0.0029
6	100	3	2	1	0.113	0.18	0.0029

Table IV.4

Microchemistry of carbides that evolve in the weld region at 823 K

Sl. No.	Ageing Time	Type of carbide	% of M in Metal Sublattice		
	h		Fe	Cr	Mo
				%	
1.	2	Fe rich $M_{23}C_6$	53	38.5	8.5
2.	2	Cr rich $M_{23}C_6$	13	73	14
3.	10	$M_{23}C_6$	7.7	12.5	10.5
4.	20	$M_{23}C_6$	34.1	58.6	7.3
5.	50	$M_{23}C_6$	19	71	10
6.	75	$M_{23}C_6$	22	66	12
7.	100	$M_{23}C_6$	21	70	9
8.	250	$M_{23}C_6$	20	70	10
9.	500	$M_{23}C_6$	13	76	11

Table IV.5

Microstructural parameters of carbides that evolve in the weld region at 923 K

Sl. No.	Ageing time	Number density			Dimensions		Area fraction
		Total(N_f) $/\mu\text{m}^2$	Globular	Acicular	Globular(d)	Acicular(lxb)	
			$/\mu\text{m}^2$	$/\mu\text{m}^2$	$/\mu\text{m}^2$	μm	
t							A_f
h							
1	20	6	4	2	0.1	0.23	0.0017
2	75	5	1	4	0.2	0.27	0.0019
3	100	4	1	3	0.2	0.22	0.0022

Table IV.6

Microchemistry of carbides that evolve in the weld region at 923 K

Sl. No.	Ageing Time h	Type of carbide	% in M of Metal Sublattice		
			Fe	Cr	Mo
				%	
1.	2	$M_{23}C_6$	26.6	65.37	8.04
2.	20	$M_{23}C_6$	23.75	67.29	8.97
3.	75	$M_{23}C_6$	24.72	66.78	8.5
4.	75	M_2X	3.19	91.18	5.63
5.	100	$M_{23}C_6$	23.13	67.49	9.38
9.	100	M_2X	1.1	95.34	3.57

Table IV.7

Microstructural parameters of carbides that evolve in the weld region at 1023 K

Sl. No.	Ageing time	Number density		Dimensions		Area fraction
		Total(N_f)		Globular(d)	Acicular(lxb)	
	t	$/\mu\text{m}^2$	Globular	$/\mu\text{m}^2$	μm	A_f
	h				μm	
1	2	4	1	3	0.18	0.37
						0.1
						0.0013
2	10	4	1	3	0.08	0.34
						0.1
						0.0009
3	20	3	1	2	0.14	0.47
						0.1
						0.0028
4	75	2	1	1	0.2	0.33
						0.1
						0.0027
5	250	3	2	1	0.2	0.6
						0.2
						0.003

Table IV.8

Microchemistry of carbides that evolve in the weld region at 1023 K

Sl. No.	Ageing Time	Type of carbide	% in M of Metal Sublattice		
	h		Fe	Cr	Mo
1.	2	M ₂₃ C ₆	29.2	63.37	7.41
2.	2	M ₂ X	2.86	92.8	4.3
3.	10	M ₂₃ C ₆	28.8	63.9	7.3
4.	10	M ₂ X	2.3	94.1	3.6
5.	20	M ₂₃ C ₆	28.7	63.66	7.7
6.	20	M ₂ X	3.0	91.72	5.0
7.	50	M ₂₃ C ₆	30.07	62.95	6.98
8.	50	M ₂ X	2.8	95.4	1.8
9.	75	M ₂₃ C ₆	27.46	64.7	7.8
10.	75	M ₂ X	2.5	94.93	2.6
11.	250	M ₂₃ C ₆	24.7	67.98	7.35
12.	250	M ₂ X	1.7	96.34	1.96

concentration of chromium to that of iron (Table IV.8) in $M_{23}C_6$ has increased considerably. The precipitates at 1023 K have become richer in chromium than those at 823 and 923 K.

The results presented above regarding the microstructural evolution and the microchemistry of carbides in the weld region at the three temperatures, are discussed in detail below.

4.4.2 Weld Region : Comparison of Microstructural Parameters

A careful comparison of the variation of microstructural parameters of carbides that evolve at high temperatures in the weld region has been carried out. These values for two typical ageing times are listed in Table IV.9, for the purpose of easy comparison. The following features are evident from these values.

The total number density of carbides, N_f reduces with ageing temperature, for a given ageing time. Despite the reduction in N_f , there is a small increase in the total area fraction of carbides, A_f . This can be attributed to the significant increase in the size of the carbides, both globular and acicular types, with increase in temperature. These observations suggest that there is a high density of fine carbides at lower temperature in contrast to less number of coarse carbides at high temperatures. This is in good agreement with the heterogeneous nucleation and growth theory of precipitation. It is known that at low temperatures, higher supersaturation and lower diffusivity results in high density of fine precipitates. Whereas, at high temperatures, lower supersaturation and higher diffusivity leads to rapid growth of less precipitates.

The next parameter of interest is the variation of the area fraction of carbides, A_f . Figure 4.12 shows the variation of the area fraction of carbides as a function of time,

Table IV.9

Comparison of microstructural parameters of the carbides in the weld region at various temperatures

Sl. No.	Tempera- ture	Time	Number density	Dimensions			Area fraction
	T	t	N_f	Globular(d)	Acicular(lxb)		A_f
	K	h	$/\mu\text{m}^2$	μm	μm	μm	
1.	823	20	22	0.016	0.06	0.014	0.0027
2.	923	20	6	0.1	0.23	0.14	0.0017
3.	1023	20	3	0.14	0.47	0.1	0.0028
4.	823	75	6	0.032	0.14	0.02	0.0029
5.	923	75	5	0.2	0.27	0.1	0.0019
6.	1023	75	2	0.2	0.3	0.1	0.0027

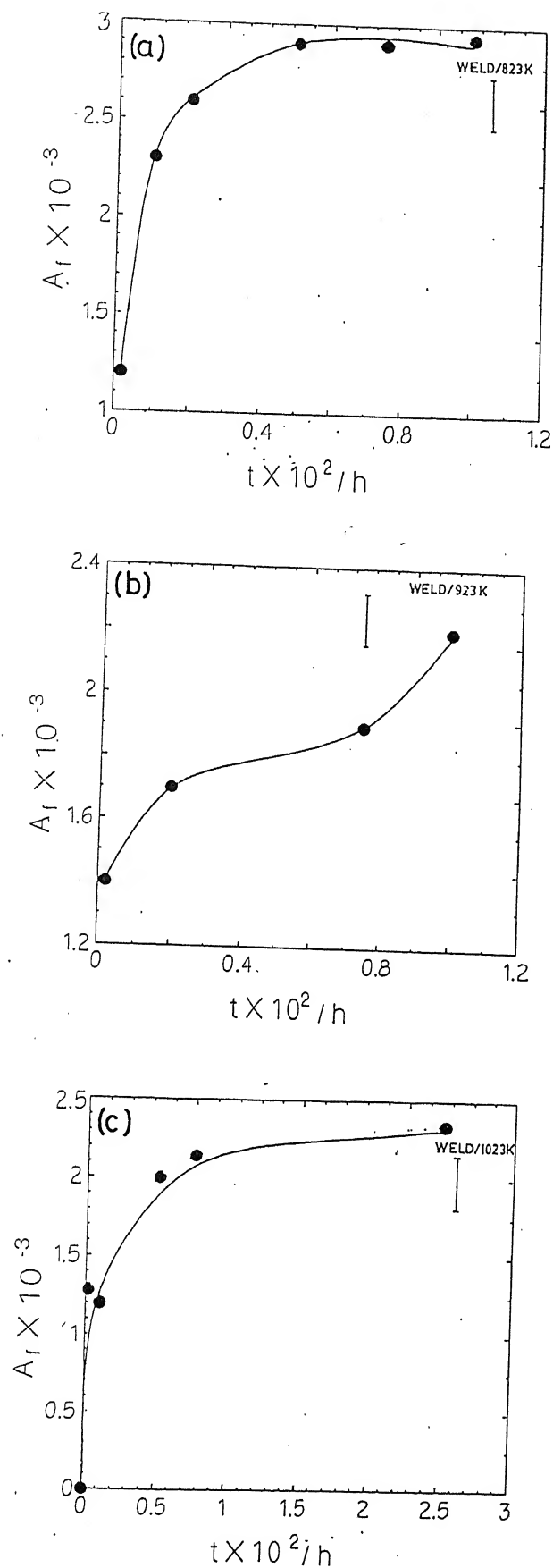


Figure 4.12 Variation of area fraction (A_f) of carbides with time at different temperatures. (a) 823 K, (b) 923 K and (c) 1023 K. The region corresponds to the weld zone of 9Cr-1Mo weldment.

at the three temperatures. A similar change in the area fraction of carbides has been reported in one of the earlier studies also (19). The increase in A_f in figure 4.12 (a and c) followed by a saturation, -a sigmoidal behaviour, is typical of a first order transformation. The rate of increase of A_f , is high at 823 K and 1023 K and low at 923 K (figure 4.12) . This is due to the following effects :- At 823 K, there is only one type of carbide that is evolving, i.e., $M_{23}C_6$. At 923 K, there is a delayed onset of precipitation of M_2X , after 75 h. The reduction in the growth rate curves is due to this reaction whose kinetics is much slower. It is to be mentioned that A_f represents the total area fraction of all the carbides, without distinguishing the two types. At a higher temperature of 1023 K, the kinetics is fastest due to higher diffusion rates, though the nucleation and growth of M_2X had occurred from 2 h onwards. The variation of area fraction of carbides at different temperatures could serve as a useful kinetic parameter. The analysis of kinetics of growth rate of carbides has, however, not been attempted due to the following reasons: (1) the rate of growth of the carbides does not show a distinct relationship with temperature and (2) two different types of carbides are evolving in this temperature range.

The morphology of the carbides, whether acicular or globular, is found to depend on the ageing time and temperature. At 823 K, almost all the carbides were found to be only acicular. Whereas at the other two temperatures, initially, the carbides were predominantly acicular, which undergo spheroidisation with further ageing. A typical example, in the case of evolution of carbides at 1023 K is shown in figure 4.13. The area fraction of acicular particles increases (figure 4.13b), reaches a maximum followed by a decrease, thus showing a peak at 20 h. The variation of area fraction of globular particles, at the same temperature shows a complimentary behaviour, as can be seen in figure 4.13a. Such a behaviour is a direct manifestation of the onset of coarsening reactions, wherein minimisation of interfacial free energy is the driving force, for the spheroidisation of acicular carbides, at longer ageing

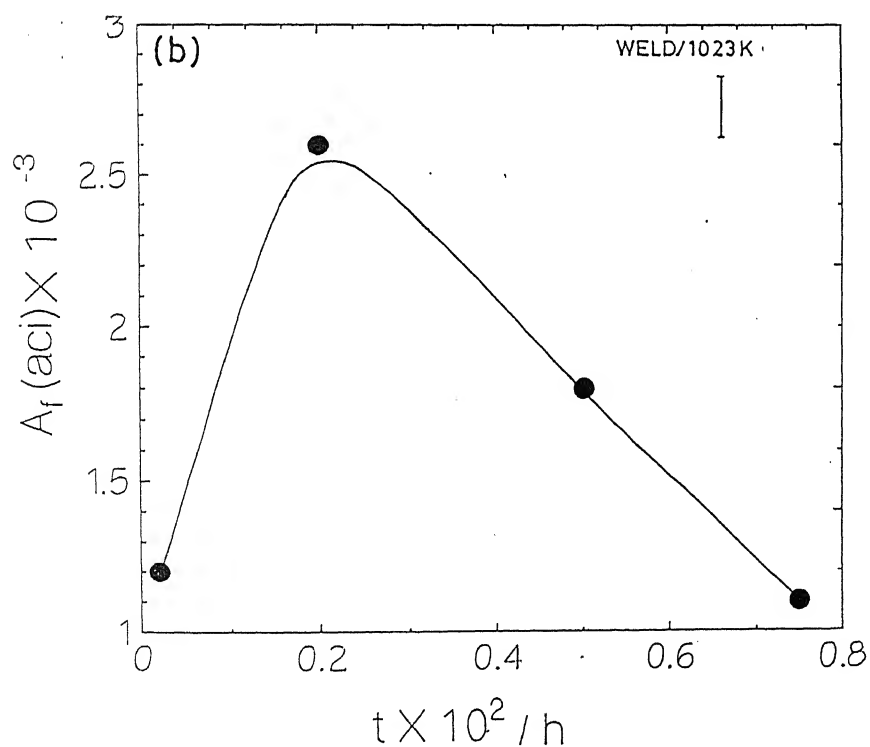
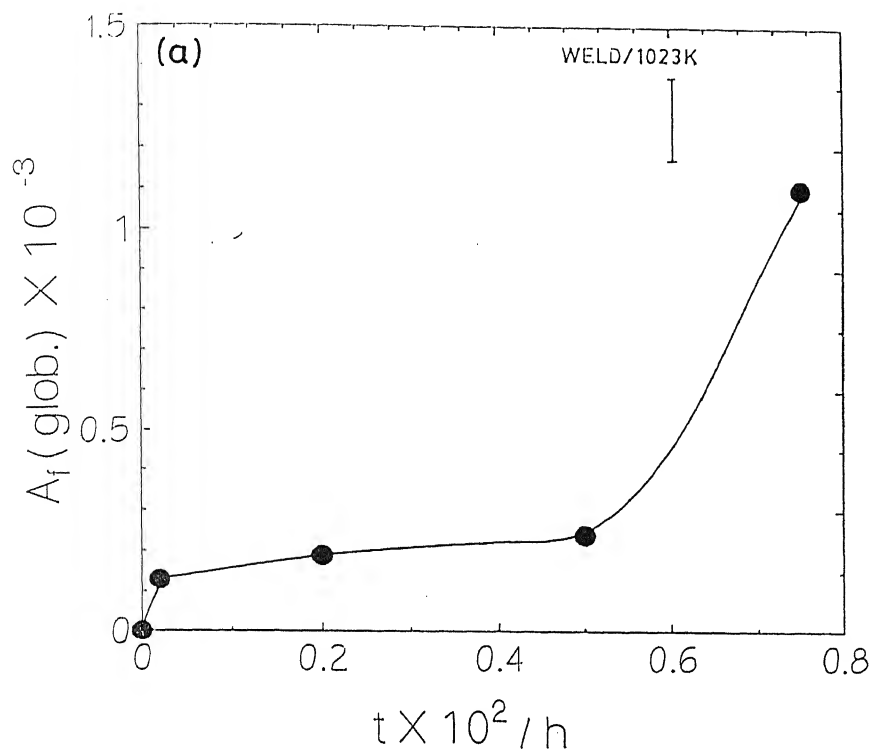


Figure 4.13 Complimentary behaviour in the evolution kinetics of globular and acicular carbides at 1023 K. (a) Variation of area fraction of globular carbides $A_f(\text{glob.})$ with time, (b) Variation of area fraction of acicular carbides $A_f(\text{aci.})$ with time.

times.

4.4.3 Weld Region : Comparison of Microchemistry of Carbides

Having compared the variation of microstructural parameters of carbides of the weld zone at various temperatures, it is appropriate to compare the variation in their microchemistry.

Figure 4.14 shows the ratio of concentration of chromium to that of iron (C_{Cr}/C_{Fe}) in $M_{23}C_6$ carbides, as a function of time at the three different temperatures. It is quite clear that the ratio increases with ageing time and temperature. A similar behaviour has been observed in studies of carbide precipitation in wrought 9Cr-1Mo steels (18). The variation in the microchemistry is understood in terms of kinetic factors and solubility limits of the two elements in $M_{23}C_6$. The equilibrium $M_{23}C_6$ dissolves more chromium than iron. It is known that the solubility of iron and chromium in $M_{23}C_6$ has a wide range of values (20). The observed change in the ratio C_{Cr}/C_{Fe} , could be attributed to the relative differences in the flux of chromium and iron at the precipitate/matrix interface. At 823 K, the mobility of chromium atoms is less and the availability of iron atoms is high. These two factors could have facilitated higher flux of iron atoms, at the precipitate/matrix interface, with a consequent decrease in the ratio of C_{Cr}/C_{Fe} content. At 1023 K, the higher rate of diffusion of chromium atoms is expected to outweigh the effect of higher availability of iron atoms around each precipitate, leading to higher values of ratio of concentration of chromium and iron. These two factors lead to a higher ratio of C_{Cr}/C_{Fe} ratio, with increase in ageing temperature and time.

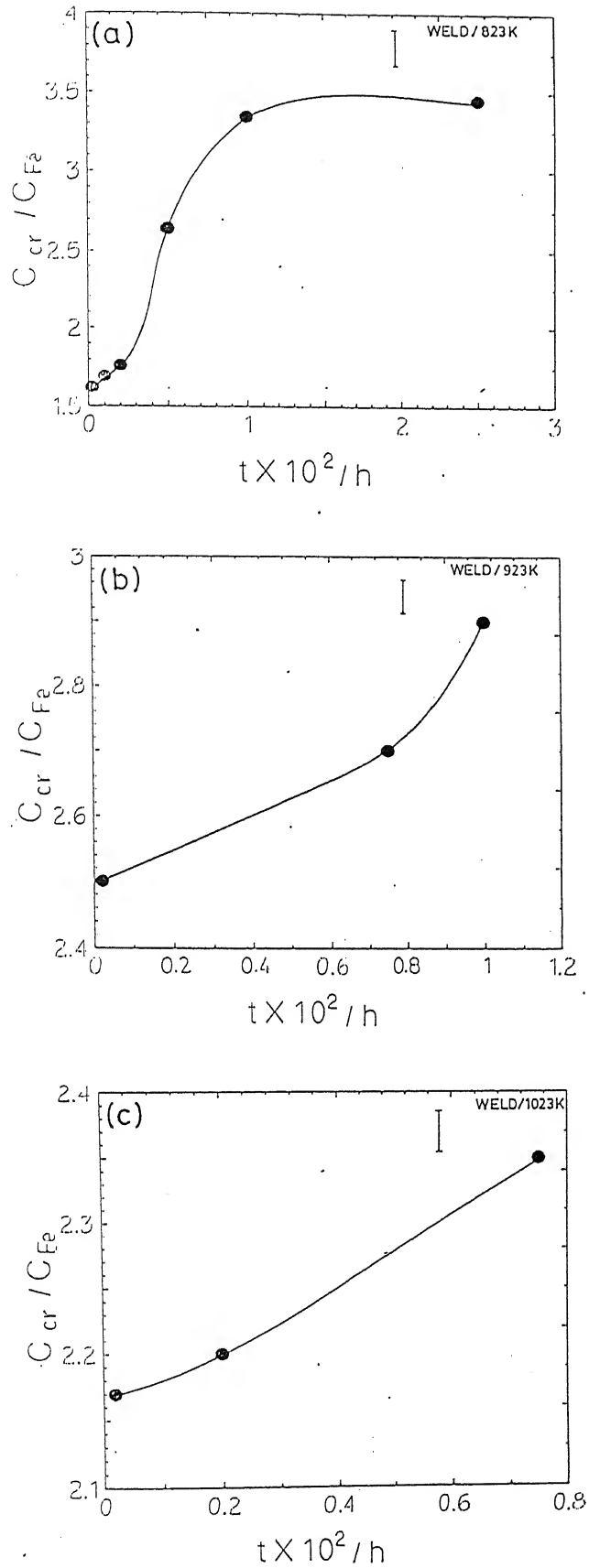
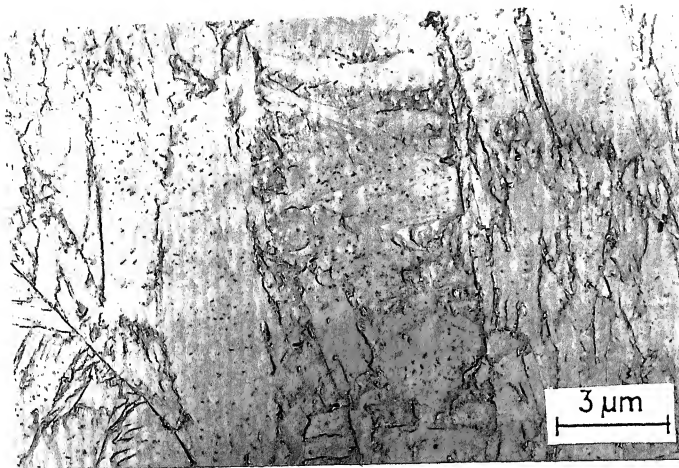
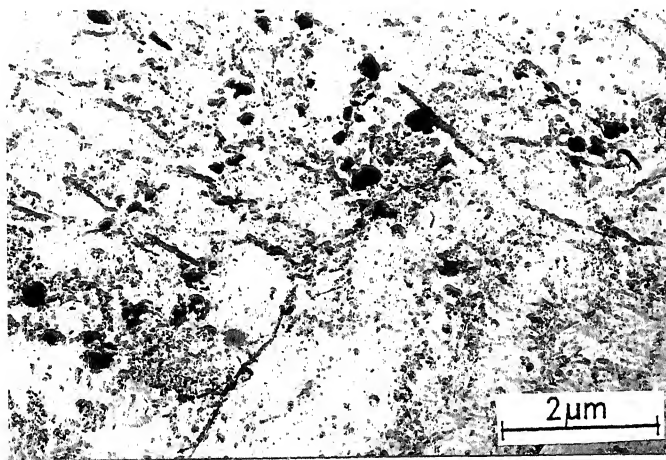


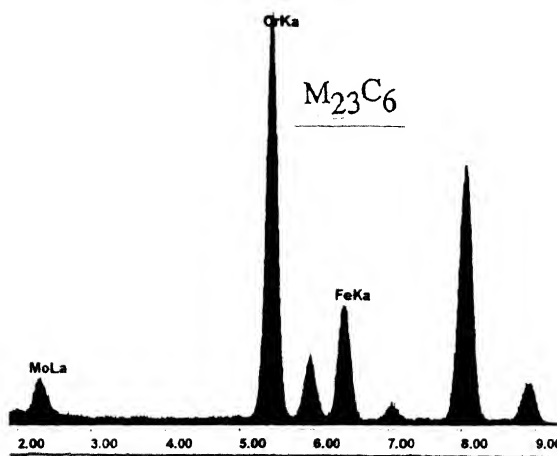
Figure 4.14 Variation in the ratio of concentration of chromium to iron (C_{Cr}/C_{Fe}) of $M_{23}C_6$ with ageing time, at different temperatures. (a) 823 K, (b) 923 K and (c) 1023 K. The region corresponds to the weld zone of 9Cr-1Mo weldment.



(a)



(b)



(c)

Figure 4.15 Evolution of secondary carbides in the HAZ region at 823 K. (a) 2 h, (b) Growth of carbides after 250 h and (c) EDAX spectrum of a typical $M_{23}C_6$, shown in (b).

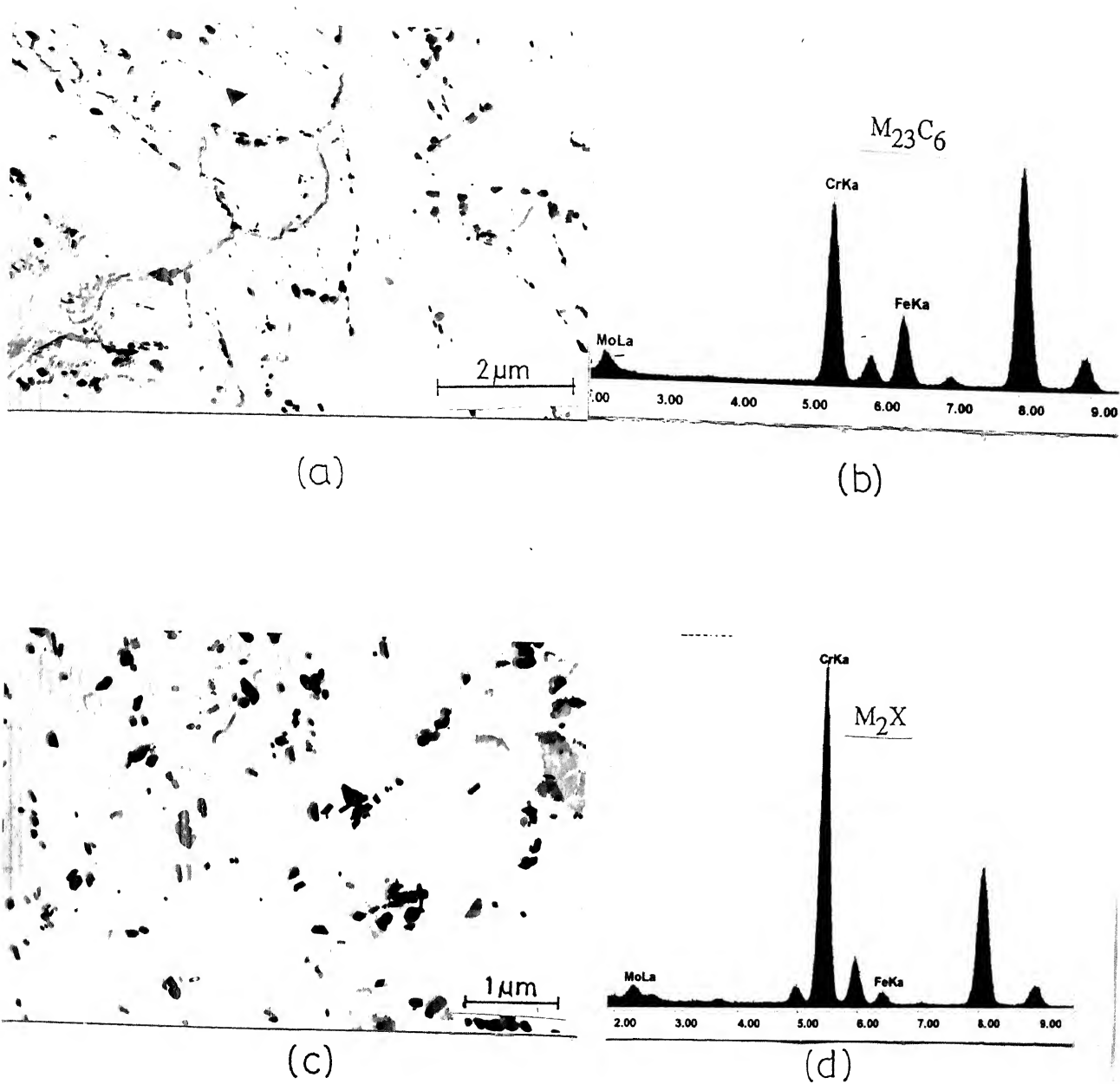


Figure 4.16 Evolution of secondary carbides in the HAZ region at 923 K. (a) 2 h, (b) typical EDAX spectrum of $M_{23}C_6$, shown in (a), (c) microstructure after ageing upto 100 h and (d) confirmation for the formation of Cr-rich M_2X after 100 h.

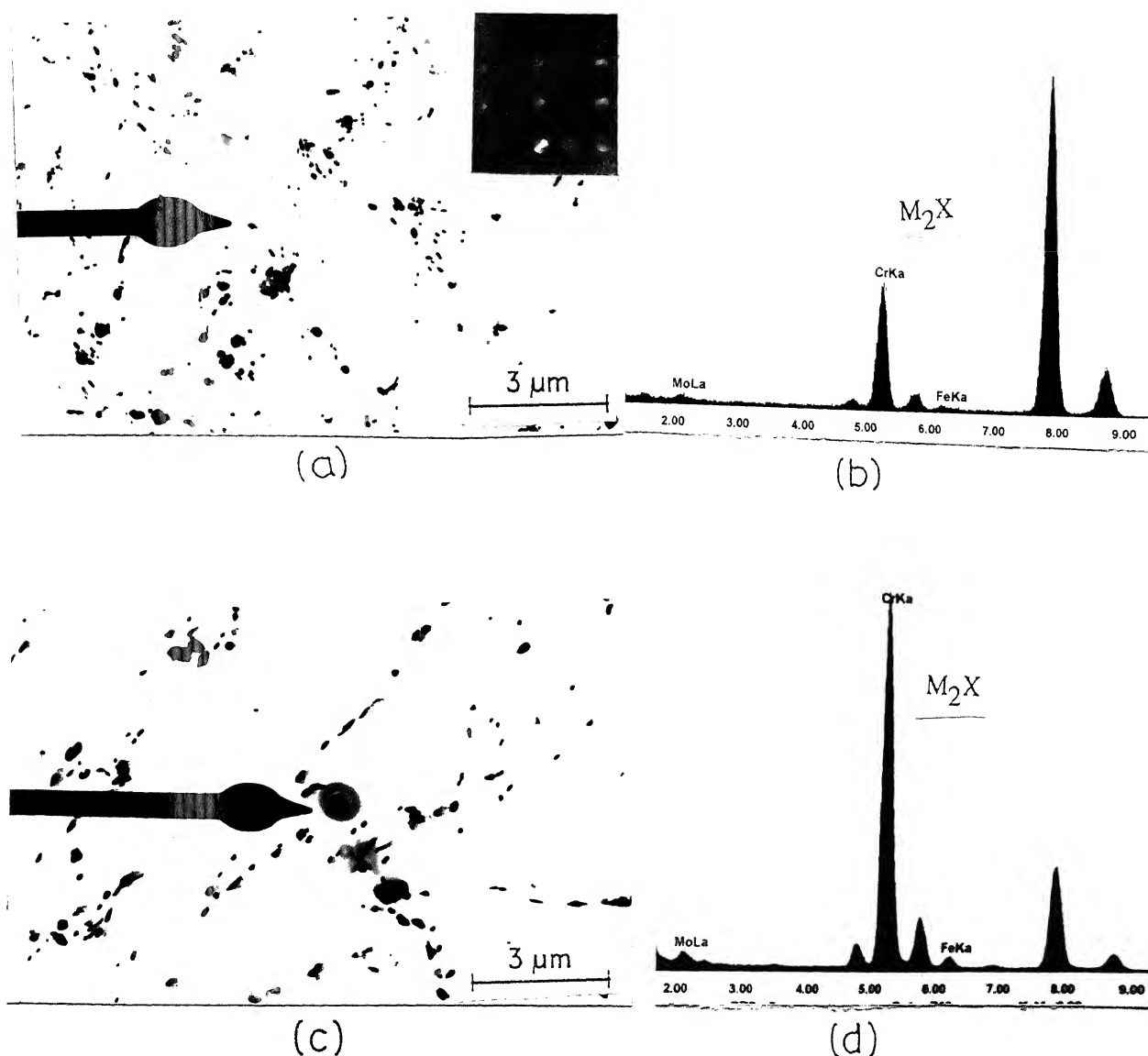


Figure 4.17 Evolution of secondary carbides in the HAZ region at 1023 K. (a) 2 h. Inset shows microdiffraction pattern of M_2X (arrow marked) along $\langle 220 \rangle$. (b) EDAX spectrum of same carbide. (c) Growth of carbides after ageing upto 100 h and (d) EDAX spectrum from the carbide arrow marked in (c), confirming the retention of Cr-rich M_2X even after 100 h.

Table IV.10

Microstructural parameters of carbides that evolve in the HAZ region at 823 K

Sl. No.	Ageing time	Number density			Dimensions		Area fraction	
		Total(N_f) $/\mu\text{m}^2$	Globular $/\mu\text{m}^2$	Acicular $/\mu\text{m}^2$	Globular(d) μm	Acicular(lxb) μm		
t							A_f	
h								
1	2	4	2	2	0.06	0.3	0.03	0.0018
2	10	15	0	15	0	0.07	0.01	0.0018
3	20	3	0	3	0	0.17	0.01	0.0018
4	75	10	0	10	0	0.12	0.02	0.002

Table IV.11

Microchemistry of carbides that evolve in the HAZ region at 823 K

Sl. No.	Ageing Time	Type of carbide	% in M of Metal Sublattice		
			Fe	Cr	Mo
	h			%	
1.	2	$M_{23}C_6$	34.9	56.62	8.48
2.	10	$M_{23}C_6$	34.3	58.1	7.98
3.	20	$M_{23}C_6$	33.3	58.6	7.5
4.	50	HAZ near weld. $M_{23}C_6$	25.1	66.2	8.7
5.	"	HAZ near weld. "	24.1	67.2	8.7
6.	"	B.M. "	12.9	69.1	16.3
7.	75	$M_{23}C_6$	7.3	77.9	14.8
8.	"	"	33.6	60.0	6.4
9.	100	$M_{23}C_6$	20.99	70.3	8.7
10.	250	$M_{23}C_6$	20.2	69.6	10.3
11.	500	$M_{23}C_6$	18.8	71.67	9.5
12.	"	"	6.1	76.5	17.5
13.	"	"	27.5	64.1	8.3

Table IV.12

Microstructural parameters of carbides that evolve in the HAZ region at 923 K

Sl. No.	Ageing time	Number density			Dimensions		Area fraction
	t	Total(N_f)	Globular	Acicular	Globular(d)	Acicular(lxb)	A_f
	h	$/\mu\text{m}^2$	$/\mu\text{m}^2$	$/\mu\text{m}^2$	μm	μm	
1	2	11	7	4	0.12	0.2	0.1
2	20	11	6	5	0.08	0.2	0.1
3	75	2	0	2	0.12	0.3	0.1
4	100	3	0	3	0.1	0.2	0.1
							0.0008
							0.0019
							0.0019
							0.0021

Table IV.13

Microchemistry of carbides that evolve in the HAZ region at 923 K

Sl. No.	Ageing Time h	Type of carbide	% in M of Metal Sublattice		
			Fe	Cr	Mo
				%	
1.	2	$M_{23}C_6$	27	64	9
2.	20	$M_{23}C_6$	26.5	65.08	8.4
3.	75	$M_{23}C_6$	26.27	64.86	8.88
4.	75	M_2X	16.64	75.82	7.54
5.	100	$M_{23}C_6$	23.5	67.7	8.8
6.	100	M_2X	2.85	92.77	4.4

****** In addition to general rapid precipitation at 1023 K (figure 4.17), the major difference is in the precipitation of M_2X . It is found that M_2X forms at much smaller times, i.e., 2 h. The relevant data are included in Tables IV.14 and IV.15.

4.4.5 Heat Affected Zone : Comparison of Microstructural Parameters and Microchemistry of Carbides

The microstructural parameters and microchemistry of carbides that evolve in the HAZ are compared, along the same lines as that for the weld zone in sections 4.4.2 and 4.4.3. A brief discussion on the comparison of these features is given below.

The microstructural parameters like number density (N_f), area fraction (A_f), diameter (d), length (l) and breadth (b) of carbides in HAZ are compared at various temperatures, for same ageing times. It is generally found that there is a significant increase in the dimensions of the globular and acicular carbides and the total area fraction A_f of carbides at higher temperatures as expected.

The microchemistry of $M_{23}C_6$ in HAZ shows variations with respect to ageing time and temperature, as shown in figure 4.18(a to c). The changes are identical to those discussed for the weld zone. Hence, no further discussion of the results is considered essential.

4.4.6 Heat Affected Zone : Sequence of Carbide Evolution

The general sequence of carbide evolution in the HAZ of the weldment is as

Table IV.14

Microstructural parameters of carbides that evolve in the HAZ region at 1023 K

Sl. No.	Ageing time	Number density		Dimensions		Area fraction		
		Total(N_f) $/\mu\text{m}^2$	Globular $/\mu\text{m}^2$	Acicular $/\mu\text{m}^2$	Globular(d) μm		Acicular(lxb) μm	
t	h						A_f	
1	2	3	1	2	0.14	0.3	0.1	0.00083
2	10	2	1	1	0.14	0.5	0.1	0.0013
3	20	2	1	1	0.14	0.4	0.1	0.0012
4	50	2	1	1	0.12	0.3	0.2	0.0013
5	100	2	1	1	0.3	0.4	0.1	0.0014

Table IV.15

Microchemistry of carbides that evolve in the HAZ region at 1023 K

Sl. No.	Ageing Time	Type of carbide	% in M of Metal Sublattice		
			Fe	Cr	Mo
			%		
h					
1.	2	M ₂₃ C ₆	30.05	62.27	7.68
2.	2	M ₂ X	3.48	90.93	5.59
3.	10	M ₂₃ C ₆	29.21	62.89	7.89
4.	10	M ₂ X	3.45	93.01	3.54
5.	20	M ₂₃ C ₆	27.79	63.49	8.7
6.	20	M ₂ X	2.17	94.34	3.51
7.	50	M ₂₃ C ₆	31.47	61.04	7.48
8.	50	M ₂ X	11.98	84.78	3.24
9.	75	M ₂₃ C ₆	27.79	65.33	6.89
10.	75	M ₂ X	1.1	96.58	2.31
11.	100	M ₂₃ C ₆	27.91	64.65	7.44
12.	100	M ₂ X	3.08	94.88	2.03

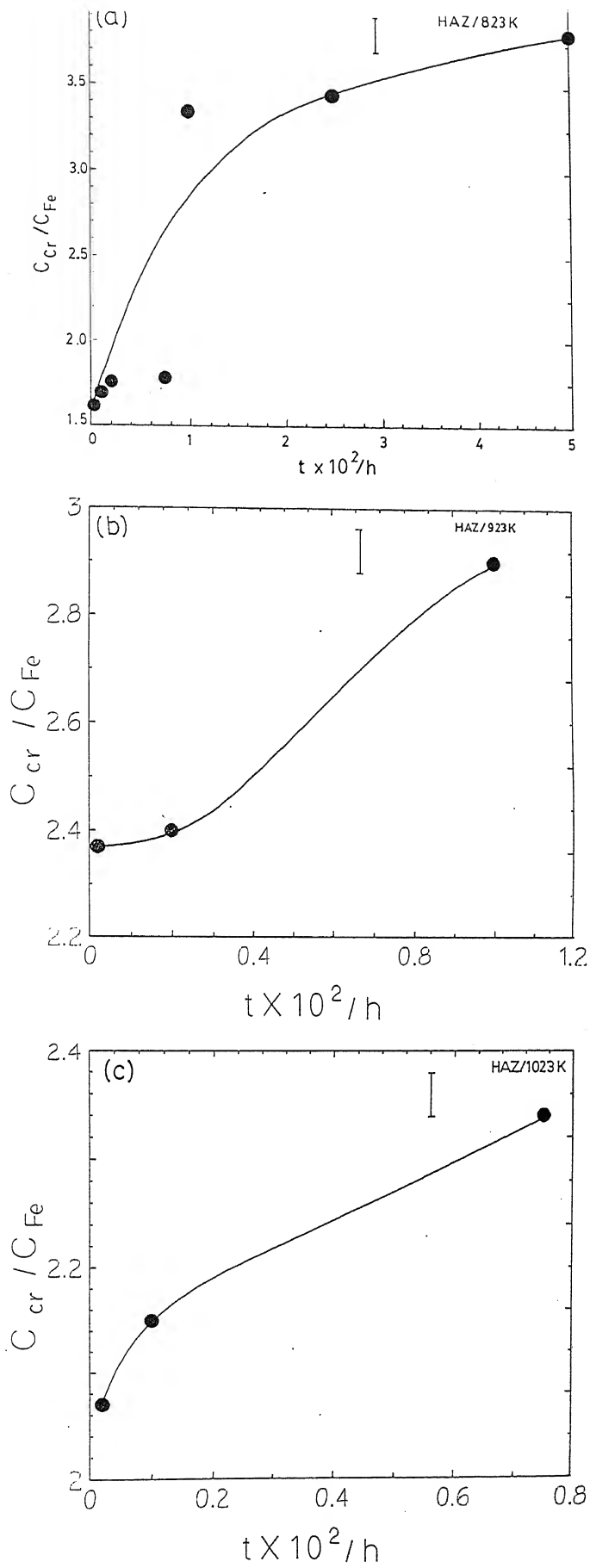
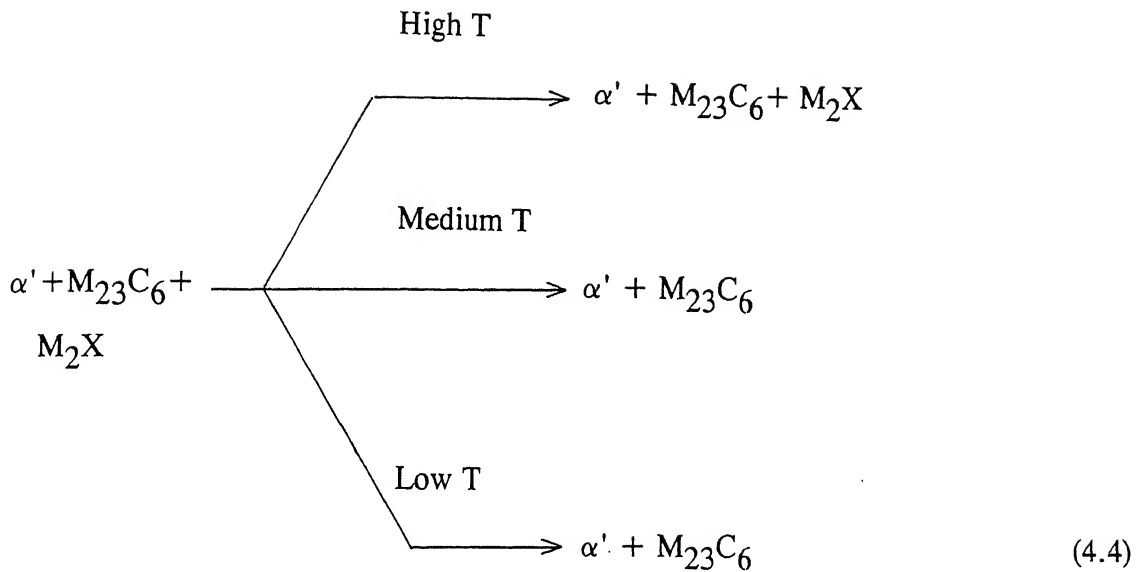


Figure 4.18 Variation in the ratio of concentration of chromium to iron (C_{Cr}/C_{Fe}) of $M_{23}C_6$ with ageing time, at different temperatures. (a) 823 K, (b) 923 K and (c) 1023 K. The region corresponds to the HAZ of 9Cr-1Mo weldment.

follows:



4.4.7 Microstructural Evolution of Base Metal at High Temperatures

The precipitation of carbides in the base metal was found to be comparable with those of the normalised and tempered wrought steel (13,14,18,21). Hence, no detailed discussion based on the data generated in the base metal is considered essential. However, the calculated composition of carbides, at the three different temperatures for various ageing times are reported in the context of phase evolution diagrams, discussed in the next section.

4.5 PHASE EVOLUTION DIAGRAMS

The precipitation behaviour of supersaturated ferrite (α^{ss}) is a manifestation of a number of synergistic factors (13). These factors are the difference in the initial concentration, affinity of the solutes to carbon, efficiency of various carbides in scavenging the matrix of its solutes and the consequent differences in the shift of phase stability of the local region. Despite the overall similarity in the sequence of

evolution of carbides, there is an extensive variation in the kinetics and chemistry of carbides from one region to another, (Tables IV.3 to IV.15), for a given treatment. Therefore, it was found essential to identify the basic parameter, in terms of which the carbide evolution of different regions of the weldment can be understood. A concept of 'phase evolution diagram' is introduced for this purpose, which is explained below.

4.5.1 Concept of Phase Evolution Diagram

Let us consider a simple binary system, with respect to its time evolution, ignoring the variations from one region to another, for the purpose of simplicity. Consider a binary MC alloy, in a hypothetical situation wherein a variety of metastable carbides evolve with time.

Figure 4.19a shows the typical phase diagram of a binary alloy, in which C_0 represents the initial composition of the alloy. It is seen from the figure that the alloy decomposes into two equilibrium phases, α and β of composition α_{eq} and β_{eq} , after infinite time at temperature, T . Consider the precipitation of two metastable phases X and Y. The dotted line in figure 4.19a shows the metastable solvus lines. The metastable phases, X of composition β_X and Y of composition β_Y are in coexistence with α of composition α_X and α_Y at time $t=t_1$ and t_2 respectively. The corresponding free-energy vs composition diagram is shown in figure 4.19b. It is clear from figure 4.19b that the driving force for the precipitation of X, Y and β at times t_1 , t_2 and t_3 is $-\Delta F_X$, $-\Delta F_Y$ and $-\Delta F_\beta$, corresponding to a reduction in solute concentration of parent matrix from C_0 to α_{eq} . The changes in the concentration of solute in the matrix consequent to precipitation of X, Y and β at time $t=t_1$, t_2 and t_α respectively, are shown in figure 4.19c. The composition of α at t_0 is given by C_0 . The interfacial composition of α co-existing with X at $t=t_1$ and Y at $t=t_2$ is α_X

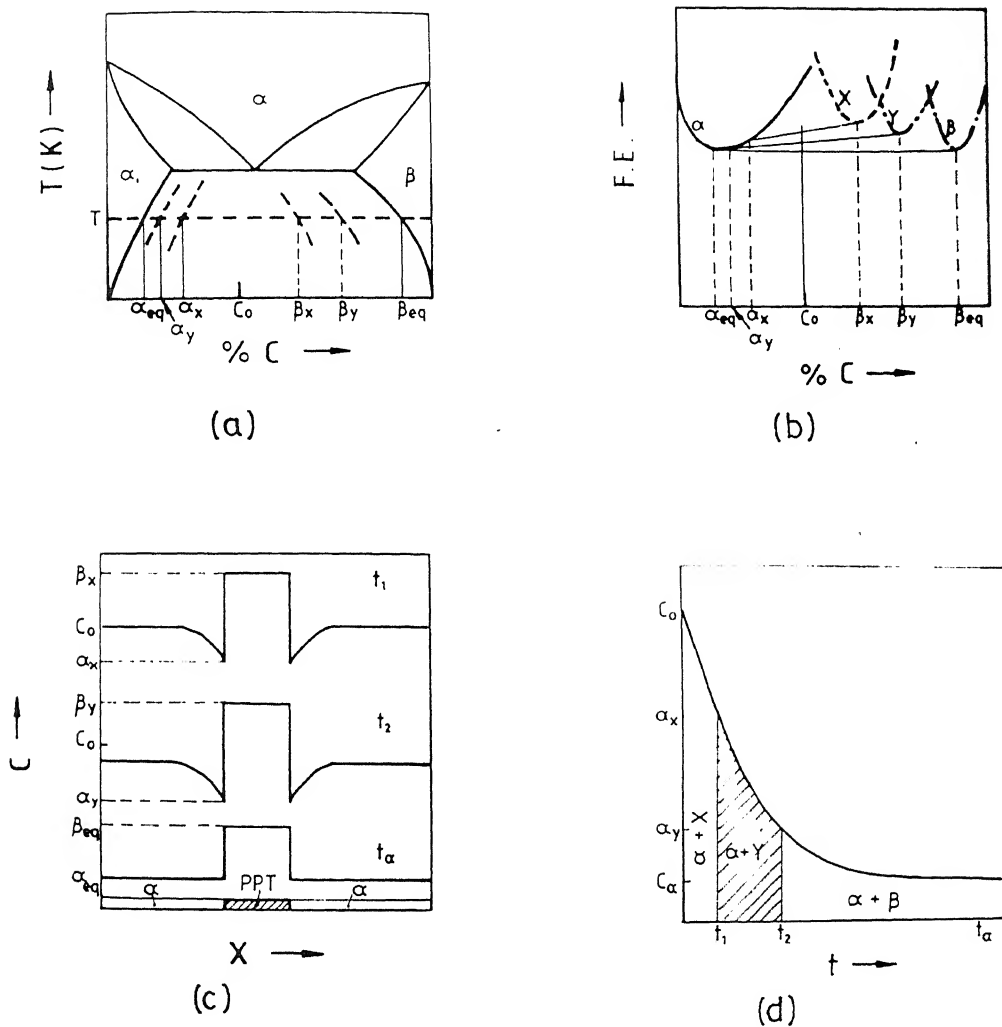


Figure 4.19 (a) Schematic of a M-C binary diagram. (b) Schematic free energy vs. composition diagram for the precipitation of metastable phases. X, Y and equilibrium β phases in the M-C alloy. (c) Schematic illustration of changes in the solute concentration of the parent matrix as a consequence of precipitation of X, Y and β phases and (d) Schematic phase evolution diagram for the M-C alloy.

and α_Y respectively. The values of α_X and α_Y are known to vary with respect to coherency of the precipitate (22). However, at distances far away, a very small, but perceptible reduction in composition of α is expected, as governed by the mass balance requirements. When equilibrium is reached after infinitely long time, composition of α reaches α_{eq} . Thus, composition of the α matrix, i.e., C_α changes gradually during the evolution of metastable states. This change along with the information regarding the range of C_α 's which coexist with different types of metastable phases can be utilised to construct the 'phase evolution diagram'. This is schematically shown for a hypothetical situation in figure 4.19d. This figure shows the variation of C_α with time and the phase fields for the different ranges of C_α . Figure 4.19d is called the 'phase evolution diagram', which depicts the variation of composition of solute in the matrix with time. The above arguments can be conveniently extended for the presence of more than a single metastable phase, taking into account the variations from region to region for a given treatment.

4.5.2 Applicability of Concept of Phase Evolution Diagrams for 9Cr-1Mo Weldment

In the concept of phase evolution diagram considered above, the alloy MC is considered as a homogeneous system, with no transfer of mass or solute atoms, either from the alloy to outside or from external sources to the alloy MC. While trying to apply this concept to the case of weldment, an additional precaution is essential. The structure and the local chemistry of the three different regions of the weldment are quite different. For example, the initial composition of the weldment, in the three regions (Table IV.16) shows that a composition difference of 0.03 for carbon is introduced over distances of the order of 3 mm. This introduces a steep concentration gradient. In addition, the composition of other solutes, like molybdenum and chromium, which have strong affinity for carbon, are also different (Table IV.16) in

Table IV.16

Composition of α -ferrite in the three regions of the
weldment of 9Cr-1Mo steel

Sl. No.	Region	Composition		
		Cr	Mo	C
			w/o	
1.	Weld	8.85	0.923	0.079
2.	HAZ	8.17	0.91	0.063
3.	Base Metal	8.076	0.91	0.053

the three regions of the weldment. A system with such gradients in composition of solutes would have differences in the activity of solutes in various regions, resulting in mass flow. Thus, it would be incorrect to propose a phase evolution diagram for each region assuming that each region is independent of the other. Prior to such an attempt, it is required to find out if there is significant mass flow from one region to another and apply appropriate corrections to account for this factor. Therefore, the following calculation was done to verify if the concept of phase evolution diagram can be extended to the case of weldment.

The distances through which carbon can diffuse were estimated using the following equations (23),

$$D = 0.02 \times \exp (-20,100 / R T) \quad (4.5)$$

$$x = 2\sqrt{(Dt)} \quad (4.6)$$

wherein D is the interdiffusion coefficient of carbon, R , the gas constant, T , the absolute temperature, x , the diffusion distance and t , the time.

The distances that carbon can diffuse in 2 h at 823 and 1023 K are around 0.5 and 1.8 mm respectively. In other words, the rate at which the carbon atoms migrate at these two temperatures is 4 and 150 $\mu\text{m}/\text{min}$. These values appear to be quite high, suggesting that diffusion of carbon from one region of the weldment to another cannot be ignored. However, instead of computing the absolute mobilities, if a gradient in carbon concentration can be superimposed, based on the actual values of composition of the three regions stated above, the true state of diffusion of carbon can be understood.

The composition of carbon $C_{(x,t)}$, at a distance x at time t , in a gradient of $(C_0 - C_x)$, is obtained using the equation(22),

$$C_{(x,t)} = C_0 + ((C_0 - C_x)/2)(1 + \operatorname{erf}(x/2\sqrt{Dt})) \quad (4.7)$$

Composition of carbon using the values of composition of carbon in weld and base metal, were calculated at 823 and 1023 K. It turns out that the composition at a distance of 1 μm is altered only by about 0.00008%, after 2 h even at 1023 K. This change is much smaller than the statistical accuracy of experimental determination of composition of α at various times at the three temperatures. Moreover, the width of the HAZ is very high, of the order of 3 to 4 mm. Therefore, it is reasonable to extend the concept of 'phase evolution diagram' to the three regions of the weldment.

4.5.3 Phase Evolution Diagrams of 9Cr-1Mo Weldment

The generation of 'phase evolution diagrams' based on laboratory experiments, requires the following information : (1) Variation of C_α with time and (2) the different ranges of C_α , for which α can coexist with either a typical metastable phase or a set of metastable phases. These requirements lead to the next problem, i.e., the determination of solute concentration of matrix, which is explained below. The equilibrium concentration of carbon in α -ferrite is expected to be 0.001 % (20). The original composition of carbon in α -ferrite of the steel in the three regions is in the range of 0.07 %. So, the composition of α for various ageing treatments, can at best vary only between these two values. These values clearly rule out the possibility of using any of the conventional techniques like the analytical electron microscopy - AEM or the parallel electron energy loss spectroscopy - PEELS, for the purpose of

Table IV.17

Stoichiometry and composition of the carbides at 823 K

Sl. No.	Ageing Time h	Stoichiometry of the carbide	Composition of the carbide (w/o)			
			Fe	Cr	Mo	C
(a) Weld Region						
1.	2	Fe ₁₂ Cr ₉ Mo ₂ C ₆	48.5	33	13	5.2
2.	2	Fe ₃ Cr ₁₇ Mo ₃ C ₆	12	61.5	21.5	5.15
3.	10	Fe ₁₈ Cr ₃ Mo ₂ C ₆	68.5	10.5	16	5.1
4.	20	Fe ₈ Cr ₁₃ Mo ₂ C ₆	31.7	51.2	11.8	5.3
5.	50	Fe _{4.3} Cr ₁₆ Mo _{2.7} C ₆	17.4	61.3	16.1	5.2
6.	75	Fe ₅ Cr ₁₅ Mo ₃ C ₆	19.6	56.3	18.9	5.1
7.	100	Fe ₅ Cr ₁₆ Mo ₂ C ₆	19	61	14	5.2
8.	250	Fe ₅ Cr ₁₆ Mo ₂ C ₆	18.6	60.4	15.8	5.2
9.	500	Fe ₃ Cr ₁₈ Mo ₂ C ₆	11	67	17	5.15
(b) HAZ Region						
1.	2	Fe ₈ Cr ₁₃ Mo ₂ C ₆	32	49	14	5.2
2.	10	Fe ₈ Cr _{13.5} Mo _{1.5} C ₆	31.6	50.5	13	5.25
3.	20	Fe _{7.8} Cr _{13.5} Mo _{1.7} C ₆	31	51	12	5.3
4.	50	Fe ₆ Cr ₁₅ Mo ₂ C ₆	23	57.6	14	5.2
5.	75	Fe _{7.7} Cr _{13.8} Mo _{1.5} C ₆	31.5	52.8	10.4	5.3
6.	100	Fe ₅ Cr ₁₆ Mo ₂ C ₆	19.5	61.3	13.9	5.2
7.	250	Fe _{4.6} Cr ₁₆ Mo _{2.4} C ₆	18.5	59.9	16.4	5.2
8.	500	Fe _{4.3} Cr _{16.5} Mo _{2.2} C ₆	17.4	62.2	15.2	5.2

Table IV.17 contd...

Sl. No.	Ageing Time h	Stoichiometry of the carbide	Composition of the carbide (w/o)			
			Fe	Cr	Mo	C
(c) Base Metal Region						
1.	2	Fe ₉ Cr ₁₃ Mo ₁ C ₆	37	48.4	9.4	5.3
2.	10	Fe ₈ Cr ₁₃ Mo ₂ C ₆	32.2	50.6	11.9	5.3
3.	20	Fe ₈ Cr ₁₃ Mo ₂ C ₆	32.3	50.6	11.8	5.3
4.	50	Fe ₇ Cr ₁₄ Mo ₂ C ₆	27.6	54.1	13.0	5.2
5.	75	Fe ₇ Cr ₁₄ Mo ₂ C ₆	28.1	54.5	12.1	5.3
6.	100	Fe ₈ Cr ₁₃ Mo ₂ C ₆	31.1	50.8	12.9	5.3
7.	250	Fe ₉ Cr ₁₃ Mo ₁ C ₆	36.3	48.3	10.1	5.3
8.	500	Fe _{7.4} Cr ₁₄ Mo _{1.6} C ₆	31.1	52.1	11.5	5.3

Table IV.18

Stoichiometry and composition of the carbides at 923 K

Sl. No.	Ageing Time h	Stoichiometry of the carbide	Composition of the carbide (w/o)			
			Fe	Cr	Mo	C
(a) Weld Region						
1.	2	Fe _{6.1} Cr ₁₅ Mo _{1.9} C ₆	24.72	57.08	12.95	5.26
2.	20	Fe _{5.5} Cr _{15.5} Mo _{2.1} C ₆	21.95	58.45	14.37	5.23
3.	75	Fe _{5.7} Cr _{15.4} Mo _{1.9} C ₆	22.91	58.17	13.67	5.24
4.	100	Fe _{5.3} Cr _{15.5} Mo _{2.2} C ₆	21.33	58.47	14.99	5.21
(b) HAZ Region						
1.	2	Fe _{6.2} Cr _{14.7} Mo _{2.1} C ₆	24.93	55.43	14.43	5.22
2.	20	Fe _{6.1} Cr _{14.97} Mo _{1.9} C ₆	24.57	56.67	13.53	5.24
3.	75	Fe _{6.1} Cr _{14.9} Mo ₂ C ₆	24.26	56.29	14.21	5.23
4.	100	Fe _{5.4} Cr _{15.6} Mo ₂ C ₆	21.7	58.89	14.13	5.24
(c) Base Metal Region						
1.	2	Fe _{7.8} Cr _{13.5} Mo _{1.7} C ₆	31.59	51.24	11.91	5.26
2.	20	Fe ₇ Cr _{14.2} Mo _{1.8} C ₆	28.44	53.76	12.55	5.25
3.	75	Fe _{7.4} Cr _{13.8} Mo _{1.8} C ₆	29.82	52.32	12.6	5.25
4.	100	Fe ₇ Cr _{14.2} Mo _{1.8} C ₆	28.1	53.94	12.68	5.25

Table IV.19

Stoichiometry and composition of the carbides at 1023 K

Sl. No.	Ageing Time h	Stoichiometry of the carbide	Composition of the carbide (w/o)			
			Fe	Cr	Mo	C
(a) Weld Region						
1.	2	Fe _{6.7} Cr _{14.6} Mo _{1.7} C ₆	27.24	55.51	11.97	5.28
2.	10	Fe _{6.6} Cr _{14.7} Mo _{1.7} C ₆	26.9	56.1	11.8	5.3
3.	50	Fe _{6.9} Cr _{14.5} Mo _{1.6} C ₆	28.11	55.29	11.3	5.29
4.	75	Fe _{6.3} Cr _{14.9} Mo _{1.8} C ₆	25.6	56.6	12.59	5.26
5.	250	Fe _{5.7} Cr _{15.6} Mo _{1.7} C ₆	23.07	59.72	11.92	5.29
(b) HAZ Region						
1.	2	Fe _{6.9} Cr _{14.3} Mo _{1.8} C ₆	27.95	54.41	12.37	5.26
2.	10	Fe _{6.7} Cr _{14.5} Mo _{1.8} C ₆	27.13	54.89	12.7	5.25
3.	20	Fe _{6.4} Cr _{14.6} Mo ₂ C ₆	25.69	55.12	13.96	5.23
4.	50	Fe _{7.2} Cr ₁₄ Mo _{1.7} C ₆	29.29	53.79	12.07	5.26
5.	75	Fe _{6.4} Cr ₁₅ Mo _{1.6} C ₆	26.03	57.5	11.18	5.29
6.	100	Fe _{6.4} Cr _{14.9} Mo _{1.7} C ₆	26.03	56.66	12.03	5.28
(c) Base Metal Region						
1.	2	Fe ₇ Cr _{14.2} Mo _{1.8} C ₆	28.37	53.98	12.39	5.26
2.	10	Fe _{6.6} Cr _{14.5} Mo _{1.8} C ₆	26.8	55.11	12.79	5.25
3.	20	Fe _{6.8} Cr _{14.4} Mo _{1.8} C ₆	27.35	54.67	12.73	5.25
4.	50	Fe _{6.2} Cr ₁₅ Mo _{1.7} C ₆	25.33	57.17	12.23	5.27

- * The microchemistry of the carbides show more scatter in the weld regions than in the base metal. This could be due to the different stages of evolution of carbides in the weld region than in the base metal. It has been shown that the weld zone consists of microscopic regions, which have experienced thermal cycles which are significantly different from adjacent regions. The exposure of such weldment with heterogeneous structures, to elevated temperatures, results in a wide spectrum of carbides, with varying microchemistry.

Based on the composition of different types of carbides and their respective area fractions, the composition of the α matrix was calculated using the mass balance equation

$$C_0 = C_\alpha A_\alpha + \sum C^n A^n \quad (4.8)$$

$$n = M_2X, M_{23}C_6, \text{ etc.}$$

wherein C_0 is the initial concentration of carbon in α , C_α is the concentration of carbon in α of area fraction A_α at a particular time, C^n is the concentration of carbon in the n^{th} carbide of area fraction A^n at the same time. The results of these calculations, i.e., the concentration of individual elements in the α -matrix for various regions, are tabulated in Tables IV.20 to IV.22.

Having determined the concentration of solutes in the α -matrix, the next step is to depict the variations of these values with time along with the corresponding metastable phase fields in the 'phase evolution diagrams'.

The representation of the evolution of various metastable phases in binary system has been fairly easy (figure 4.19) and straightforward, due to the following

Table IV.20
Composition of the α matrix at 823 K

Sl. No.	Ageing Time (h)	Composition of the α -ferrite (w/o)		
		Cr	Mo	C
(a) Weld Region				
1.	0	8.85	.923	.079
2.	2	8.82	.91	.073
3.	10	8.85	.89	.068
4.	20	8.74	.894	.065
5.	50	8.696	.88	.064
6.	75	8.71	.87	.064
7.	100	8.675	.879	.062
8.	250	8.11	.71	.063
(b) HAZ Region				
1.	0	8.17	.91	.063
2.	2	8.095	.887	.054
3.	10	8.096	.889	.054
4.	20	8.09	.889	.0536
5.	50	8.08	.89	.054
6.	75	8.054	.87	.053

Table IV.21Composition of the α matrix at 923 K

Sl. No.	Ageing Time (h)	Composition of the α -ferrite. (w/o)		
		Cr	Mo	C
(a) Weld Region				
1.	0	8.85	0.923	.079
2.	2	8.78	.906	.0717
3.	20	8.76	.899	.07
4.	75	8.75	.898	.069
5.	100	8.74	.89	.068
(b) HAZ Region				
1.	0	8.17	0.91	.063
2.	2	8.13	.899	.0586
3.	20	8.07	.884	.053
4.	75	8.08	.885	.053
5.	100	8.07	.882	.052

Table IV.22

Composition of the α matrix at 1023 K

Sl. No.	Ageing Time (h)	Composition of the α -ferrite. (w/o)		
		Cr	Mo	C
(a) Weld Region				
1.	0	8.85	.923	.079
2.	2	8.79	.91	.072
3.	10	8.81	.91	.074
4.	20	8.72	.89	.064
5.	50	8.715	.89	.069
6.	75	8.72	.89	.065
7.	250	8.695	.889	.063
(b) HAZ Region				
1.	0	8.17	.91	0.063
2.	2	8.13	.9	.0586
3.	10	8.11	.895	.0561
4.	20	8.113	.896	.0566
5.	50	8.11	.896	.056
6.	75	8.12	.896	.057
7.	100	8.1	.894	.0557

reason. The variation of the end compositions of the tie lines between the co-existing phases could be directly shown on the phase diagram. Such a representation in a multi-component system is difficult due to the reasons given below.

- 1) In addition to redistribution of carbon between coexisting phases, the substitutional solute elements also get partitioned, depending on their partition coefficients (25).
- 2) The solubility of carbon in α -ferrite, is a function of concentration of other substitutional solutes. Therefore, the driving force, which is proportional to the supersaturation of carbon is influenced by the changes in the concentration of substitutional solute elements.
- 3) For the sake of simplicity, the procedure that is adopted in the present study neglects the presence of steep solute gradients near carbide-matrix interface and soft impingement effects caused by overlapping concentration profiles of adjacent carbides. This assumption is reasonable due to the low volume fraction of carbides and the consequent high values of the distance between adjacent particles.

The reason for the choice of 'concentration of carbon' as an index for the generation of PED's is as follows: the primary thermodynamic driving force for the evolution of different metastable states is the relief of supersaturation of carbon in α -ferrite. The selection of such a thermodynamic criterion needs to be distinguished from the conventional kinetic criterion wherein the diffusion of the slowest diffusing species is the rate limiting factor for the reaction to proceed. The

typical diffusion distances for C, Cr and Mo at 1023 K for 1000 h are about 4, 1.1×10^{-3} and 1.8×10^{-3} cm respectively. Based on these values, it can be seen that carbon, being the fastest element to diffuse, does not play a significant role in deciding the kinetics of carbide precipitation reaction. However, in the present studies, the main concern is the stability of various carbides. Hence, a thermodynamic criterion rather than a kinetic one is considered to be more appropriate.

The phase evolution diagrams, depicting the variation of carbon content of α -ferrite in different regions of 9Cr-1Mo weldment as a function of time are shown in figures 4.20 and 4.21. Figure 4.20 corresponds to that of weld region at the three temperatures of interest. While, figure 4.21 corresponds to the same for HAZ. It is seen that the concentration of carbon in α -ferrite decreases with ageing time. The dashed lines in figures.4.20b and 4.21b represent the boundary between the two types of phase fields. There is a high degree of supersaturation remaining in the unprecipitated α -ferrite matrix, at 823 K than 1023 K. The higher saturation value of carbon content at 923 K is due to the lesser ageing time of 100 h. Though the saturation value of carbon content in the HAZ (figure 4.21) appears to be lower than that of the weld region, it is only due to the lower value of carbon content of the HAZ region prior to ageing, compared to that of weld region. The reduction in the amount of substitutional elements is not significant, despite a steep reduction in the carbon content. This could be explained based on the low amount of substitutional elements required to maintain the stoichiometry of $M_{23}C_6$ and the low amount of carbides (A_p). The low amount of carbides, in turn, is due to the low carbon content of the weldment. The phase fields superimposed in the PED's show that M_2X forms at 1023 K from as short ageing times as 2 h, whereas at 923 K it forms only after 75 h while at 823 K it does not form at all.

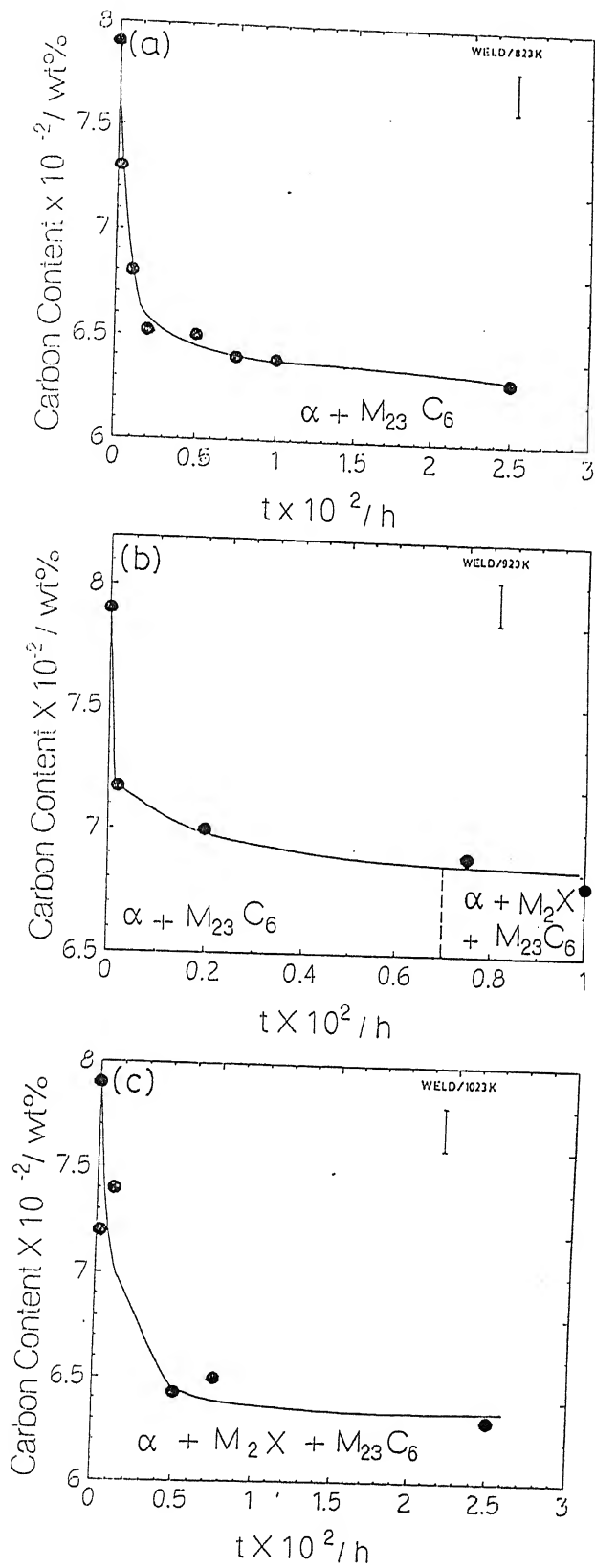


Figure 4.20 Phase evolution diagrams for the weld regions at different temperatures. Variation of concentration of carbon in α -ferrite with ageing time at (a) 823 K, (b) 923 K and (c) 1023 K.

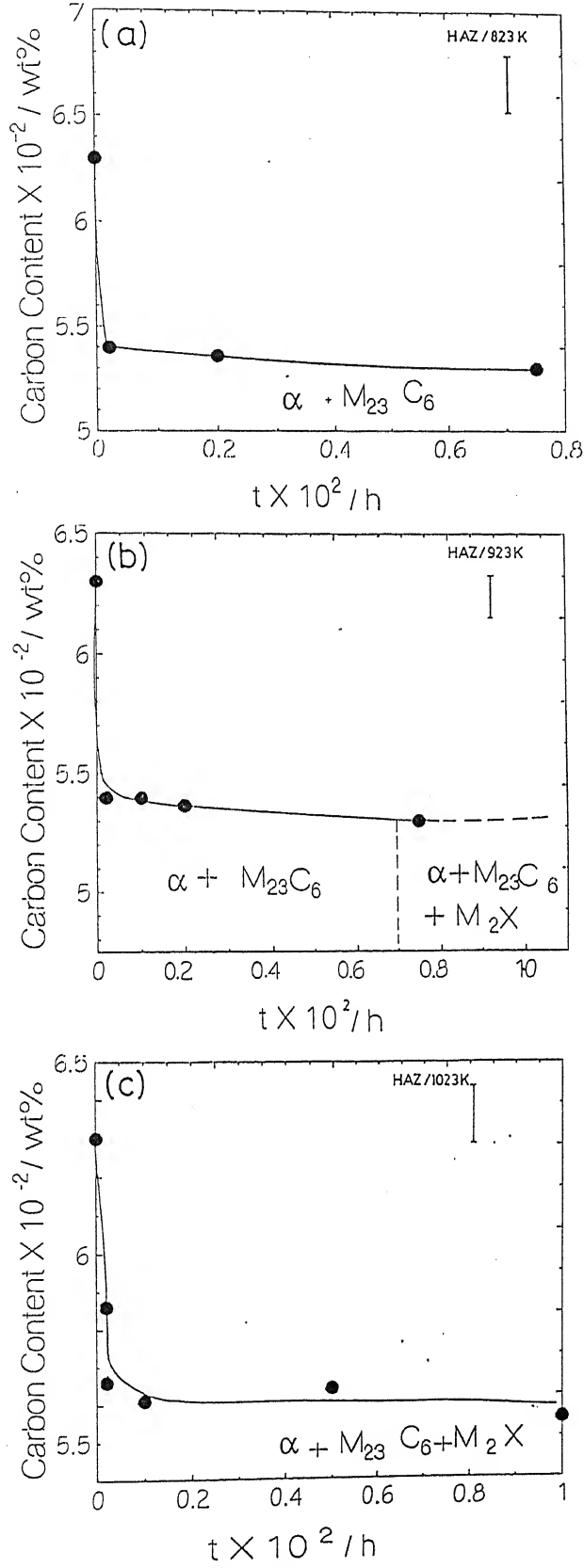


Figure 4.21 Phase evolution diagrams for the HAZ at different temperatures. Variation of concentration of carbon in α -ferrite with ageing time at (a) 823 K, (b) 923 K and (c) 1023 K.

4.5.4 Usefulness of Phase Evolution Diagrams

The 'phase evolution diagrams' generated for various regions of the weldment, offer information regarding the types of metastable carbides that co-exist with α -ferrite for various ageing times, in addition to the changes in the composition of α -ferrite. The type of secondary carbide is a fingerprint of the temperature of exposure and the carbon content of α is characteristic of time of exposure. It is seen in the phase evolution diagrams that the carbon content can be an index of exposure time, only at shorter ageing time. At longer times, carbon content of α reaches saturation and hence, cannot be used effectively as an index for exposure time. However, it may be noted that the present studies have only demonstrated the concept, applicability and the use of phase evolution diagrams, based on accelerated ageing times at temperatures much higher than the operating temperature. It is expected that such a diagram at the operating temperature of around 720 K, would enable the useful application of estimating the exposure time. This requires the identification of the metastable phase fields of different carbides and the estimation of solute concentration of α -ferrite, at the operating temperature. This diagram would help in the determination of the past thermal history and prediction of microstructural evolution in future, in a steel which has been exposed to a particular temperature for an unknown period of time. Such a situation could arise in commercial practice, wherein it becomes difficult to identify the exact details of the thermal cycles experienced by the weldment during service.

The applicability of phase evolution diagram becomes more significant in the light of the range of methods available for the determination of solute concentration of α -ferrite. The concentration of ferrite can be determined either by

chemical analysis, after dissolving the carbides or by estimation of chemical composition of the carbides using microanalytical techniques with extraction replica methods. The latter procedure is specially suitable in situations wherein the component cannot be subjected to destructive methods of analysis.

4.6.SUMMARY

- ** Microstructural modification of heterogeneous structure of weldment of 9Cr-1Mo steel at high temperatures has been studied in detail.
- ** Study of tempering kinetics of the weld region shows that the activation energy for the tempering process is around 0.63 eV. This value compares very well with the activation energy of 0.8 eV for migration of carbon in α -ferrite. Hence, it can be concluded that the migration of interstitial carbon is the rate limiting step, for the tempering process.
- ** Sequence of evolution, microstructural parameters and the variation in the microchemistry of carbides evolved during high temperature exposures have been studied in detail. The variation in microchemistry of $M_{23}C_6$ with temperature and time has been understood in terms of reduction in the total free energy of the system, due to relief of supersaturation of carbon.

** Recognising the need for a basic parameter to understand the evolution of carbides in the case of weldments, a new concept of phase evolution diagram has been proposed. It has been shown that the complex microstructures of the weldments require distinction between the three regions and accordingly, adapt the phase evolution diagram. Phase evolution diagrams have been generated for the weld and HAZ regions of weldments of 9Cr-1Mo steel, at three temperatures. The application of these diagrams to predict the microstructural evolution has been demonstrated.

REFERENCES

1. M.K. Brooker, V.K. Sikka and B.L.P. Booker, Proc. Int. Conf. on "*Production, Fabrication, Properties and Applications of Ferritic Steels for High Temperature Applications*", Ed. Ashok Khare, ASM, Metals Park, Ohio (1982), p.257
2. S.J. Sanderson, *ibid*, p.85
3. J. Orr, F.R. Beckitt, A. Met and G.D. Fawkes, in Proc. Int. Conf. on "*Ferritic Steels for Fast Reactor Steam Generators*", Ed. S.F. Pugh and L.A. Little, BNES, London (1978), p.91
4. N. Gope, T. Mukherjee and D.S. Sarma, *Mater. Trans. JIM* 33 (1992) 110
5. J.M. Titchmarsh, *Harwell Report AERE-R 9661* (1979)
6. R.L. Klueh and A.M. Nasreldin, *Metall. Trans.* 18A (1987) 1279
7. J.M. Titchmarsh, Martin Wall and B.C. Edwards, Proc. Workshop on "*Analytical Electron Microscopy*", Ed. D.B. Williams and D.C. Joy, Pennsylvania (1984), p.247
8. S.J. Sanderson, Proc. Int. Conf. on "*Ferritic Steels for Fast Reactor Steam Generators*", Ed. S.F. Pugh and E.A. Little, BNES, London (1978), p.120
9. P. Billiard, J.R. Donati, D. Guttman, S. Licheron and J.C. Van Duysen, Proc. Conf. on "*Ferritic Alloys for use in Nuclear Energy Technologies*", Ed. J.W. Davis and D.J. Michel, TMS-AIME, Pennsylvania (1984), p.425

10. J.J. Kai and G.L. Kulcinski, *Scripta Metall.* 23 (1989) 1151
11. R.L. Klueh and P.J. Maziasz, *J. Nucl. Mater.* 155 (1988) 602
12. F. Abe, H. Araki, T. Noda and M. Okada, *J. Nucl. Mater.* 155 (1988) 656
13. S. Saroja, P. Parameswaran, M. Vijayalakshmi and V.S. Raghunathan, *Acta Metall. Mater.* 43,8 (1995) 2985
14. S. Saroja, M. Vijayalakshmi and V.S. Raghunathan, *J. Mater. Sci.* 27 (1992) 2389
15. F.B. Pickering and A.D. Vassiliou, *Metals Technol.* (1980) 409
16. Shaju K. Albert, Ph.D. Thesis submitted to Indian Institute of Technology, Mumbai (1996)
17. J. Nutting, Proc. Topical Conf. on "*Ferritic Alloys for use in Nuclear Energy Technologies*", Ed. J.W. Davis and D.J. Michel, TMS-AIME, Pennsylvania (1984), p.3
18. S. Saroja, M. Vijayalakshmi and V.S. Raghunathan, *Mater. Trans. JIM*, 34 (1993) 901
19. B.A. Senior, F.W. Noble and B.L. Eyre, *Acta Metall.* 34 (1976) 1321

20. W.D. Forgeng and W.D. Forgeng Jr., *Metals Handbook* 8, ASM, Metals Park, Ohio (1973), p.402
21. S. Saroja, M. Vijayalakshmi and V.S. Raghunathan, *Trans. Indian Inst. Metals* 48,3 (1995) 271
22. A.D. Romig Jr., *Bull. Alloy Phase Diagram* 8 (1987) 308
23. J. Burke, "*The Kinetics of Phase Transformations in Metals*", Pergamon Press, 1965, Chapter 3, p.61
24. D.B. Williams, *Practical Analytical Electron Microscopy in Materials Science* (Philips Electron Optics Publishing) Mahwah, 1984
25. S. Saroja, M. Vijayalakshmi and V.S. Raghunathan, *Mater. Sci. and Engg. A* 154 (1992) 59

CHAPTER 5

STUDY OF LATTICE DISORDER IN ION IRRADIATED CRYSTALS USING CONVERGENT BEAM ELECTRON DIFFRACTION

5.1 INTRODUCTION

The ferritics are chosen to be the candidate materials for core component applications in high power fast breeder reactors, due to their exceptionally high void swelling resistance (1-5). The conventional materials used in nuclear industry like the austenitics, have very poor void swelling resistance (3,6), as can be seen in figure 5.1. While the percentage of swelling at 813 K for a fluence level of 1.5×10^{23} neutrons/cm², is around 8% for modified austenitics, the same for ferritics is negligibly small, i.e., < 1%. This can be attributed to major differences in some of the basic properties of bcc α - ferrite and fcc γ - austenite (7-10). These include the binding energy between vacancy and interstitial, mobility of defects, relaxation volume and the interaction between dislocation and solute atoms. Another relevant requirement of candidate materials for fast reactors is their excellent high temperature mechanical properties. The ferritic steels are found to be acceptable for commercial applications, with respect to their high temperature mechanical properties. Of the various advantages, resistance to void swelling of the ferritics is the outweighing factor, which makes them the most suitable material for fast reactor applications (1-5,11). The conventional structural materials for nuclear application are the austenitics of different

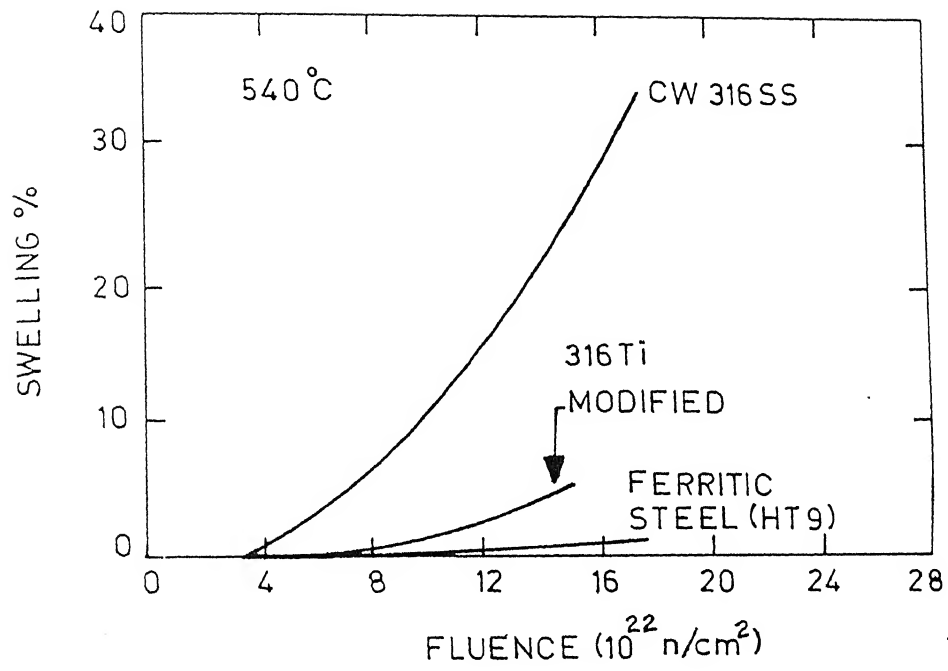


Figure 5.1 Variation of percentage of void swelling with fluence for different nuclear materials (Ref. 3).

types. Though the austenitics have excellent high temperature mechanical properties, their low void swelling resistance renders them unsuitable for high power fast reactor applications (11-13). However, one of the major shortcomings of the ferritics is their susceptibility to different types of embrittlement, which needs to be overcome if they have to emerge as alternate materials for fast reactor applications.

Extensive research on the behaviour of ferritic steels in irradiation environment has been carried out in the last two decades (21-27). The data on void swelling behaviour has been generated using irradiations with neutrons in nuclear reactors and ions in accelerators (28-30). Extensive data on void swelling behaviour are available, for dose levels upto 80 dpa during irradiations in reactor. The mechanisms of evolution of defect clusters (31,32), the role of matrix dislocations/interfaces (33-35) and the type of dislocation loops (36) have all been well established. Almost all these studies pertain to the parent α - ferrite matrix, role of ferrite/matrix interfaces and irradiation induced precipitation of carbides like M_6C , σ , etc. There are only few studies concerning the effect of irradiation on the carbides (37). The reason could be due to their low volume fractions and the difficulty in observing the irradiation effects in such small amount of carbides. This problem is overcome in the present study by extracting the carbides in carbon extraction replica and then subjecting the carbides to ion irradiation. The merits and demerits of such an approach is discussed later.

Most of the earlier studies use transmission electron microscopy (TEM) quite extensively. Hence, these studies pertained to only those stages for which TEM could be applied, like the formation of two or three-dimensional clusters. Study of initial stages of defects, i.e., prior to the agglomeration of isolated defects into clusters was beyond the scope of transmission electron microscopy, so far. Therefore, information about the early stages of defect evolution was obtained only by resorting to bulk measurements like X-ray diffraction (38,39), positron annihilation spectroscopy (40,41)

and dilatometry (42). However, these techniques cannot be applied for the study of defects in microscopic volumes, like in the case of ion irradiation. It is possible to overcome this difficulty by the use of more advanced techniques recently developed in transmission electron microscopy.

The field of transmission electron microscopy has progressed considerably in recent years. Presently newer and more powerful techniques like Atom Location by Chemical Analysis (ALCHEMI) (43-45), Z-contrast microscopy (46,47), Convergent Beam Electron Diffraction (CBED) (48-50) etc. have been developed. Hence, it was found worthwhile to explore the possibility of applying these developments of electron microscopy for the study of the initial stages of evolution of defects. CBED was chosen for this purpose, since this technique is very sensitive to lattice defects.

Though CBED has been used in many types of studies like determination of symmetry (50-52), unit cell dimensions (53), misorientation across interfaces (54) and nature of defects (54), like dislocations, stacking faults, twin boundary etc., its application to point defects has not been attempted so far. It is expected that there would be recognisable changes in CBED patterns with increase in point defect density, since the CBED patterns are sensitive to strain around defects.

The present chapter, therefore describes our attempts to investigate if CBED can be used successfully for the study of isolated point defects. The system chosen is the weld region of weldments of 9Cr-1Mo steel. The process chosen to introduce point defects is ion irradiation. The main reason for this choice is that controlled concentration of point defects can be introduced during ion irradiation. Initially, the relevant features of CBED patterns of the two major crystals - α -ferrite and $M_{23}C_6$, prior to irradiation are discussed. The changes in these patterns during ion irradiation with two types of incident ions, argon and helium of different incident energies, are discussed in the

subsequent sections. The effect of post-irradiation annealing, studied using in-situ hot stage electron microscopy is presented in the third section.

Identification of the nature of disorder that is responsible for the observed changes in CBED patterns required comparison of experimental results with computed CBED patterns. Therefore, similar studies were carried out in a simple, binary system, an Al-14 at/o Mn alloy. The basic reason for the choice of this system is that computation of CBED patterns could be carried out without any loss of accuracy of description of the crystal. These studies suggested that the changes in CBED patterns were found to originate from the static displacement disorder caused by point defects introduced during ion irradiation, which is discussed in the last section. Finally, the computed and the experimental patterns have been compared in detail. These studies have established that CBED can be successfully used to identify the presence of point defects.

5.2 SELECTION OF CRYSTALS IN WELDMENTS OF 9Cr-1Mo STEEL FOR THE STUDY OF POINT DEFECTS

The initial microstructure of the weldments of 9Cr-1Mo steels and their changes at high temperatures were explained in the third and fourth chapters of this thesis. The weld region of weldments of 9Cr-1Mo steel equilibrated at 1023 K for 500 h was chosen for ion irradiation studies. This particular treatment (1023 K/500 h) was chosen, in order to obtain the equilibrium phases of the steel, i.e., α -ferrite and $M_{23}C_6$. It is expected that irrespective of the particular combination of temperature and time chosen, the irradiation effects would remain the same if the two phases have the same crystal structure as that of the equilibrium phases. The choice of the crystals, α -ferrite and $M_{23}C_6$ is based on the following reasons: (a) existence of well-separated, simple string

potentials in α -ferrite and (b) very high unit cell dimensions in $M_{23}C_6$. These two features enable imaging of the relevant CBED features of interest with ease, as can be seen clearly later.

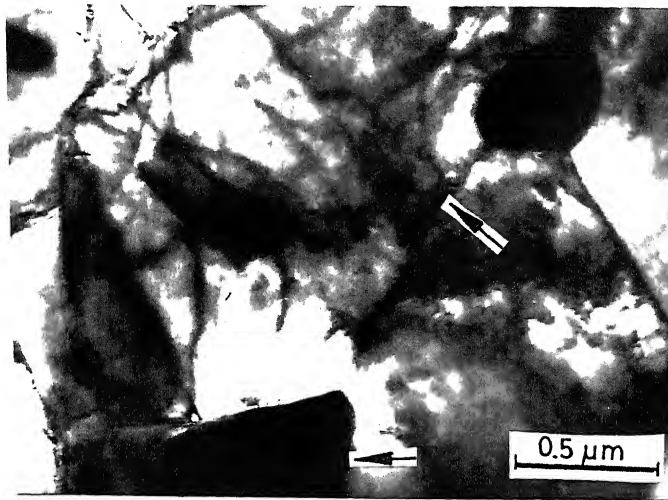
Pre-thinned foils were used for irradiation to follow the changes in the parent bcc α -ferrite matrix. However, the thin foils were not suitable for carbides because of their low volume fraction and also less chance of retaining the carbides within the transparent regions due to the preferential attack on carbides during preparation of thin foils. Therefore, the studies on carbides were carried out using carbon extraction replica. The irradiations were carried out on the carbon extraction replica in which a large number of carbides were present, making it easy for obtaining good statistical and reliable results. Another advantage of the choice of carbon extraction replica was that the CBED patterns taken were truly representative of carbides alone. There is no ambiguity about interference from the parent phase into which the carbide could be sandwiched, as would be the case if thin foils were used. The only disadvantage in using carbon extraction replica is that the evolution of defects observed in the carbides is not truly representative of those embedded in the parent matrix. The reported evolution of defects does not take into account the role of interfaces between α -ferrite and carbide. However, the choice is considered to be reasonable since the main purpose of the study is to find out if CBED can be employed for the unambiguous identification of point defects and not the kinetics of evolution of defects.

5.3 CHARACTERISATION OF CBED PATTERNS OF UNIRRADIATED CRYSTALS IN THE WELDMENTS OF 9Cr-1Mo STEEL

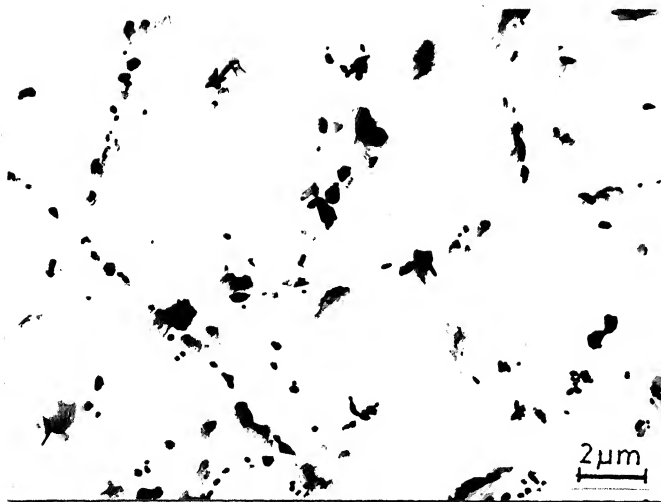
While doing CBED experiments, care was taken to avoid regions with dislocations. The patterns presented are representative of observations in a number

of dislocation free regions. Of the three regions of the weldment, equilibrated at 1023 K for 500 h, the weld region is selected for the present study. Figure 5.2a shows the microstructure of α -ferrite and figure 5.2b shows a high number density of carbides in the carbon extraction replica of weld portion of 9Cr-1Mo steel weldment equilibrated at 1023 K for 500 h. The microstructure of α -ferrite is found to consist of a random distribution of dislocations, a well-developed subgrain structure (arrow-marked) and a few carbides (arrow-marked), predominantly along sub-grain boundaries and triple points. The carbides in figure 5.2b are found to be coarse and globular (diameter of the order of 25 nm), along the sub-grain boundaries. The average composition of the carbides shown in figure 5.2b is found to be around 23 w/o Fe, 60 w/o Cr, 12 w/o Mo and 5 w/o C.

The CBED patterns of α -ferrite along various zone axes, are shown in figure 5.3 (a to c). The zone axes are determined based on patterns obtained using smaller C2 aperture of 50 μm (insets), taken from the same regions. The angle of convergence in the CBED patterns was changed by suitable choice of C2 aperture, using either 50 or 100 or 200 μm . The CBED patterns clearly provide three types of information which are as follows: **(i) the whole pattern symmetry, (ii) three dimensional information about the reciprocal lattice and (iii) the interference pattern within the (000) disc.** The first feature, namely, the whole pattern symmetry of the CBED patterns offers information about symmetry of the diffracting crystal. The patterns in figure 5.3 are obtained using high convergence angle. C2 aperture of size 200 μm was used. The fine lines, in these patterns (arrow marked) contain the symmetry information of the zone-axis. It is clear that there is a four-fold axis along $\langle 200 \rangle$ (figure 5.3a), a six-fold axis along $\langle 111 \rangle$ (figure 5.3b) and a two fold axis along $\langle 113 \rangle$ (figure 5.3c). It is of interest to observe that the symmetry derived based on these patterns is consistent with the expected point group symmetry of the bcc α -alpha ferrite crystal (56).



(a)



(b)

Figure 5.2 Micrographs of the weld region of the 9Cr-1Mo weldment, aged at 1023 K for 500 h. Characteristic initial microstructure of the weld prior to irradiation. (a) Subgrain boundaries and carbides (both arrow marked) in thin foil micrograph of α -ferrite. (b) Morphology and distribution of carbides, in carbon extraction replica of the same.

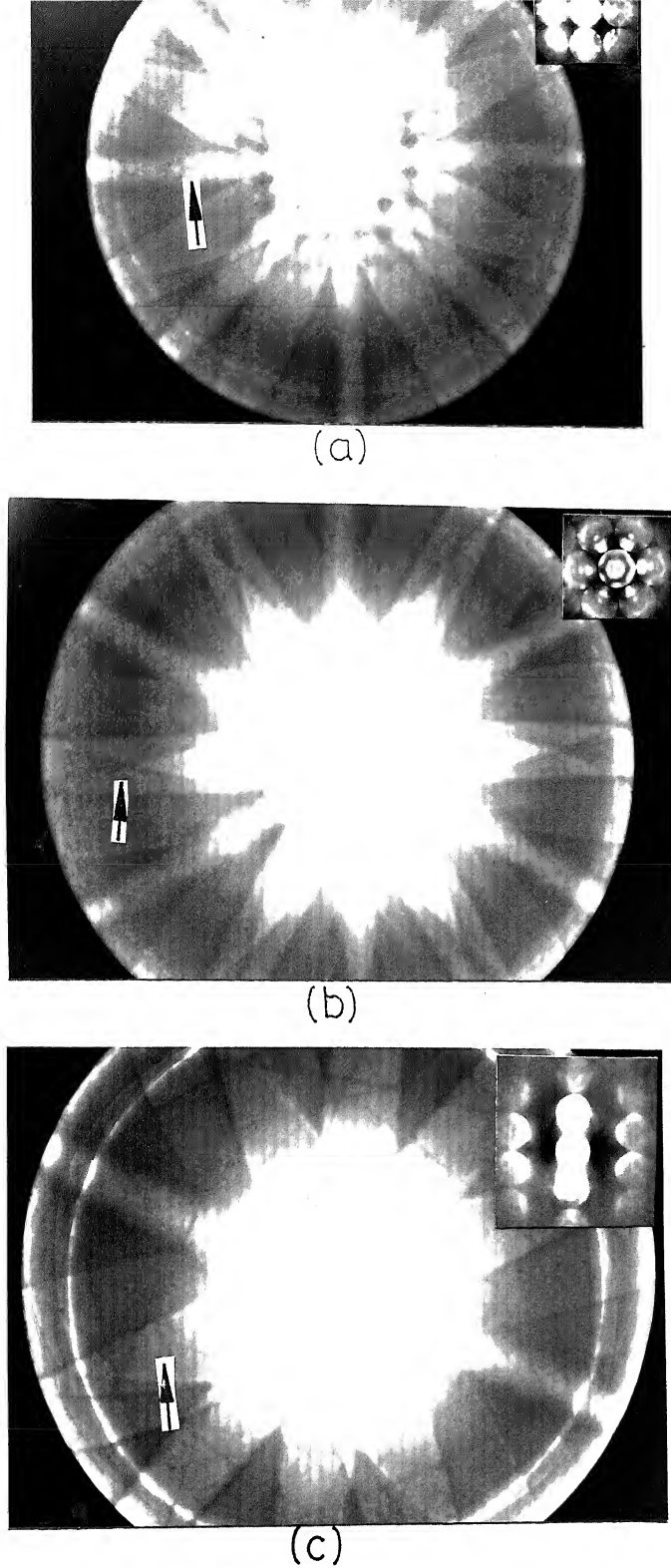


Figure 5.3 CBED patterns of α -ferrite in the weld region of 9Cr-1Mo weldment, aged at 1023 K for 500 h. The zone axes, as analysed using the representative insets (obtained using C2 aperture of 50 μm) are (a) $\langle 200 \rangle$, (b) $\langle 111 \rangle$ and (c) $\langle \bar{1}13 \rangle$. The arrow marks show the fine lines that contain information about the symmetry of the crystal.

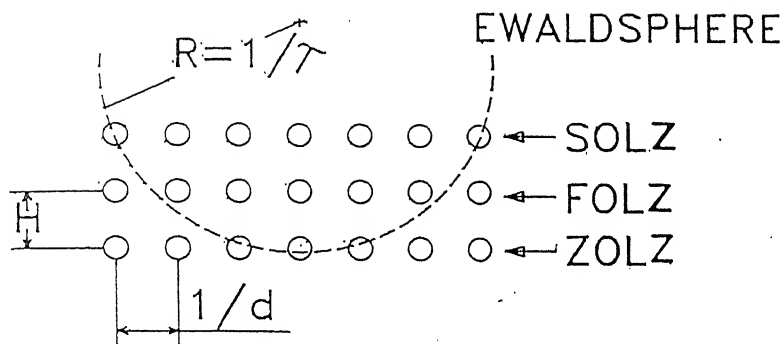
The second feature, namely, three dimensional information about the reciprocal lattice is obtained using the FOLZ ring. The reciprocal lattice layer distances are calculated (49,52) based on the diameter of the FOLZ ring and using the equation

$$G = \sqrt{2} R H, \quad (5.1)$$

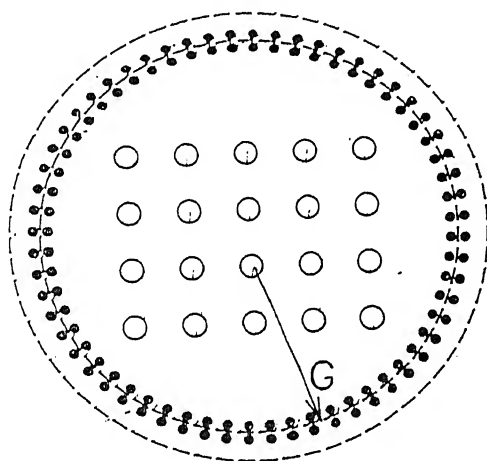
wherein G is the diameter of the FOLZ ring, $R=1/\lambda$ and H is the reciprocal lattice layer distance. The physical meaning of the values of H can be clearly understood based on the plan and sectional views of the Ewald sphere construction for electron diffraction illustrating the formation of higher order Laue zones, (figure 5.4 a and b). For example, in the simple case of CBED patterns of cubic crystals along one of the cube axes, the discs in the zero order Laue zone provide information about two sets of planes, say (020) and (200). Similar information about the third dimension, i.e., along the zone axis, $\langle 002 \rangle$ can be derived using the value of H . For CBED patterns along other zone axes, simple geometrical expressions have been derived to obtain the three-dimensional information about the reciprocal lattice (53).

The third feature, most relevant to the present study, is the intensity oscillation within the (000) disc of the CBED patterns. These are shown more clearly in figure 5.5 (a to c), for the close-packed directions like $\langle 200 \rangle$, $\langle 111 \rangle$ and $\langle \bar{1}13 \rangle$. These figures show the presence of concentric, geometrical patterns within (000) disc. These patterns are strong near Brilluoin zone boundaries and generally seen within the first Brilluoin zone. These are caused by the interference between strongly excited Bloch states. It is known that the Bloch states are excited strongly near the Brilluoin zone boundary due to dynamic interaction of the incident electrons with the well-aligned, atom string potential of the lattice along close-packed directions. In addition, these patterns also reveal the basic symmetry of the respective zone axes. For example, 4 fold axis along

BACK FOCAL PLANE OF OBJECTIVE LENS



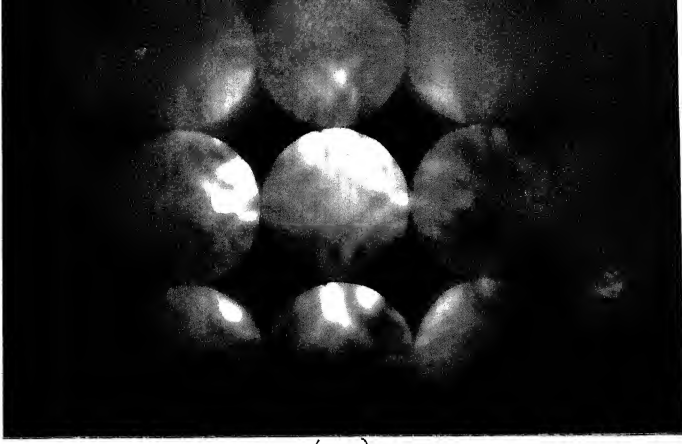
(a)



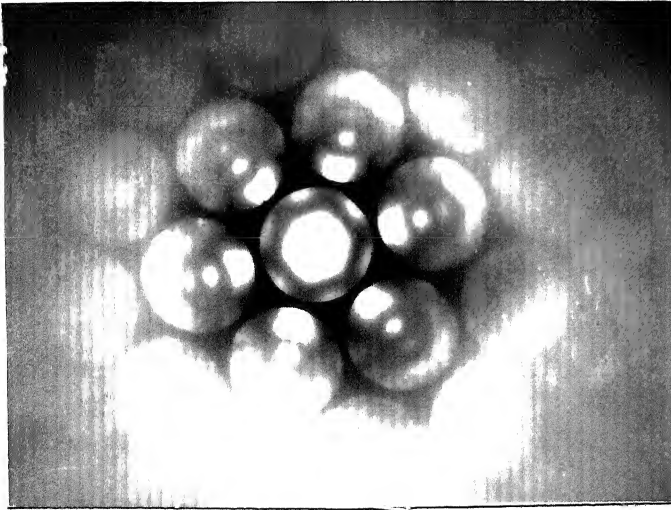
$$H = G^2 \lambda / 2$$

(b)

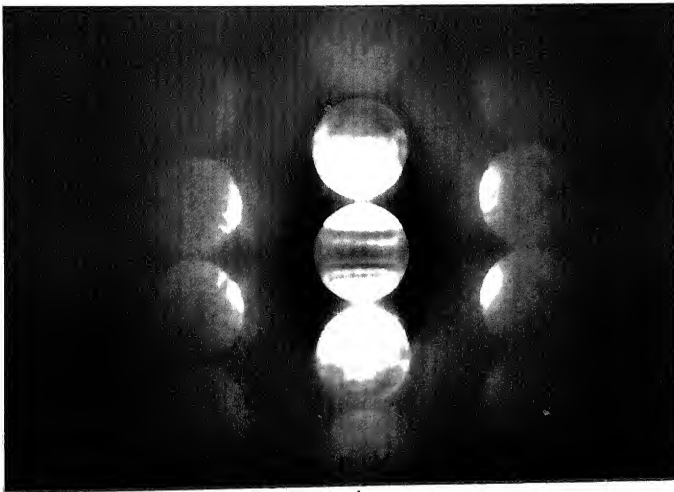
Figure 5.4 (a) Plan and (b) sectional views of the Ewald sphere construction for electron diffraction illustrating the formation of high order Laue zone (HOLZ). The description of the parameters used in this figure are as follows: R - radius of Ewald sphere; λ - wavelength of incident beam; H - reciprocal lattice layer distance; d - interplanar distance of the diffracting crystal and G - radius of the first order Laue zone (FOLZ) ring.



(a)



(b)



(c)

Figure 5.5 Zero order Laue zone of CBED patterns of α -ferrite of the same sample as figures 5.2 and 5.3. ZAP symmetry along different zone axes is clearly seen. (a) 4 mm along $\langle 200 \rangle$, (b) 6 fold along $\langle 111 \rangle$ and (c) 2 fold along $\langle \bar{1}13 \rangle$.

$\langle 200 \rangle$, 6-fold along $\langle 111 \rangle$ and 2-fold along $\langle \bar{1}13 \rangle$, are clearly seen, in figure 5.5.

Figure 5.6 shows the CBED patterns of the $M_{23}C_6$ carbide. There are two features relevant to the present study in figure 5.6, which are **(1) the large number of HOLZ rings and (2) the low inelastic scattering in the zero order Laue zone**. The large unit cell dimension of the carbide ($a=1.06$ nm) is conducive for viewing more number of HOLZ rings. As a consequence of large unit cell dimensions, the reciprocal layer distance, H , (figure 5.4) decreases. This results in an increase in the number of Laue planes that can intersect the Ewald sphere, within the angular range of visibility. This advantage, i.e., larger angular range of visibility of the reciprocal lattice, is not available in the conventional selected area diffraction (SAD) technique. The dependence of excitation of HOLZ rings on convergence angle, accelerating voltage, and unit cell dimensions has been taken into consideration, in this study, by maintaining the first two parameters nearly constant (49,52). The third parameter, namely, change in unit cell dimensions is not likely to be significant since the changes in the CBED patterns due to any minor change in the unit cell dimensions are very small in comparison with those observed in the present study.

5.4 IDENTIFICATION OF RELEVANT FEATURES OF CBED PATTERNS IN THE STUDY OF POINT DEFECTS

In the previous section, it is shown that the CBED patterns of unirradiated crystals of α -ferrite show three distinct characteristics and those of $M_{23}C_6$, show a large number of HOLZ rings. Of these, there are two characteristic features which are sensitive to the presence of point defects. These are (a) the intensity oscillations within (000) disc, shown in figure 5.5 and (b) the number of HOLZ rings, shown in figure 5.6. A brief

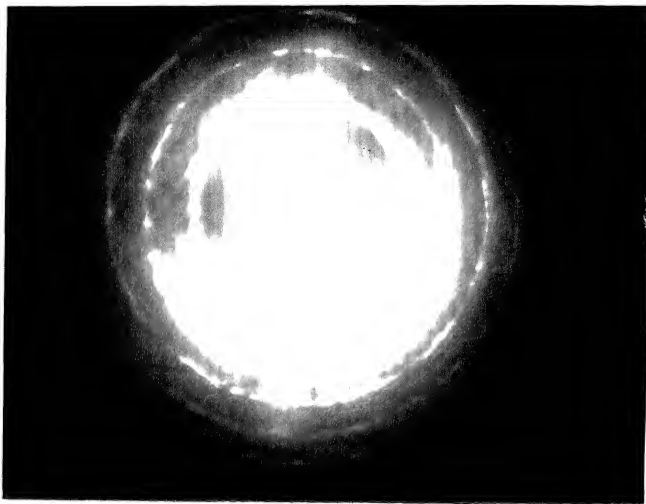


Figure 5.6 CBED pattern of face centered cubic $M_{23}C_6$ in the weld, aged at 1023 K for 500 h. The HOLZ rings are visible upto fourth order, due to the large unit cell dimension, 1.062 nm (Ref. 55).

understanding of the origin of these two features would highlight the role of point defects.

The intensity oscillations in (000) disc arise due to the dynamic interaction of incident electrons with sharp, strong, well-separated projected potential of the diffracting crystal. Such a projected potential along close packed zone axes is indicative of the presence of well-defined atom strings. The point defects disturb the arrangement of atoms from their equilibrium position in a random way. This leads to overlap of string potentials, which changes the intensity oscillations in (000) disc of CBED patterns.

The second feature, i.e., the number of HOLZ rings that can be imaged depends on the strength of large angle scattering. It is known that the lattice disorder caused by point defects and the increase in the amplitude of lattice vibration at elevated temperatures reduce the strength of scattering at large angles and hence the number of HOLZ rings.

Thus, these two features, i.e., the intensity oscillations within (000) disc of CBED pattern and the number of HOLZ rings are expected to be sensitive to the introduction of point defects.

5.5 CHARACTERISATION OF CBED PATTERNS OF ION IRRADIATED WELDS OF 9Cr-1Mo

The weld region of weldments of 9Cr-1Mo is chosen for the experiments explained in this chapter. The thin foils of the weld with α -ferrite and the carbon extraction replica of the same containing $M_{23}C_6$ precipitates were irradiated using argon and helium ions, at room temperature. Various values of the incident energy in the range 30 to 100 keV were used. The dose levels used were in the range of 10^{12} to 10^{15} ions/cm²,

for argon ions and 10^{16} to 10^{18} ions/cm², for helium ions. Implantation of energetic ions in a lattice is known to introduce defects. The concentration profile of implanted ions and the depth dependant profiles of defects generated for α -ferrite and $M_{23}C_6$ have been calculated using TRIM code, for argon and helium ions. The variation of the amount of helium deposited and the defects produced at various depths is shown in figure 5.7. The thickness 't' of most of the transparent regions of the thin foils can be assumed to be around 100 nm. This variation has been ignored, for the present purpose of identifying the possible changes in CBED patterns due to defects.

Detailed studies have been carried out to follow the changes in CBED patterns with differences in the mass and energy of the incident ions. The systematic changes in these experimental parameters would be useful to ensure that the observed changes in CBED are genuinely due to the introduction of point defects. Such experiments could serve as an index to confirm if CBED can be used to identify the presence of point defects. However, all these results are analysed with major emphasis on the changes in the characteristics of corresponding CBED patterns, caused by the point defects. The two chosen features of CBED patterns and the changes in them due to ion irradiation are described in detail. Initially, the changes in the intensity oscillations within (000) disc of CBED patterns are discussed, using the CBED patterns of ion irradiated α -ferrite. Following this, the changes in the number of HOLZ rings in the CBED patterns of $M_{23}C_6$ are discussed.

5.5.1 Changes in the Central Disc of CBED Patterns of Ion-irradiated α -ferrite

The feature relevant to the present section is the intensity oscillations within (000) disc of CBED patterns of α -ferrite. The periodicity of these concentric patterns is related to

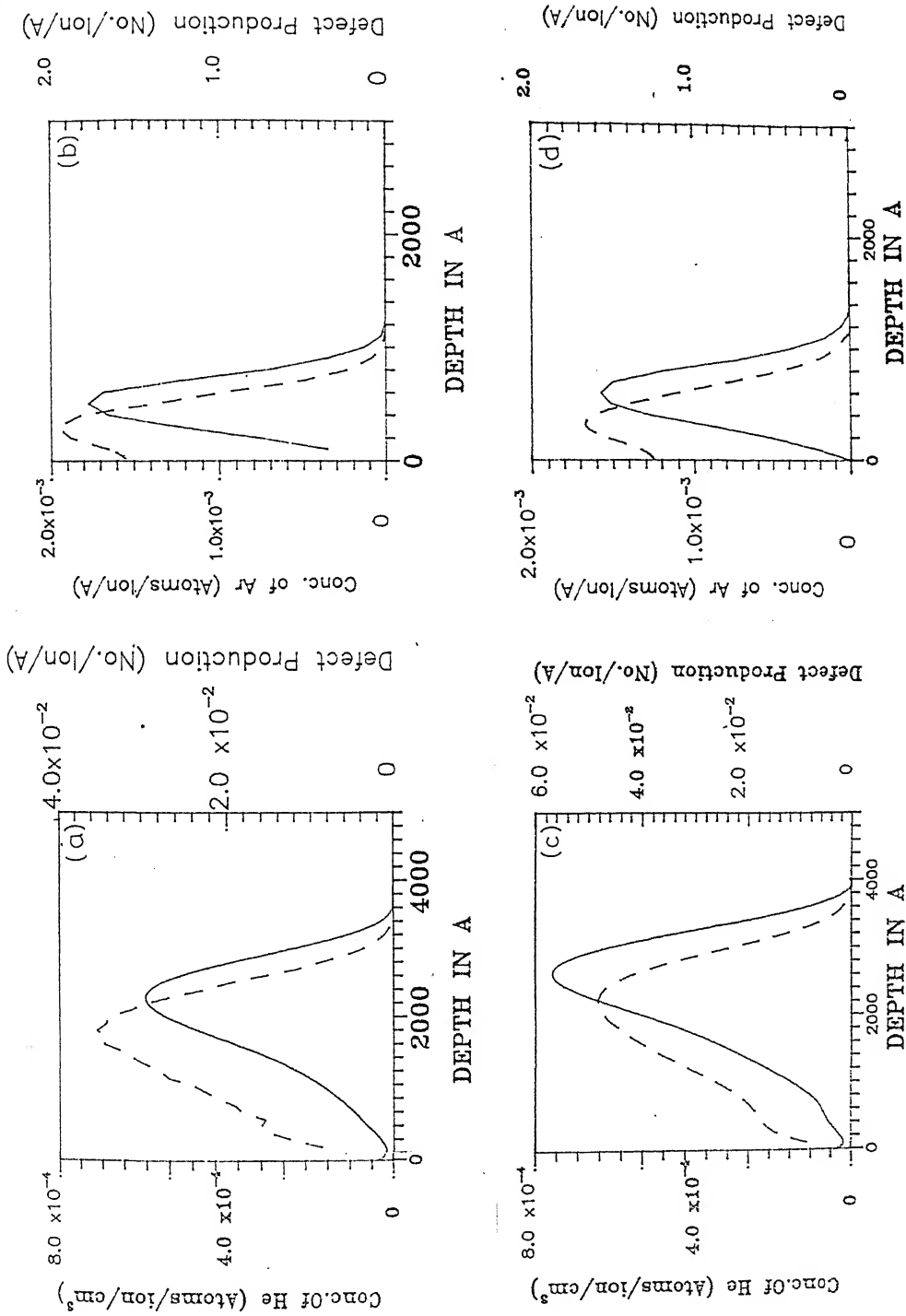
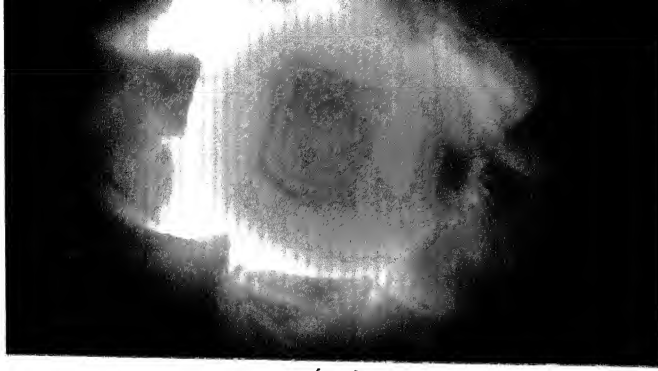


Figure 5.7 TRIM Code calculations: Depth profile (-----) of displacement damage and number of helium atoms (—) for (a) and (b) α -ferrite and (c) and (d) $M_{23}C_6$. (a) α -Fe : 55 keV He; (b) α -Fe : 100 keV Ar; (c) $M_{23}C_6$: 55 keV He; and (d) $M_{23}C_6$: 100 keV Ar.

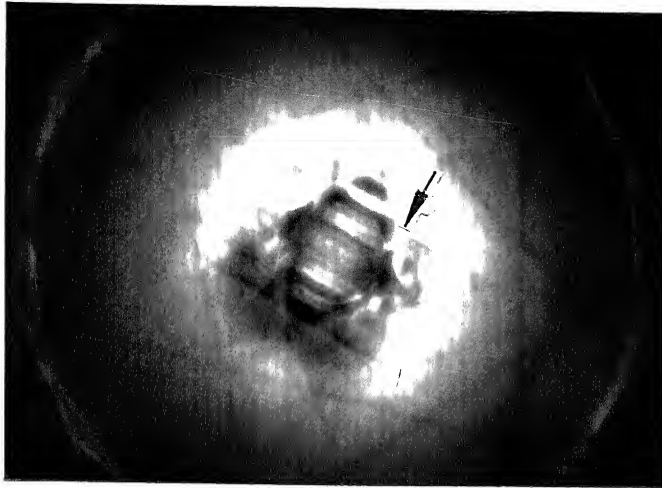
the extinction distance and hence, the thickness of the thin foils. Therefore, care was taken to ensure that these studies were confined to regions of similar thicknesses. Figure 5.8 shows the influence of irradiation with 100 keV argon ions, for three different dose levels. The CBED patterns in figure 5.8 are taken along $\langle \bar{1}13 \rangle$ of α -ferrite. At a low dose level of 3×10^{12} ions/cm², the concentric geometric patterns within the (000) disc, are retained without any change. However, an additional dose upto a level of 10^{13} ions/cm², reduces the angular range of formation of these intensity oscillations. Figure 5.8b shows the corresponding CBED pattern of α -ferrite along the same zone axis, $\langle \bar{1}13 \rangle$. The interference fringes are confined to regions near the Brilluoin zone boundary (arrow-marked). Further irradiation had led to the complete disappearance of these intensity oscillations (figure.5.8c). Similar sequence of changes was observed along other close-packed zone-axes, like $\langle 200 \rangle$ and $\langle 111 \rangle$.

The α -ferrite irradiated with 100 keV argon ions upto 10^{14} ions/cm², was found to be devoid of fine defect clusters like dislocation loops or voids. The absence of clustering at such dose levels is consistent with the low amount (< 10 appm) of argon deposited and the low temperature of irradiation ($< 0.3 T_m$). The clustering of defects has been reported in earlier studies only at the temperature of irradiation higher than 573K at higher dose levels (58,59). Hence, it is reasonable to assume that the observed effect i.e., gradual disappearance of interference fringes is due to the free, isolated point defects, introduced during irradiation of α -ferrite with argon to small dose levels at room temperature.

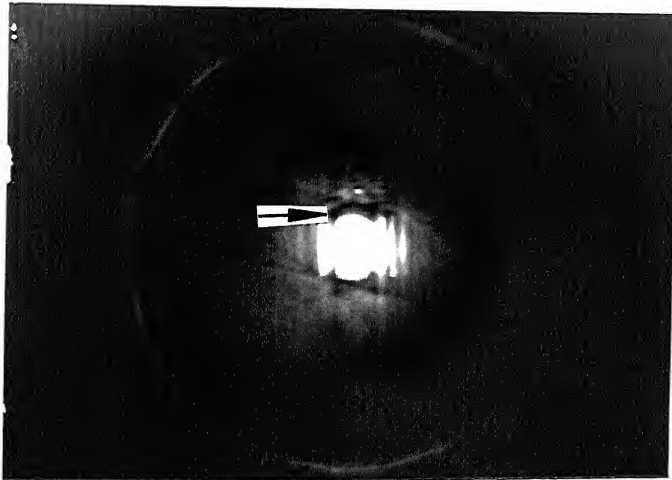
Studies on the changes in the CBED patterns of α -ferrite during irradiation with 55 keV helium ions, show changes similar to those observed during argon ion irradiation. Figure 5.9a shows the presence of interference fringes within the (000) disc, in a sample irradiated with 55 keV helium ions to a dose of 10^{16} ions/cm². These fringes extend from the Brilluoin zone boundary to the center of the (000) disc. The selected



(a)

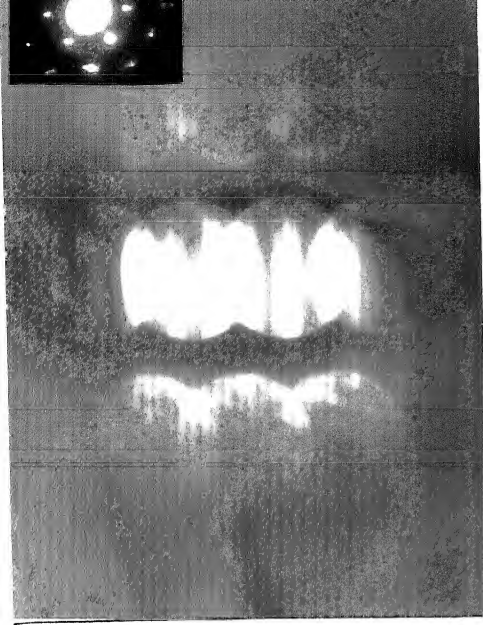


(b)



(c)

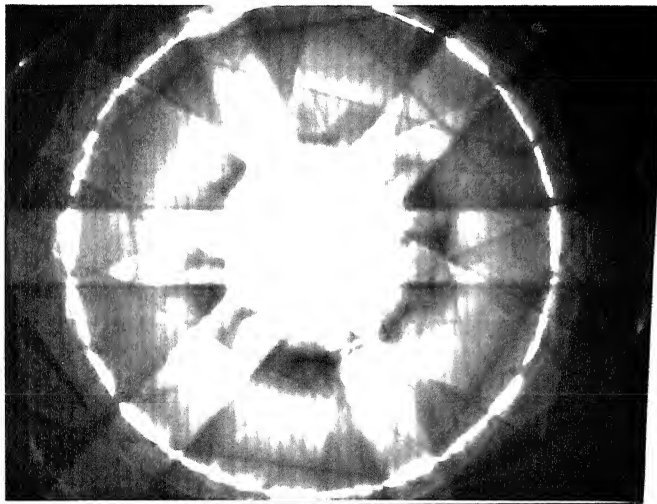
Figure 5.8 Effect of argon ion irradiation on the CBED patterns of bcc α -ferrite irradiated with 100 keV argon ions upto dose levels of (a) 3×10^{12} , (b) 10^{13} and (c) 10^{14} ions/cm². Zone axis is along $\langle \bar{1}13 \rangle_{\alpha}$. The arrow marks show the Brillouin zone boundary. The gradual weakening and disappearance of the geometrical, concentric patterns in (000) disc is seen, eventually leading to complete disappearance



(a)



(b)



(c)

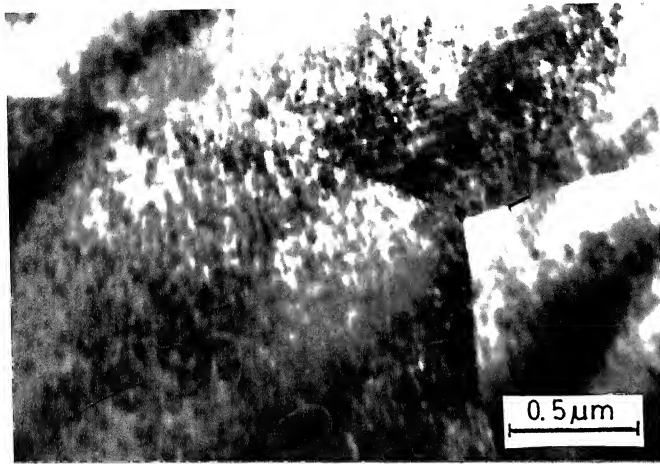
Figure 5.9 Effect of helium ion irradiation on CBED patterns of α -ferrite. CBED patterns of α -ferrite irradiated with 55 keV helium ions to two dose levels. (a) 10^{16} and (b) 10^{17} ions/cm². Effects similar to figure 5.8 are seen. The arrow mark in (b) shows the Brillouin zone boundary. The interference fringe is confined to only narrow region near the boundary, due to strong scattering effects at the boundary. (c) shows the retention of whole pattern symmetry. Insets show the diffraction patterns, without any signature of presence of defects.

area diffraction (SAD) patterns do not show any signature of presence of defects in the α -ferrite lattice. An additional dose of helium ions upto 10^{17} ions/cm², has resulted in the reduction of the angular range of the interference fringes. Figure 5.9b shows the CBED patterns of α -ferrite, irradiated with 55 keV helium upto a dose level of 10^{17} ions/cm². The interference fringes are seen only near the Brilluoin zone boundary. This is in contrast to their extension upto the center of the (000) disc, in the patterns obtained from unirradiated crystal (figure 5.5b) and those irradiated to low dose levels (figure 5.9a). However, there is no significant change in the whole pattern symmetry of the crystal, as can be seen in figure 5.9c.

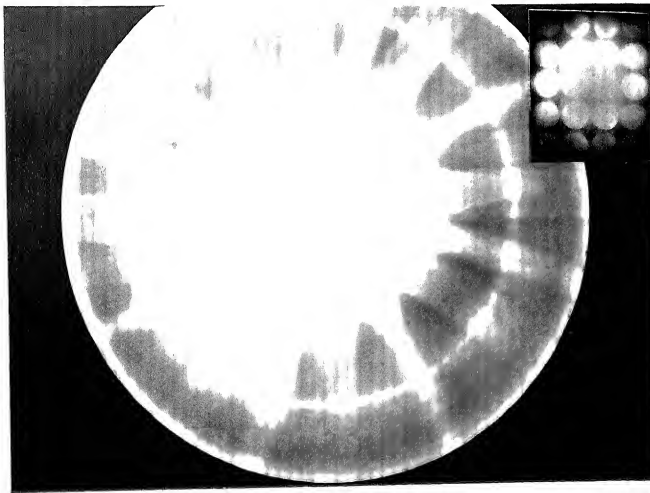
Further increase in the irradiation dose level upto 10^{18} ions/cm², had led to the formation of a high density of fine defect clusters (Figure 5.10a). However, the whole pattern symmetry of the CBED pattern of α -ferrite from a region, devoid of such clusters, retained the symmetry details (Figure 5.10b). The inset in figure 5.10b shows the zone axis to be along $\langle 200 \rangle_{\alpha}$. Since the main aim of the study is to investigate if CBED can be used to identify the presence of isolated point defects, prior to their agglomeration into clusters, the experiments were confined to dose levels upto 10^{17} ions/cm².

The extensive literature regarding irradiation effects in ferritic steels suggests that the formation of loops and secondary phases like M_6C , σ , etc., proceed in the range of temperature, 0.3 to 0.5 T_m at fluence levels of around 10 to 100 appm of helium (31-33,35,37,60,61). The formation of clusters of point defects during irradiation with 55 keV helium ions, at a dose level of 10^{18} ions/cm², observed in the present study is in agreement with the literature.

The results presented above may be summarised using a schematic representation of the changes observed in the CBED patterns of ion irradiated α -ferrite. A schematic



(a)



(b)

Figure 5.10 Evidence of formation of defect clusters at high doses. (a) Microstructure of α -ferrite irradiated with 55 keV helium to a dose level of 10^{18} ions/cm², showing formation of defect clusters. (b) Retention of whole pattern symmetry in the same. The inset shows microdiffraction pattern used for analysis of zone axis as $\langle 200 \rangle_{\alpha}$.

representation of the results discussed in this section is given in figure 5.11 (a to d), for increasing concentrations (arbitrary values) of point defects. The intensity oscillations in the central disc of CBED pattern of unirradiated α -ferrite along $\langle 200 \rangle$, extend from the Brillouin zone boundary to the centre. The angular range of visibility of these oscillations decreases with increase in defect density, as shown in (b) and (c). With a further increase in the density of point defects, these fringes are not seen even near the Brillouin zone boundary, along which the scattering is the strongest.

In all the experiments explained above, it becomes essential to confirm that the observed effects are genuine and not introduced due to the variation in thickness or oxide scale. The regions of thin foil which were chosen for CBED experiments were confirmed to be devoid of any visible oxide layer. In order to find out the role of variations in thickness, CBED experiments were performed in the same regions of the thin foil, both prior to and after ion implantation, using the same regions of the thin foil. These preliminary experiments suggested that the observed effects are genuine. Hence, further CBED experiments were carried out using regions of more or less same thickness.

The systematic variation in the angular range of the interference fringes is another feature which confirms that the observed gradual disappearance in the concentric, geometric patterns inside the (000) disc of CBED patterns during irradiation is genuine. It is known that these patterns are caused by interference between strongly excited Bloch states. The probability of excitation of the Bloch states is highest near the Brillouin zone boundaries, where the scattering effect is the strongest. The observed (Figures 5.8b and 5.9b) dependence of the angular range of intensity oscillations with increase in dose suggests that the subsequent disappearance of the interference pattern within (000) disc is genuine and not an artefact of the foil thickness.

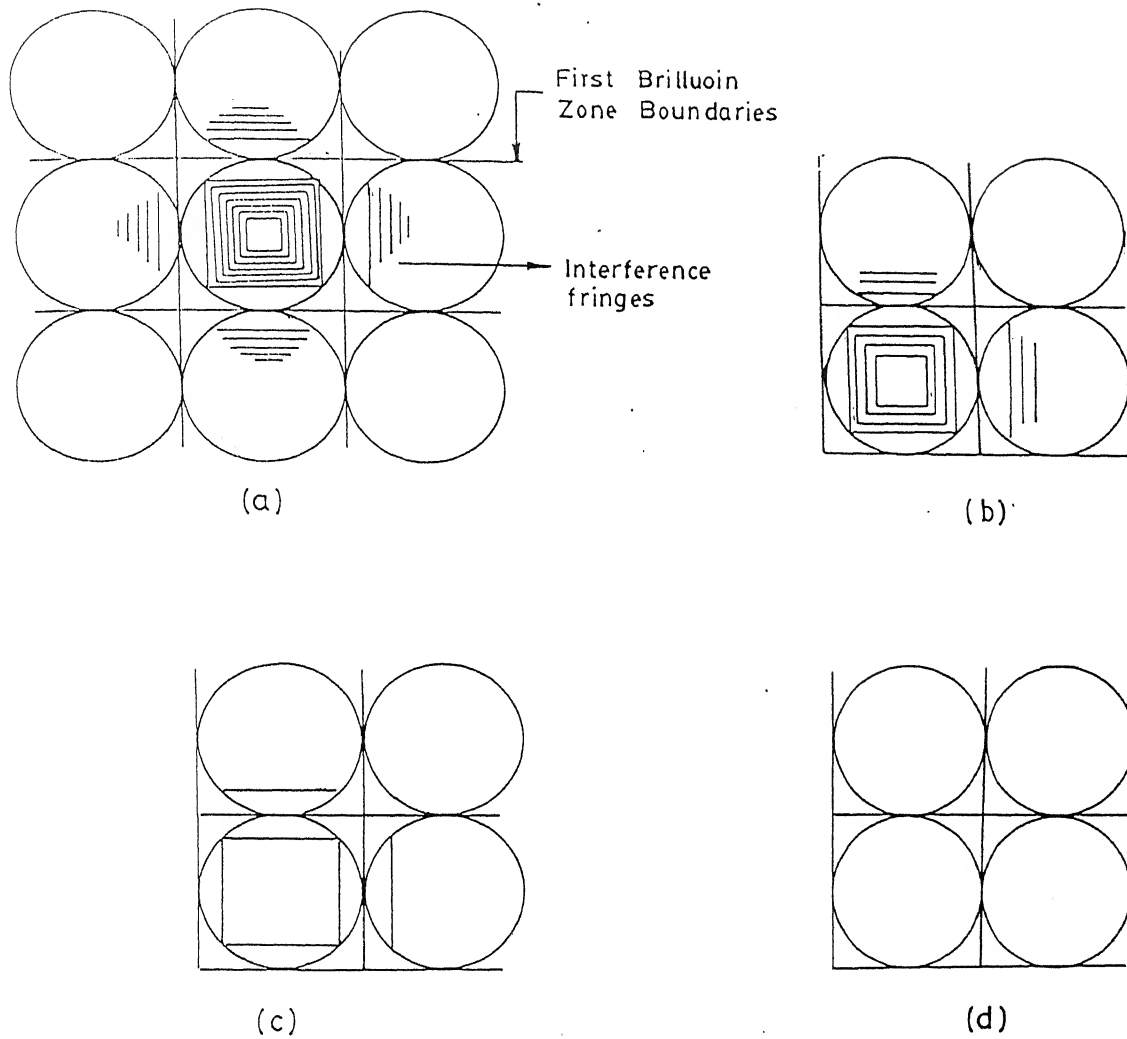


Figure 5.11 Schematic representation of effect of ion irradiation on the interference pattern in (000) disc of CBED pattern. (a) Perfect cubic crystal along $\langle 200 \rangle$. (b) and (c) Gradual reduction in the angular range of interference pattern. (d) Complete disappearance at high dose level. Thickness of the diffracting crystal is assumed to be constant.

Thus, the above results suggest strongly that the gradual reduction of the angular range of the interference pattern within (000) disc of CBED pattern of α -ferrite is caused by randomly distributed, isolated point defects.

5.5.2 Changes in the High Order Laue Zone (HOLZ) Rings of CBED

Patterns of Irradiated $M_{23}C_6$

Figure 5.12 shows the effect of irradiation on the equilibrium carbide, $M_{23}C_6$ with 100 keV argon ions to various dose levels. The CBED patterns show the following general trends: (1) a gradual increase in background intensity is seen in the ZOLZ and (2) the number of high order Laue zones reduce with increase in dose. The insets in figure 5.12 (a to c) show the microdiffraction patterns of the carbides, which were used to identify the zone axis as $\langle 220 \rangle$ of $M_{23}C_6$. As far as possible, the zone axis was maintained constant.

The above mentioned changes are seen at a low dose level of 3×10^{12} ions/cm² upto a dose level of 10^{14} ions/cm². It is seen that beyond 10^{14} ions/cm² of argon, an increase of dose upto 10^{15} ions/cm² did not introduce any further change in the CBED patterns.

The studies on carbides irradiated with helium also showed trends similar to that of argon, discussed above. These results are shown in figure 5.13. The reduction in the number of HOLZ rings from fourth order in the unirradiated crystal to second order, after an irradiation with 55 keV helium ions upto a dose level of 10^{16} ions/cm² is quite clearly seen in figure 5.13a. In addition, the background intensity has also increased considerably, consistent with the expected increase in the contribution of inelastic scattering processes in the diffraction patterns of crystals with defects. Increase in

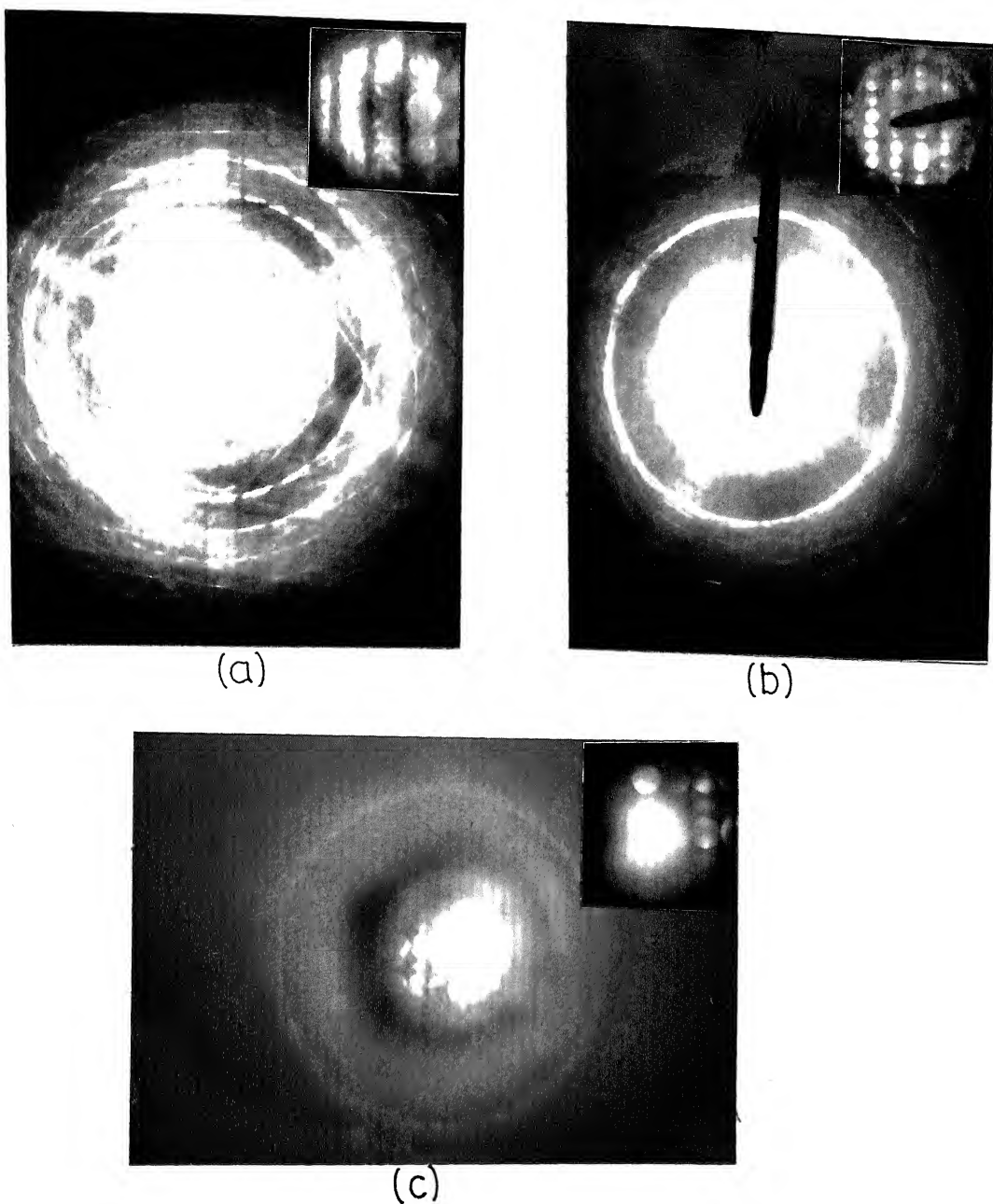
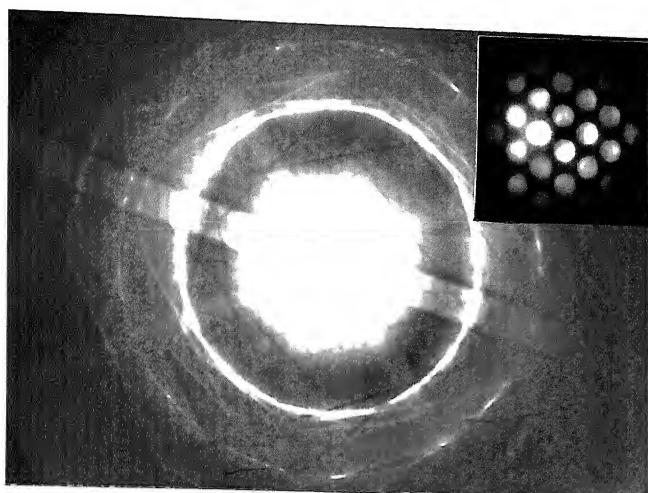
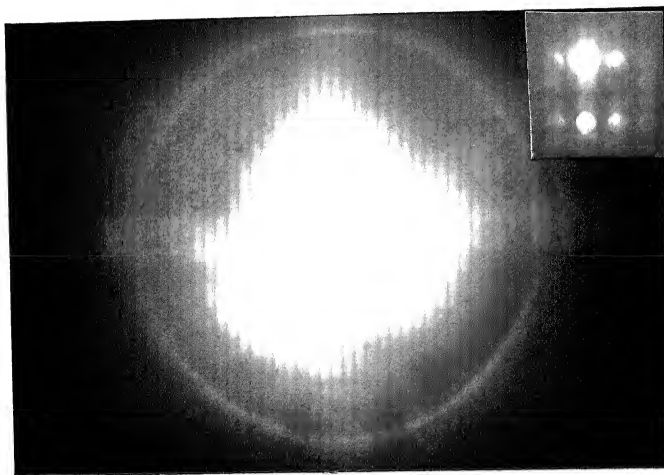


Figure 5.12 Effect of 100 keV argon ion irradiation on CBED pattern of $M_{23}C_6$ of the weld region of 9Cr-1Mo weldment (aged at 1023 K for 500 h). (a) 3×10^{12} , (b) 1.5×10^{13} and (c) 10^{14} ions/cm². The analyses of the insets in the figures confirm that the zone axis is along $\langle \bar{2}20 \rangle$ of $M_{23}C_6$. A gradual reduction in number of HOLZ rings is seen as the dose is increased. C2 aperture used for all the three was 200 μm .



(a)



(b)

Figure 5.13 Effect of 55 keV helium ion irradiation on CBED patterns of $M_{23}C_6$. Dose levels are (a) 10^{16} and (b) 10^{17} ions/cm². The insets show that the zone axes are $\langle 110 \rangle$ and $\langle \bar{1}12 \rangle$ in (a) and (b) respectively. A reduction in the number of HOLZ rings is visible.

dose level upto 10^{17} ions/cm², further reduced the strength of large angle scattering, resulting in the visibility of only FOLZ (Figure.5.13b). Though a significant change is seen in the CBED patterns, with increase in point defect density, the corresponding SAD patterns did not show any change due to introduction of point defects. Thus, the presence of characteristic changes in the CBED patterns of irradiated crystals assumes more importance, especially since there is no observable change in the corresponding SAD patterns. A schematic illustration of the influence of ion irradiation on the number of visible HOLZ rings of $M_{23}C_6$ is shown in figure 5.14. A gradual decrease in the maximum number of visible HOLZ rings is a distinct characteristic feature of CBED patterns from crystals with high density of defects.

At this juncture, it is essential to examine the factors which influence the imaging of HOLZ rings in CBED patterns. These factors are: (i) the accelerating voltage, (ii) the temperature at which CBED experiments are performed, (iii) the lattice parameter and (iv) the reciprocal lattice layer distance. In the present study, all the CBED experiments were carried out at room temperature using a constant accelerating voltage of 100 kV. The lattice parameter has a strong influence on the angular position of each HOLZ ring, rather than the maximum number of visible HOLZ rings, within a particular angular range. The last parameter, namely, the reciprocal lattice layer distance, for a given unit cell, depends on the zone axis. In most cases, the zone axis was maintained the same. In cases, where it was not possible, it was ensured that one of the close packed directions was chosen as the zone axis. The change in the reciprocal lattice layer distance can be assumed to be negligible, so long as the above precautions are taken. Normally, maximum number of HOLZ rings is visible in CBED patterns taken along close packed zone axes. However, the magnitude of the change in the maximum number of visible HOLZ rings due to variation in zone axis is expected to be much smaller than the reduction observed in figures 5.12 and 5.13. This feature, when analysed along with the observed enhanced inelastic scattering with increase in dose of

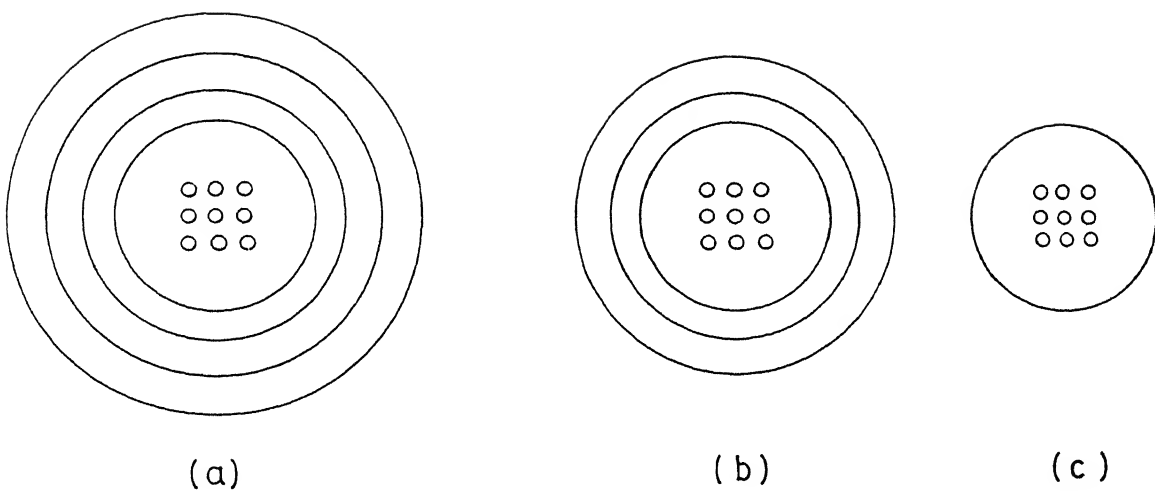


Figure 5.14 Schematic representation of effect of ion irradiation on the HOLZ rings of CBED patterns of crystals with large unit cell dimensions. a) Perfect crystal, (b) and (c) reduction in number of visible HOLZ rings with increase in dose.

ion irradiation, confirms that the reported reduction in the maximum number of visible HOLZ rings is genuinely due to the defects introduced during irradiation.

5.6 SIGNATURES OF POINT DEFECTS IN CBED PATTERNS OF IRRADIATED WELDS OF 9Cr-1Mo

The results discussed so far, suggest that there are two distinct features of CBED patterns, which show characteristic changes when the crystals are irradiated with high energy ion beams. These features are: **(a) the interference fringes within (000) disc and (b) the number of HOLZ rings of CBED patterns.** These two features appear to reduce gradually and finally disappear with increase in dose levels.

The presence of these two signatures of point defects in CBED are of considerable importance. It has been shown that there is no visible change in the corresponding selected area diffraction patterns. The conventional techniques which are used for the study of point defects like X-ray diffraction, dilatometry and positron lifetime spectroscopy require larger size of the irradiated samples. However, in situations wherein defects are generated in localised regions as in the case of ion irradiation, no technique has been found to be suitable so far. In the light of these facts, the identification of the two characteristic features in the CBED patterns of ion irradiated crystals offers an attractive method for the study of point defects.

Another interesting feature in the results discussed above relates to the changes in the CBED patterns, when the samples were irradiated with incident ions of different mass. The results of the present studies show that there is a difference in the dose levels of argon and helium for which similar effects are observed. The effect seen at a dose level of 10^{13} ions/cm², in the case of irradiation with argon ions is seen only at 10^{17}

ions/cm² in the case of helium ions. This dose level for helium ions, is nearly four orders of magnitude higher than that of argon. This could be attributed to the following factors : higher mass of argon leading to transfer of higher energy during each collision with the host lattice atom, leading to more number of displacements. This, in turn, results in a larger concentration of defects (32), in the case of argon ions than helium ions.

5.7 CBED PATTERNS AFTER POST-IRRADIATION ANNEALING

Another interesting observation in the present study is the reversion of the irradiated crystal to the defect-free state of the original crystal and the consequent changes in the CBED patterns, after post-irradiation annealing. In order to confirm that the changes in the CBED patterns were caused only by the point defects introduced during irradiation, CBED experiments were carried out on samples subjected to post-irradiation annealing. The carbon extraction replica, irradiated using argon and helium upto a dose of 10^{13} and 10^{17} ions/cm² respectively, were subjected to post-irradiation anneal using in-situ hot stage microscopy. The isochronal temperature anneal schemes are shown in figure 5.15.

Figure 5.16 shows the sequence of micrographs depicting the evolution of bubbles at high temperatures, in samples irradiated with argon, to a dose level of 5×10^{13} ions/cm². It can be seen from figure 5.16a that the onset of formation of argon bubbles was observed only at 673 K. The growth and coalescence of the bubbles was quite rapid and completed within few minutes. Continuous growth in both the number density and the diameter of the bubbles, was observed only for a short time, probably due to the small concentration of implanted ions. The constant value of the diameter of the bubbles at 723 and 873 K (Figure 5.16 (b and c)) suggests that the saturation in the

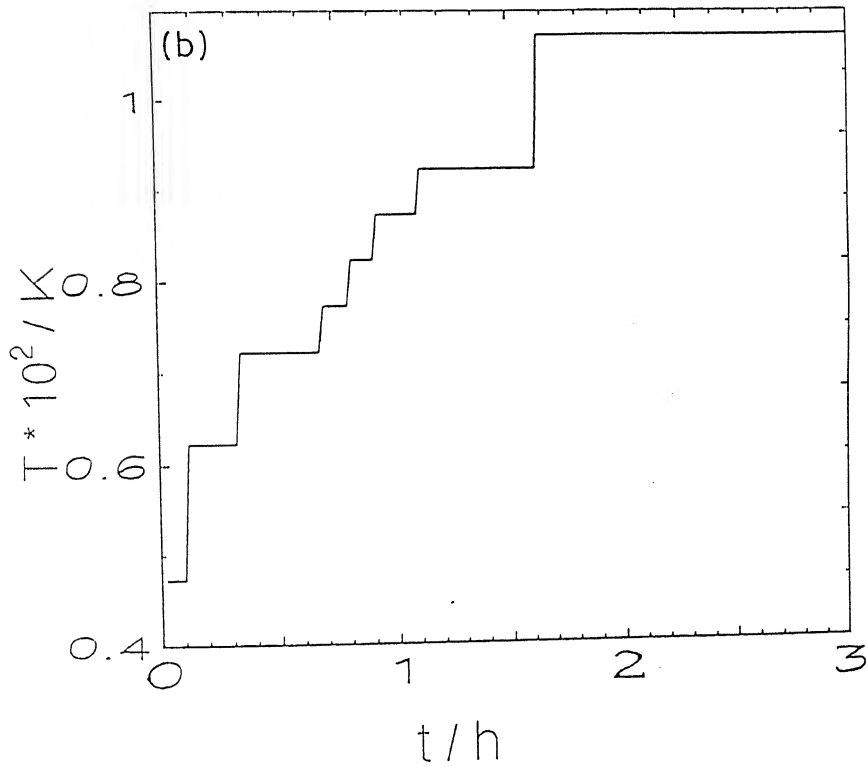
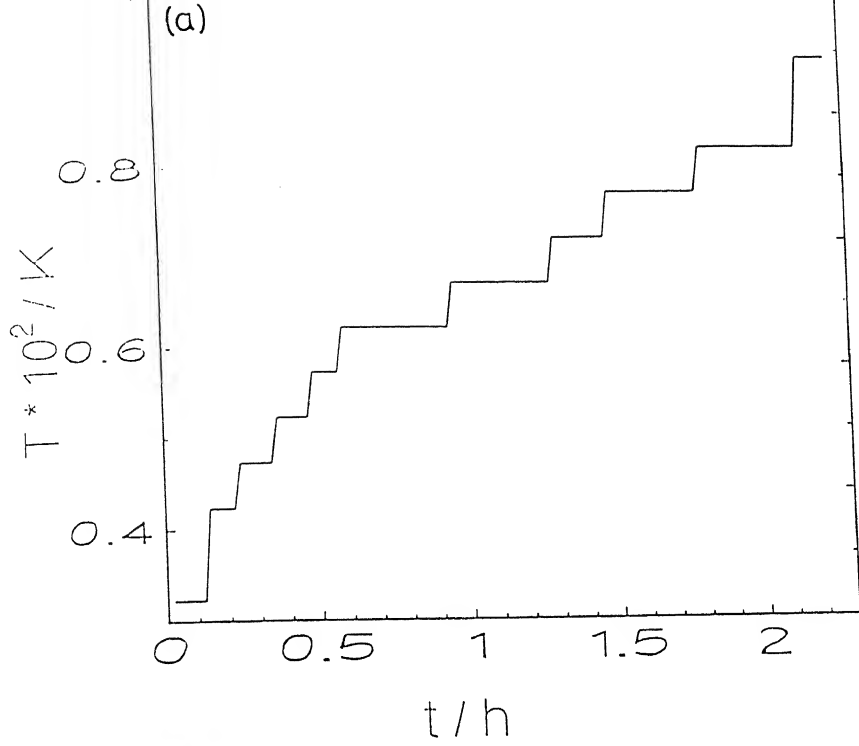
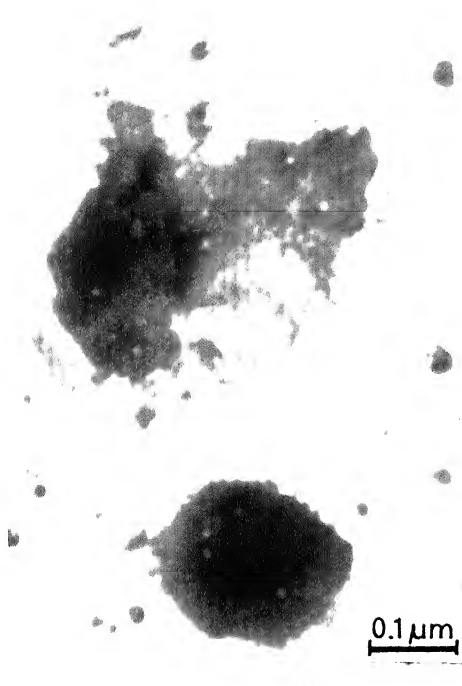


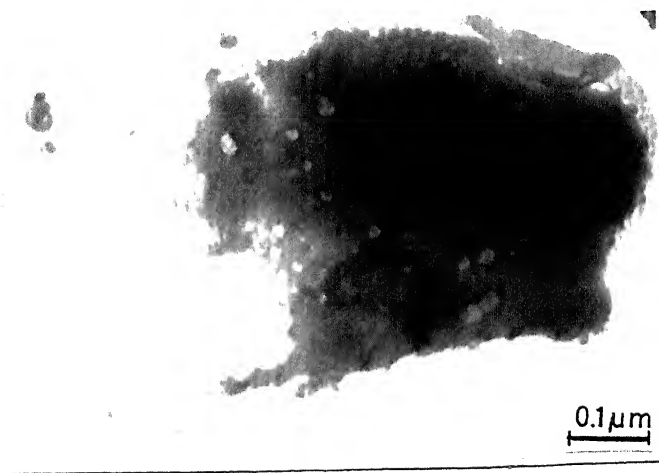
Figure 5.15 Temperature vs. hold time schedule during in-situ hot stage electron microscopy studies on irradiated carbon extraction replica of weld. Prior irradiation is with (a) 100 keV argon ions to a dose of 5×10^{13} ions/cm² (b) 55 keV helium ions to a dose of 10^{17} ions/cm².



(a)



(b)



(c)

Figure 5.16 Sequence of micrographs of $M_{23}C_6$, irradiated with 100 keV argon ions upto a dose level of 5×10^{13} ions/cm², subjected to post-irradiation anneal, as in figure 5.15a. Evolution of very fine bubbles at (a) 673 K, (b) 723 K and (c) 873 K.

recovery processes has already been attained. In any case, in order to ensure that the crystal is completely free of defects, the samples were annealed again at 1073K for 30 minutes.

Post-irradiation annealing of carbon extraction replica irradiated with helium to a dose level of 10^{17} ions/cm², did not result in the formation of helium bubbles, as shown in figure 5.17. This could be either due to the loss of defects from the surfaces of the carbides in the replica or the deposition of small concentration of helium atoms within the thickness of the foil, due to larger range of helium.

In the present study, the temperature at which vacancies became mobile was found to be 673 K, in the case of irradiation with argon ions. This value compares well with those reported in literature, i.e., 623 K (59). The nucleation and growth of bubbles could not be observed in either extremely thin or thick crystals. This could be due to the loss of defects from the two surfaces of the thin samples and the poor contrast in very thick particles of carbides. Since CBED experiments at high temperatures would increase inelastic scattering and reduce the strength of large angle scattering, the formation of visible defect clusters during in-situ annealing was chosen as the index for the onset of recovery process. During many trials of hot stage experiments, it was found that this was also not a unique choice. Very often, the formation of defect clusters could not proceed to the extent of visible bubbles, due to surface losses. However, only those samples in which formation of bubbles could be clearly observed were chosen for CBED experiments at room temperature.

The CBED patterns of samples implanted with argon and helium ions followed by isochronal annealing, are shown in figure 5.18 (a and b), respectively. It was ensured that these CBED patterns are taken from regions devoid of bubbles in samples. The presence of four HOLZ rings is seen clearly, in these patterns. These CBED patterns

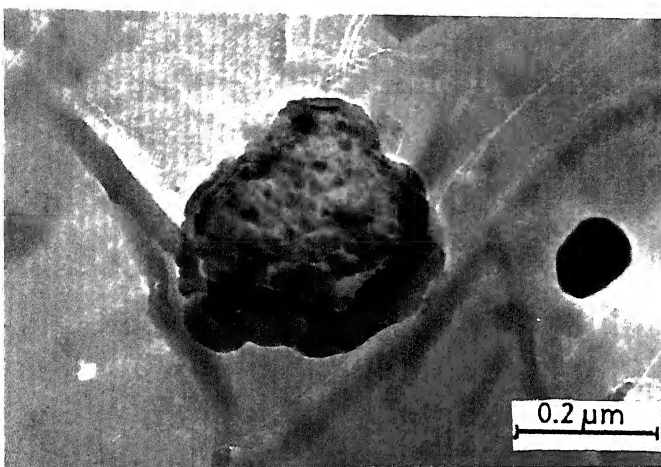
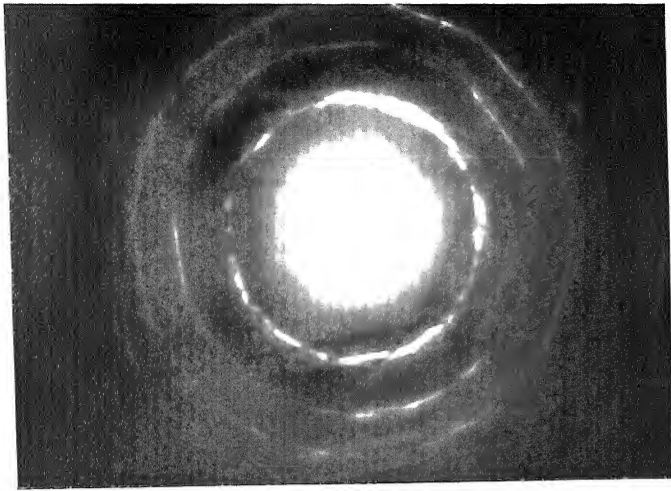
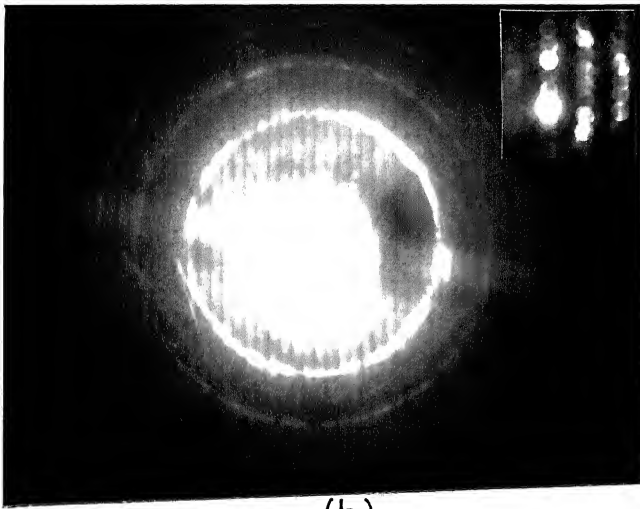


Figure 5.17 Absence of evolution of helium bubbles in $M_{23}C_6$ of carbon extraction replica irradiated with 55 keV helium ions upto a dose level of 10^{17} ions/ cm^2 and subjected to post-irradiation anneal as in figure 5.13b.



(a)



(b)

Figure 5.18 Reversion of CBED patterns of $M_{23}C_6$ after post-irradiation anneal to those of the virgin, unirradiated crystal. (a) CBED pattern of $M_{23}C_6$ at the end of anneal as in figure 5.15a. (b) CBED pattern of $M_{23}C_6$ at the end of anneal as in figure 5.15a. The inset shows microdiffraction pattern along $\langle \bar{1}23 \rangle$ of $M_{23}C_6$. The number of HOLZ ring has increased in both. (Compare with figures 5.12 and 13).

are similar to those of unirradiated crystals. The increase in the number of HOLZ rings suggest that the strength of high angle scattering has increased after post-irradiation annealing. These experiments confirm, beyond doubt that the changes observed in CBED patterns during irradiation are, indeed, due to the isolated point defects only and their recovery during post-irradiation annealing results in the CBED patterns similar to that of the unirradiated crystal.

A brief summary of the results regarding the changes in CBED patterns of two crystals of 9Cr-1Mo welds, during irradiation and post-irradiation anneal is as follows: The distinct features which show systematic changes during irradiation and post-irradiation anneal are (a) the interference pattern within (000) disc of CBED pattern and (b) the number of HOLZ rings. The two features, i.e., the angular range of intensity oscillations and the strength of large angle scattering reduce gradually with increase in dose.

In-situ post-irradiation annealing leads to significant increase in the strength of large angle scattering, resulting in CBED patterns similar to that of the original crystal. These results show that the point defects introduced during ion irradiation are mainly responsible for the changes observed in the CBED patterns.

5.8 ORIGIN OF CHANGES IN SIGNATURES OF POINT DEFECTS IN CBED PATTERNS : SIMULATION STUDIES IN MODEL Al-14 at/o Mn SYSTEM

Having established that point defects in the crystals of α -ferrite and $M_{23}C_6$ provide characteristic changes in their CBED patterns, it is worthwhile to understand the role of

these point defects in the diffraction of electrons. Hence, the next problem is to identify the origin of the observed characteristic changes in CBED patterns due to point defects, in the light of the known dynamical theory of electron diffraction. Since such an attempt required computation of CBED patterns, projected potential of atoms in the crystal, etc., it was necessary to choose a simple, binary system, whose unit cell can be described unambiguously. The following sections describe the choice of such a system, initial microstructure of this system, the changes in the experimental CBED patterns during ion irradiation and their comparison with computed CBED patterns.

An Al-14 a/o Mn alloy was chosen for the purpose of studying the influence of point defects on the CBED patterns. The two crystals - the fcc α -Al and the orthorhombic Al_6Mn , in this alloy have the required properties. These are the presence of simple projected potential in α -Al and the large unit cell dimensions in Al_6Mn . The irradiation behaviour of the two phases in this alloy has been established in detail, in one of our earlier studies (62). The Al-14 a/o Mn alloy (Figure 5.19) exists in equilibrium in a two phase field of α -Al and orthorhombic Al_6Mn (62). The optical micrograph of the equilibrated Al-14 a/o Mn alloy (figure 5.20a) confirms the presence of 80% of the intermetallic compound, as expected from lever rule. The microhardness of α -Al is 30 VHN and that of Al_6Mn is 600 VHN. The quantitative estimate of Mn in Al_6Mn and α -Al is found to be 14.6 ± 0.2 a/o and 0.5 ± 0.3 a/o, respectively. The X-ray diffraction peaks taken from the well annealed alloy using Cu-K_α match very well with reported values of Al_6Mn and α -Al (62). The size of the particles of Al_6Mn show a wide variation, the histogram of which is shown in figure 5.20b. The presence of submicroscopic particles along with their SAD pattern taken along $\langle 220 \rangle$ is shown in figure 5.20c.

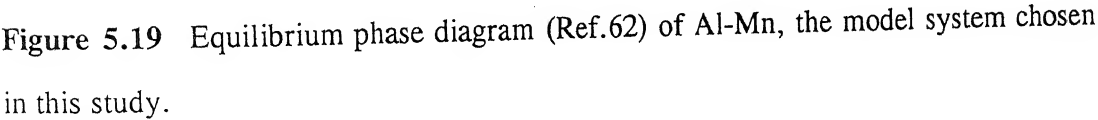
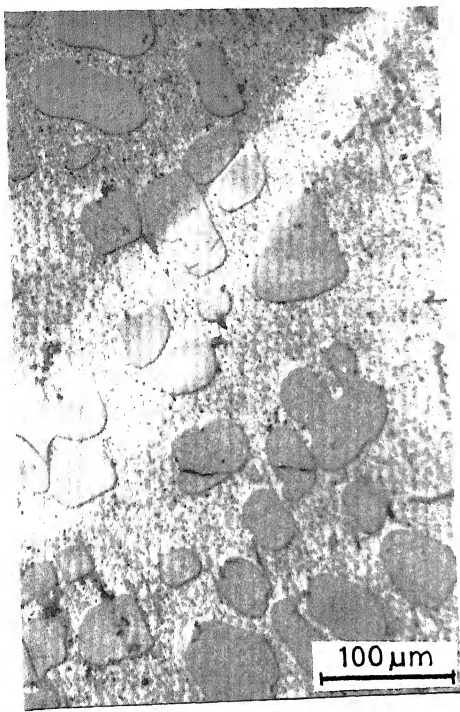
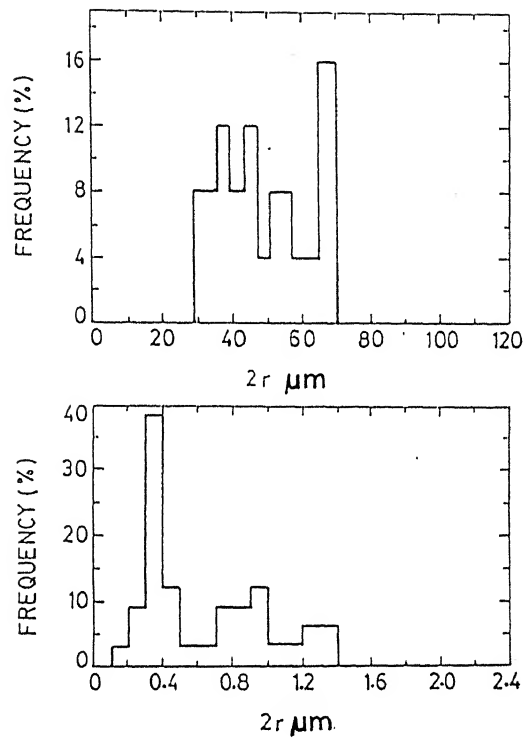


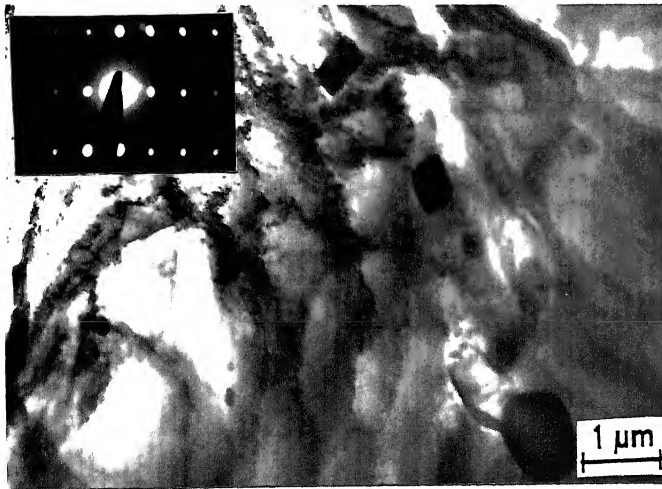
Figure 5.19 Equilibrium phase diagram (Ref.62) of Al-Mn, the model system chosen in this study.



(a)



(b)



(c)

Figure 5.20 (a) Optical micrograph of Al-14 at. Mn alloy showing coarse distribution of Al_6Mn in an $\alpha\text{-Al}$ matrix. (b) Histogram showing the size distribution of Al_6Mn . (c) Transmission electron micrograph of the same. Inset shows the SAD of Al_6Mn along $\langle 220 \rangle$.

5.9 CHARACTERISATION OF CBED PATTERNS OF UNIRRADIATED Al-14 a/o Mn ALLOY

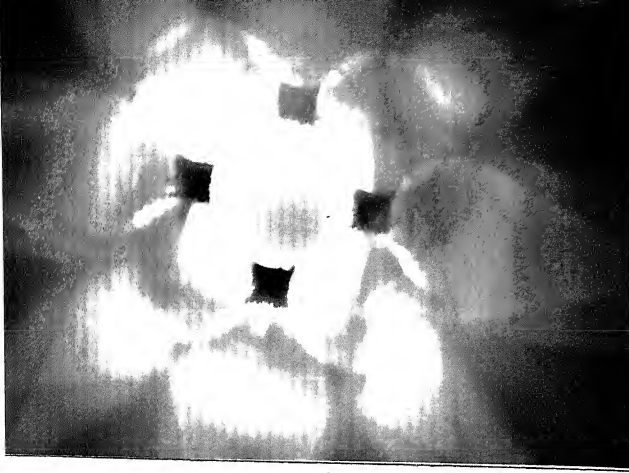
Since the two equilibrium constituents of Al-14 a/o Mn alloy are α -Al (fcc) and orthorhombic Al_6Mn , the important features of CBED patterns of these two crystals will be discussed in sequence below.

5.9.1 Characterisation of CBED Patterns of Unirradiated α -Al

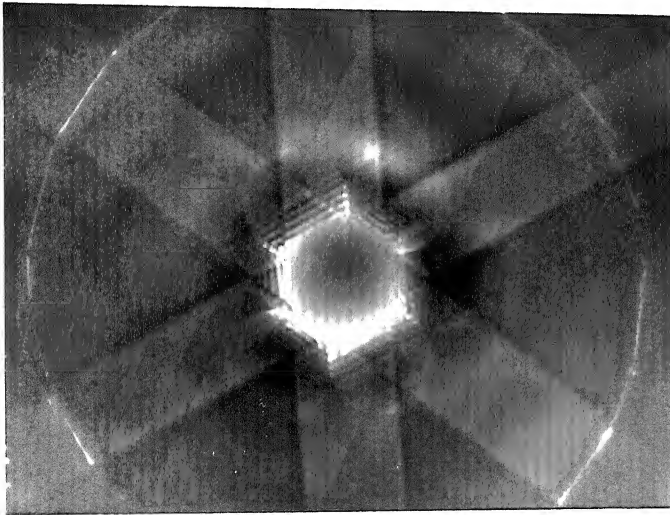
Figure 5.21 shows the CBED patterns of α -Al along three different close-packed directions. These patterns reveal the whole pattern symmetry, three-dimensional information about the reciprocal lattice and the interference pattern within (000) disc, similar to those of bcc α -ferrite discussed earlier. Since the most relevant feature of CBED patterns is the concentric, geometric pattern within (000) disc, further discussion will be restricted only to this feature. Figure 5.22 shows the interference pattern within (000) disc of CBED patterns along the same three zone axes as figure 5.21. These patterns also reveal the projection symmetry along the zone-axis and the intensity oscillations extend from Brillouin zone boundary till almost the centre of the (000) CBED disc. An attempt has been made to compute the CBED patterns of unirradiated α -Al, the details of which are given below.

5.9.2 Computation of CBED Patterns of Unirradiated α -Al

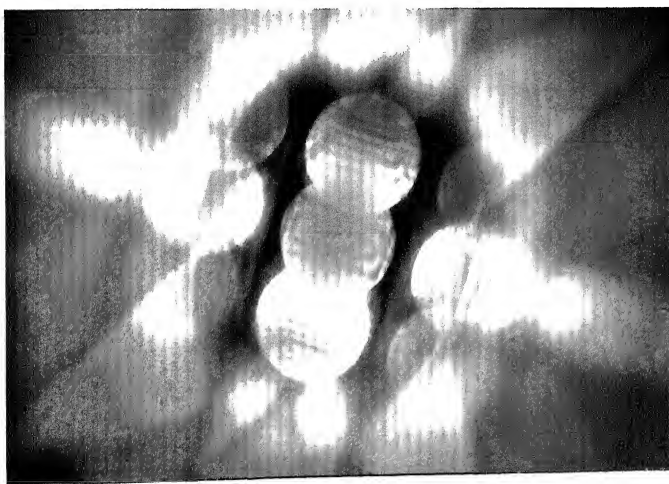
The cause of the interference patterns described earlier is related (Figure 5.23a) to the presence of well separated, simple atom strings (49). Computation of the same for α -Al, along the three close-packed directions has been carried out using EMS software



(a)

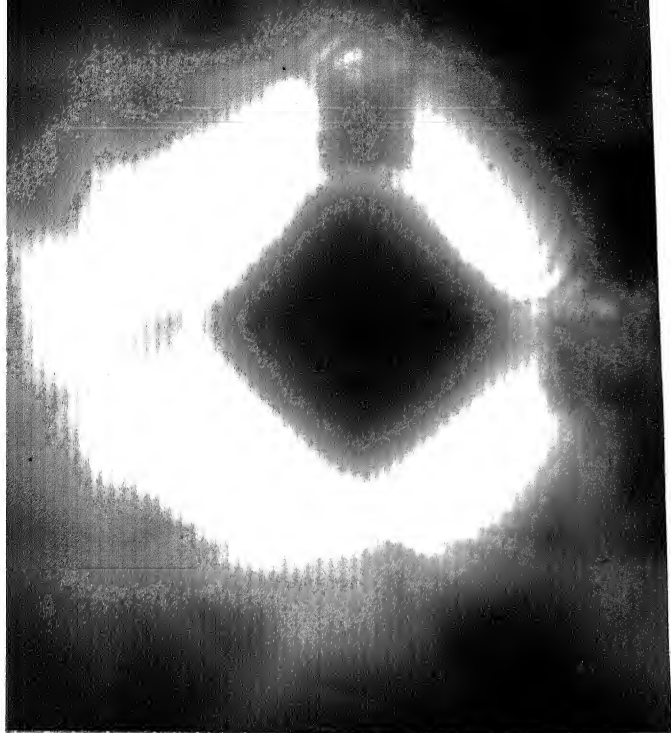


(b)

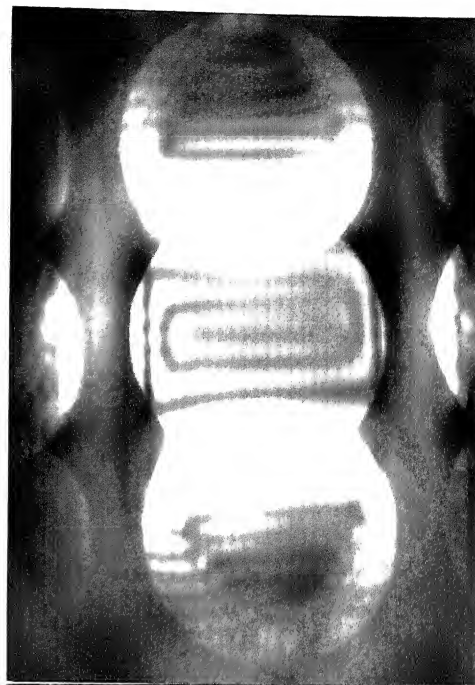


(c)

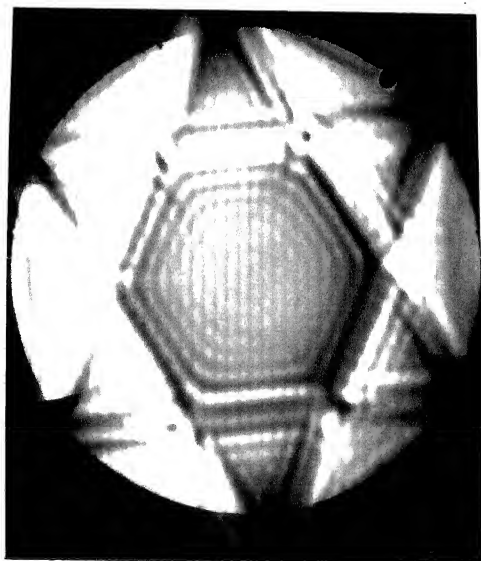
Figure 5.21 CBED patterns of α -Al in Al-14 a/o Mn alloy. The zone axis is along (a) $\langle 200 \rangle$, (b) $\langle 111 \rangle$ and (c) $\langle \bar{1}12 \rangle$.



(a)

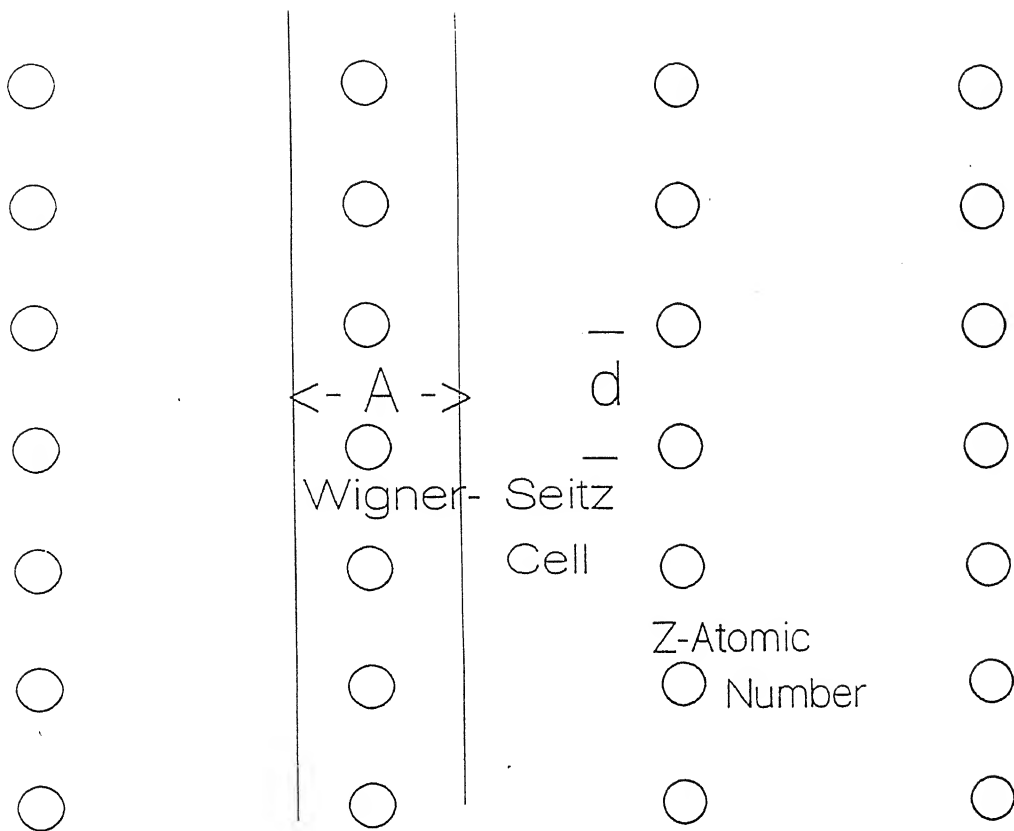


(b)



(c)

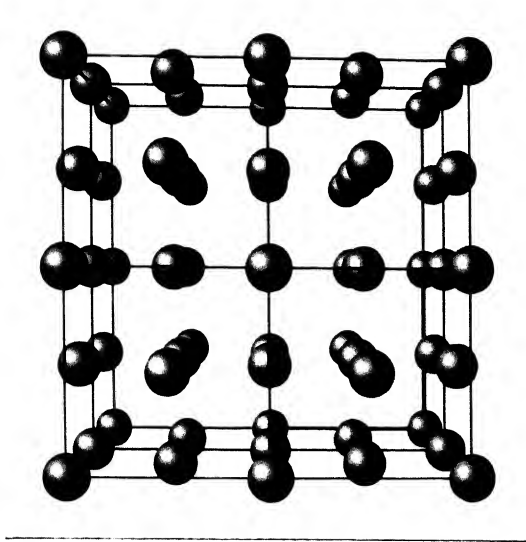
Figure 5.22 CBED patterns of the same as in figure 5.20, showing the ZAP symmetry. (a) 4 fold axis along $\langle 200 \rangle$, (b) 6 fold axis along $\langle 111 \rangle$ and (c) 2 fold axis along $\langle \bar{1}12 \rangle$.



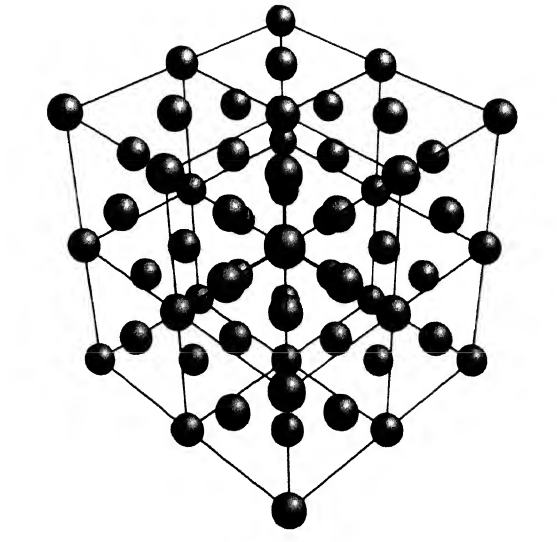
$$\text{String Strength} = (m \times Z \times A) / m_0 \times d$$

(a)

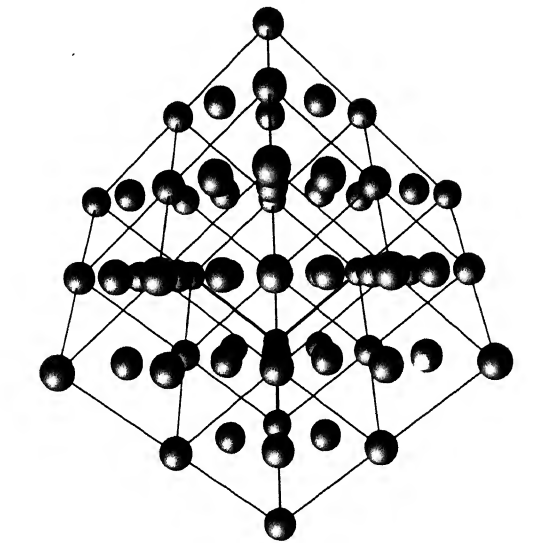
Figure 5.23 (a) Schematic representation of string potentials, in simple crystals. m/m_0 - relativistic mass factor, Z - atomic number, A - area of cross-section of each string and d - interatomic spacing. Calculated (using EMS) atom strings in α -Al along (b) $\langle 100 \rangle$, (c) $\langle 111 \rangle$ and (d) $\langle 112 \rangle$.



(b)



(c)



(d)

Figure 5.23 Continued....

and shown in Figure 5.23b. The incident electrons arrange themselves into a number of Bloch states within the crystal, as a result of strong dynamic, interaction with the crystal potential. The concentric patterns within the (000) disc, observed earlier is due to the interference of the strongly excited Bloch states. Therefore, an attempt has been made to compute the projected potential of the crystal along close-packed directions and the Bloch states excited for various directions of the incident beam. The results of these computations for the input parameters listed in Table V.1, are shown in Figures 5.24 and 5.25. The two-dimensional crystal potential projected along the close packed directions, is distinct, non-overlapping and reflects the projection symmetry, as expected. The projection is computed for $2 \times 2 \times 2$ unit cells. The contour maps of the projected potential in figure 5.24 for various zone axes, have the same distribution as that of the position of atoms, seen along the respective directions (figure 5.23). The Bloch states excited by a dynamic interaction of the incident electrons with simple potentials shown above are calculated, using EMS software. The contour maps of the strongly excited Bloch states are shown in figure 5.25. The intensity at any point in the reciprocal lattice, contributed by these Bloch states i.e., the CBED patterns are computed and shown in figure 5.26, for two typical zone axes. The input parameters of CBED computations are also included in Table V.1. The computed CBED patterns show very good qualitative agreement with the experimental patterns in figure 5.22, especially with respect to the concentric, geometric patterns within the (000) disc.

5.9.3 Characteristics of CBED Patterns of Unirradiated Al_6Mn in Al-14 at/o Mn Alloy

CBED patterns of the orthorhombic Al_6Mn phase ($a = 0.6497 \text{ nm}$, $b = 0.7552 \text{ nm}$ and $c = 0.887 \text{ nm}$) along various zone axes are shown in figure 5.27. The interesting features in these figures pertain to the presence of a large number of HOLZ rings and

Table V.1

Input Parameters for various computations using EMS.

a) CBED Patterns

Accelerating voltage	100 kV
Number of Laue zones	2
Deviation vector, s_g	0.5
Thickness	200 nm
Convergence angle	2.25 or 3
Camera length	50 or 150 mm

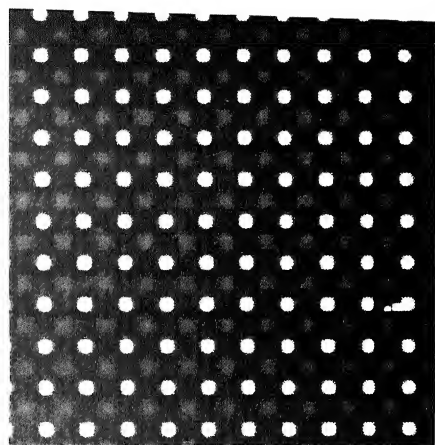
101 'g' vectors are used for computing intensity with 2123 orientations of incident beam.

b) Projected Potential

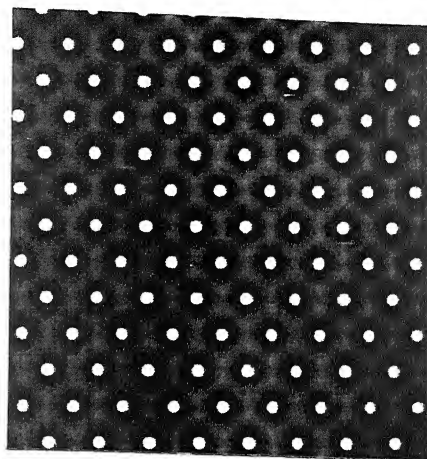
Programme used	pg2
Number of units	64 x 64
Subslices	2

c) Block Waves

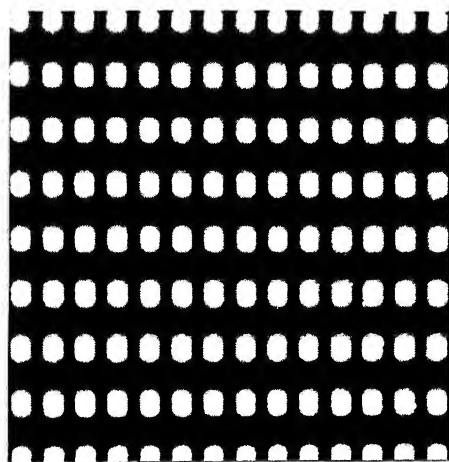
Accelerating voltage	100 kV
Number of beams	81
Thickness	10 nm
n sam. x n row	32 x 32



(a)

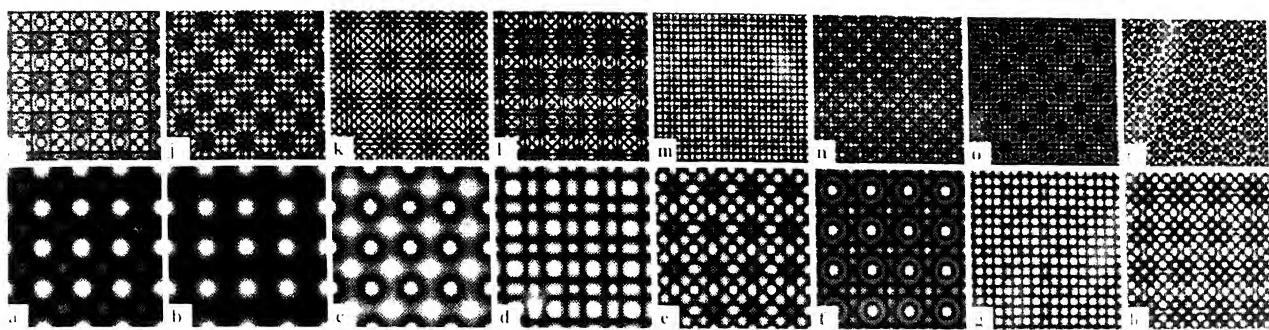


(b)

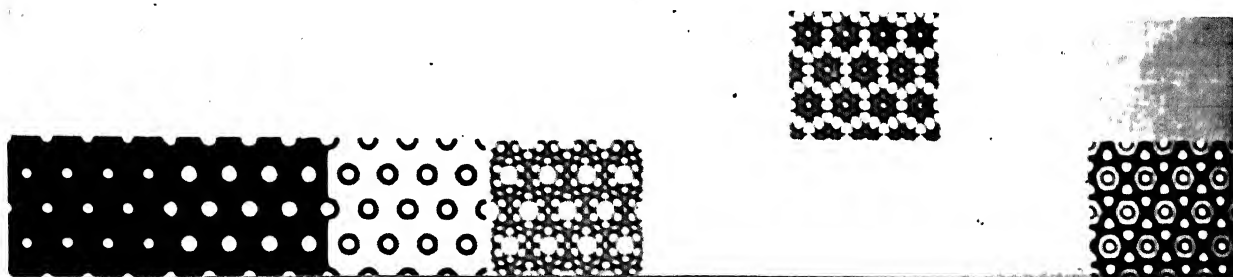


(c)

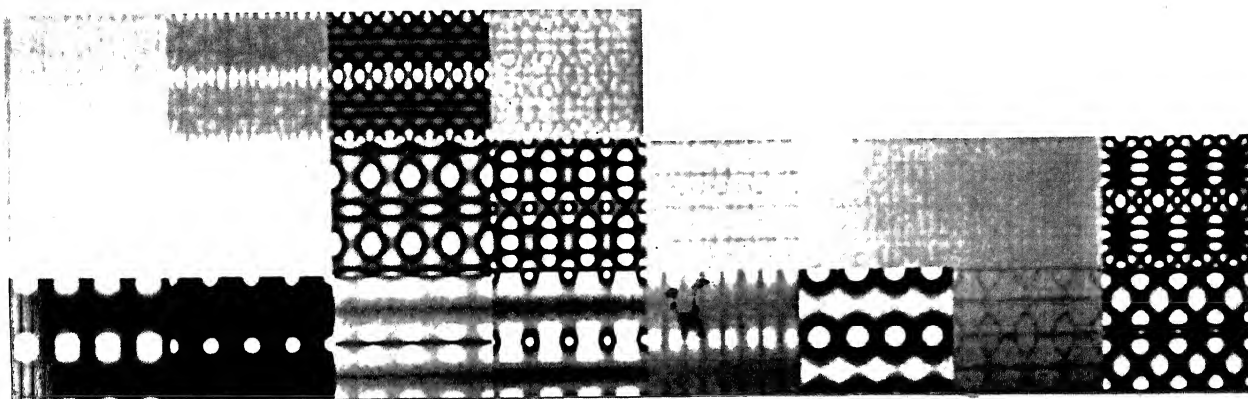
Figure 5.24 Calculated (using EMS) projected potential of α -Al along (a) $\langle 200 \rangle$, (b) $\langle 111 \rangle$ and (c) $\langle 112 \rangle$. The unit cell is sliced into two subslices and calculations are over 64×64 sample points.



(a)

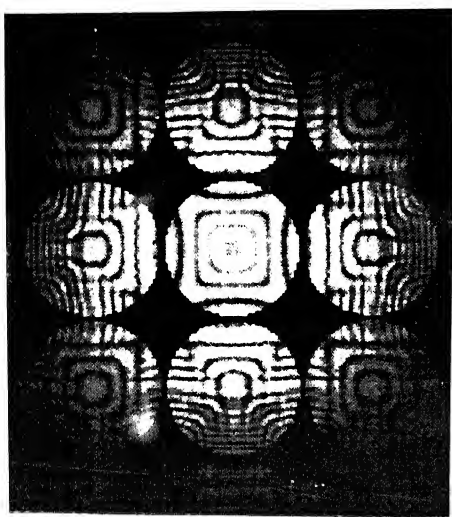


(b)

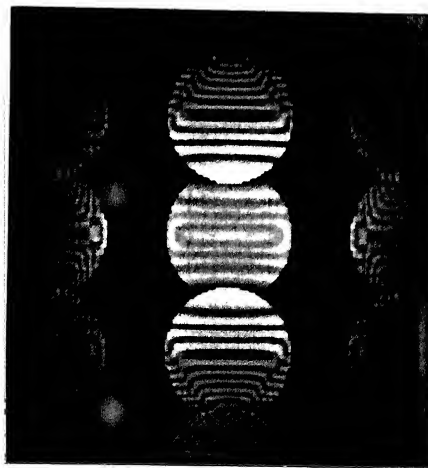


(c)

Figure 5.25 Bloch states excited for an incident electrons of 100 keV along (a) $\langle 200 \rangle$, (b) $\langle 111 \rangle$ and (c) $\langle 112 \rangle$ of α -Al. The input parameters for the computation are given in Table V.1.

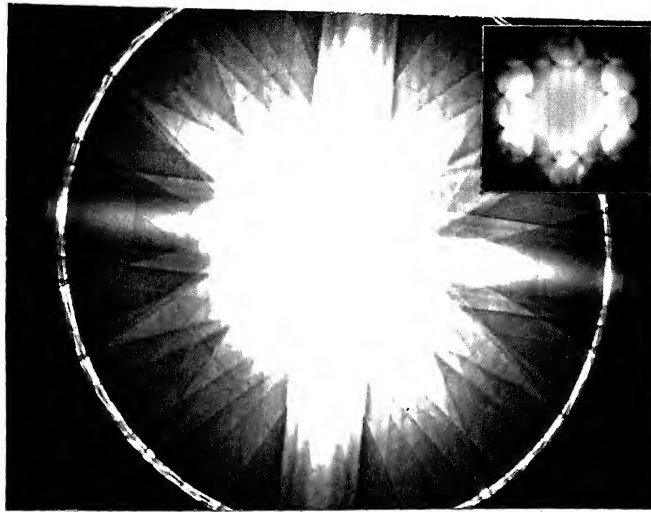


(a)

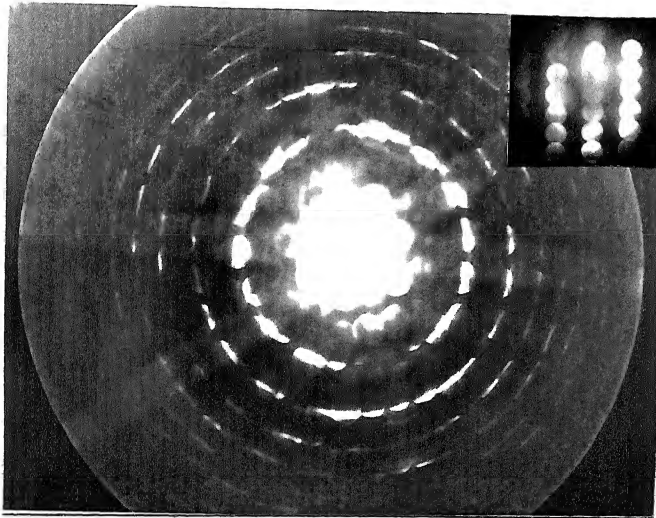


(b)

Figure 5.26 Computed CBED patterns of α -Al along (a) $\langle 200 \rangle$ and (b) $\langle 112 \rangle$ using EMS. 101 reflections and 2123 orientations have been used for the calculations (see Table V.1 for other input parameters).



(a)



(b)

Figure 5.27 Whole pattern symmetry and large number of HOLZ rings in CBED patterns of orthorhombic Al_6Mn along (a) $\langle 001 \rangle$ and (b) $\langle 06\bar{6} \rangle$. Insets show the ZOLZ used for determination of zone axis. As many as six HOLZ rings are clearly visible in (b).

the low background, inelastic scattering at low angles. The large unit cell dimensions are the most favourable factors for the visibility of a large number of HOLZ rings.

Another feature in figure 5.27 is the absence of concentric geometrical patterns in the central disc of CBED patterns. This is due to the following reasons. Unlike the case of α -Al, the unit cell of Al_6Mn is quite complicated and has 28 atoms per unit cell. The position of the two types of atoms is given in Table V.2. The calculation of projected potential of such a crystal along close-packed directions (figure 5.28), shows that the projected potential along all these directions is not distinct and there is a high degree of overlap of potential along adjacent rows of atoms. This explains the absence of the concentric, geometric figures inside (000) disc of CBED patterns of Al_6Mn .

5.10 CHARACTERISATION OF CBED PATTERNS OF ION IRRADIATED Al-14 a/o Mn ALLOY

Since there are two characteristic features of CBED patterns, which change systematically with dose, these changes will be discussed sequentially, in this section. The changes in the first feature, namely, intensity oscillations in (000) disc are clearly shown in α -Al and the second, namely, HOLZ rings in the orthorhombic Al_6Mn . Hence, the results on CBED patterns of these two crystals will be discussed, one after another.

5.10.1 Changes in the Central Disc of CBED Patterns of Ion Irradiated α -Al in an Al-14 a/o Mn Alloy

The presence of simple projected potential in α -Al crystal has provided an important feature i.e. the geometric patterns in the first Brillouin zone which changes (section

Table V.2Atom Positions of Al and Mn in Al_6Mn

Sl. No.	Position or Co-ordinates	Number of Atoms	Type of Atom
1.	(0.457,0,0.25)	4	Mn
2.	(0,0.3,0)	8	Al_1
3.	(0.14,0.0,0.1)	8	Al_2
4.	(0.29,0.32,0.25)	8	Al_3

Total number of atoms/unit cell - 28.

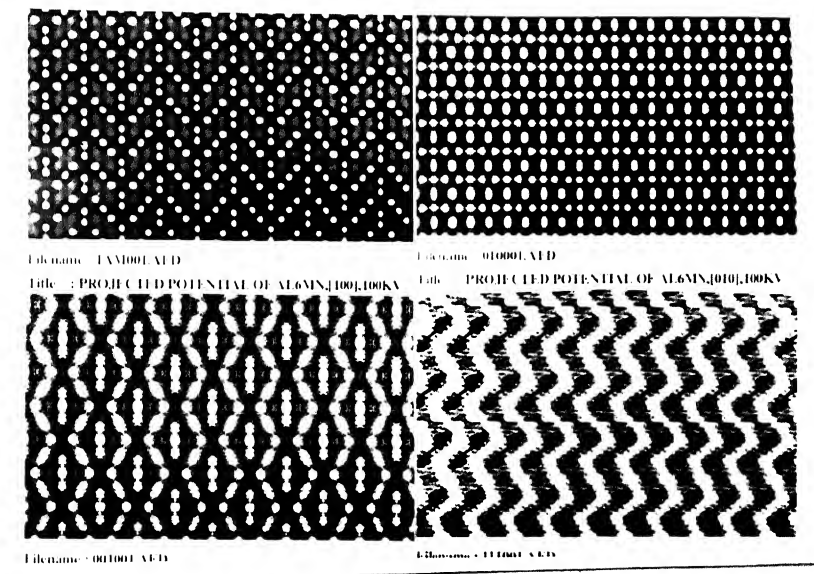
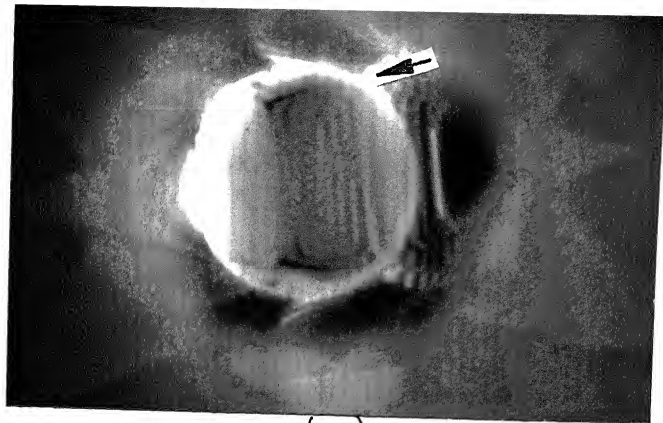


Figure 5.28 Projected potential of orthorhombic Al_6Mn in Al-14 a/o Mn alloy along four directions. Absence of well separated, string potential is confirmed.

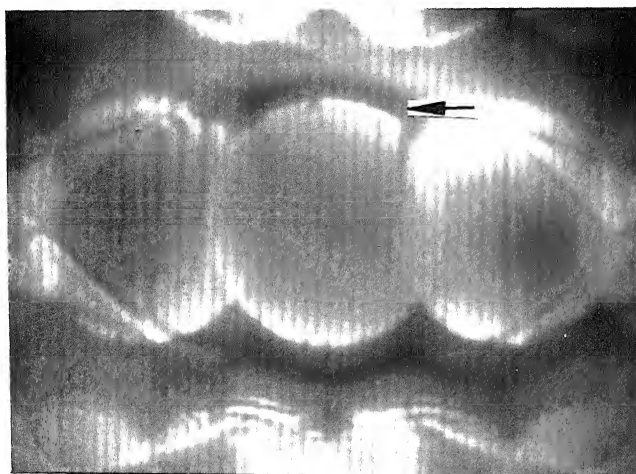
5.5.1) during ion irradiation. The series of CBED patterns in figure 5.29 shows CBED patterns of α -Al irradiated with 100 keV helium ions to dose levels ranging from 10^{13} to 5×10^{16} ions/cm². Irradiation to a dose level as small as 10^{13} ions/cm² with 100 keV helium ions leads to the retention of the fine intensity oscillations within the (000) disc of CBED pattern (figure 5.29a). These extend from the Brilluoin zone boundary to the center of the (000) disc. An increase in the dose level upto 10^{16} ions/cm² reduces the angular range of the interference pattern seen within (000) disc, as can be seen in figure 5.29b. The interference patterns are confined to regions only near the Brilluoin zone boundary. Further increase in the dose level upto 5×10^{16} ions/cm², has resulted in the complete disappearance of the interference pattern (figure 5.29c), though the whole pattern symmetry (figure 5.30a) and the SAD (figure 5.30b) remain essentially unaffected. Similar results along other zone axes were also obtained.

Though the microstructure of α -Al at these dose levels was devoid of clusters, the dose is quite high for low melting phase like α -Al, to show clustering effects. In fact, dislocation loops in α -Al after implantation with helium to lower dose levels at 300 K have been reported in earlier studies (64-66). It is possible that the damage peak of 100 keV helium is not completely confined to the thickness of the electron transparent portion of the thin foils.

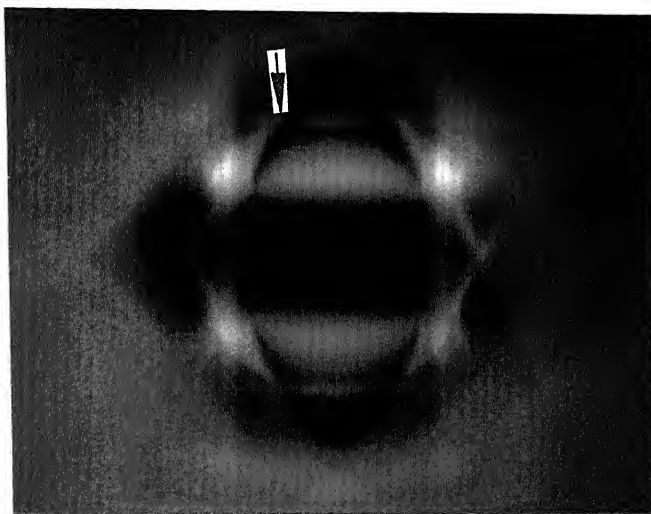
The changes in the CBED patterns of α -Al during irradiation with argon ions, were generally the same as those of helium. However, significant differences were observed in the values of the dose levels required to produce the same effects. Typical CBED patterns of α -Al irradiated with 100keV argon ions to a small dose level of 5×10^{12} ions/cm², is shown in figure 5.31a. This shows that even at such low dose level, a reduction in the angular range of the interference fringes is observed. The interference fringes in (000) disc are confined to only a narrow angular range near the Brillouin



(a)

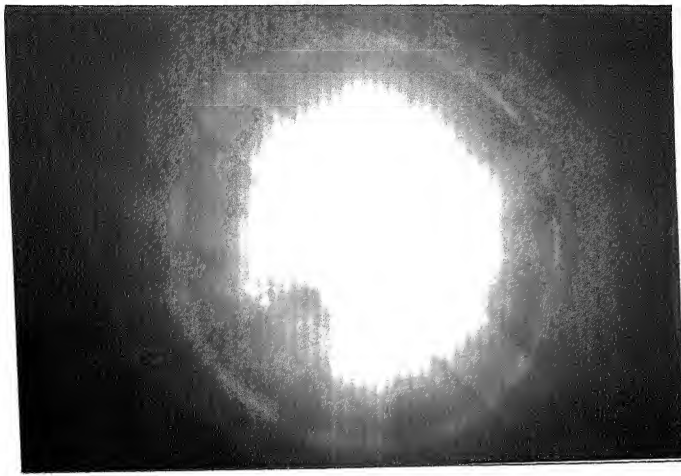


(b)

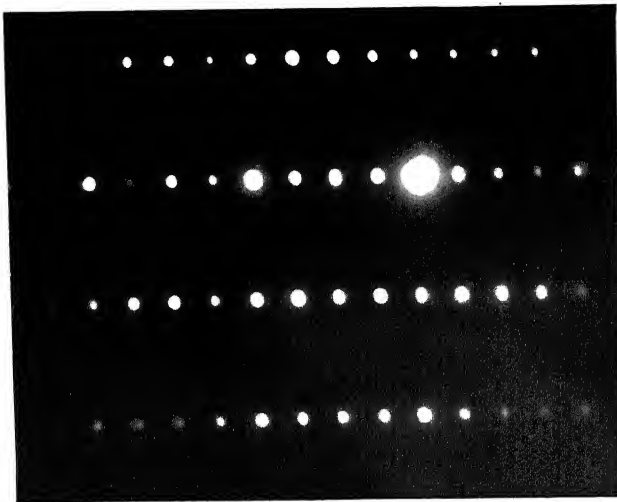


(c)

Figure 5.29 Effect of irradiation with 100 keV helium ions in the CBED patterns of α -Al, along $\langle \bar{1}12 \rangle$. The dose levels used are (a) 10^{13} , (b) 10^{16} and (c) 5×10^{16} ions/cm². Gradual disappearance of interference patterns is seen. Arrow mark shows the Brillouin zone boundary.

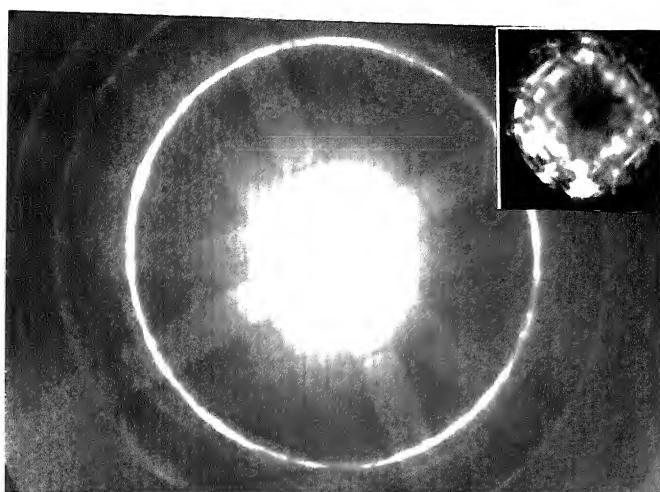


(a)

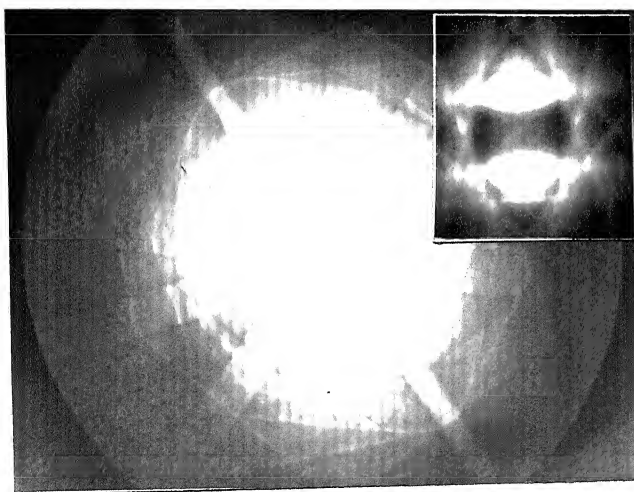


(b)

Figure 5.30 Retention of the whole pattern symmetry in the CBED pattern of α -Al, along $\langle 012 \rangle$ irradiated with 100 keV helium to a dose level of 5×10^{16} ions/cm². The corresponding selected area diffraction pattern in (b) shows no signature of defects. Compare (b) with CBED pattern in figure 5.29c.



(a)



(b)

Figure 5.31 Effect of irradiation with 100 keV argon ions in α -Al of Al-14 a/o Mn alloy. Retention of whole pattern symmetry after a dose level of (a) 5×10^{12} and (b) 10^{13} are seen. Inset in (a) shows the (000) disc, with faint, distorted intensity oscillations. Inset (b) shows the complete absence of the interference fringes.

zone boundary. An increase in dose upto 10^{13} ions/cm², retains the whole pattern symmetry (figure 5.31b) while leading to the complete disappearance of the fringes (inset of figure 5.31b) within the (000) disc of CBED pattern. Irradiation upto a dose level of 2×10^{14} ions/cm², did not result in the formation of point defect clusters. The microstructure of α -Al (figure 5.32), irradiated upto a dose level of 2×10^{14} ions/cm², does not show formation of point defect clusters, in the form of either dislocation loops or voids.

Thus, the above results can be summarised as follows: the angular range of the interference pattern in the (000) disc of CBED patterns of α -Al, reduced after irradiation using helium and argon ions, at low dose levels followed by complete disappearance at higher doses. There was no evidence for the formation of point defect clusters in the range of dose levels in which these changes were observed.

5.10.2 Changes in the High Order Laue Zone (HOLZ) Rings of CBED

Patterns of Irradiated Al₆Mn in Al-14 at/o Mn Alloy

Figure 5.33 shows a series of diffraction patterns of Al₆Mn phase irradiated with 100 keV helium ions to different doses. The feature of interest is the number of HOLZ rings in the CBED patterns of Al₆Mn in figure 5.33 (a and b). Irradiation upto a low dose of 10^{13} ions/cm², had retained four to five order Laue zones (figure 5.33a). Figure 5.33b shows the CBED pattern of Al₆Mn irradiated with 100keV helium ions upto a dose of 5×10^{16} ions/cm². There is a significant reduction in the strength of large angle scattering, reducing the visibility to only FOLZ. In fact, meaningful studies had to be restricted to this dose level, since beyond this dose, another reaction, namely amorphisation of Al₆Mn had set in. Further increase in dose upto 10^{17} ions/cm² resulted in only ZOLZ in the CBED pattern (57,66). But, there is a weak,

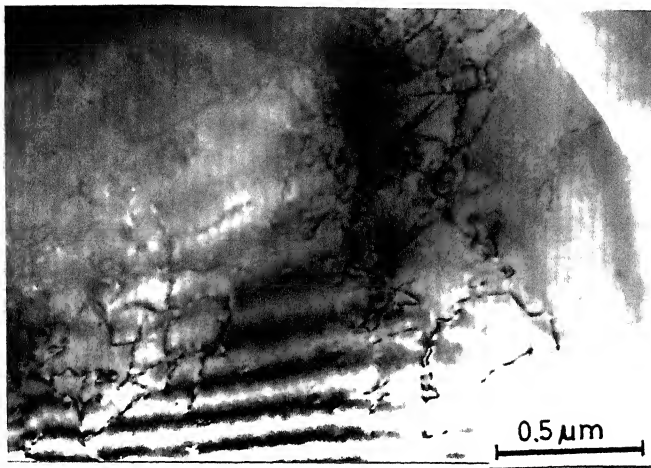
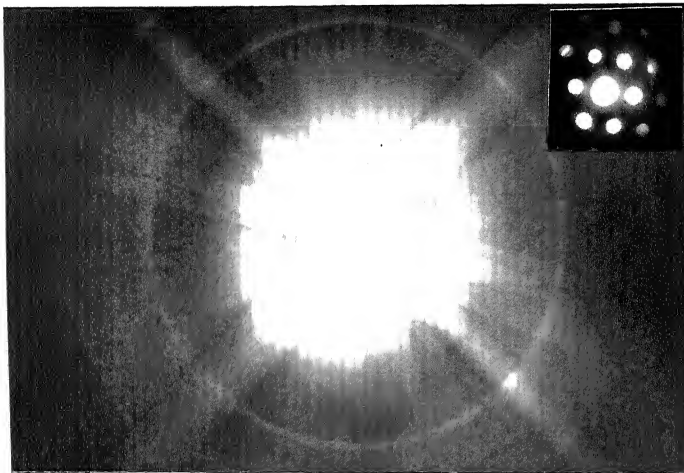


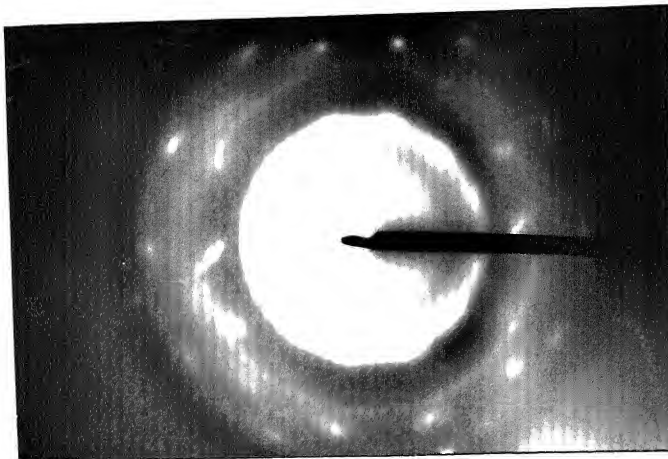
Figure 5.32 Absence of point defect clusters at low doses: Microstructure of α -Al of Al-14 at/o Mn alloy irradiated with 100 keV argon ions upto a dose of 2×10^{14} ions/cm².



(a)



(b)



(c)

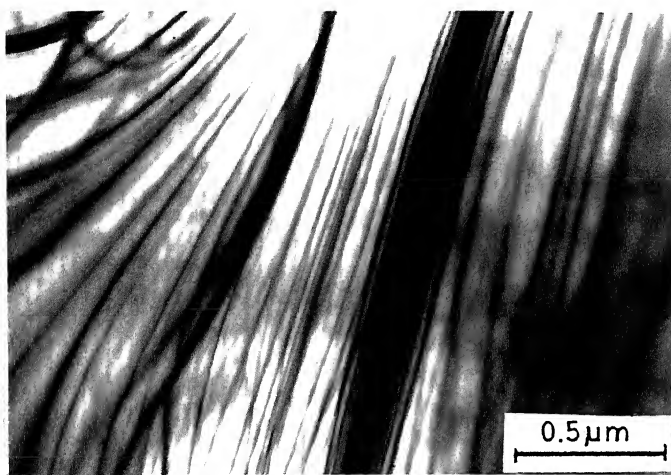
Figure 5.33 Reduction in the number of HOLZ rings in CBED patterns of Al_6Mn , irradiated with 100 keV helium ions. The dose levels are (a) 10^{13} and (b) 5×10^{16} ions/ cm^2 . The selected area diffraction pattern in (c) shows the diffuse ring indicating the onset of amorphisation of Al_6Mn at a dose level of 10^{17} ions/ cm^2 .

diffuse ring in the SAD pattern, as shown in figure 5.33c. This is a consequence of amorphisation of Al_6Mn crystal (66), which is not the subject of the present study. The microstructures at different dose levels, (figure 5.34 (a and b)), do not show any evidence for the presence of defects. In fact, the microstructure of Al_6Mn shows the presence of strong bend contours and is devoid of any other feature. Even when the dose was increased to 10^{17} ions/cm², defect clusters were not found to form in the crystal, as can be seen in figure 5.34b. Instead, uniform distribution of fine, amorphous zones was observed.

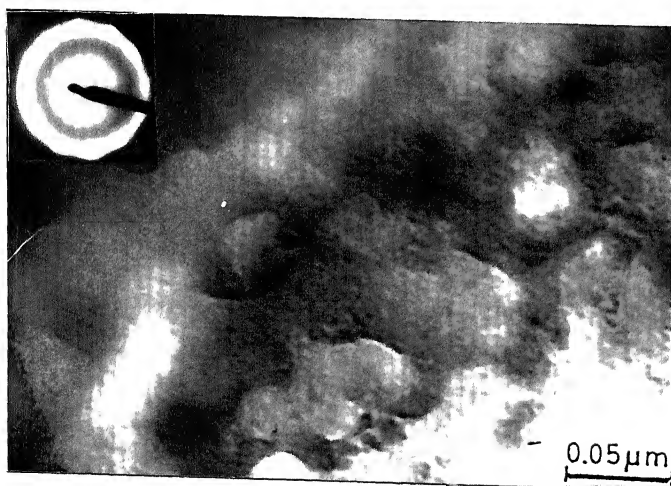
Irradiation with 100keV argon ions showed similar results, as can be seen in figure 5.35. While a dose level of 5×10^{12} ions/cm², had resulted in a considerable degree of loss of strength of large angle scattering (figure 5.35a), the microstructure and SAD did not show any change. The SAD pattern is shown in the inset of figure 5.35a. Similar trend is observed (figure 5.35b) at a dose level of 10^{13} ions/cm². Additional dose upto 2×10^{14} ions/cm², led to the onset of the amorphisation reaction (figure 5.35c). The inset in figure 5.35c shows the presence of diffuse, broad rings confirming the amorphisation of Al_6Mn . Hence, conclusions were based on CBED patterns of Al_6Mn irradiated only upto dose levels less than 10^{14} ions/cm².

The results of these studies can be summarised as follows:-

- ** A gradual decrease in the number of HOLZ rings with increase in dose is seen. Complete disappearance of the discs in ZOLZ is observed at higher doses, as a consequence of amorphisation of the crystal.
- ** The SAD patterns do not show any indication of the presence of defects upto a dose level of 2×10^{14} ions/cm², though CBED patterns reveal a significant reduction in the extent of large angle scattering. Similar behaviour is observed



(a)



(b)

Figure 5.34 Microstructure of Al_6Mn after 100 keV helium irradiation upto dose levels of (a) 10^{13} and (b) 10^{17} ions/cm². Microstructure in (a) is devoid of defect clusters. The formation of coarse, amorphous regions at higher dose is seen in (b).

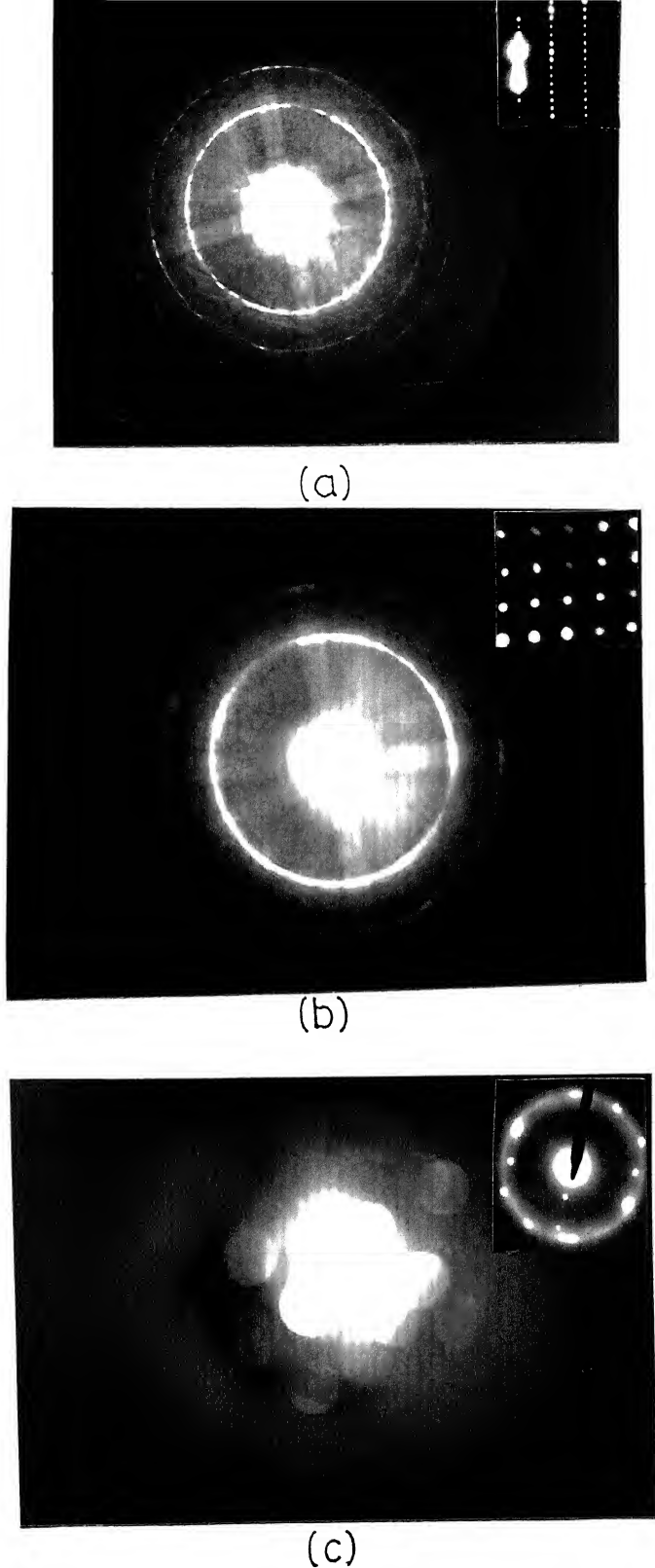


Figure 5.35 Effect of 100 keV argon ion irradiation in HOLZ rings of CBED patterns of Al_6Mn . The dose levels used are (a) 5×10^{12} , (b) 10^{13} and (c) 2×10^{14} ions/cm². The insets show the SAD's. There is no signature of defects in the SAD's of (a) and (b) while (c) shows diffuse, broad ring indicating the onset of amorphisation of Al_6Mn .

during irradiation with helium ions upto dose levels two to three orders of magnitude higher than argon ions.

- ** There is a systematic deterioration of the Whole Pattern symmetry also. Symmetry loss is due to the loss of crystallinity and amorphisation of Al_6Mn during irradiation. However, it is to be noted that the reduction in the number of HOLZ rings of Al_6Mn is observed at dose levels wherein the crystallinity was retained.
- ** Though a similar trend in the visibility of HOLZ rings is expected in $\alpha\text{-Al}$, the availability of only two HOLZ rings within the angular range of visibility does not offer much scope for viewing these changes, in a systematic way for a large number of dose levels.
- ** The microstructures of $\alpha\text{-Al}$ and Al_6Mn , irradiated with the two ions to the dose levels of interest, do not show any clustering of defects into loops or bubbles. In the range of dose levels studied in this work, the individual point defects generated during implantation remained as point defects, without clustering into loops or fine voids. This is a unique advantage of ordered, intermetallic line compounds, like Al_6Mn , with high melting point. The high ordering energy of such compounds does not favour the formation of point defect clusters and hence retain point defects (67).
- ** The differences between helium and argon ion irradiation have been explained in terms of larger number of displacement of lattice atoms from their equilibrium positions by heavier argon atoms than helium and more lattice distortion due to accommodation of argon atoms.

The results discussed so far, confirm the existence of distinct features in CBED patterns which respond systematically to the introduction of point defects. Ion irradiation causes a gradual disappearance of two characteristics of CBED patterns, namely, the concentric, geometrical features in the (000) disc and the number of HOLZ rings.

5.11 IDENTIFICATION OF ORIGIN OF CHANGES IN CBED PATTERNS OF ION IRRADIATED CRYSTALS

In order to identify the origin of the changes in CBED patterns discussed so far, computations of CBED patterns were carried out using EMS code. The α -Al is chosen as representative of both the crystals studied, the fcc α -Al and the bcc α -Fe, since the effects observed are same. Similarly, Al_6Mn is chosen as representative of a large unit cell, like M_{23}C_6 . The irradiation of energetic ions causes displacement of a large number of host lattice atoms from their equilibrium position, introducing a high degree of static displacement disorder. The degree of disorder increases as the dose level increases. Introduction of such a disorder in the crystal strongly modifies two factors, namely, the string potential and the static term in the Debye-Waller factor. These two changes influence the angular dependance of diffracted intensity of electrons, which is discussed in detail below.

The static displacement disorder of the crystal destroys the well defined, atomic rows as shown schematically in figure 5.36. This would lead to an overlap of adjacent atomic strings, with the consequent weakening of the string potential. This process is expected to distort the two-dimensional projected potential, leading to gradual disappearance of the geometric patterns. The weak, persistent retention of the intensity oscillations specially around the Brilluoin zone boundary is due to the strong scattering at these boundaries. The second factor, namely, the static term in the Debye-Waller term, has

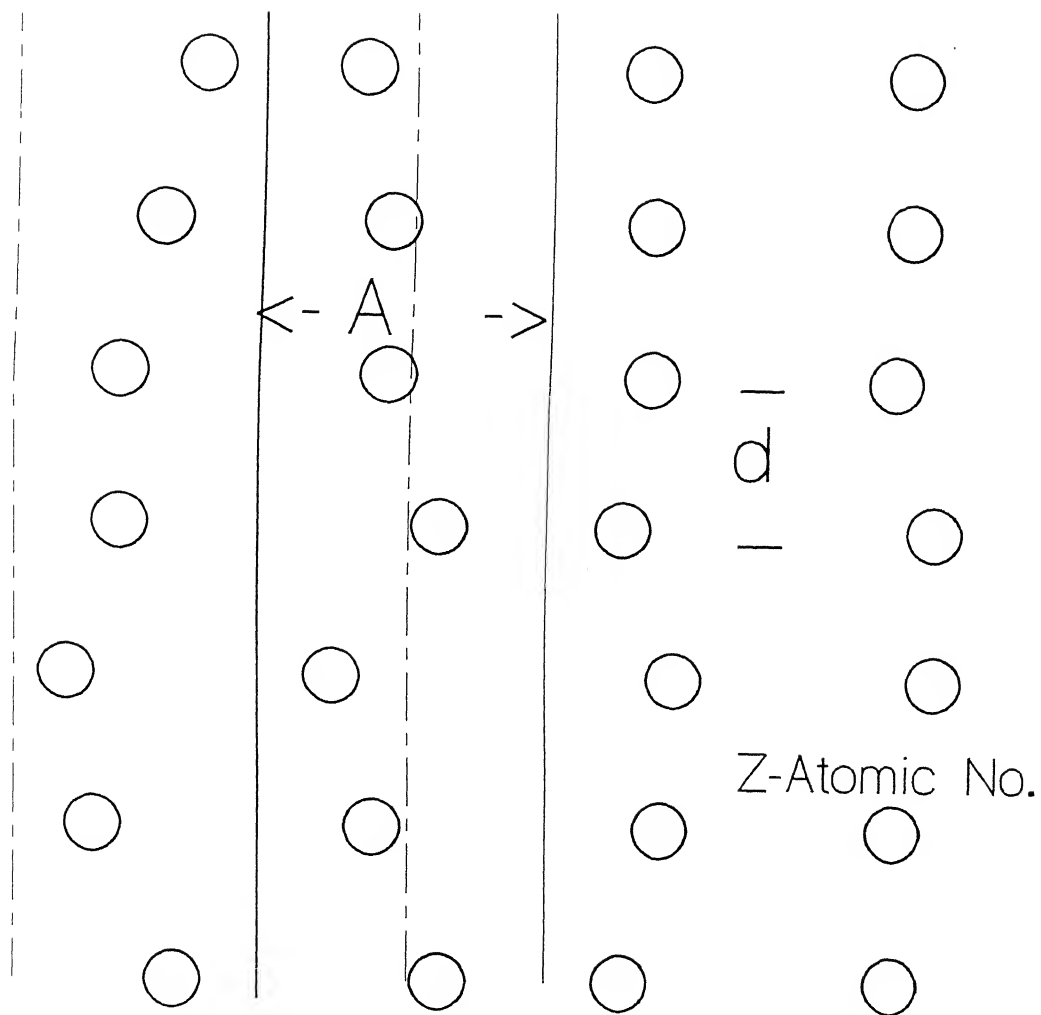


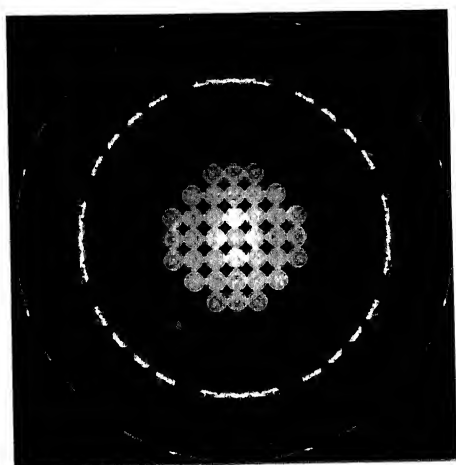
Figure 5.36 Schematic representation of the overlapping atom strings, in a crystal containing defects (compare with figure 5.23).

a direct influence on the strength of large angle scattering (49,68). This qualitative understanding of the observed trends in the results discussed above, would be supported by the computations using the EMS code, in the present section.

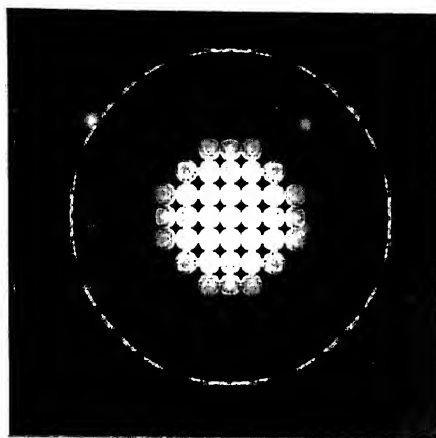
The static displacement disorder in the lattice was introduced into the lattice by artificially increasing the Debye-Waller factor- the temperature factor which takes into consideration the displacement of atoms due to phonon vibrations. Under adiabatic approximations, the static displacement of the atom can be regarded as equivalent to thermal disorder. Therefore, an increase in Debye-Waller factor is assumed to represent the static displacement of atoms in implanted crystals.

Figure 5.37 shows the computed CBED patterns of α -Al and Al_6Mn along a representative zone axis, for different Debye-Waller factors. The reduction in the number of HOLZ rings in this figure is a reflection of the reduction in the strength of large angle scattering. The disappearance of the geometric patterns in (000) disc of computed CBED patterns of α -Al, with increase in Debye-Waller factor is shown in figure 5.38. These results of the computed CBED patterns agree well with the experimental results explained earlier. Having shown that there exists a qualitative agreement between the experimental and computed CBED patterns, the next attempt is to identify the origin of these changes.

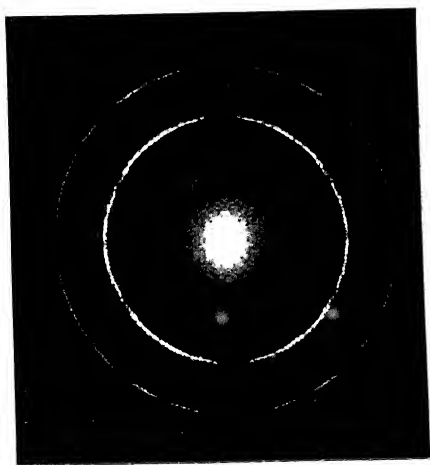
It is known that the concentric, geometric pattern within (000) disc is related to the existence of separate, simple, string potentials, in the diffracting crystal. Therefore, it is possible to intuitively predict that the observed disappearance of the same must be related to the string potentials. Hence, computation of the projected potential of lattice was carried out, with different values of Debye-Waller factors. Figure 5.39 shows that there is a considerable dispersion of the projected potential, for various projection directions. Similar computation for Al_6Mn was not considered useful, since even in



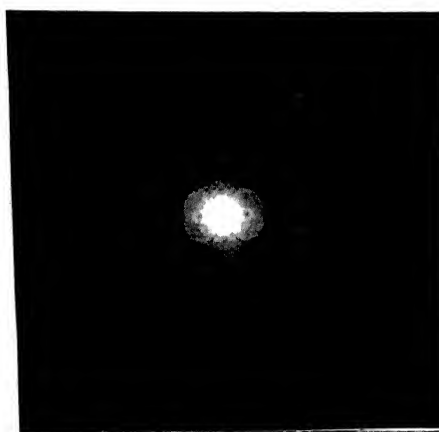
(a)



(b)



(c)

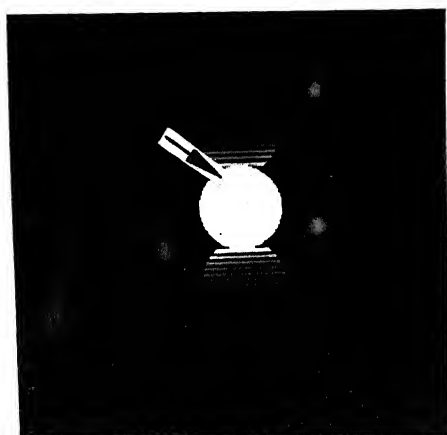


(d)

Figure 5.37 Computed CBED patterns of (a) and (b) α -Al and (c) and (d) Al_6Mn crystals, with different Debye-Waller (DW) factors. (a) and (c) - DW factor is $.005 \text{ nm}^{-1}$ and (b) and (d) - DW factor is $.3 \text{ nm}^{-1}$. The reduction in number of HOLZ rings with increase in DW factor for both crystals is clearly seen. Computations were carried out using 101 reflections and 2123 orientations, with $\alpha = 2.25$ (see Table V.1 for input parameters).

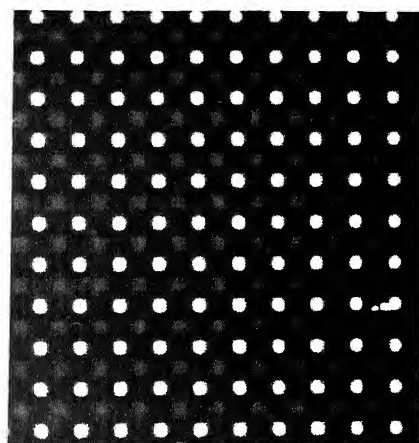


(a)

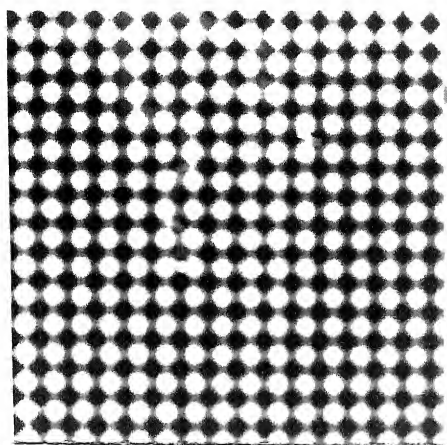


(b)

Figure 5.38 Computed CBED patterns of α -Al along $\langle 112 \rangle$ for different DW factors, (a) $.005$ and (b) $.3 \text{ nm}^{-1}$. Computations were carried out for 101 reflections using 2123 orientations of incident 100 keV electron beam. α was 3 and camera length was maintained as 150 mm. Arrow mark shows the presence of weak, intensity oscillations, only near the Brilluoin zone boundary.



(a)



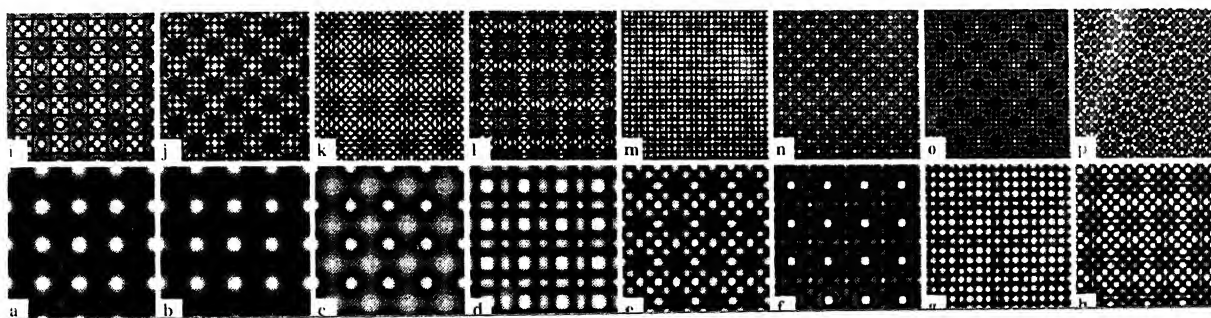
(b)

Figure 5.39 Computed projected potential of α -Al along $\langle 200 \rangle$ for different DW factors of (a) 0.005 and (b) 0.3 nm^{-1} . The smearing of the projected potential is seen with increase in DW factor. The unit cell is divided into two subslices and 64×64 sample points were used for computation.

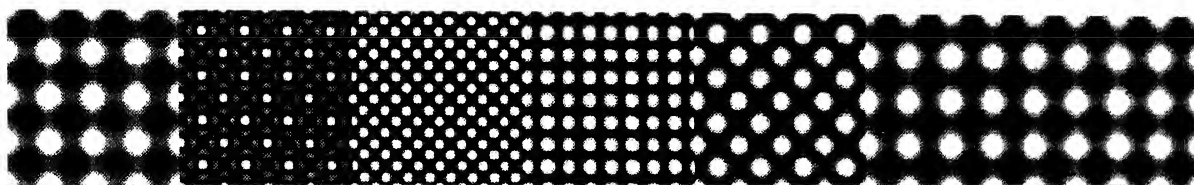
perfect crystal, Al_6Mn does not exhibit strong, simple, string potentials. The Bloch states of the incident electrons excited by the dispersive potential of $\alpha\text{-Al}$ crystal with high D-W factors, are also weak and dispersed (figure 5.40). Hence, the basic requirement to produce the observed interference pattern, i.e., strong excitation of non-dispersive, Bloch states is not satisfied in crystals with high static displacement disorder. Thus, the cause of disappearance of the geometrical pattern in (000) disc of $\alpha\text{-Al}$, during irradiation could be attributed to the weakening and smearing of the string potential, due to point defects.

The second observation, namely, the reduction in the large angle scattering is a direct manifestation of the increase in the static term in the D.W. factor.

These results show that there exists good agreement between the changes in the CBED patterns obtained experimentally in implanted crystals of $\alpha\text{-Al}$ and Al_6Mn and the computed images using Debye-Waller factor to represent the static displacement disorder. The changes being the (a) gradual disappearance of interference patterns within the (000) discs of CBED patterns and (b) the reduction in the number of HOLZ rings. These two features are demonstrated using two specific crystals, in a model system. It is expected that the same processes must be operative for any other crystal with similar characteristics, namely simple, isolated projected potential in one case and high unit cell dimensions for the other. These results suggest that CBED is a promising technique with an excellent scope for the study of point defects. However, it is to be remembered that the same effects would be observed in the CBED patterns, whenever there is a severe displacement of atoms from their equilibrium positions, irrespective of the cause of the displacement. The exact source of displacement could be quenching (69), phase transformation (32) or fatigue loading (70,71). Therefore, the identification of the type of defect causing the 'static displacement disorder' needs to be recognised based on the specific situation.



(a)



(b)

Figure 5.40 Bloch states excited for 100 keV incident electrons along $\langle 200 \rangle$ of α -Al for different DW factors, (a) 0.005 and (b) 0.3 nm^{-1} . Increase in DW factor has resulted in excitation of smeared Bloch states.

5.12 QUANTIFICATION OF POINT DEFECTS

The methods explained in earlier sections illustrate how the two features of CBED patterns of irradiated crystals, namely, the intensity of large angle scattering and the interference pattern within the (000) disc of ZOLZ help to identify qualitatively, the increase in the density of point defects. Quantification of the concentration of point defects has been attempted, but with little progress. It was felt that if $\langle u^2 \rangle$ - the average mean square displacement corresponding to each dose could be identified, by quantitative comparison of the rocking curves obtained experimentally and using computations, it may be possible to arrive at the density of point defects. It is to be remembered that even this step is difficult in view of the necessity to compare equivalent intensity values (either elastic or inelastic), while trying to compare experiments and computations. Assuming that it is possible to arrive at such meaningful comparisons if one proceeds along the same lines as that of determination of low order structure factors, it is worthwhile to find out if the value of $\langle u^2 \rangle$ can be used further to arrive at the point defect density (72).

One of the methods considered was to make use of static lattice calculations to calculate the mean square displacement based on the assumed lattice relaxation around each point defect. However, in these calculations, though it is possible to arrive at $\langle u^2 \rangle$ values for dilute concentrations of point defects, the reverse problem of obtaining point defect density for given values of $\langle u^2 \rangle$ cannot be handled easily. Therefore, it appears that the evaluation of quantitative values of concentration of point defects based on CBED patterns is very difficult despite the satisfactory qualitative agreement in the changes in the experimental and computed CBED patterns with increase in density of point defects.

5.13 SIMILARITIES IN THE SIGNATURES OF POINT DEFECTS IN CBED PATTERNS OF MODEL SYSTEM AND 9Cr-1Mo WELDMENT

The simulation studies on simple, model binary system to understand the influence of ion irradiation on the CBED patterns, suggest that the point defects introduce characteristic changes in (1) the interference pattern within the (000) disc and (2) the number of HOLZ rings of CBED patterns of crystals with point defects . These changes have been identified as due to static displacement disorder caused by point defects.

Based on this background information, if the results on the two crystals of 9Cr-1Mo welds, α -ferrite and $M_{23}C_6$ are analysed, it is seen that the observations in the two crystals are similar to those of the model system. The interference pattern in (000) disc of α -ferrite, deteriorate with increase in dose. The number of HOLZ rings in the CBED patterns of $M_{23}C_6$ with large unit cell dimension, reduce with increase in dose of either helium or argon ions. In addition, post-irradiation annealing of defects, causes the reversion to the original defect-free crystal, in which large number of HOLZ rings could be seen. These results, when compared with those observed in model crystals, suggest that the characteristic changes are caused only by the point defects introduced during irradiation.

Thus, the attempt to identify characteristic signatures of isolated, point defects in the two equilibrium crystals of 9Cr-1Mo welds using CBED has been successful.

5.14 SUMMARY

The possibility of applying CBED technique for the study of point defects in four crystals subjected to low doses of ion irradiation has been studied. A systematic study of changes in the CBED patterns of ion irradiated crystals of α -ferrite and $M_{23}C_6$ in welds of 9Cr-1Mo steel has been carried out. Two distinct features of CBED patterns have been identified which contain information about the presence of point defects. These are the intensity oscillations in the (000) disc of CBED pattern of simple crystals and the large number of HOLZ rings in those crystals with high unit cell dimensions. These two features show unique, systematic changes with change in the concentration of point defects i.e., the dose and the post-irradiation anneal.

In order to identify the origin of the observed changes, detailed experiments and computations have been carried out in a model alloy, an Al-14 at/o Mn alloy. It is found that the changes in the CBED patterns of the two crystals in this system are similar to those in the commercial alloy. A detailed comparison of the experimental results with those of computations, showed that there is a very good qualitative agreement between the experimental and computed CBED patterns. The origin of the observed changes is identified to be the static displacement disorder of the lattice.

The presence of these two signatures of point defects in CBED patterns is of considerable importance especially since conventional electron microscopy does not offer much scope for the study of point defects. Moreover, there is no other technique which can be used to identify the presence of point defects in localised regions, at these concentrations. It has been demonstrated that there is no visible change in the selected area diffraction patterns. The conventional techniques which are normally used for the study of point defects like X-ray diffraction, dilatometry and positron lifetime spectroscopy require larger size of the irradiated samples. However,

in situations wherein defects are generated in localised regions as in the case of ion irradiation, no technique has been found suitable, so far, for the identification of point defects. In the light of these facts, the presence of the two characteristic features in CBED patterns of ion irradiated crystals which are sensitive to concentration of point defects offers an attractive method for identification of point defects.

REFERENCES

1. P. Patriarca, Proc. Conf. on "*Ferritic Alloys for use in Nuclear Energy Technologies*", Eds. J.W. Davis and D.J. Michel, TMS-AIME, New York (1984) p.107
2. C.V. Sundaram, P. Rodriguez and S.L. Mannan, *IE(I) Journal-MM* 67, Sept. (1986) 1
3. P. Rodriguez, S.L. Mannan and Baldev Raj, Proc. Seminar on "*Fast Reactor Fuel Cycle*", Vol.II, Feb. 10-12, (1986), IGCAR, Kalpakkam, India, p. 53
4. E.A. Little and D.A. Stow, *J. Mater. Sci.* 14 (1980) 89
5. R. Bullough, M.H. Wood and E.A. Little, Proc. Tenth Int. Symp. on "*Effect of Radiation in Materials*", Eds. D. Kramer, H.R. Brager and J.S. Perrin, ASTM Special Tech. Pub. No.725 (1981) p.593
6. B.A. Chin, R.J. Neuhold and J.L. Straalsund, *Nucl. Tech.* 57 (1982) 426
7. G.R. Odette, *J. Nucl. Mater.* 155-157 (1988) 921
8. E.A. Little, *J. Nucl. Mater.* 87 (1979) 11
9. E.A. Little, R. Bullough and M.H. Wood, *Proc. Roy. Soc. London* A372 (1980) 565

10. E.A. Little and D.A. Stow, *J. Nucl. Mater.* 87 (1979) 25
11. J.S. Straalsund, R.W. Powell and B.D. Chin, *J. Nucl. Mater.* 108/109 (1982) 299
12. S.L. Mannan, *Trans. Ind. Inst. Metals* 42 (1989) 545
13. M.K. Booker, V.K. Sikka and B.L.P. Booker, *Ferritic Steels for High Temperature Applications*, Ed. Ashok K. Khare, Proc. ASM Int. Conf. on "Production, Fabrication, Properties and Applications of Ferritic Steels for High Temperature Applications", Warren, Pennsylvania (1981) p.257
14. B.J. Cane, Proc. Symp. "*Creep Resistant Steels for Power Plants*", BHEL Corporate R&D, Hyderabad, India (1983) p.15
15. Roy C. Wilcox and Bryan A. Chin, *J. Nucl. Mater.* 122 (1984) 349
16. K.J. Harrelson, S.H. Rou and R.C. Wilcox, *J. Nucl. Mater.* 141/143 (1986) 508
17. B.C. Edwards and E.A. Little, Proc. Int. Conf. on "*Ferritic Steels for Fast Reactor Steam Generators*", Eds. S.F. Pugh and E.A. Little, British Nuclear Energy Society (BNES), London (1978) p. 145
18. M. Menyhard and C.J. McMahon Jr., *Acta Metall.* 37(8) (1989) 2287
19. R.N. Wright, *Toughness of Ferritic Stainless Steel*, ASTM-STP 706, Ed. R.A. Lula, ASTM (1980) p. 2

20. F.W. Noble, B.A. Senior and B.L. Eyre, *Acta Metall.* 38(5) (1990) 709
21. P.J. Maziasz, *J. Nucl. Mater.* 168/169 (1989) 95
22. D.S. Gelles, *J. Nucl. Mater.* 108/109 (1982) 515
23. J.M. Dupouy, Y. Carteret, H. Aubert and J.L. Boutard, Proc. Conf. "*Ferritic Alloys for use in Nuclear Energy Technologies*", Eds. J.W. Davis and D.J. Michel, TMS-AIME, New York (1984) p.125
24. D.R. Harries, *ibid*, p.141
25. K.Q. Bagley, E.A. Little, V. Levy, A. Alamo, K. Ehrlich, K. Anderko and A. Calza Bini, Proc. Int. Conf. on "*Materials for Nuclear Reactor Core Applications*", Bristol, BNES, London, Vol.2 October (1987) p.37
26. W.L. Bell, T. Lauritzen and S. Vaidyanathan, Proc. Conf. on "*Ferritic Alloys for Use in Nuclear Energy Technologies*", Eds. J.W. Davis and D.J. Michel, TMS-AIME, New York (1984) p.113
27. T. Lauritzen, W.L. Bell and S. Vaidyanathan, *ibid*, p.623
28. K. Anderko, *J. Nucl. Mater.* 95/96 (1980) 31
29. E.A. Little, Proc. Int. Conf. on "*Materials for Nuclear Reactor Core Applications*", Bristol Vol.2 (1987) p.47

30. D.S. Gelles, *J. Nucl. Mater.* 122/123 (1984) 207
31. E.H. Lee, P.J. Maziasz and A.F. Rowcliffe, Proc. Conf. on "*Phase Stability during Irradiation*", Eds. J.R. Holland et. al., The Metallurgical Society of AIME, Warrendale, PA (1981) p.191
32. Gary S. Was, *Prog. in Surface Science* 32 (1990) 211
33. K. Farrell, J. Bentley and D.N. Braski, *Scripta Met.* 11 (1977) 243
34. S. Hamada and P.J. Maziasz, *J. Nucl. Mater.* 170 (1990) 124
35. T. Aruga, Y. Katano and K. Shiraishi, *J. Nucl. Mater.* 122/123 (1984) 1401
36. K. Suganuma and H. Kayano, *Radiation Effects* 54 (1981) 81
37. T.M. Williams, J.M. Titchmarsh and D.R. Arkell, *J. Nucl. Mater.* 107 (1982) 222
38. Peter Ehrhart, *J. Nucl. Mater.* 216 (1994) 170
39. H. Peisl, *J. Appl. Crystallogr.* 8 (1975) 143
40. G. Amarendra, *Phys. News* 61 (1992) 23
41. A. Bharathi and C.S. Sundar, *Metals Materials and Processes* 8(1) (1996) 31
42. W. Jager, P. Ehrhart and W. Schilling, *Solid State Phen.* 3/4 (1988) 279

43. J. Tafto and Z. Liliental, *J. Appl. Cryst.* 15 (1982) 260
44. J. Tafto and J.C.H. Spence, *Science* 218 (1982) 49
45. J. Tafto, *J. Appl. Cryst.* 15 (1982) 378
46. J. Tafto and J.C.H. Spence, *Ultramicroscopy* 9 (1982) 243
47. D.L. Davidson, *International Metals Reviews* 29 (1984) 2
48. R. Vincent and D.R. Exelby, *Acta Cryst.* A51 (1995) 801
49. J.W. Steeds, *Introduction to AEM*, Ed. J.J. Hren, J.I. Goldstein and D.C. Joy, Chapter 15, p. 387
50. M. Tanaka, R. Saito and H. Sekii, *Acta Cryst.* A39 (1982) 357
51. P.M. Jones, G.M. Rackham and J.W. Steeds, *Proc. Roy. Soc. Lond.* A354 (1977) 197
52. F.W. Schapink and S.K.E. Forghany, *Acta Cryst.* A39 (1983) 805
53. M. Raghavan, J.Y. Koo and R. Petkovic-Luton, *J. of Metals*, June (1993) 44
54. M. Tanaka and M. Terauchi, "Convergent Beam Electron Diffraction", Published by JEOL Ltd. (1985)

55. K.W. Andrews, D.J. Dyson and S.R. Keown, *"Interpretation of Electron Diffraction Patterns"*, Adam Hilger Ltd., London (1971) p.202
56. *ibid*, p. 211
57. K.G.M. Nair, M. Vijayalakshmi and Kanwar Krishan, *Scripta Met. et. Materialia* 29 (1993) 913
58. A.K.Tyagi and R.V.Nandedkar, *J.Nucl.Mater.* 148 (1987) 76
59. Z.H.Luklinska, G.von Bradsky and P.J.Goodhew, *J.Nucl.Mater.* 135 (1985) 206
60. P.J.Maziasz, R.L.Klueh and J.M.Vitek, *J. Nucl. Mater.* 141/143 (1986) 929
61. J.L.Brimhall, D.R.Baer and R.H.Jones, *J. Nucl. Mater.* 103/104 (1981) 1379
62. *"Binary Alloy Phase Diagrams"*, Eds. T.B. Massalski, H. Okamoto, P.R. Subramanian and L. Kacprzak, ASM (1986) p.131
63. P. Stadelmann, *Private Communication*, I2M, EPFL, CH-1015, Lausanne, Switzerland
64. K.G.M. Nair, M. Vijayalakshmi and Kanwar Krishan, Proc. Symp. on *"Solid State Physics"*, December 1991, BHU, Varanasi (India)
65. N. Kamigaki, S. Furuno, K. Hojou, K. Ono, E. Hashimoto, K. Izui and T. Kino, *J. Nucl. Mater.* 191 (1992) 1214

66. K.G.M. Nair, "*A Study of Low Energy Helium and Argon Ion Implantation in Concentrated Al-Mn Alloys*", Ph.D Thesis, submitted to University of Madras (1992)
67. J.P. Riviere, *Radiation Effects* 33 (1977) 21
68. J.C.H. Spence and J.M. Zuo, "*Electron Microdiffraction*", Plenum Press, New York and London (1992) p. 30
69. J. Burke, "*The Kinetics of Phase Transformations in Metals*", Pergamon Press, Oxford (1965) Chapter 3, p.61
70. K.B.S. Rao, M. Vijayalakshmi, M. Valsan, S.L. Mannan and P. Rodriguez, *Scripta Met.* 23 (1989) 157
71. K.B.S. Rao, M. Vijayalakshmi, M. Valsan, S.L. Mannan and P. Rodriguez, *Scripta Met.* 20 (1986) 989
72. D.M. Bird and M. Saunders, *Ultramicroscopy* 45 (1992) 241

CHAPTER 6

SUMMARY

6.1 SUMMARY

The present thesis, entitled " **APPLICATION OF ANALYTICAL ELECTRON MICROSCOPY AND CONVERGENT BEAM ELECTRON DIFFRACTION FOR THE STUDY OF MICROSTRUCTURAL EVOLUTION IN THE WELDMENTS OF 9Cr-1Mo STEEL**" presents two major themes, which can be stated as follows:

- ** A complete understanding of the microstructural state of weldments of 9Cr-1Mo steel, with respect to microstructure, microchemistry and lattice strain of the constituent phases have been arrived at. The emphasis in this part of the study has been to understand the evolution of different microstructures during welding and the modification in the as-welded structure, at elevated temperatures.
- ** The second theme pertains to the identification of the defects and the lattice strain, using recent advances in electron microscopy. The problems chosen for the unambiguous, unique description of structure correspond to those which could not be solved using conventional techniques.

The first chapter of the thesis presents a brief introduction to the study of metastable microstructures. Recent advances in electron microscopy are briefly reviewed. Advanced electron microscopy techniques have been used to solve some of the problems relating to the unambiguous characterisation of such structures.

6.2 MICROSTRUCTURAL STUDIES ON WELDMENTS OF 9Cr-1Mo STEEL

Detailed description of the primary and secondary microstructures that evolve during the solidification of weldments of 9Cr-1Mo steel has been provided. Modification of these structures during exposure to high temperatures is studied using AEM and CBED. The salient features of these studies are highlighted, in this section.

6.2.1 Salient Features Of 'As-Welded' Structure

The as welded structure of the weldments of 9Cr-1Mo steel is heterogeneous and complex. Hence, four experimental classification schemes have been followed to propose a comprehensive understanding of the 'as-welded' structure. These classifications are as follows: a) the primary structure, b) the secondary or the re-heated structure, c) strain from the top to the root of the weld and d) variation of strain from the weld to the base metal.

The microstructurally distinct zones within the primary structure have been identified. The possible thermal cycles which various regions have been subjected to are deduced, based on the comparison of the results with available data on wrought 9Cr-1Mo steel.

The secondary structure is characterised by the presence of repetitive structures, within the weld region, caused by the multiple passes during MMA welding process.

Based on the detailed studies, a three dimensional "phase field map" has been proposed for the weldments of 9Cr-1Mo steel. This map depicts the steep variation in the phase fields of the different regions of the weldment.

Variation of lattice strain from the top of the weld to the root, along the weld centre line has been understood in terms of the precipitation of carbides and softening of substructure, as a result of differences in the thermal cycles in these regions.

The relative changes in the strain of the α -ferrite, from the base metal to the weld region have been evaluated using shift in the HOLZ lines in the CBED patterns of α -ferrite. The same principle is used to identify the presence of δ -ferrite in a martensitic matrix.

Thus, an attempt has been made to provide a complete description of the weldments of 9Cr-1Mo steel in their as-welded state, with respect to the microstructure, microchemistry and strain, based on detailed studies using AEM and CBED.

6.2.2 Modification of the "As-welded" Structure of Weldment of 9Cr-1Mo Steel at Elevated Temperatures

Next, the microstructural modification of the heterogeneous structure of weldment of 9Cr-1Mo steel at elevated temperatures has been studied. These studies are carried out in the three distinct regions of the weldment - the weld, the HAZ and the base metal. The salient features of these studies are as follows:

Tempering kinetics of the weld region has been studied, using the rate of change of hardness i.e., the recovery rate as the kinetic parameter. The temperature dependence of this parameter shows an Arrhenius behaviour. The activation energy of the process is found to be 0.63 eV, which is reasonably close to the activation energy of 0.8 eV,

for migration of carbon in α -ferrite. Hence, the migration of interstitial carbon is found to be the rate controlling process for the tempering kinetics.

Sequence of evolution of secondary carbides and the variation in their microstructural and microchemical parameters, in the three different regions of the weldment exposed to elevated temperatures, have been studied in detail.

Recognising the need for a fundamental parameter to describe the evolution of carbides in the weldments, a new concept of 'phase evolution diagram' has been proposed. The phase evolution diagrams have been generated for the weld and the HAZ regions of the weldments of 9Cr-1Mo steel, at three temperatures. The application of these diagrams to predict microstructural evolution has been demonstrated.

Thus, the results with respect to the first theme of the thesis, namely, evaluation of microstructural states in the weldments of 9Cr-1Mo steel may be summarised as follows:

- ** Three-dimensional representation of primary and secondary structures.
- ** Identification of a method to distinguish strain-free high temperature δ -ferrite in a strained martensitic matrix.
- ** Measurement of lattice strain across different regions of welds.
- ** Study of tempering kinetics, evaluation of the activation energy for the tempering process and identification of the rate-limiting step.
- ** Evaluation of the changes in the microstructure and microchemistry of secondary phases that evolve at elevated temperatures.

- ** Generation of phase evolution diagrams for different regions of the weld at high temperatures.
- ** Demonstration of the predictive abilities of these diagrams.

6.3 APPLICATION OF CONVERGENT BEAM ELECTRON DIFFRACTION TO THE ANALYSIS OF STRUCTURES

The second theme, namely, unique, unambiguous identification of structure using a recent technique like CBED, is explained in this section. CBED has been found to be an appropriate technique for the study of three problems: evaluation of lattice strain, identification of δ in a matrix of α' and the study of point defects in ion irradiated crystals. Since the first two features have already been explained, this section would summarise the results pertaining to the third feature.

A systematic study of changes in the CBED patterns of ion irradiated crystals of α -ferrite and $M_{23}C_6$ in welds of 9Cr-1Mo weldment has been carried out. Two distinct features of CBED patterns have been identified, which contain information about the presence of point defects. These are the a) **intensity oscillations inside (000) disc** and b) **the number of HOLZ rings of CBED patterns**. These two features show unique, systematic changes with the concentration of point defects i.e., with the dose, mass of incident ions and post-irradiation anneal.

In order to identify the origin of the observed changes, the experiments have been repeated in an Al-14 at/o Mn alloy, in which computations of various features like the

projected potential, the Bloch states and the CBED patterns can be carried out, with ease. Based on good qualitative agreement between the experimental and the computed CBED patterns, the origin of the observed changes is identified to be the static displacement disorder of the lattice.

Thus, an attempt has been successfully made for the first time to study the presence of isolated, point defects in equilibrium phases of welds of 9Cr-1Mo steel using CBED. Characteristic signatures of CBED patterns due to the presence of point defects are identified. Systematic changes in these features with variations in the defect density during irradiation and post-irradiation annealing confirm that they can be used for identification of point defects. Comparison of experimental results with computed patterns suggests that the changes in CBED patterns are a manifestation of the static displacement disorder introduced in the crystal.

The possibility of applying CBED for the identification of point defects is of considerable importance, since other techniques like conventional TEM, X-ray diffraction, positron spectroscopy or dilatometry cannot be used to identify point defects in fine regions. Hence, the presence of the two unique features in CBED patterns of ion irradiated crystals, which are sensitive to the concentration of point defects, offers an attractive method for the study of point defects.

Thus, the thesis has presented useful, extensive results on the i) the microstructural evolution in weldments of 9Cr-1Mo steel and ii) the application of CBED for the study of point defects.

6.4 SCOPE OF FUTURE WORK

The possible future directions for work in the areas of physical metallurgy of ferritic steels and application of advanced techniques are as follows:

- ** Application of high resolution AEM to the study of segregation of deleterious elements to grain boundaries and an attempt to develop healing treatments to overcome embrittlement problems in ferritics.

- ** Application of CBED to the study of quantification of point defects, defects and determination of atom positions.

LIST OF PUBLICATIONS

- 1) Initial Stages of Precipitation Reactions in an Al-38a/o Zn alloy, M.VIJAYALAKSHMI, V.Seetharaman and V.S.Raghunathan in Proc. National Conference on Aluminium Metallurgy held in Indian Institute of Science, Bangalore, India during 5-7 October, 1979. p.259-265.
- 2) On the sequence of Precipitation Reactions in an Al-38a/oZn Alloy, M.VIJAYALAKSHMI, V.Seetharaman and V.S.Raghunathan in Physica Status Solidi., (a) 59, K121, (1980).
- 3) Determination of Activation Energy for the Eutectoid Transformation in Al-Zn Alloys, M.VIJAYALAKSHMI, V.Seetharaman and V.S.Raghunathan, Scripta Met., 15, 985 (1981).
- 4) Morphological Features of Discontinuous Reactions in Al-Zn Alloys, M.VIJAYALAKSHMI, V.Seetharaman and V.S.Raghunathan, Materials Science and Engineering, 52, 249 (1982).
- 5) On the various stages of Spinodal Decomposition in an Al-38a/o Zn alloy, M.VIJAYALAKSHMI, V.Seetharaman and V.S.Raghunathan, J. of Materials Science, 17, 126 (1982).
- 6) Cellular Decomposition in Al-Zn Alloys, M.VIJAYALAKSHMI, V.Seetharaman and V.S.Raghunathan, Acta Metall., 30, 1147 (1982).
- 7) Zener Analysis of Cellular Decomposition in concentrated Al-Zn alloys, M.VIJAYALAKSHMI, V.Seetharaman and V.S.Raghunathan, Trans. Ind. Inst. Metals., 36, 4 & 5, 275, (1983)
- 8) A Rapid Method for the Determination of Spinodal Solvus Applied to Al-Zn system, M.VIJAYALAKSHMI, V.Seetharaman and V.S.Raghunathan, Acta Metall., 32, 9, 1371 (1984).
- 9) Positron Annihilation Study of Precipitation in Al-22 a/o Zn Alloy, A.Bharathi, C.S.Sundar and M.VIJAYALAKSHMI, Materials Science Forum, 3, 379 (1985).
- 10) Isothermal Decomposition of the beta phase in a Cu-Zn-Al Alloy, S.K.Mannan, Vaidehi Ganesan, M.VIJAYALAKSHMI, and V.Seetharaman, J.of Materials Science, 19, 2465, (1984).
- 11) Influence of Deformation on Sensitisation Kinetics and its Microstructural Correlation in a Nuclear Grade 316 Stainless Steel, S.K.Mannan, R.K.Dayal M.VIJAYALAKSHMI, and N.Parvathavarthini, J. of Nucl. Materials, 126, 1, (1984).

- 12) Microstructural Changes During Thermal Ageing of Type 316 Stainless Steel Weld Deposit, T.P.S.Gill, M.VIJAYALAKSHMI, J.B.Gnanamoorthy and K.A.Padmanabhan, Presented in the seminar on Welding Metallurgy held at BARC, Bombay during February, 1985 organised by BRNS-DAE and IIW-Bombay.
- 13) Spheroidisation Kinetics of Sigma phase in Aged Type 316L Stainless Steel Weld Metal, T.P.S.Gill, M.VIJAYALAKSHMI and J.B.Gnanamoorthy, Indian Welding Journal, 19,(2) p.200 (1987).
- 14) Transformation of Delta-Ferrite during the post-weld heat treatment of Type 316L Stainless Steel Weld Metal, T.P.S.Gill, M.VIJAYALAKSHMI, P.Rodriguez and K.A.Padmanabhan, Metallurgical Transactions, 20A, 1115 (1989).
- 15) Changes in the decomposition mechanisms of Delta-Ferrite in duplex 316L Stainless Steel Weld Metal with varying carbon contents, T.P.S.Gill, M.VIJAYALAKSHMI, V.S.Raghunathan and J.B.Gnanamoorthy, Presented at the 41st Annual Technical Meeting of Ind.Inst. of Metals., held at Trivandrum during November, 1987.
- 16) Influence of carbon on the transformation kinetics of delta-ferrite in Type 316 Stainless Steel, T.P.S.Gill, V.Shankar, M.VIJAYALAKSHMI and P.Rodriguez, Scripta Met. et Materialia, 27,313,(1992).
- 17) Uniform Matrix Cavitation in High Temperature Fatigue, K.B.S.Rao, M.VIJAYALAKSHMI, M.Valsan, S.L.Mannan and P.Rodriguez, Scripta Met, 20,989,(1986).
- 18) On the mechanism of uniform matrix cavitation in high temperature fatigue, K.B.S.Rao, M.VIJAYALAKSHMI, M.Valsan S.L.Mannan and P.Rodriguez, Scripta Met., 23,2,157 (1989).
- 19) Substructural Changes during Low Cycle Fatigue of AISI 304 Stainless Steel, K.B.S.Rao, M.VIJAYALAKSHMI, S.L.Mannan and P.Rodriguez, Presented at the XVII Annual Meet of EMSI held at Chandigarh during 31st January to 3 Feb. 1986.
- 20) Micromechanisms of Low Cycle Fatigue Deformation and Fracture in Nimonic PE16 Superalloy, M.Valsan, P.Parameswaran, M.VIJAYALAKSHMI, K.B.S.Rao and S.L.Mannan, Presented at the 41st ATM of IIM held at Trivandrum, India during November, 1987.
- 21) High Temperature Low Cycle Fatigue Behaviour of a Nimonic PE16 Superalloy - Correlation with Deformation and Fracture, M.Valsan, P.Parameswaran, K.B.S.Rao, M.VIJAYALAKSHMI, S.L.Mannan and D.H.Shastry, Metall. Trans., 23A,1751 (1992).
- 22) Cavitation Studies on Type 304 Stainless Steel subjected to strain controlled Fatigue Deformation, K.B.S.Rao, M.VIJAYALAKSHMI, M.Valsan, S.L.Mannan and P.Rodriguez in High Temperature Materials and Processes, 9, 1-8, (1988).

- 33) Nature of Phase Transformations in a 9Cr-1Mo Steel, S.Saroja, M.VIJAYALAKSHMI and V.S.Raghunathan, Proc. of Symp. on Solid State Physics held during Jan. 1991, in BARC, Bombay.
- 34) Influence of Cooling Rates on the Transformation Behaviour of 9Cr-1Mo-0.07C steel, S.Saroja, M.VIJAYALAKSHMI and V.S.Raghunathan, J. of Materials Science, 27, 2389, (1992).
- 35) Influence of solutionising treatment on the Microstructure of 9Cr-1Mo-0.07C Steel, S.Saroja, M.VIJAYALAKSHMI and V.S.Raghunathan, Materials Science and Engineering, A154, 59, (1992).
- 36) Microstructural Stability of a 9Cr-1Mo-0.07C Steel during Long Term Exposure at Elevated Temperatures, S.Saroja, M.VIJAYALAKSHMI and V.S.Raghunathan, Materials Transactions Japan Institute of Metals, 34, 10, 901 (1993).
- 37) Microstructural Evolution in Ferritic Steels, M.VIJAYALAKSHMI, Invited talk at the 47th ATM of IIM held at Hyderabad, Nov., (1993).
- 38) Influence of Cr Content on the driving force for martensitic transformation in Cr-Mo steels, P.Parameswaran, S.Saroja, M.VIJAYALAKSHMI and V.S.Raghunathan, *ibid.*
- 39) Influence of initial microstructure on tempering behaviour of 2.25Cr-1Mo steel, P.Parameswaran, M.VIJAYALAKSHMI and V.S.Raghunathan
- 40) Influence of carbon content on the transformation behaviour of austenite in 9Cr-1Mo steel, S.Saroja, M.VIJAYALAKSHMI and V.S.Raghunathan, *ibid.*
- 41) Development of Predictive Procedures for Evolution of Metastable Microstructures in 9Cr-1Mo Steels, S.Saroja, M.VIJAYALAKSHMI and V.S.Raghunathan, Trans. Ind. Inst. Metals., 48, 3, 271 (1995).
- 42) Prediction of Microstructural states in Cr-Mo steels using Phase Evolution Diagram, S.Saroja, P.Parameswaran, M.VIJAYALAKSHMI and V.S.Raghunathan, Acta Met. Mater., 43, 8, p.2985 (1995).
- 43) Decomposition modes of austenite in Cr-Mo Steels, P.Parameswaran, M.VIJAYALAKSHMI and V.S.Raghunathan, J. Nucl. Materials, 232, 226 (1996).
- 44) Effect of carbon content on the microstructural evolution in 9Cr-1Mo steel, S.Saroja, M.VIJAYALAKSHMI and V.S.Raghunathan, To appear in Mat. Sci. & Technology.
- 45) Analytical Electron Microscopy studies of secondary carbides in ferritic steels, M.VIJAYALAKSHMI, S.Saroja, P.Parameswaran and V.S.Raghunathan, Proc. of International Congress on Electron Microscopy held in Paris, 1994.

46) Transmission Electron Microscopy of Irradiation Induced Effects in Al-Mn Alloys, M.VIJAYALAKSHMI, K.G.M.Nair, V.S.Raghunathan and K.Krishan, *ibid*.

47) Convergent Beam Electron Diffraction Studies of Al Mn Phase in an Al-14a/oMn Alloy and the effect of irradiation on CBED, M.VIJAYALAKSHMI, V.S.Raghunathan and K.G.M.Nair, *Proc. of International Congress on Electron Microscopy held in Paris, 1994*.

48) Effect of 50 keV-Alpha particle irradiation in an Al-40a/o Mn Alloy, K.G.M.Nair, M.VIJAYALAKSHMI and Kanwar Krishan, *Proc. National Symposium on Solid State and Nuclear Physics held at BARC, Bombay, Dec., (1987)*.

49) Disappearance of coherent twin interfaces in an Al-40a/o Mn alloy during ion irradiation, K.G.M.Nair, M.VIJAYALAKSHMI and V.S.Raghunathan, *Scripta Met.*, 25, 5,1217, (1991).

50) Early stages of metastable clustering in intermetallic alloys induced by irradiation, K.Krishan, K.G.M.Nair and M.VIJAYALAKSHMI, *Proc. of Indo-US Workshop on "Metastable Microstructures" held at Goa March, 1989, p.205*.

51) Early stages of evolution of bubbles in an Al-40 a/o Mn alloy during Ar ion irradiation, K.G.M.Nair, M.VIJAYALAKSHMI and K.Krishan, *STP ASTM publication of the Proc. of 15th ASTM Symp. on Radiation Effects on Materials at Nashville, Tennessee, USA, June, (1990), p.486*.

52) Formation of two-dimensional Argon clusters in an Al-40 a/o Mn Alloy during 50 keV Argon irradiation, K.G.M.Nair, M.VIJAYALAKSHMI and K.Krishan, *Proc. Symp. on Solid State Physics, Jan. 1991, By*.

53) Radiation induced Amorphisation of ordered Al₆Mn Phase in an Al-14 a/o Mn alloy, K.G.M.Nair, M.VIJAYALAKSHMI and Kanwar Krishan in *Proc. of Symp. on Solid State Physics held during December, 1991, in BHU, Varanasi*.

54) Amorphisation of Al₆Mn Phase in an Al-14 a/o Mn alloy during low energy helium ion bombardment, K.G.M.Nair, M.VIJAYALAKSHMI and Kanwar Krishan, *Scripta Met. et. Materialia*, 29,913, (1993).

55) Irradiation Induced Amorphisation of Al₆Mn Phase in an Al-14a/o Mn Alloy and its crystallisation during Post-irradiation Annealing, K.G.M.Nair, M.VIJAYALAKSHMI and Kanwar Krishan, *Presented at the International Conference on Advances in Physical Metallurgy, March, 1994 at BARC, Bombay*.